

Department of Mechanical and Aerospace Engineering
Faculty of Engineering
University of Strathclyde



Reconfiguring Smart Structures using Approximate Heteroclinic Connections

Jiaying Zhang

Submitted in fulfilment of the requirements for the degree of

Doctor of Philosophy

2017

This thesis is the result of the author's original research. It has been composed by the author and has not been previously submitted for examination which has led to the award of a degree.

The copyright of this thesis belongs to the author under the terms of the United Kingdom Copyright Acts as qualified by the University of Strathclyde Regulation 3.50. Due acknowledgement must always be made of the use of any material contained in, or derived from, this thesis.

Jiaying Zhang
Swansea, Wales, October 2017

This thesis is dedicated to my parents
for their love, endless support
and encouragement.

Supervisors

Professor Colin R. McInnes
School of Engineering
University of Glasgow
Glasgow, United Kingdom

Dr. Malcolm Macdonald
Department of Mechanical and Aerospace Engineering
University of Strathclyde
Glasgow, United Kingdom

Examiners

Professor Paul M. Weaver
Department of Aerospace Engineering
University of Bristol
Bristol, United Kingdom

Professor Matthew P. Cartmell
Department of Mechanical and Aerospace Engineering
University of Strathclyde
Glasgow, United Kingdom

"If you can dream it,
you can do it."
– Walt Disney

Acknowledgement

It is really a challenge to pursue a doctoral degree study in a different country, especially for those who are not a native speaker of English. When I was given the opportunity to research in Glasgow, this was an entirely new adventure not just for my academic, but for my lifetime.

In the end stage of my PhD period, also my schoolchild's life, I am obliged gratitude to many kind, warm-hearted and accommodating people. First of all, I wish to thank Professor Colin McInnes, for providing me with this fantastic journey, and for his excellent supervision during my time at both the University of Strathclyde and the University of Glasgow. I was fortunate to be his first Chinese student and have been amazed by his passion for research and commitment to his students. This thesis cannot successfully be completed without his guidance and support.

Furthermore, I would like to recognize our group members, Dr Patricia Verrier, Dr Giorgio Mingotti, Dr. Jeannette Heiligers, Dr. Andreas Borggrfe, Dr. Daniel Garca-Yrnoz, Stephen Greenland, Garrie Mushet, Michael Robertson, Jianlin Cao, Callum Arnot, Federica Bonetti, Frank-Minghu Tan, George Knox and Nemo-Xiaoyu Liu. I would also like to thank the visiting scholars in our group, Dr Dong Qiao, Dr. Jiafu Liu, Dr. Francisco Tipn, Dr Ming Xu and Yuki Kawai. I will always remember our friendship with its good memories. My time at Glasgow (both Strathclyde and Glasgow Uni) started 4 years ago, met amazing people along the way and have been given many great opportunities. Thank you for that, for all the support and all the good times, I didnt want to finish my PhD without saying a massive thank you to you all. I will most definitely miss it and wish you all the very best!

I would also like to thank Dr Malcolm Macdonald for his helpful support and make great efforts for my thesis and Viva. My thanks also go to Dr Irina Trendafilova,

Professor Paul Weaver and Professor Matthew Cartmell for providing such a welcoming atmosphere and constructive feedback during my Viva.

Last, but not the least, I express my gratitude to my parents whom I have much missed, and many thanks for supporting me in my studies in the United Kingdom. Their patience and encouragement in every moment were so motivating to me.

Jiaying Zhang
Swansea, Wales
April, 2018

Abstract

The term smart structures is commonly used to describe structures which have the ability to actively change their geometry or mechanical properties. Potential applications can be found in the aerospace, energy and marine sectors, e.g. use of MEMS-type devices which require frequent switching of compliant components and morphing of advanced aerofoils to generate additional lift. Traditional reconfigurable smart structures are designed with multi-stable characteristics. In particular, such structures can use stored strain energy to enable motion from one stable position to another stable position. However, the means of reconfiguring smart structures between stable configurations requires the input of, and then dissipation of energy to cross the potential barrier separating the stable configurations. Therefore, the accumulated work done for frequently actuated devices in reconfiguring between stable states can be significant. Considering reconfigurable smart structures for power and energy constrained applications, this thesis investigates a novel concept of reconfiguring smart structures between unstable states. The vision is to take advantage of modern dynamical system theory to develop entirely new devices that use the instability of mechanical systems to deliver energy-efficient shape-changing structures. This thesis indicates that theoretically in a simple model, transitioning between unstable states (so-called heteroclinic connections) can be more energy-efficient than traditional structures which transition between stable states and so need to cross a potential barrier. However, further experimental work will be required to verify this initial finding for real engineering systems. Clearly, energy is required to stabilize the unstable configurations, but if the energy required for active control of the instability is sufficiently small, or devices need to be frequently switched between different states, this concept is likely to be of benefit.

The concept of using instability for reconfiguration is demonstrated first by control-

ling a mass-spring chain model through a simple cubic nonlinearity, which is sufficient to provide the required qualitative behaviour of the system. A sufficiently smooth set of functions is then used to generate a path to approximate the heteroclinic connection, which is then used as reference trajectory for reconfiguring between different unstable configurations. Moreover, the model is extended to a smart surface as a two-dimensional spring-mass array without dissipation. It is shown that the active reconfiguration scheme can be used to connect equal-energy unstable (but actively controlled) configurations for the purpose of energy-efficient morphing of the smart surface. However, in consideration of the difference between the cubic and real spring model, a spring-mass model with fully geometric non-linearity is also developed to verify the possibility of using heteroclinic connections to reconfigure future real smart structures.

Furthermore, by considering a compliant mechanism, the concept of reconfiguration of a four-bar mechanism using heteroclinic connections is also investigated. Different models varying from fully rigid to purely elastic are employed to be controlled for reconfiguring between different unstable configurations. In addition, a continuous buckled beam model has been investigated with its characteristics based on the Euler-Bernoulli beam theory. An experimental beam was fabricated with shape memory alloy actuators for active control. Although the shape memory alloy was a slow response to time, it illustrates the possibility of reconfiguration of smart structures by using heteroclinic connections.

In summary, this thesis demonstrates the potential of using heteroclinic connection to reconfigure smart structures with both numerical investigation and experimental validation. This entirely new approach to smart structures offers potentially significant benefits for power and energy constrained applications which require frequent reconfiguration.

Contents

Abstract	viii
Table of Contents	x
List of Figures	xiii
List of Tables	xx
1 Introduction	1
1.1 Background and motivation	1
1.2 Review of previous work	3
1.3 Thesis outline	8
1.4 Contributions of the thesis	10
1.5 Published work	12
1.5.1 Peer-reviewed journal publications	12
1.5.2 Conference paper	12
1.6 Thesis structure	13
2 Theory and Methods	15
2.1 Nonlinear systems and stability	15
2.2 Heteroclinic connections	17
2.3 Control methods	19
2.4 Conclusion	22

3	Cubic Nonlinearity in a N-dimensional Chain	23
3.1	Single mass problem	24
3.2	Two mass chain	25
3.3	Constructing the reference polynomial	28
3.4	Energy evaluation criteria	33
3.5	Inverse methods	35
3.6	Control of approximate heteroclinic connections	37
3.7	Three mass chain	46
3.8	Conclusion	52
4	Spring-Mass Model	54
4.1	2 degree-of-freedom buckling beam model	55
4.2	Optimal control	62
4.3	Bifurcation control	66
4.4	Controlled heteroclinic connections in a dissipative system	71
4.5	Conclusion	78
5	Surface Model	79
5.1	Single mass problem	80
5.2	General methods	82
5.3	Heteroclinic connections	91
5.4	Structure-preserving stabilisation control	95
5.5	Connected smart surface units	97
5.6	Conclusion	100
6	Linkage Mechanism	102
6.1	Rigid four-bar model	103
6.2	Pseudo-rigid four-bar model	110
6.2.1	Pseudo-rigid model	110
6.2.2	Numerical solution	112

6.3	Fully-elastic four-bar model	116
6.3.1	Modelling and analysis	116
6.3.2	Euler-Bernoulli beam model	119
6.3.3	Energy analysis	120
6.3.4	Numerical validation	121
6.4	Conclusion	127
7	Continuous Beam Model and Experiment Validation	128
7.1	Nondimensional buckling problem	128
7.2	Numerical simulation and experimental validation	129
7.3	Conclusion	137
8	Conclusions	138
8.1	Summary and review	138
8.2	Future research	140
	Appendix	142
A	Additional condition of the buckling problem	142
	Bibliography	147

List of Figures

1.1	Integrated smart structure (reprinted from [1] with permission from Elsevier).	3
1.2	Different categories of the existing work on structural reconfiguration.	4
1.3	Operational principle of the LaDEM (laterally driven electromagnetic microactuator) (reprinted from [2] with permission from IOP Publishing).	5
1.4	Potential applications of the SMA-based self-folding laminate: (a) locomotion by wormlike walking; (b) locomotion by rolling; (c) and (d) examples of self-constructed 3D structures via active folding operations (reprinted from [3] with permission).	6
1.5	Reconfiguration of a structure by connecting two equal-energy unstable states (with local energy minima used for control at each state).	9
2.1	Typical phase diagrams arising from the fixed points (adapted from [4]).	18
2.2	A saddle surface with stable and unstable manifolds.	19
2.3	Heteroclinic connection between two distant equilibria E_i^U and E_{i+1}^U in the phase space, formed by the intersection of the stable manifold W^S of E_{i+1}^U and unstable manifold W^U of E_i^U .	20
2.4	Inverse control method.	21
3.1	1 degree-of-freedom buckling beam model.	24
3.2	2 degree-of-freedom buckling beam model.	26
3.3	Bifurcation diagram for the 2 degree-of-freedom buckling beam model.	27
3.4	Potential $V(\mathbf{q}, \boldsymbol{\mu})$ and equilibria (3 unstable equilibria E_0 , E_1 and E_2 , and 2 stable equilibria E_3 and E_4).	29

3.5	Transitions between different equilibria (with potential energy contour levels) (a) Ideal heteroclinic connection through E_3 or E_4 between E_1 and E_2 (b) Crossing the potential barrier E_1 between E_3 and E_4	29
3.6	Control effort evaluation criteria using a simple spring model. Shaded block represents smart material element with internal stiffness (a) Element under external load F (b) Element attached to external spring (adapted from [5]).	34
3.7	Composite feedback linearisation control scheme.	37
3.8	4 th order polynomial as reference trajectory from E_1 at (1, 1) to E_2 at (-1, -1) (a) Controlled transition (b) Geometry of transition process (c) Controls actuated through the parameters μ_1 , μ_2 and μ_3 (d) Mass displacements during the transition from E_1 to E_2 with the reference trajectory and actual trajectory.	38
3.9	4 th order polynomial as reference trajectory from E_3 at (-2/3, 2/3) to E_4 at (2/3, -2/3) (a) Controlled transition (b) Geometry of transition process (c) Controls actuated through the parameters μ_1 , μ_2 and μ_3 (d) Mass displacements during the transition from E_3 to E_4 with the reference trajectory and actual trajectory.	40
3.10	Comparison of energy input for different reconfigurations.	41
3.11	6 th order polynomial as reference trajectory from E_1 at (1, 1) to E_2 at (-1, -1) (a) Controlled transition (b) Controls actuated through the parameters μ_1 , μ_2 and μ_3	42
3.12	Comparison of energy input to track different approximate trajectories.	43
3.13	8 th order polynomial as reference trajectory from E_1 at (1, 1) to E_2 at (-1, -1) (a) Controlled transition (b) Geometry of transition process (c) Controls actuated through the parameters μ_1 , μ_2 and μ_3 (d) Mass displacements during the transition from E_1 to E_2 with the reference trajectory and actual trajectory.	44
3.14	Comparison of energy input to track different approximate trajectories with varying polynomial degree.	45
3.15	Energy required for reconfiguration as a function of reconfiguration duration.	45
3.16	3 degree-of-freedom buckling beam model.	46

3.17	27 equilibria (21 unstable equilibria and 6 stable equilibria).	47
3.18	Potential surface with saddles (blue circle) (a) Potential -0.5 with E_1 and E_2 (b) Potential -0.482 with E_{23} to E_{26} (c) Potential -1.125 with E_3 and E_4 (d) Potential -0.844 with E_{11} and E_{22}	47
3.19	4^{th} order polynomials as reference trajectory from unstable equilibrium E_{12} to unstable equilibrium E_{13} (a) Controlled transition (b) Geometry of transition process, (c) Controls actuated through parameters μ_1, μ_2, μ_3 and μ_4 (d) Mass displacements during the transition from E_{12} to E_{13} with the reference trajectories.	49
3.20	8^{th} order polynomials as reference trajectory from unstable equilibrium E_{12} to unstable equilibrium E_{13} (a) Controlled transition (b) Geometry of transition process (c) Controls actuated through parameters μ_1, μ_2, μ_3 and μ_4 (d) Mass displacements during the transition from E_{12} to E_{13} with the reference trajectories.	50
3.21	Comparison of energy input to track different approximate trajectories.	51
3.22	Comparison of energy to track different approximate trajectories.	52
4.1	2 degree-of-freedom buckling beam model.	56
4.2	Potential $V(\mathbf{x}, \mathbf{L})$ and equilibria (6 stable equilibria E_1 to E_6 , and 6 unstable equilibria E_7 to E_{12}).	58
4.3	Equilibria for a two mass chain with stable equilibria E_{1-6} and unstable equilibria E_{7-12} . The unstable equilibria have equal potential V (Axes are shown in Fig. 4.1).	59
4.4	Controlled transition from E_9 at (1.732,0) to E_{10} at (0,-1.732) with the controller active in the neighbourhood of E_{10} . Contour represents the allowed region of motion with $T(\mathbf{p}) > 0$	61
4.5	Mass displacements during the transition from E_9 at (1.732,0) to E_{10} at (0,-1.732).	61
4.6	Controls in region R of the neighbourhood of E_{10} actuated through the coupling parameters L_2 and L_3	62
4.7	Minimum energy transition with free end time. (a) Mass displacements during the transition from E_9 to E_{10} . (b) Controls actuated through the parameters L_1, L_2 and L_3 . (c) Total energy input.	64

4.8	Controlled transition and optimal transition from E_9 to E_{10}	65
4.9	Energy required for reconfiguration as a function of reconfiguration duration.	65
4.10	Schematic representation of bifurcation control (a) and (c) are different locally stable configurations of the structure (b) heteroclinic connection between the two equal-energy unstable configurations.	66
4.11	Bifurcation diagram for the spring-mass model. Projection of the location of the equilibria onto the x_1 axis for $L_1 = 2$, $L_3 = 2$ and $1 \leq L_2 \leq 3$. Solid line: stable equilibria, dashed line: unstable equilibria.	67
4.12	Effective potential $V(x, \mathbf{L})$ with $L_1 = 2$, $L_2 = 1$ and $L_3 = 2$. E_1 and E_2 are stable, E_3 and E_4 are unstable.	68
4.13	Effective potential $V(x, \mathbf{L})$ with $L_1 = 2$, $L_2 = 2.5$ and $L_3 = 2$. E_1 and E_2 are unstable, E_3 and E_4 are stable.	68
4.14	Controlled transition from E_1 at $(\sqrt{3}, \sqrt{3})$ to E_2 at $(-\sqrt{3}, -\sqrt{3})$ with bifurcation control. The coupling parameters $L_1 = 2$ and $L_3 = 2$ with L_2 switched from 2.5 to 1 to manipulate the stability properties of E_1 and E_2	69
4.15	Potential energy contour plot and ideal path from E_1 at $(\sqrt{3}, \sqrt{3})$ to E_2 at $(-\sqrt{3}, -\sqrt{3})$	70
4.16	Controlled transition from E_1 at $(\sqrt{3}, \sqrt{3})$ to E_2 at $(-\sqrt{3}, -\sqrt{3})$ with bifurcation control with L_2 switched from 1.3 to 2 to manipulate the stability properties of E_1 and E_2	70
4.17	A step change of L_2 (1.3 to 2) during the bifurcation control.	71
4.18	2 degree-of-freedom buckling beam model with damping coefficient β	72
4.19	Control strategy (a) End-point control (b) Continuous control.	73
4.20	Controlled transition from E_9 at (1.732051,0) to E_{10} at (0,-1.73205) with the controller active in the neighbourhood of E_{10} with different dissipation. Solid line: dissipation parameter $\beta = 0.01$, dashed line: dissipation parameter $\beta = 0.05$	75
4.21	Controlled transition from E_9 at (1.732051, 0) to E_{10} at (0, -1.73205) with the controls actuated through L_2 and L_3 in the neighbourhood of E_{10} . (a) Dissipation parameter $\beta = 0.01$. (b) Dissipation parameter $\beta = 0.05$	76

4.22	Controlled transition from E_9 at $(1.732051, 0)$ to E_{10} at $(0, -1.73205)$ with the controller active under the continuous control method (dissipation parameters $\beta = 0.01, 0.05$).	76
4.23	Controlled transition from E_9 at $(1.732051, 0)$ to E_{10} at $(0, -1.73205)$ with the controls actuated through L_2 and L_3 under the continuous control method. (a) Dissipation parameter $\beta = 0.01$. (b) Dissipation parameter $\beta = 0.05$	77
5.1	Spring-mass element.	80
5.2	A simple surface model with fixed boundary condition.	82
5.3	Example of a simple adjacency relationship.	84
5.4	Example of a simple adjacency relationship.	86
5.5	Number of equilibria of the smart surface structure with varying coupling parameter μ_2 with $\mu_1 = 1$	89
5.6	The value of \dot{Q}_2 at the first crossing of the unstable manifold with the Q_2 axis, with the increasing parameter μ_2 ($\mu_1 = 1$).	93
5.7	Heteroclinic connection between at E_1 $(8, 0)$ and at E_2 $(-8, 0)$ for $\mu_1 = 1$ and $\mu_2 = 1.687\mu_1$. The projection of the phase path in the new coordinate space $(Q_2 \rightarrow -Q_2)$	94
5.8	New coordinates $(Q_1 - Q_2)$ for a heteroclinic connection between at E_1 $(8, 0)$ and at E_2 $(-8, 0)$ for $\mu_1 = 1$ and $\mu_2 = 1.687\mu_1$	94
5.9	Transition from unstable equilibria E_1 $(1, 1, 1, 1)$ at $t = 0$ to unstable equilibria E_2 $(-1, -1, -1, -1)$ at $t=10$ for $\mu_1 = 1$ and $\mu_2 = 1.687\mu_1$	95
5.10	Mass displacements under small disturbance around E_1 $(1, 1, 1, 1)$ (a) without control (b) with control.	97
5.11	Control actuators generated through the parameters $\mu_{1,1}, \mu_{1,2}, \mu_{1,3}$ and $\mu_{1,4}$	98
5.12	Schematic diagram of two connected smart surface units.	99
5.13	Configuration change during transition from unit 1 to unit 2.	99
5.14	Corresponding shapes of the connected smart surface (a) initial condition (b) final condition.	100
6.1	Four-bar mechanism with torsional springs model.	103

6.2	Energy and moment for the rigid four-bar mechanism.	105
6.3	Shape of the four-bar mechanism in equilibrium positions.	106
6.4	Experimental four-bar mechanism in equilibrium positions.	107
6.5	Bifurcation diagram for the four-bar mechanism, solid line: stable equilibria, dashed line: unstable equilibria.	107
6.6	Variation of θ_3 during the transition from E_1 to E_2	109
6.7	Control in the neighbourhood of E_2 actuated through the parameter κ_2	109
6.8	Kinematics of the transition process.	110
6.9	Pseudo-rigid model with a single axial spring.	110
6.10	Potential $V(\boldsymbol{\theta}, \boldsymbol{\kappa})$ and equilibria (3 unstable equilibria E_0 , E_1 and E_2 , and 2 stable equilibria E_3 and E_4).	113
6.11	Heteroclinic connection between E_1 and E_2 with the projection of the phase space onto the configuration space shown (note the perpendicular crossing of $\Theta_1 = 0$).	114
6.12	Transformed coordinates Θ_1 and Θ_2 for a heteroclinic connection between E_1 and E_2	114
6.13	Value of $\dot{\Theta}_2$ at the first crossing of the unstable manifold of E_1 with the Θ_2 axis, with increasing parameter ratio κ/k	115
6.14	Uncontrolled heteroclinic connection between E_1 and E_2 in the original untransformed coordinate axes (θ_1, θ_2)	115
6.15	Untransformed coordinates θ_1 and θ_2 for an uncontrolled heteroclinic connection between E_1 and E_2	116
6.16	Fully elastic four-bar mechanism/buckling beam model.	117
6.17	Buckling modes of a clamped-clamped buckling beam.	119
6.18	Buckling modes of a clamped-clamped buckling beam.	120
6.19	Energy comparison between the fully elastic spring model and Euler-Bernoulli beam model for first 2 modes. U_b is the bending energy, U_c is the compressive energy, $U = U_b + U_c$	121
6.20	Corresponding shape of fully elastic model in equilibrium positions.	123

6.21	Controlled transition from E_3 to E_4 with the controller active in the neighbourhood of E_4 (a) Homoclinic connection in the $x_1 - x_2$ coordinate space (b) Heteroclinic connection in the $y_1 - y_2$ coordinate space.	124
6.22	Displacements during the transition from E_3 to E_4	125
6.23	Controls actuated at the end of the transition (a) torsional spring stiffness (b) axial spring stiffness.	126
6.24	Geometry of the transition process wherethe red point is the mid-point of the structure, which has a trajectory shown as a dashed line.	127
7.1	The buckled beam model (a) schematic of an unstable buckled-beam (b) different stage (1-2-3-4) during the reconfigure through.	130
7.2	Simulation result of the deflection history during reconfiguration. τ is the nondimensional time. E_i^u , E^s and E_e^u are the initial unstable configuration, the in-between stable configuration and the terminal unstable configuration, respectively.	131
7.3	The schematic diagram of the heteroclinic connection between two distant equilibria E_i^u and E_i^u in the assumed phase space. w_1 and w_2 are the two extremum of deflection during reconfiguration.	132
7.4	Resulting load-displacement curve of a test beam.	133
7.5	Typical stress-strain-temperature behaviour of Shape Memory Alloys. The pseudo-elastic effect and the Shape memory effect with microscopic phenomenology.	134
7.6	Photograph of the buckled beam(a) acrylic beam without load (b) initial unstable configuration (c) final symmetric unstable configuration.	135
7.7	Load graph during the reconfiguration with three stages (a) numerical result, solid line: with residual tensile force, dash line: without residual tensile force (b) experimental result.	136

List of Tables

3.1	Stability properties of the 5 equilibria of 2 degree-of-freedom buckling beam model.	28
3.2	Stability properties of the 27 equilibria of a three mass chain with $\mu_1 = 1$, $\mu_2 = 1.5$, $\mu_3 = 1.5$ and $\mu_4 = 1$.(Type: 1. S \times S \times S; 2. S \times C \times C; 3. C \times C \times C; 4. S \times S \times C.)	48
4.1	Stability properties of the 13 equilibria of 2 degree-of-freedom buckling beam model.	57
5.1	Stability properties of the equilibria with $\mu_1 = \mu_2 = 1$ and the corresponding surface configuration.	90
6.1	Properties of the four-bar mechanism model.	104
6.2	Equilibrium points and corresponding potential energy.	106
6.3	Equilibrium points with corresponding potential energy.	112
6.4	Stability properties of the 5 equilibria of the fully elastic model.	123
7.1	Geometry property of the proposed beam.	132
7.2	Selected SMA materials properties.	134

Chapter 1

Introduction

In this first Chapter, the scientific framework and the research objectives of the thesis will be defined. The development of smart structures as an architecture for a range of engineering applications will be discussed in Section 1.1, in the context of the limitations and challenges of this technology to date. Section 1.2 will highlight smart structures in applications, provide a brief description of the required key technologies and review current methods for design. This discussion is then used to define the research objectives in Section 1.3. The contributions of the thesis will be highlighted in Section 1.4, while Section 1.5 will provide an overview of published work. Finally, in Section 1.6, an outline of the thesis will be presented.

1.1 Background and motivation

The demand for high-performance engineering structures is continuously increasing, especially in the aerospace, energy and marine sectors. It is clear that modern industry demands structures to have capability for key applications, particularly for energy harvesting, vibration control and structural health monitoring. This also includes structures which actively change their geometry or mechanical properties, e.g. MEMS-type devices which require frequent switching for compliant components and morphing of advanced aerofoils [1]. Therefore, considerable attention has been given to developing advanced materials which have properties that can be changed in a controlled fashion by external stimuli, such as stress, temperature, electric or magnetic fields (e.g. shape memory alloys). These materials can convert a mechanical signal to non-mechanical output for sensing or convert a non-mechanical input into a mechanical output for actuation [6]. Generally, recent developments in smart materials technol-

ogy can be divided in three fields: self-healing materials, smart sensing materials and shape changing materials. Self-healing materials have the ability to respond to damage through some repair mechanism; smart sensing materials can sense stresses, loads and other parameters; shape changing materials exhibit the ability to change shape with low strain/displacements [7]. Therefore, these novel materials can be designed, modelled and manufactured with desired mechanical characteristics which can then be used to develop smart structures. The term smart structure is commonly used to describe structures which have the ability to actively change their geometry or mechanical properties [8]. Smart structures, intelligent structures, adaptive structures and active structures all belong to the same field as they are an integrated system with actuators and sensors embedded in structural components, as shown in Fig. 1.1 [1]. It is clear that the structural control problem for such structures has a great number of specific features compared to other control problems, such as the large number of degree of freedom and light damping ($\xi \sim 0.001$ to 0.05), which can cause the control system to destabilise the flexible modes outside the control bandwidth [9]. These control problems are usually solved by using modal coordinates, such as beam [10], plate [11] and truss [12].

Meanwhile, smart structures can also be used to provide power as an energy source for small electronic devices without external power suppliers, which extract power from the environment as an energy harvesting structure [13]. Both numerical simulation and experimental validation have investigated harvesting vibrational energy in a simple model, and with additional periodic forcing which can be added to enhance energy harvesting [14, 15, 16]. In addition, damage can reduce safety and reliability of in-service structures, so that structural health monitoring (SHM) is a key strategy to implement damage identification through embedding smart materials [17, 18].

Among the development of advanced engineering and scientific applications, structures are required to deform from their initial configuration to another configuration in order to accommodate a desired new geometry. For example, in botany, the Venus flytrap (*Dionaea muscipula*) leaf can snap from curved outward (convex) in the open state, to curved inward (concave) in the closed state in about 100 ms [19]. This change of state can provide the means to investigate deformable biomimetic smart structures.

The concept of reconfiguring a structure normally implies changing the spatial shape of a structure from its initial shape to a desired shape. According to previous research reviews [20, 21], this can be classified in two categories, as shown in Fig. 1.2: 1) shape control in which the structure is maintained in a shape obtained from elastic or plastic deformation using actuating forces, or by moving rigid bodies by a driving

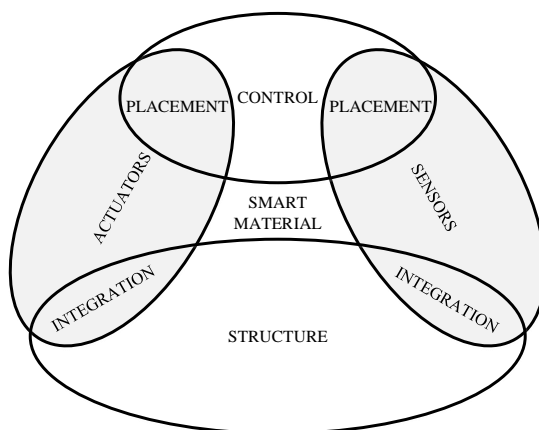


Figure 1.1: Integrated smart structure (reprinted from [1] with permission from Elsevier).

mechanism [22, 23]; and 2) shape morphing in which the structure can be changed by using stiffness and force. It is clear that such structures can be designed and fabricated by smart materials so that they can morph to other configurations upon a stimulus. The dimension, stiffness and force of smart materials are related by the material constitutive equation, and can then derive the dynamical equations of the structure [24]. These reconfigurable structures can be designed as a fully integrated system with distributed sensing and actuation.

1.2 Review of previous work

Traditional shape control methods have long been applied to structures, from simple structures such as beams and plates to complex multi-body structures. Numerous studies have investigated beams and plates to provide the governing equation of a coupled structure/actuator system. For example, a cantilever beam with an active vibration damper designed using a piezoelectric polymer actuator. The governing equation of the composite beam were obtained based on the conventional Bernoulli-Euler beam [25]. A nonlinear model of an electrically actuated microbeam was also investigated to study its mechanical behavior and static and dynamic characteristics, e.g. static deflection and natural frequencies, which were compared with experimental results to validate the proposed numerical model [26]. In addition, the stability of beam-type structures has been enhanced using piezoelectric transducers and studied through theoretical, numerical and experimental methods [27]. The buckling of beams as a classic problem of stability has attracted many researchers, and the problem of buckling control was addressed by using smart materials [28]. Meanwhile, active control of a plate was ex-

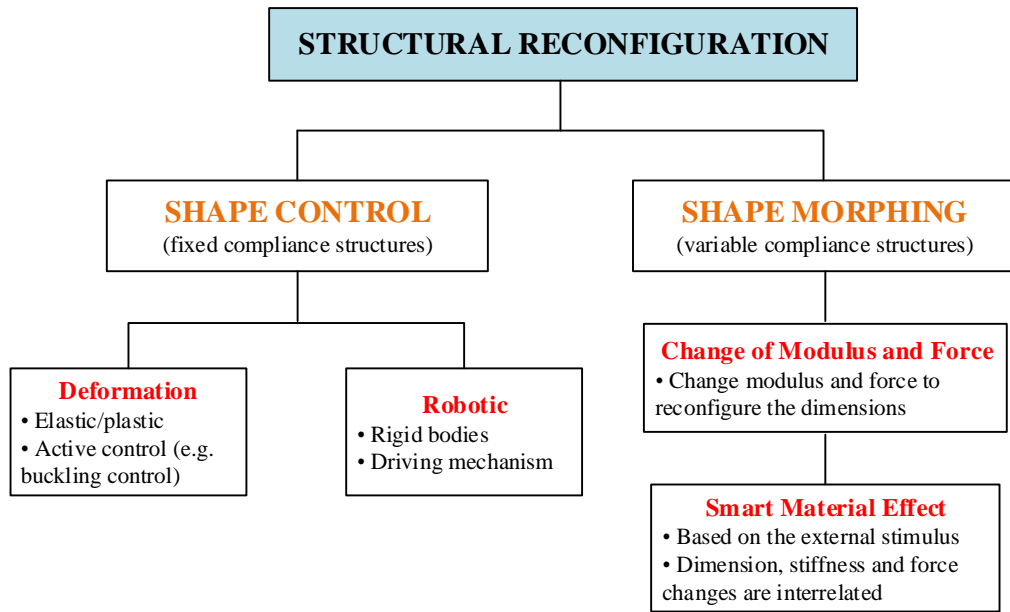


Figure 1.2: Different categories of the existing work on structural reconfiguration.

explored by means of embedded smart materials such as shape memory alloys (SMA) [29]. A prototype of a planar bending actuator was developed by embedding SMA wires in an elastic substrate, and the dynamical characteristics were verified through simulation and experimental methods [30]. Furthermore, the stability problem of a plate that is similar to a beam, is a core characteristic of active control of structures and therefore is always used to address the buckling by piezoelectric actuator/sensor pairs. The governing equations developed based on classical elastic theory and the piezoelectric effect can provide an analytical method which can change the buckling behavior of the plate effectively [31].

Over the past few decades, a number of active structures using smart materials such as electromagnetic materials, piezoelectric materials and shape memory materials have been suggested for various applications. A microactuator was developed to switch a large-displacement optical system by using electromagnetic materials, as shown in Fig. 1.3. Based on classical electromagnetism, a force could be induced along the arch-shaped leaf spring when current is applied to the micro-structure. A snap-through buckling behaviour could then be produced at a critical current applied to the structure to increase its displacement as an actuator [2]. With the advent of bio-compatible materials, many biomedical actuators have been developed for both the medical field and bionic technology. For example, a bending fluidic actuator (BFA) can correlate

deflection and pressure input, which can provide the highest ratios of angular deflection [32].

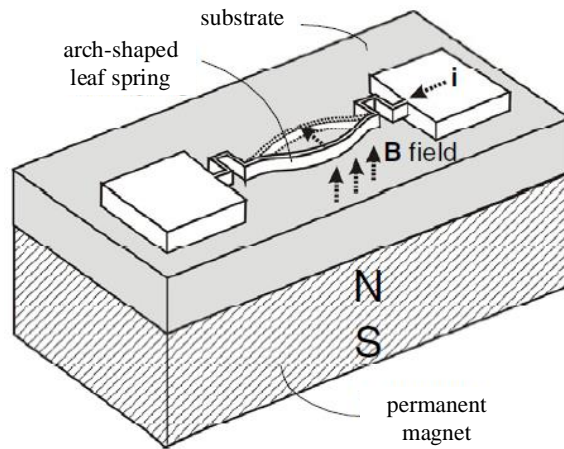


Figure 1.3: Operational principle of the LaDEM (laterally driven electromagnetic microactuator) (reprinted from [2] with permission from IOP Publishing).

A self-folding reconfigurable structure was designed as an active compliant laminate by embedding thermally-actuated shape memory alloy elements. This programmable structure was fabricated with different layers. The active layers were thin films of pre-strained thermally-activated SMA materials, so that such structures could be formed and reconfigured in three dimensions with the appropriate heating zone, as shown in Fig. 1.4 [3]. Another composite laminate was developed to have an asymmetric bistable property that can be controlled to snap-through by adhered piezoelectric MFC (macro fiber composite). Finite element analysis was used to predict induce voltage and track the voltage-deflection behavior of the smart bistable laminate, and then experiments were performed to validate the results [33].

Some structures have been design to be deployable for advanced applications, such as space exploration missions. These kinds of structure can offer high packing efficiency for reduced mass and launch cost and reliable performance. Some intelligent flexible materials have been used for deployable space structures that can be used in a variety of system architectures [34]. The shape memory polymer (SMP) has been used to fabricate shape memory composites (SMC) to change their stiffness or volume. In order to prove the possibility of this method, a SMC self-deployable structures was prototyped as a composite frame of a conceptual solar sail, which can successfully self-deploy following desired constraints and without damage [35]. A new concept to reconfigure structures from two-dimensional into three-dimensional objects according to origami has been

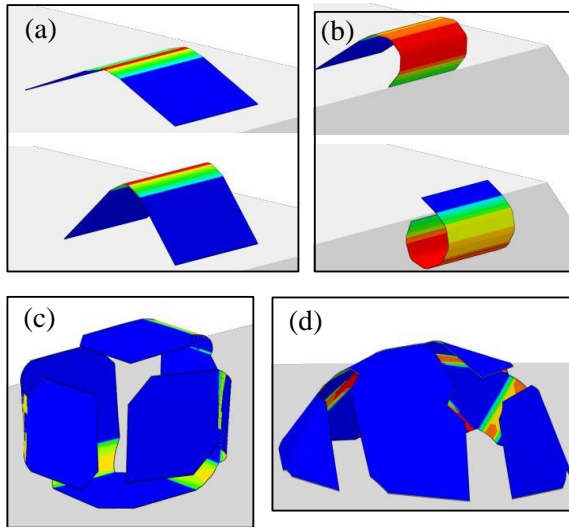


Figure 1.4: Potential applications of the SMA-based self-folding laminate: (a) locomotion by wormlike walking; (b) locomotion by rolling; (c) and (d) examples of self-constructed 3D structures via active folding operations (reprinted from [3] with permission).

investigated. Rigid origami of thick panels were joined together by creases under a specific design pattern and kinematic theory was then used to simulate folding [36]. In order to implement a self-folding origami concept, programmable matter has been investigated to achieve specific shapes upon command. An end-to-end approach was presented to create self-folding origami sheets, which can realise multiple shapes based on the embedded actuator and control algorithms [37]. Meanwhile, a shape-memory composite has been fabricated to fold itself along embedded hinges, and then the three-dimensional shape mechanism can translate as a crawling machine [38]. Moreover, shape-memory material has also been used to design an auxetic structure that could deploy under external stimulus. Shape memory polymers were used to demonstrate that they can release sufficient strain energy at thermally-triggered shape recovery to assist self-deployment and two different chiral auxetic structures were fabricated and tested [39]. Another study proposed a foldable bar structure which consists of pairs of straight bars connected by pivots, with cables used as active and passive elements to form a three-dimensional pantograph [40, 41].

Moreover, many structures are designed to be multi-stable equilibrium systems, so-called compliant mechanisms such as bi-stable and tri-stable mechanisms. These structures have a number of advantages compared to conventional mechanisms, such as reducing the number of components required [42]. An arbitrarily shaped, precurved,

clamped beam has been described under distributed mechanical loading or electrostatic loading and different solution methodologies used to predict equilibrium paths [43]. A mathematical approach had been investigated to synthesise multistable compliant systems by combining multiple bistable mechanisms. This multistable structure could be designed to have a desired number of stable positions, and the key parameters could be obtained through the potential energy path that connects stable points to each other [44]. A new formulation has been used to generate multistable compliant mechanism upon snap behavior, the shape could optimized to satisfy desired displacements [45]. A refined analytical approach has been presented to predict the geometry of stable shapes of bistable plates, which facilitates methods for a systematic and parametric exploration of the design space [46]. Furthermore, a number of morphing structures capable of large deformations have been investigated to combine material properties and structure geometry [47, 48]. Some were inspired by biology (virus bacteriophage T4) and act as a bistable cylindrical lattice of helices [48]. The purpose of the investigation of multistable structures is that numerous engineering applications could benefit from these kinds of devices with multistable equilibrium positions, for example, a micromechanism can be designed for multistable switches [49], a helicopter rotor blade can be designed to extensible with cosine bistable arches [50] and a scalable honeycomb shell has been investigated without using composite or prestressed materials [51].

Structures likewise have been designed to be adaptive systems and integrated with smart materials, such as laminated composite plates, which could provided adaptive shape control by using piezoelectric materials [52]. These adaptive structures could fulfill many modern engineering requirements. For example, a deformable wheel has been designed to possess the potential for obstacle avoidance, from narrow gaps to high steps [53]. Some length-adjustable bars have been assembled to create an adaptive slow-moving space crane, which can change its geometry without creating internal stresses and vibration [54, 55]. The concept of adaptive structures has been applied in aeronautical and astronautical engineering. The feasibility of employing adaptive materials to build both sensors and actuators to suppress higher harmonic loads has been investigated to develop new helicopter rotor blades [56]. Another type of novel active aeroelastic structure (AAS) could actuate UAV wings to provide roll control, which changes the relative chord-wise positions of the front and rear spar webs to produce varying torsional stiffness of the wing-box [57]. Moreover, Earth-orbiting satellites regularly pass from sunlight to shade and back, and these transitions are naturally accompanied by significant temperature changes. Thermal mismatch stresses therefore arise in the structures of the satellites. Based on this situation, adaptive biomaterial lattices have been designed to eliminate thermal mismatch stresses and their consequences

[58]. A novel future space telescope concept has been proposed to assemble multi-layer adaptive thin shells, which could guarantee optimum morphing with an arbitrary profile through active control [59]. In addition, rather than proposing an actual physical model, the design of smart structures by connecting multiple unstable configurations through a representative model have been explored, using of heteroclinic connections between unstable equilibria [60, 61, 62]. In summary, smart structures have the potential to provide a unique competitive advantage to future engineering applications over conventional static structures.

1.3 Thesis outline

From the discussion of reconfigurable smart structures in Section 1.1 and their application to deliver actively controllable, multistable mechanisms in Section 1.2, the vision of this thesis is to take advantage of modern dynamical system theory to develop new devices that use the heteroclinic connections to deliver energy-efficient shape-changing structures. A heteroclinic connection is a special trajectory which is formed if the unstable manifold of an equilibrium point intersects the stable manifold of another distant equilibrium point in phase space. In particular, transitions using heteroclinic connections between equal-energy unstable equilibrium points could be significantly more energy-efficient than traditional structures which transition between stable equilibrium points. It is considered that the mechanical systems here exhibit conservation of energy, so that the internal distributions of kinetic and potential energies can therefore be exchanged during the transition process. Transitioning along the heteroclinic connection, the potential energy of the system is firstly converting to kinetic energy until kinetic energy is at a maximum at the intermediate stable equilibria and then converted back to potential energy at the new unstable equilibrium point.

Figure 1.5 shows the key concept of reconfiguring smart structures using approximate heteroclinic connections. Here x_1 and x_2 indicate the displacement of two masses connected by springs, where time is non-dimensional, and so the figures present a brief introduction to the strategy where more details will be discussed in later chapters (including non-dimensional variables).

In stage I, the structure is in a locally stable condition, which has a local potential well. This condition is therefore locally stabilising and considered as an initial state. Then, in the stage II, active control is used to change the local characteristics of the system from stable to unstable to initiate reconfiguration by using a heteroclinic connection. For example, the properties of the spring material could be changed and so the local

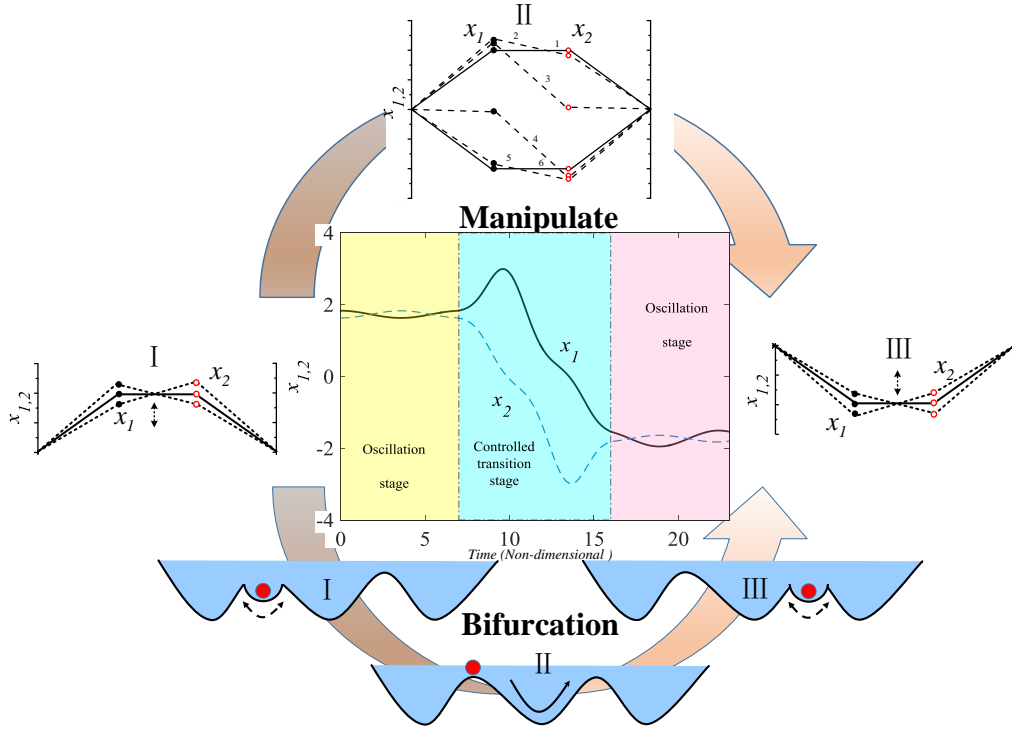


Figure 1.5: Reconfiguration of a structure by connecting two equal-energy unstable states (with local energy minima used for control at each state).

potential well therefore disappears. Finally, in stage III, the structure can be reconfigured from the final unstable state, with a local potential well created for the structure to remain in that final state.

The focus on this thesis is primarily to use simple models to demonstrate the feasibility of reconfiguration of a smart structure between unstable states using heteroclinic connections in phase space. This strategy provides insights into the problem which can be exploited to develop the concept towards the reconfiguration of real smart structures.

The following **research objectives** can be defined:

Spring-mass model

- Develop a simple representative spring-mass model to exploit instability using modern dynamical systems theory.
- Reconfigure this type of structure using heteroclinic connection in phase space formed through the unstable manifolds of equilibrium points.
- Investigate approximations to heteroclinic connections in the simple model.

- Use different order polynomials to approximate heteroclinic connection.
- Investigate a two dimensional array of connected springs and masses as a smart surface.

Linkage mechanism

- Investigate a four-bar mechanism with elastic elements to exploit their significant nonlinearity.
- Develop a reconfiguration through connections in the phase space of this rigid bar mechanism.
- Develop a pseudo-rigid model to illustrate interesting complexities over the rigid model.
- Reconfigure this type of structure between different buckling configurations.

Continuous Beam Model

- Investigate a classical clamped-clamped beam based on the Euler-Bernoulli beam theory.
- Develop different buckling conditions through the mathematical analysis for potential reconfiguration.
- Fabricate an experimental beam by using joints with the shape memory alloy wires.
- Use the experimental set-up to verify the concept using heteroclinic connection for reconfiguring a structure.
- Compare numerical simulations and experiment results.

1.4 Contributions of the thesis

In this thesis, the potential of reconfiguring smart structures using heteroclinic connection is demonstrated, in order to realise new and more energy-efficient reconfiguration strategies.

The smart structure is firstly modelled as a single lumped mass and the stiffness of a beam by two linear springs with both ends clamped. The nonlinear characteristic of this mechanical system is introduced, and by using dynamical system theory, a set of equilibria can then be obtained that represent different configurations of the structure. Some of these equilibria are unstable, but active control can in principle be used to stabilise these unstable states. For energy-efficiency, the transitions between unstable states are more advantageous than transitions between stable states, since the transition between stable configurations requires the input of, and then dissipation of energy to cross the potential barrier separating the stable equilibria. As noted earlier, the use of heteroclinic connections appears attractive, although work is required to stabilize the structure when operating in the unstable configurations. Therefore, bifurcation methods are investigated through manipulating some internal parameters of the structure. A property of such nonlinear systems is that there may exist a series of equilibria which do not change their location under manipulation of internal parameters, but the stability or instability of these equilibria will be changed. Such phenomena can be used to produce a local potential well for a reconfiguration of smart structures using bifurcation control. Moreover, a smart surface structure is investigated consisting of a two-dimensional array of connected springs and masses and heteroclinic connections used as a means to reconfigure this simple model.

Some mechanisms have been developed that possess two or more equilibrium configurations, so-called multi-stable mechanisms. A linkage mechanism has then been investigated to exploit this multi-stable property based on nonlinearity for reconfiguration between different states. The difference between structures and mechanisms is that structures can be deformed under external loads, therefore, some elastic components (e.g. torsional spring) are considered to join with the rigid elements for establishing a pseudo-rigid compliant mechanism. Moreover, this elastic component could be made of smart materials for active control to realise the reconfiguration of this mechanism. In order to confirm the reliability of the control method, a Lyapunov function is proposed to demonstrate convergence to the required equilibrium point. This analysis again supports the concept of using heteroclinic connection for reconfiguring mechanisms between unstable configurations.

Following these results, the concept of reconfiguring smart structures using heteroclinic connections is further demonstrated for continuous beam structures. Partial differential equations are used to establish the analytical beam model, and the corresponding theory is used to analyse elastic behaviour of the beam. Smart materials, such as piezoelectric materials, could be used to control the stability of the beam and actuate the beam for

reconfiguration between different buckling shapes.

In summary, this thesis demonstrates the potential of reconfiguring smart structures using heteroclinic connections and different analytic and numerical models are provided based on the dynamical system theory. Moreover, some preliminary experiments are applied to verify relevant simulation results and provide insight to high fidelity models for further applications.

1.5 Published work

1.5.1 Peer-reviewed journal publications

- Zhang J., Zhang C., Hao L., Nie R. and Qiu J. *Exploiting the instability of smart structure for reconfiguring*, Applied Physics Letters, 2017, 111.6: 064102. DOI: 10.1063/1.4986795
- Zhang J, McInnes C R. *Using instability to reconfigure smart structures in a spring-Mass model*, Mechanical Systems and Signal Processing, 2017, 91:81-92. DOI: 10.1016/j.ymsp.2016.11.029
- Zhang J, McInnes C R, Xu M. *Reconfiguration of a smart surface using heteroclinic connections*, 2017. Proceedings of the Royal Society, Part A, 473: 20160614, 2017, DOI: 10.1098/rspa.2016.0614.
- Zhang J, McInnes C R. *Reconfiguration of a four-bar mechanism using phase space connections*, Mechanical Systems and Signal Processing, 2016, 81:43-59. DOI: 10.1016/j.ymsp.2016.03.024
- Zhang J, McInnes C R. *Reconfiguring smart structures using approximate heteroclinic connections*, Smart Materials and Structures, 2015, 24(10):105034. DOI: 10.1088/0964-1726/24/10/105034

1.5.2 Conference paper

- Zhang J and McInnes C R 2015 *Reconfiguring smart structures using approximate heteroclinic connections in a spring-mass model*, Proceedings of the ASME Conference on Smart Materials, Adaptive Structures and Intelligent Systems (SMASIS), Colorado Springs, USA, September 21-23, 2015. DOI: 10.1115/SMASIS2015-8819

1.6 Thesis structure

In order to pursue the research objectives stated in Section 1.3, Chapter 2 will provide the necessary theory and methods of nonlinear dynamical system and control, including an overview of modern dynamical systems, the concept of heteroclinic connection and a brief description of inverse control methods. The remainder of this thesis can then be divided into three main parts: the first part covers Chapter 3, Chapter 4 and Chapter 5, focussing on a spring-mass model of a smart structure. In particular, a simple cubic nonlinearity and a fully elastic mass-spring model will be considered. Moreover, a smart surface will also be illustrated through using the mass-spring array. In the second part, Chapter 6, the linkage mechanism model will be considered for reconfiguration. In the third part, Chapter 7, a continuous beam model will be analysed as a partial differential system and experimental tests will be employed for preliminary validation.

In **Chapter 3** the concept of reconfiguring a smart structure by using heteroclinic connections will be considered for a model with cubic nonlinearity. In particular, due to the difficulty in obtaining heteroclinic connections numerically in complex dynamical systems, a sufficiently smooth set of functions will be used to generate a path to approximate the heteroclinic connection and satisfy a number of boundary conditions for the problem. An inverse control method will be introduced and applied to the cubic nonlinearity model of the smart structure. An evaluation criteria will be defined and applied to the smart structure reconfiguration problem in order to assess the relative energy costs of different reconfiguration methods.

In the following, **Chapter 4**, in consideration of the difference between the cubic and real spring model, a spring-mass model of a simple smart structure will be developed to verify the possibility of using the heteroclinic connections to reconfigure future real smart structures. An optimal control method will be employed to find the required control histories and state trajectories. Then, dissipation will be considered again to approximate a more realistic smart structure. Some strategies will be considered to deal with the dissipation term.

In **Chapter 5**, a simple discrete model of a two-dimensional smart surface structure will be considered and reconfigured using heteroclinic connections. As an approximation, the surface will be modelled as a two-dimensional spring-mass array without dissipation and with a simplifying cubic nonlinearity, which has a range of both stable and unstable configurations. A feedback control strategy will be proposed to actively maintain the structure in an unstable configuration.

As a next step, a classical four-bar mechanism with rigid linkages and torsional springs

will be investigated in **Chapter 6**. This investigation will use the same control method in Chapter 3. The rigid mechanism model will demonstrate the possibility of actively reconfiguring the mechanism between two unstable equilibria. A single axial spring will then be used to substitute for one rigid bar to develop a pseudo-rigid model for exploring interesting complexities over the rigid model. Lastly, a purely elastic model with torsional springs and axial springs for linkages will be developed which allows bending, stretching and compression and some numerical results will be presented to elaborate on the feasibility of the reconfiguration manoeuvre using heteroclinic connections. The model will also provide insight into a fully elastic beam.

The last section, in **Chapter 7**, a classical clamped-clamped beam will be investigated based on the Euler-Bernoulli beam theory. The equation of motion and associated boundary conditions governing the nonlinear dynamics of such a buckled beam will be derived as partial differential system. Different buckled configurations (stable or unstable) and their corresponding shapes will be obtained. In addition, a model of a real structure will be fabricated by using smart materials in the laboratory. Both numerical simulation and experimental demonstration have been used to provide preliminary verification of the concept.

Each Chapter includes a summary and conclusion, which will be presented together in the overall conclusions in **Chapter 8** at the end of this thesis, along with a discussion on future work.

Chapter 2

Theory and Methods

In this Chapter, some fundamental theory of dynamical systems in the context of ordinary differential equations will be briefly discussed in Section 2.1 to obtain key properties of a system, such as equilibrium and stability. The relevant mathematical principles will be reviewed in Section 2.2 to illustrate heteroclinic connections. In addition, the control method for smart structure models exploited in this thesis will be introduced in Section 2.3.

2.1 Nonlinear systems and stability

In general, structures can be defined as a mechanical system, which can therefore use modern dynamical systems theory for the analysis of their characteristics [60]. Usually, non-linear dynamical systems typically possess a number of equilibria which may be connected through paths in the phase space of the system [4]. In the study of dynamical systems the independent variable is often referred to as time $t \in \mathbb{R}^1$ for n-dimensional state $x \in \mathbb{R}^n$ and a set of parameters μ so that an ordinary differential equation can be used of the form

$$\frac{dx}{dt} = f(x, t; \mu) \quad (2.1)$$

Equation 2.1 is also referred to as a vector field or ordinary differential equation. A solution of Eq 2.1 can therefore be defined as a map, $x(t)$, such that $x(t)$ satisfies Eq 2.1, i.e.,

$$\frac{d(x(t))}{dt} = f(x(t), t; \mu) \quad (2.2)$$

There is then a geometrical interpretation of a curve of the map x in \mathbb{R}^n , and Eq. 2.2 gives the tangent vector at each point of the curve, which is the reason for referring to

Eq. 2.1 as a vector field. Therefore, the space of the independent variable of Eq. 2.1 (i.e., \mathbb{R}^n) is the phase space of Eq. 2.1. Clearly, different characteristics of an ordinary differential equation depend explicitly on the time or not. In other words, it is considered as a non-autonomous or time dependent ordinary differential equation (or vector fields) that depends explicitly on time (i.e. $\dot{x} = f(x, t; \mu)$) or it is considered as an autonomous or time independent ordinary differential equations (or vector fields) that does not depend explicitly on time t (i.e. $\dot{x} = f(x; \mu)$).

Therefore, the forecast or future states of the system is given by $x(t)$. Generally, dynamical systems are therefore initial-value problems governed by ordinary differential equations, or by difference equations. This is often included in the expression for solutions by representing $x(t, t_0, x_0)$ for some initial state x_0 at time t_0 . Similarly, the parameters μ play an important role in the evolution of $x(t)$, for example representing mechanical properties of a structure.

A mechanical system is usually an autonomous system (i.e. $\dot{x} = f(x; \mu)$), which is considered that its state does not change with time. It shows an important property that an equilibrium state corresponds to a constant solution of the differential equation. Equation. 2.2 can be now considered by a general autonomous system form

$$\frac{d(x(t))}{dt} = f(x, \mu) \quad (2.3)$$

An equilibrium solution of Eq. 2.3 is a point $\bar{x} \in \mathbb{R}^n$ such that

$$f(\bar{x}, \mu) = 0$$

That is to mean

$$x(t_0) = x(t) = x(t_\infty) = \bar{x}$$

It is obvious that if solutions starting close to a fixed point at a given time remains close to this point for all later times, i.e. \bar{x} is stable. Then, it is necessary to consider the property of solution near \bar{x} . Let

$$x = \bar{x} + r(\bar{x}) \quad (2.4)$$

$r(\bar{x})$ is a neighbourhood of the fixed point \bar{x} , and Taylor expanding about \bar{x} of Eq. 2.3 can therefore obtain

$$f(x, \mu) = f(\bar{x}, \mu) + Dr(\bar{x}) + O(|r(\bar{x})|^2) \quad (2.5)$$

where $D = Df(\bar{x}, \mu)$ is the total derivative of f and O describes the limiting behaviour. Substituting Eq. 2.4 into Eq. 2.3 and Eq. 2.5 gives

$$\dot{x} = \dot{\bar{x}} + \dot{r}(\bar{x}) = f(\bar{x}) + Dr(\bar{x}) + O(|r(\bar{x})|^2) \quad (2.6)$$

The overdot in Eq. 2.6 represents a derivative with respect to time, and the parameters μ will be ignored at present. It shows that \dot{x} can be express by D by using the big O notation. Using the additional fact that $\dot{\bar{x}}(t) = f(\bar{x}(t))$, Eq. 2.6 becomes

$$\dot{r}(\bar{x}) = Df(\bar{x})y + O(|r(\bar{x})|^2) \quad (2.7)$$

Equation. 2.7 then describes the characteristic of $r(\bar{x})$, the neighbourhood of the equilibrium \bar{x} . The stability properties of \bar{x} can be addressed by solving the associated linear system

$$\dot{r}(\bar{x}) = Dr(\bar{x}) \quad (2.8)$$

If \bar{x} is an equilibrium solution, then D is a matrix with constant coefficients, and the solution of Eq. 2.8 through the point $y_0 \in \mathbb{R}^n$ of $t = 0$ can be written as

$$r(\bar{x}, t) = e^{Dt}r(\bar{x}, t_0) \quad (2.9)$$

Thus, if negative real parts exist for all eigenvalues λ of D , it means that $r(\bar{x}, t)$ is asymptotically stable. Therefore, the equilibrium solution \bar{x} of x is distinctly asymptotically stable. Eigenvalue analysis will be used in later Chapters to assess full stability of equilibria of a range of smart structure models.

2.2 Heteroclinic connections

In the phase plane, the state at time t_0 consists of a pair of numbers, which can be regarded as initial conditions for the dynamical system, and therefore determines all states through which the system goes in a particular motion. The vector of states given as $x = x(t)$ traces out a successive curve through the initial condition called a phase path, a trajectory or an orbit. The direction of the vector can be obtained from the relation of the general autonomous vector Eq. 2.1, when $f(x, \mu) > 0$, then $\dot{x} > 0$, so that x is increasing with time, and when $f(x, \mu) < 0$, then $\dot{x} < 0$, so that x is decreasing with time. The complete pattern of the phase paths including the directional arrow constitutes the phase diagram.

Figure 2.1 shows the types of equilibrium point arising from three different types of

turning points of V , which is the potential energy of the dynamical system. A minimum of potential energy generates a centre (stable), a maximum of potential energy generates a saddle and a point of inflection leads to a cusp, as shown in Fig. 2.1.

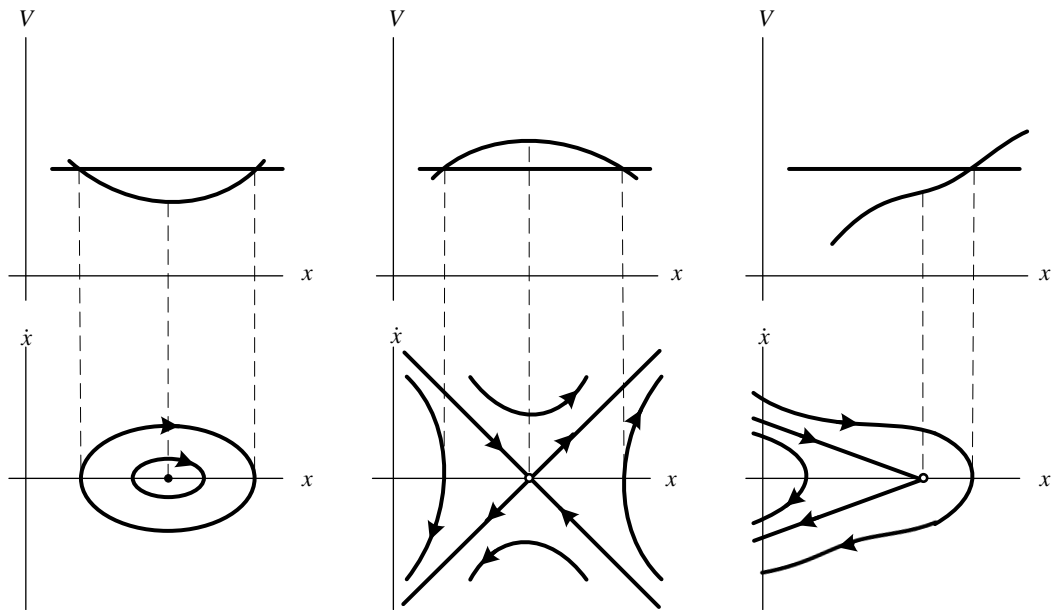


Figure 2.1: Typical phase diagrams arising from the fixed points (adapted from [4]).

A heteroclinic connection, is an asymptotic trajectory which joins two different equilibrium points. In the event the equilibrium points at the start and end of the path are the same, then it is called a homoclinic connection. Both a heteroclinic and homoclinic connection are of great importance both in theory and in real applications [63]. Here, a manifold is defined as a surface embedded in phase space. The unstable manifold then represents the family of trajectories diverging from an equilibrium point, while the stable manifold represents the family of trajectories asymptotically approaching an equilibrium point. A heteroclinic connection is formed if the unstable manifold of an equilibrium point intersects the stable manifold of another distant equilibrium point in phase space. In dynamical systems theory, there are finitely many equilibrium points in a smooth dynamical system, which satisfy a transversality condition on the stable and unstable manifolds, yields a phase space connection.

Figure 2.2 shows a saddle surface: there are several stable and unstable equilibrium points E_u , E_{saddle} and E_s , which are defined by an energy function E . The energy function is defined here as $E = \sin(x_1) + \sin(x_2)$ for illustration. The unstable equilibrium points E_u have maximum potential energy and the stable equilibrium points E_s

have minimum potential energy, respectively. It is clear that two saddle points E_{saddle} can be connected by a heteroclinic connection (blue trajectory), which departs from the unstable manifold of one equilibrium point and intersects the stable manifold of another equilibrium.

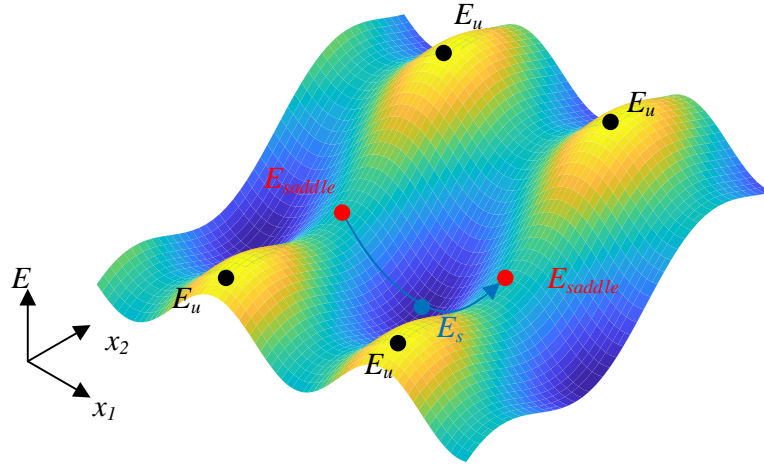


Figure 2.2: A saddle surface with stable and unstable manifolds.

More specifically, it is assumed that a set of equilibrium configurations E for a dynamical system can be found. E will contain both linearly stable equilibria E^S ($Re(\lambda) = 0$) and unstable equilibria E^U ($Re(\lambda) > 0$) for some eigenvalue spectrum λ . If the unstable manifold W^U of an equilibrium point E_i^U intersect the stable manifold W^S of another distant equilibrium point E_{i+1}^U in the phase space, then a heteroclinic connection exists between the equilibria, as shown in Fig. 2.3. Moreover, if the set of hyperbolic equilibria E^U exist on the same energy surface, the heteroclinic connections between these points do not in principle require the addition of or dissipation of energy. The application of heteroclinic connections to reconfiguring smart structures, will be investigated in this thesis with the significant benefits in terms of the energy required for reconfiguration [60].

2.3 Control methods

In this thesis the class of control problems for a time-varying reference trajectory is of interest, called the trajectory tracking problem. It is considered that the end point problem is a particular kind of the trajectory tracking problem, which allows the controller to capture trajectories in the neighbourhood of an end point [64], as will be used

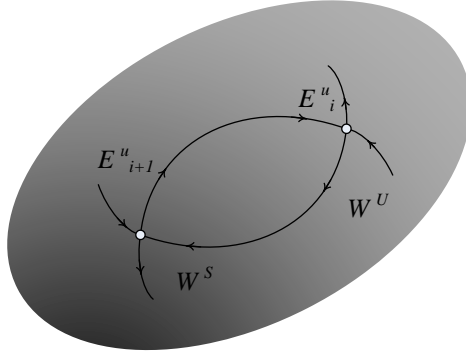


Figure 2.3: Heteroclinic connection between two distant equilibria E_i^U and E_{i+1}^U in the phase space, formed by the intersection of the stable manifold W^S of E_{i+1}^U and unstable manifold W^U of E_i^U .

in later Chapters. In particular, it is desired to find a control law $u = \alpha(x, r(\cdot))$ such that

$$\lim_{t \rightarrow \infty} (x(t) - r(t)) = 0 \quad (2.10)$$

The notation $r(\cdot)$ indicates the control law can depend not only on the reference signal $r(t)$ but also derivatives of the reference signal. A feasible trajectory for the system is a pair $(x(t), u(t))$ that satisfies the dynamical equation and generate the desired trajectory. If the system can be defined as a feasible trajectory, control methods can be searched of the form $u = \alpha(x, r(\cdot))$ that track the desired reference trajectory. A standard nonlinear system is assumed to have a generic form of

$$\dot{\mathbf{x}}(t) = f\{\mathbf{x}(t), \mathbf{u}(t); t\}, \quad \mathbf{x} \in \mathbb{R}^m, \quad \mathbf{u} \in \mathbb{R}^n, \quad t \in [0, T] \quad (2.11)$$

where $\mathbf{x}(t)$ is the system state, $\mathbf{u}(t)$ is a vector of inputs and f is a smooth function describing the dynamics of the process. The generic boundary conditions and constraints are defined as

$$\mathbf{x}(0) = \mathbf{x}_0, \quad \mathbf{x}(T) = \mathbf{x}_f, \quad t \in [0, T] \quad (2.12)$$

The inverse control method has been used to provide stable tracking results which are computationally efficient and offer a high degree of user flexibility [65]. The system can then track a desired trajectory if it is actuated by the controllers, as shown in Fig. 2.4. In general, dynamical systems require inputs to produce certain outputs (Fig. 2.4.a).

Therefore, it is easier to obtain the potential inputs by inverting the system with certain outputs (Fig. 2.4.b). The whole system then can be constituted by combining the inverted system and the original system (Fig. 2.4.c) with some gain and feedback variables (Fig. 2.4.d).

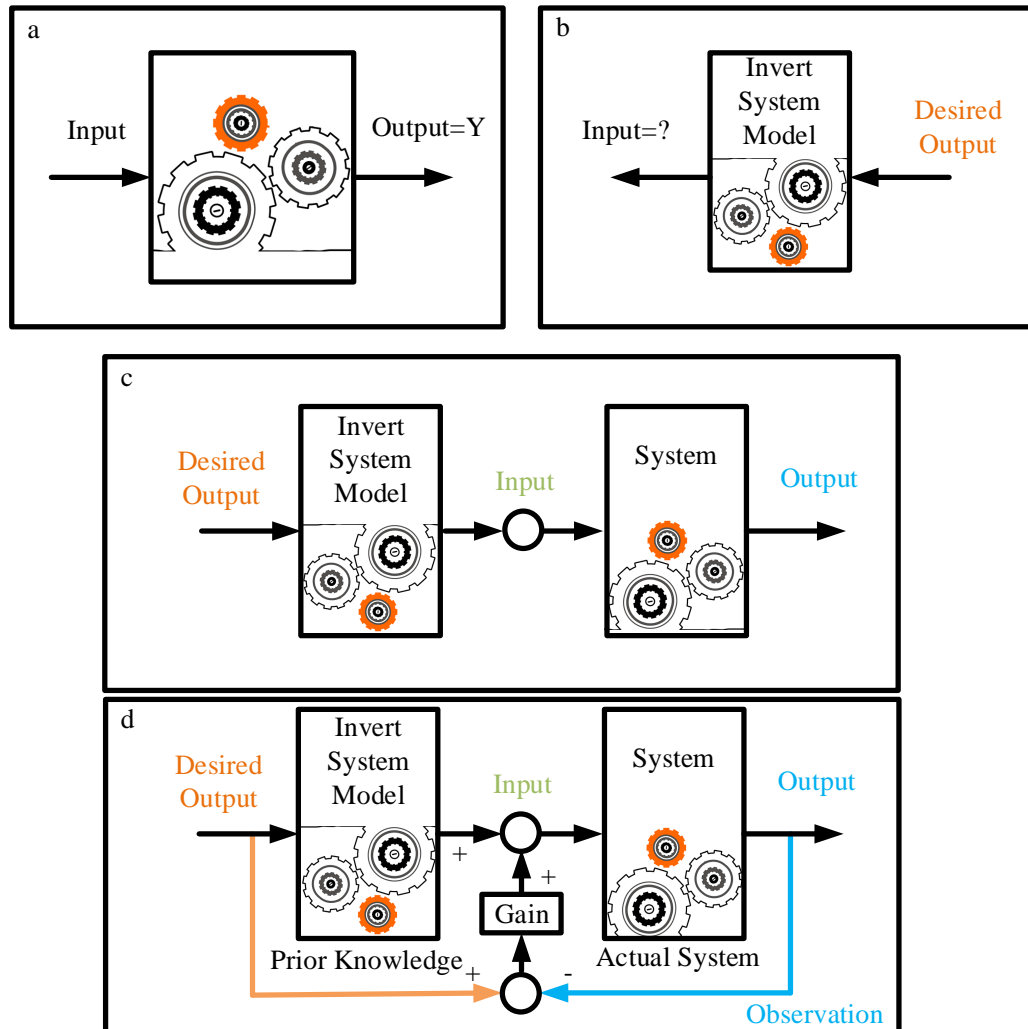


Figure 2.4: Inverse control method.

The inverse dynamics problem is then to find a control vector $\mathbf{u}(t)$ which satisfies the constraints.

$$\mathbf{s}(\mathbf{x}(t), \mathbf{c}(t); t) = 0 \quad (2.13)$$

where \mathbf{s} is a sufficiently smooth function and $\mathbf{c}(t)$ represents desired outputs from the system.

To obtain the required control which satisfies the constraints, Eq. 2.13 is repeatedly

differentiated until the control appears explicitly, *viz*

$$\mathbf{s}(\mathbf{x}(t), \mathbf{u}(t), \mathbf{c}(t), \dot{\mathbf{c}}(t); t) = 0 \quad (2.14)$$

This relation can then be solved algebraically or numerically to obtain the control vector $\mathbf{u}(t)$ that is required to track the desired reference trajectory. For the following dynamical systems it is required to extend this method to provide nonlinear control to track the reference trajectory in the presence of uncertainties. The detailed process is illustrated in Section 3.5.

2.4 Conclusion

In this Chapter, modern dynamical systems theory has been briefly reviewed to analyse the characteristics of nonlinear systems. It is shown that a set of equilibria can be identified in a nonlinear dynamical systems which may be connected through paths in phase space. In particular, heteroclinic connections have been considered as paths which connect equilibria through both stable and unstable manifolds. In addition, this Chapter provides a brief review of control methods for nonlinear dynamical systems which ensures convergence to a desired reference trajectory, which can be effectively used in reconfiguring smart structures. Both heteroclinic connections and inverse control methods will be used in later Chapters.

Chapter 3

Cubic Nonlinearity in a N-dimensional Chain

In order to investigate the potential of using heteroclinic connection to reconfigure smart structures, dynamical system theory is used to investigate the characteristics of an N-dimensional chain with a cubic nonlinearity. A reconfigurable smart structure is again defined here as a mechanical system which has the ability to change its kinematic configuration between a finite set of stable or unstable equilibria. A set of stable and unstable equilibrium configurations is identified in the chain model and the reconfiguration of the smart structure between the equal-energy unstable states is investigated. It is assumed that active control can maintain the structure in an unstable state [37]. To achieve such a reconfiguration, heteroclinic connections between the unstable equilibria in the phase space of the problem are considered. Since unstable equilibria can be found which lie on the same energy surface in the phase space of the problem, if a heteroclinic connection between unstable, equal energy equilibria can be defined, trajectories exist between these configurations which in principle do not require the addition of or dissipation of energy.

In Section 3.2 and 3.3, a smart structure is firstly defined as a spring-mass model. An approximation is then obtained that is sufficient to provide the required qualitative behaviour of the system, through a simple cubic nonlinearity, while avoiding undue algebraic complexity. However, it can be difficult to obtain such heteroclinic connections numerically in complex dynamical systems, such as those with strong nonlinearity. Therefore, in Section 3.4, a sufficiently smooth set of functions is used to generate a path to approximate the heteroclinic connection and satisfy a number of boundary conditions for the problem. It is envisaged that being computationally efficient, the method

can form the basis for real-time reconfiguration of smart structures using heteroclinic connections between equal-energy, unstable configurations. In Section 3.5, an evaluation criteria is then defined by again using a simple mass-spring model, which under quasi-static conditions provides a relationship between the control action and the spring deformation required for control, thus developing a measure of the energy required for control. This evaluation criteria is then applied to the smart structure reconfiguration problem in order to assess the relative energy cost of different reconfiguration methods. An inverse control method which is applied to a simple double mass-spring model of the smart structure is introduced in Section 3.6. The principal advantage of the inverse method for this problem is the flexibility for path shaping. Numerical results of reconfiguring a smart structure based on the two mass chain model through the use of heteroclinic connection are provided in Section 3.7. The method is then extended in Section 3.8 from the double spring-mass model to a 3 mass problem which provides a significant step change in complexity, both in terms of the number of equilibrium states and in the difficulty of finding a true heteroclinic connection. Finally, Section 3.9 will summarise the Chapter.

3.1 Single mass problem

In order to investigate how to use a polynomial as an approximation of a heteroclinic connection to reconfigure a smart structure, a simple representative model of a smart structure is defined [60]. A beam model is firstly assumed as a single lumped mass with two linear springs to simulate structural stiffness, with both ends clamped, as shown in Fig 3.1. The parameters of the model are the mass m of the single lumped mass and the spring stiffness and natural length k and l , respectively. The distance between the two clamped ends is $2d$ and the displacement of the mass in the vertical direction is defined by x . From Fig. 1 it can be seen that the dynamics of the model can therefore be described by [60]

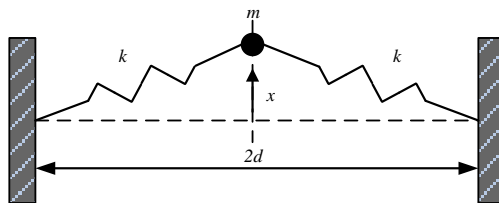


Figure 3.1: 1 degree-of-freedom buckling beam model.

$$\dot{x} = v \tag{3.1}$$

$$m\dot{v} = -2kx\left(1 - \frac{l}{\sqrt{x_1^2 + d^2}}\right) \quad (3.2)$$

Equation 3.2 can be expanded by assuming that $x/d \ll 1$ to obtain

$$m\dot{v} = -2k\left(\frac{l}{d} - 1\right)x - \frac{kl}{d^3}x^3 + \dots \quad (3.3)$$

again following [60] this can be written as

$$\dot{q} = p \quad (3.4)$$

$$\dot{p} = \mu q - q^3 \quad (3.5)$$

where the non-dimensional position variable $q = \sqrt{l/d^3}x$, the momentum p and non-dimensional time $\tau = t/\sqrt{m/k}$ are defined. The free parameter $\mu = 2(l/d - 1)$ is used as a measure of the compressive load acting on the model. Later, it is assumed that the natural length of the spring can be manipulated through the use of an appropriate material, thus allowing active control of the structure. A relationship can be therefore be found between variations of $\Delta\mu$ and variations of the real spring length Δl , where δ can be defined as the ratio of total deformation to the initial length of the spring such that

$$\delta = \frac{\Delta l}{l} = \frac{\Delta\mu}{\mu + 2} \quad (3.6)$$

Then, consider that the system is conservative so the problem also can be defined such that $\dot{p} = -\partial V(q, \mu)/\partial q$ through the use of an effective quartic potential $V(q, \mu)$, where

$$V(q, \mu) = -\frac{1}{2}\mu q^2 + \frac{1}{4}q^4 \quad (3.7)$$

and where the extrema of the potential represent the equilibrium states of the system (stable and unstable).

3.2 Two mass chain

Following [60] the 1 degree-of-freedom problem can now be extended to a chain of N masses. The system is still conservative so that the same functional form of nonlinearity is used as Eq 3.7 above. The potential can then be generalised to arbitrary pairs of neighbouring masses $i - 1$ and i as

$$V(q_{i-1}, q_i, \mu_i) = -\frac{1}{2}\mu_i(q_{i-1} - q_i)^2 + \frac{1}{4}(q_{i-1} - q_i)^4 \quad (3.8)$$

In order to control the dynamics of the problem it will again be assumed that the coupling parameters μ_i can be manipulated to achieve active control of the structure. Since there is a linear relationship between μ_i and the natural length of the spring, it can be assumed that the manipulation of μ_i through changes to the natural length of the spring in the model can be used. The behaviour of a chain of masses can now be described by a Hamiltonian $H(\mathbf{q}, \mathbf{p}, \boldsymbol{\mu}) = T(\mathbf{p}) + V(\mathbf{q}, \boldsymbol{\mu})$ with the set $\mathbf{q} = q_i (i = 1 - N)$ and the corresponding set of momenta $\mathbf{p} = p_i (i = 1 - N)$ such that $(\mathbf{p}, \mathbf{q}) \in \mathbb{R}^{2N}$, where $T(\mathbf{p})$ represents kinetic energy and $V(\mathbf{q}, \boldsymbol{\mu})$ represent the potential energy where

$$T(\mathbf{p}) = \frac{1}{2} \|\mathbf{p}^2\| \quad (3.9)$$

$$V(\mathbf{q}, \boldsymbol{\mu}) = \sum_{i=1}^{N+1} -\frac{1}{2} \mu_i (q_{i-1} - q_i)^2 + \frac{1}{4} (q_{i-1} - q_i)^4 \quad (3.10)$$

with boundary conditions $q_0 = 0$ and $q_N = 0$, so that the chain is pinned at both ends.

In order to explore the possibility of reconfiguring a smart structure, a simple two masses chain with three linear springs will firstly be considered with the springs clamped at both ends, as shown in Fig. 3.2. The model assumes that the masses are constrained to move only in the vertical direction.

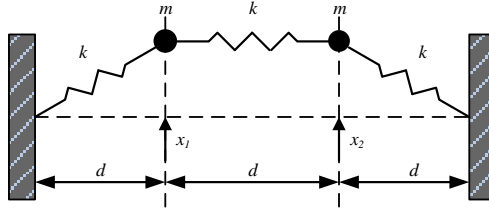


Figure 3.2: 2 degree-of-freedom buckling beam model.

The Hamiltonian for this two mass model can then be defined from the kinetic energy and potential energy through Eqs. 3.9 and 3.10 as

$$T(\mathbf{p}) = \frac{1}{2} |\mathbf{p}_1^2| + \frac{1}{2} |\mathbf{p}_2^2| \quad (3.11)$$

$$V(\mathbf{q}, \boldsymbol{\mu}) = -\frac{1}{2} \mu_1 q_1^2 - \frac{1}{2} \mu_2 (q_1 - q_2)^2 - \frac{1}{2} \mu_3 q_2^2 + \frac{1}{4} q_1^4 + \frac{1}{4} (q_1 - q_2)^4 + \frac{1}{4} q_2^4 \quad (3.12)$$

The two masses problem can then be fully defined by a dynamical system of the form

$$\dot{q}_1 = p_1 \quad (3.13)$$

$$\dot{p}_1 = \mu_1 q_1 - q_1^3 + \mu_2(q_1 - q_2) - (q_1 - q_2)^3 \quad (3.14)$$

$$\dot{q}_2 = p_2 \quad (3.15)$$

$$\dot{p}_2 = \mu_3 q_2 - q_2^3 - \mu_2(q_1 - q_2) + (q_1 - q_2)^3 \quad (3.16)$$

where full details of the development of the simple smart structure model are again provided by McInnes and Waters [60].

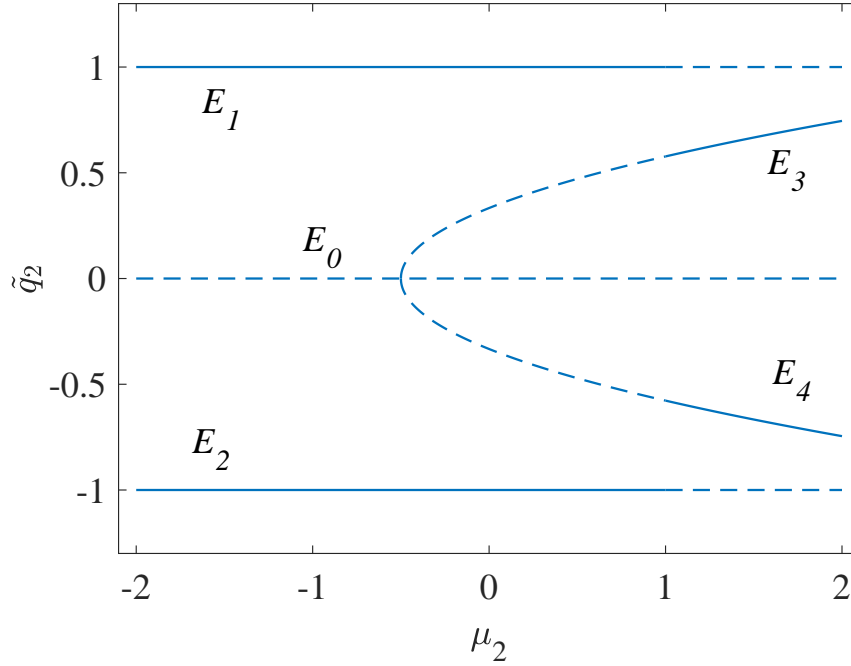


Figure 3.3: Bifurcation diagram for the 2 degree-of-freedom buckling beam model.

The location of the equilibria are listed in Table 3.1. It can be seen that E_0 has the highest potential V , which is unstable states corresponding to the two masses being undeflected, with both springs in compression. E_1 and E_2 then have equal potential which is higher than E_3 and E_4 , which means that only the central spring is in compression and can in principle relax to the lower energy equilibria at E_3 and E_4 where all springs are extended. Moreover, the stability properties of the equilibria can be considered as a function of the coupling parameters μ_{1-3} , which is shown in Fig. 3.3. In particular, the stability properties of some equilibria swap for different μ_2 , when the coupling constants are equal, such that $\mu_1 = \mu_3$. It can also be shown that the location of E_1 and E_2 are independent of μ_2 while the location of E_3 and E_4 is a function of μ_2 . Therefore, fixing μ_1 and μ_3 , a bifurcation diagram can be constructed. Although only $\mu_{1-3} > 0$ is considered here for analysis, for completeness and generalised the bifurcation diagram is shown for $-2 \leq \mu_2 \leq 2$ in Fig. 3.3 [60].

Table 3.1: Stability properties of the 5 equilibria of 2 degree-of-freedom buckling beam model.

Point	\tilde{q}_1	\tilde{q}_2	$\lambda_{1,2}$	$\lambda_{3,4}$	V	Type
E_0	0	0	± 1	± 2	0	Saddle×Saddle
E_1	1	1	$\pm\sqrt{2}i$	± 1	-0.5	Saddle×Centre
E_2	-1	-1	$\pm\sqrt{2}i$	± 1	-0.5	Saddle×Centre
E_3	-2/3	2/3	$\pm 1/\sqrt{3}i$	$\pm 2\sqrt{2}i$	-8/9	Saddle×Saddle
E_4	-2/3	2/3	$\pm 1/\sqrt{3}i$	$\pm 2\sqrt{2}i$	-8/9	Saddle×Saddle

3.3 Constructing the reference polynomial

It can be noted that the system defined in Section 3.2 has been simplified by assuming that $x/d \ll 1$. This approximation is sufficient to provide the required qualitative behaviour of the system through Eq. 3.3, which is a simple cubic nonlinearity, while again avoiding undue algebraic complexity. It will be shown that the system defined by Eqs. 3.13-3.16 has a number of equilibria which are both stable and unstable and may be connected through paths in the phase space of the problem. As discussed in Chapter 2 one type of path is the heteroclinic connection which requires the stable and unstable manifolds of two unstable equilibria to be connected. Solving Eq. 3.14 and Eq. 3.16 for equilibrium conditions yields five equilibria for the parameter set, $\mu_1 = 1$, $\mu_2 = 1.5$ and $\mu_3 = 1$. The location of the equilibria are listed in Table 3.1. The linear stability of these equilibria can be determined through linearisation of Hamilton's equations in the neighbourhood of each equilibrium point to determine the eigenvalues of the equilibria $\lambda_j (j = 1 - 4)$. A set of stable equilibria are expected with conjugate imaginary eigenvalues and a set of unstable equilibria are expected with real eigenvalues of opposite sign [66]. It can then be determined that this 2 degree-of-freedom system possesses 3 unstable equilibria E_0 , E_1 , E_2 and 2 stable equilibria E_3 and E_4 shown in Fig. 3.4 with contours of potential V .

Since the E_1 and E_2 lie on the same energy surface, there may be a heteroclinic connection connecting these equilibria, as shown in Fig. 3.5a, so that the structure can be reconfigured between these two equilibria without work being done. Similarly, if the structure is at the stable equilibria E_3 , it needs to cross the potential barrier at E_1 to transition to the other stable equilibrium E_4 , as shown in Fig. 3.5b. However, energy must be added to the system to reach the top of the barrier and then dissipated to reach the final equilibrium state.

Although heteroclinic connections are essential characteristics of non-linear dynamical

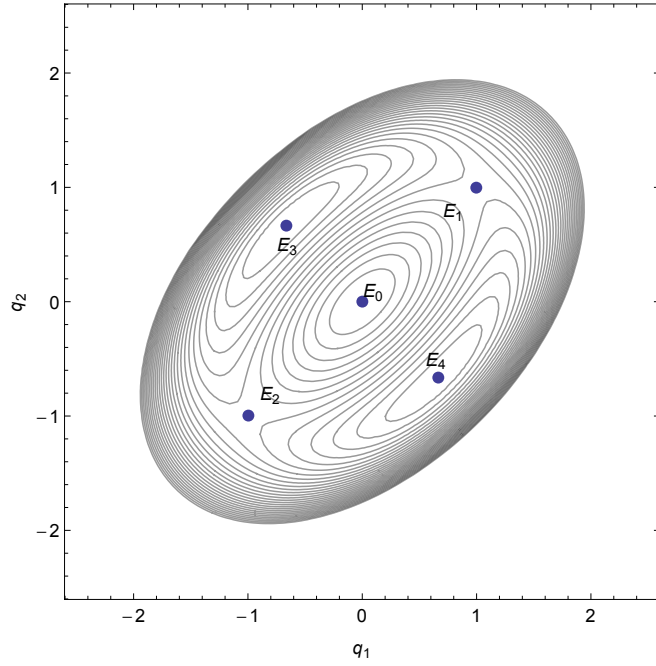


Figure 3.4: Potential $V(q, \mu)$ and equilibria (3 unstable equilibria E_0 , E_1 and E_2 , and 2 stable equilibria E_3 and E_4).

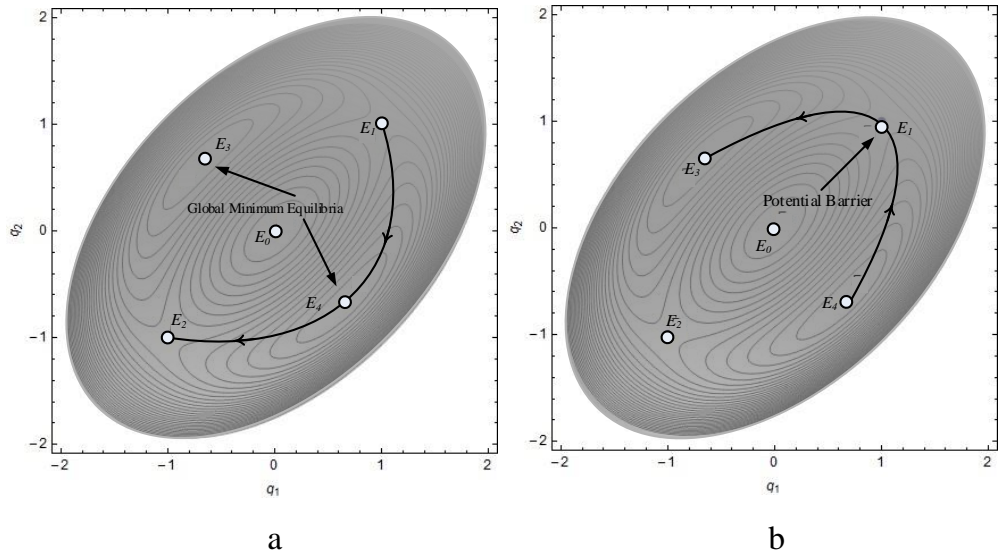


Figure 3.5: Transitions between different equilibria (with potential energy contour levels) (a) Ideal heteroclinic connection through E_3 or E_4 between E_1 and E_2 (b) Crossing the potential barrier E_1 between E_3 and E_4 .

systems, it can be difficult to find exact heteroclinic connections numerically in complex nonlinear systems. For example, McInnes and Waters[60] used an iterative numerical algorithm, which would not be suitable for embedded real-time control. Therefore, a method is presented to approximate heteroclinic connections which can form the basis for real-time reconfiguration of smart structures. The heteroclinic connection will be defined as a 4th order polynomial, *viz*

$$\mathbf{q}^*(t) = \mathbf{a}_0 + \mathbf{a}_1 t + \mathbf{a}_2 t^2 + \mathbf{a}_3 t^3 + \mathbf{a}_4 t^4 \quad (3.17)$$

The unknown vector of constants \mathbf{a}_i ($i=1-4$) in the reference polynomial can then be related to the boundary conditions of the system. The ideal heteroclinic connection in Fig. 3.5 departs from equilibrium E_1 (1, 1), goes through the global minimum at equilibrium E_4 (-2/3, 2/3) and ends in equilibrium E_2 (-1, -1). We can therefore define conditions on the polynomial which approximates the true heteroclinic connection, such that

$$\begin{bmatrix} \mathbf{q}^*(0) & \mathbf{q}^*(T/2) & \mathbf{q}^*(T) & \dot{\mathbf{q}}^*(0) & \dot{\mathbf{q}}^*(T) \end{bmatrix} = \begin{bmatrix} 1 & 1 \\ 2/3 & -2/3 \\ -1 & -1 \\ 0 & 0 \\ 0 & 0 \end{bmatrix}^T \quad (3.18)$$

Then, the only remaining free parameter to define the reference polynomial is the total reconfiguration duration T . Therefore, an approximate heteroclinic connection can be defined using Eq. 3.18 where the constant vectors in Eq. 3.17 are found to be

$$\begin{bmatrix} \mathbf{a}_0 & \mathbf{a}_1 & \mathbf{a}_2 & \mathbf{a}_3 & \mathbf{a}_4 \end{bmatrix} = \begin{bmatrix} 1 & 1 \\ 0 & 0 \\ 14/3T^2 & -50/3T^2 \\ -52/3T^3 & 76/3T^3 \\ 32/3T^4 & -32/3T^4 \end{bmatrix}^T \quad (3.19)$$

This function provides a smooth reference trajectory while ensuring that the required boundary conditions are satisfied. After repeated differentiation these polynomials provide the corresponding velocities and accelerations to be tracked to follow the reference trajectory.

Similarly, the transition from E_3 to E_4 can also be defined. This path is considered such

that it should cross the potential barrier E_1 , so the boundary conditions are defined as

$$\begin{bmatrix} \mathbf{q}^*(0) & \mathbf{q}^*(T/2) & \mathbf{q}^*(T) & \dot{\mathbf{q}}^*(0) & \dot{\mathbf{q}}^*(T) \end{bmatrix} = \begin{bmatrix} -2/3 & 2/3 \\ 1 & 1 \\ 2/3 & -2/3 \\ 0 & 0 \\ 0 & 0 \end{bmatrix}^T \quad (3.20)$$

In this case, the constants of Eq. 3.17 are therefore defined as

$$\begin{bmatrix} \mathbf{a}_0 & \mathbf{a}_1 & \mathbf{a}_2 & \mathbf{a}_3 & \mathbf{a}_4 \end{bmatrix} = \begin{bmatrix} -2/3 & 2/3 \\ 0 & 0 \\ 20/T^2 & 12/T^2 \\ -104/3T^3 & -88/3T^3 \\ 16/T^4 & 16/T^4 \end{bmatrix}^T \quad (3.21)$$

Now that the reference polynomials have been defined, an inverse method will be developed in order to track them, allowing an approximate heteroclinic connection to be followed to connect the unstable equilibria.

As discussed in Chapter 2 inverse control allows tracking of time dependent constraints and is an effective method to control non-linear systems, used extensively in a diverse range of nonlinear control problems [65]. A nonlinear system is assumed to have a generic form of

$$\dot{\mathbf{x}}(t) = f\{\mathbf{x}(t), \mathbf{u}(t); t\}, \mathbf{x} \in \mathbb{R}^m, \mathbf{u} \in \mathbb{R}^n, t \in [0, T] \quad (3.22)$$

where $\mathbf{x}(t)$ is the system state, $\mathbf{u}(t)$ is a vector of inputs and f is a smooth function describing the dynamics of the process. The generic boundary conditions and constraints are defined as

$$\mathbf{x}(0) = \mathbf{x}_0, \mathbf{x}(T) = \mathbf{x}_f \quad (3.23)$$

The inverse method represents the control problem of how to find a control vector $\mathbf{u}(t)$ which can track desired outputs of the system while meeting the requirements of the boundary conditions so that

$$\mathbf{e}\{\mathbf{x}(t), \mathbf{x}^*(t); t\} = \{\mathbf{x}(t) - \mathbf{x}^*(t)\} = 0 \quad (3.24)$$

where \mathbf{e} is a continuous constraint function and $\mathbf{x}^*(t)$ represents the desired output.

For this dynamical system it is required to extend this method to provide nonlinear control to track the reference trajectory in the presence of uncertainties. This can be achieved by differentiating the constraint vector \mathbf{e} until the control appears explicitly, then feedback terms can be added instead of defining the constraint vector to be null so that

$$\ddot{\mathbf{e}}\{\mathbf{x}(t), \mathbf{x}^*(t); t\} = -\mathbf{g}_1 \dot{\mathbf{e}} - \mathbf{g}_2 \mathbf{e} \quad (3.25)$$

where \mathbf{g}_1 and \mathbf{g}_2 are constant gain matrices defined by

$$\begin{aligned} \mathbf{g}_1 &= \text{Diag}\{g_{11}, g_{12}\} \\ \mathbf{g}_2 &= \text{Diag}\{g_{21}, g_{22}\} \end{aligned}$$

The 4th order polynomial can then be used as a reference trajectory with the inverse control method to provide an example of a controlled heteroclinic connection through E_3 between E_1 and E_2 .

Recall Eq. 3.13, 3.14, 3.15 and 3.16, which can be expressed in matrix form as

$$\begin{aligned} \begin{bmatrix} \dot{q}_1 \\ \dot{p}_1 \\ \dot{q}_2 \\ \dot{p}_2 \end{bmatrix} &= \begin{bmatrix} p_1 \\ -q_1^3 - (q_1 - q_2)^3 \\ p_2 \\ -q_2^3 + (q_1 - q_2)^3 \end{bmatrix} + \\ &\begin{bmatrix} 0 & 0 & 0 \\ q_1 & (q_1 - q_2) & 0 \\ 0 & 0 & 0 \\ 0 & -(q_1 - q_2) & q_2 \end{bmatrix} \begin{bmatrix} \mu_1 \\ \mu_2 \\ \mu_3 \end{bmatrix} \end{aligned} \quad (3.26)$$

This is now in the form $\dot{\mathbf{x}} = \mathbf{f}(\mathbf{x}) + \mathbf{h}(\mathbf{x})\mathbf{u}$, which is an affine system with drift terms, where \mathbf{x} is again a vector of state variables and \mathbf{u} is a vector of control variables. Feedback linearisation can then be used to transform the original system model into an equivalent linear model, by algebraically transforming the nonlinear system into linear dynamics, so that linear control methods can be applied. Feedback linearisation therefore uses exact feedback, while conventional (Jacobian) linearisation is a linear approximation of the actual non-linear dynamics [67].

Equation 3.26 can be rewritten in a simpler form as

$$\begin{bmatrix} \ddot{\mathbf{q}} \end{bmatrix} = \begin{bmatrix} -q_1^3 - (q_1 - q_2)^3 \\ -q_2^3 + (q_1 - q_2)^3 \end{bmatrix} + J(q)\mu, \quad (3.27)$$

$$J(q) = \begin{bmatrix} q_1 & (q_1 - q_2) & 0 \\ 0 & -(q_1 - q_2) & q_2 \end{bmatrix}$$

The invertibility matrix $J(q)$ has rank is 2 when there are two values not equal to zero among the three variables q_1 , q_2 and $q_1 - q_2$. From the discussion of Section 3.1, the control system will then have four null points, when $q_1 - q_2 = 0$, $q_1 = 0$ and $q_2 = 0$. Therefore, the three control parameters can be chosen to avoid singularities; for example when q_1 vanishes, the corresponding value of μ_1 will be unbound, so μ_2 and μ_3 are then selected as the control parameters with a constant value of μ_1 . The system is therefore controllable with two state variables and two control variables. In this way, the natural length of the spring can be used as the control (assumed through an appropriate smart material) and so the control parameters which can be used to track the reference trajectory are given by

$$\mu = J^{-1}(q) \left(\ddot{\mathbf{q}} - \begin{bmatrix} -q_1^3 - (q_1 - q_2)^3 \\ -q_2^3 + (q_1 - q_2)^3 \end{bmatrix} \right) \quad (3.28)$$

The nonlinear system is transformed to an affine system for employing the inverse control method. The above discussion provides a detailed means of defining a control strategy for the non-linear dynamical system. The relationship between the controllers and states is therefore obtained directly through analytical methods, where the efficiency of the control system will be investigated in the following sections.

3.4 Energy evaluation criteria

In order to control the reconfiguration of the smart structure it can be implicitly assumed that the natural length of the springs can be modulated through the parameter set μ_1 , μ_2 and μ_3 (again, assuming use of an appropriate smart material, such as shape-memory alloys). In order to estimate the energy requirements for such modulation a simplified description of the spring actuator is provided [5], as shown in Fig. 3.6. Two performance parameters are now considered in the model, one is the basic property of the smart material, the induced-strain effect, denoted by d_s in Fig. 3.6; the other is the

internal stiffness, k_s , again shown in Fig. 3.6.

Due to spring compressibility, an elastic displacement F/k_s can be produced by the load F . The spring can then actuate the induced-strain displacement, d_s , to increase or decrease the output displacement d_e , as shown in Fig. 3.6a, where d_e is given as

$$d_e = d_s - \frac{F}{k_s} \quad (3.29)$$

The external load, F , is now considered as a product of an external spring with the same stiffness k_s , as shown in Fig 3.6b, thus

$$F = k_s d_e \quad (3.30)$$

Combining Eq. 3.29 and Eq. 3.30, the relationship between d_e and d_s can be found as

$$d_s = 2d_e \quad (3.31)$$

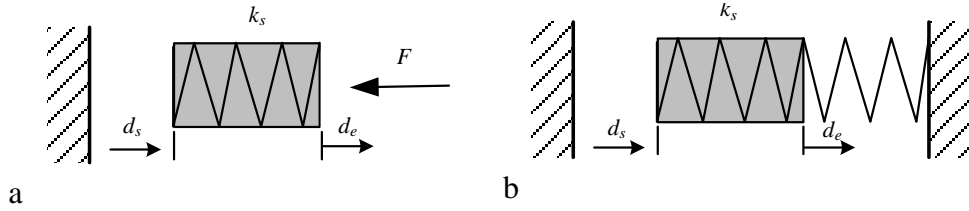


Figure 3.6: Control effort evaluation criteria using a simple spring model. Shaded block represents smart material element with internal stiffness (a) Element under external load F (b) Element attached to external spring (adapted from [5]).

Under quasi-static conditions, the output energy is then half the product between the force and the output displacement squared, i.e.

$$E = \frac{1}{2} k_s d_e^2 \quad (3.32)$$

Substituting Eq. 3.31 into Eq. 3.32 an expression for the input energy is obtained in terms of the induced-strain as

$$E = \frac{1}{2} k_s \left(\frac{1}{4} d_s^2 \right) \quad (3.33)$$

Now that the relationship has been considered between the energy input and control action more specifically an energy evaluation criteria can be found. Through the above

analysis, and from Section 3.2, the control variable $\mu=2(l/d - 1)$ is used to obtain

$$\Delta l = (d/2)\Delta\mu \quad (3.34)$$

Consider that Δl and d_s have the same physical significance in the spring model so that Eq. 3.32 may be written as

$$E = \frac{1}{2}k_s\left(\frac{1}{4}d_s^2\right) = \frac{1}{2}k_s\left(\frac{1}{4}\left(\frac{d}{2}\right)^2\Delta\mu^2\right) = \frac{1}{32}k_s d^2 \Delta\mu^2 \propto \Delta\mu^2 \quad (3.35)$$

where k_s , d are constants. A simple means of comparing the energy requirements can then be obtained by using Eq. 3.35 to track the reference polynomial trajectory between the unstable equilibrium states of the smart structure model, as will be detailed in Section 3.6 later.

3.5 Inverse methods

In this section a simple algorithm is used to determine the singular states of the problem and then provide a new set of control variables for reconfiguration. Here, δ , as defined in Section 3.1, is used as an evaluation index in this section. Although μ is the nominal control vector, the real problem should be considered; the spring is elastic but within limits. Therefore the real deformation δ is defined to be no more than 25% to approximate a realistic system. Therefore, when δ_2 is more than $\bar{\delta}$, where $\bar{\delta}$ corresponds to a deformation of 25%, as defined through Eq. 3.6, μ_1 and μ_3 are chosen as the control variables with fixed μ_2 ; when δ_1 is more than $\bar{\delta}$, μ_2 and μ_3 are choose as the control variables with fixed μ_1 ; when μ_3 is more than $\bar{\delta}$, μ_1 and μ_2 are chosen as the control variables with fixed μ_3 , with Eq. 3.28 providing the control variables μ_1 , μ_2 and μ_3 , where δ_1 , δ_2 and δ_3 represent the deformation ratio of real springs corresponding to μ_1 , μ_2 and μ_3 , respectively.

Using Eq. 3.24 and Eq. 3.25, the constraint can then be expressed as the error between the system state and desired output

$$\mathbf{e} = \mathbf{q} - \mathbf{q}^* \quad (3.36)$$

$$\dot{\mathbf{e}} = \dot{\mathbf{q}} - \dot{\mathbf{q}}^* \quad (3.37)$$

$$\ddot{\mathbf{e}} = \ddot{\mathbf{q}} - \ddot{\mathbf{q}}^* = -\mathbf{g}_1\dot{\mathbf{e}} - \mathbf{g}_2\mathbf{e} \quad (3.38)$$

In order to ensure convergence to the desired output \mathbf{q}^* a Lyapunov function will be

defined as

$$\phi(\mathbf{q}, \dot{\mathbf{q}}) = \frac{1}{2}(\mathbf{q} - \mathbf{q}^*)^T \mathbf{g}_2(\mathbf{q} - \mathbf{q}^*) + \frac{1}{2}(\dot{\mathbf{q}} - \dot{\mathbf{q}}^*)^T (\dot{\mathbf{q}} - \dot{\mathbf{q}}^*) \quad (3.39)$$

where $\phi(\mathbf{q}, \dot{\mathbf{q}}) > 0$ and $\phi(\mathbf{q}^*, \dot{\mathbf{q}}^*) = 0$ for $\mathbf{g}_2 > 0$. The time derivative of the Lyapunov function is then

$$\dot{\phi}(\mathbf{q}, \dot{\mathbf{q}}) = (\dot{\mathbf{q}} - \dot{\mathbf{q}}^*)^T \mathbf{g}_2(\mathbf{q} - \mathbf{q}^*) + (\dot{\mathbf{q}} - \dot{\mathbf{q}}^*)^T (\ddot{\mathbf{q}} - \ddot{\mathbf{q}}^*) = \dot{\mathbf{e}}^T \mathbf{g}_2 \mathbf{e} + \dot{\mathbf{e}}^T \ddot{\mathbf{e}} \quad (3.40)$$

Substituting Eq. 3.38 into Eq. 3.39 the expression for the time derivative of the Lyapunov function can be obtained. It can be seen that ϕ is monotonically decreasing corresponding to $\mathbf{g}_1 > \mathbf{0}$ and $\mathbf{g}_2 > \mathbf{0}$ such that

$$\dot{\phi}(\mathbf{q}, \dot{\mathbf{q}}) = \dot{\mathbf{e}}^T \mathbf{g}_2 \mathbf{e} + \dot{\mathbf{e}}^T (-\mathbf{g}_1 \dot{\mathbf{e}} - \mathbf{g}_2 \mathbf{e}) = -\dot{\mathbf{e}}^T \mathbf{g}_1 \dot{\mathbf{e}} \leq 0 \quad (3.41)$$

where again \mathbf{g}_1 and \mathbf{g}_2 are the gain matrices. It is clear then that the required acceleration is given by

$$\ddot{q}_1 = \ddot{q}_1^* - g_{11}(\dot{q}_1 - \dot{q}_1^*) - g_{12}(q_1 - q_1^*) \quad (3.42)$$

$$\ddot{q}_2 = \ddot{q}_2^* - g_{21}(\dot{q}_2 - \dot{q}_2^*) - g_{22}(q_2 - q_2^*) \quad (3.43)$$

Through intermediate variables \ddot{q}_1 and \ddot{q}_2 , the inverse control method can then be connected to the system dynamics. That is, Eqs. 3.42 and 3.43 are used as feedback to control the dynamics of the system defined by Eqs. 3.13-3.16. The system dynamics are therefore artificially linearised about the nominal reference trajectory so that the control variables can then be determined from Eq. 3.35 as

$$\boldsymbol{\mu} = \mathbf{J}^{-1}(\mathbf{q}) \begin{pmatrix} -g_{11}(\dot{q}_1) + \left[\ddot{q}_1^* + g_{11}\dot{q}_1^* - g_{12}(q_1 - q_1^*) + q_1^3 + (q_1 - q_2)^3 \right] \\ -g_{21}(\dot{q}_2) + \left[\ddot{q}_2^* + g_{21}\dot{q}_2^* - g_{22}(q_2 - q_2^*) + q_2^3 - (q_1 - q_2)^3 \right] \end{pmatrix} \quad (3.44)$$

This provides a composite control which ensures convergence to the desired reference trajectory while avoiding control singularities, as shown in Fig 3.7. Equation 3.44 provides a distinct relationship between the control variables $\boldsymbol{\mu}$ and the state variables \mathbf{q} , and so the state variables \mathbf{q} form the control variables $\boldsymbol{\mu}$ along with the polynomial reference trajectory \mathbf{q}^* .

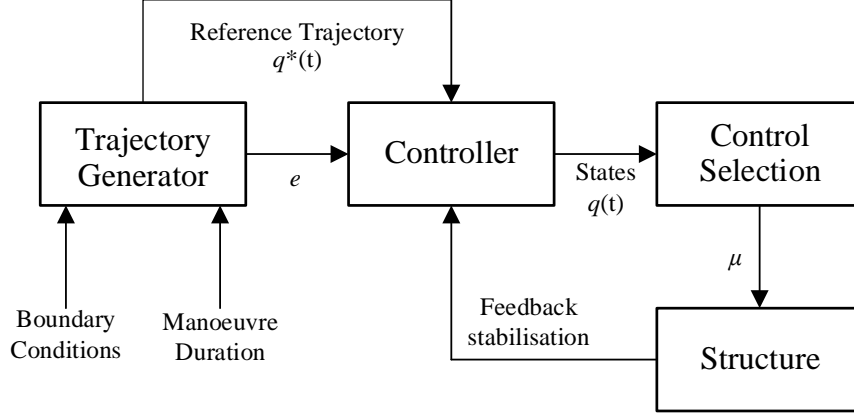


Figure 3.7: Composite feedback linearisation control scheme.

3.6 Control of approximate heteroclinic connections

The method defined in Section 3.5 will now be applied to illustrate two reconfiguration manoeuvres and the use of the inverse method to achieve effective control. The inverse method will be used to reconfigure the 2 degree-of-freedom smart structure model with a 4th order polynomial to approximate the ideal heteroclinic connection through E_3 between E_1 and E_2 . The approximate heteroclinic connection can be seen in Fig. 3.8a, where the controller tracks the approximate trajectory defined by the 4th order polynomial, with the constant gains defined as $g_{11} = g_{21} = 0.25$ and $g_{12} = g_{22} = 0.75$ and the reconfiguration duration $T=20$ (non-dimensional units). The corresponding shape of the structure during the transition from E_1 to E_2 is shown in Fig. 3.8b. The labels in Fig. 3.8b illustrate the transition process corresponding to the positions marked in Fig. 3.8a. The corresponding controls μ_1 , μ_2 and μ_3 are shown in Fig. 3.8c, where it can be seen that the controls are symmetric about $t = T/2$ as expected. The controls here are scaled variables, so that although the maximum relative change shown in Fig. 3.8c is more than 50%, the ratio of the corresponding real spring deformation is only 18%, which is calculated by Eq. 3.6, and is less than $\bar{\delta}$. There are sudden jumps in Fig. 3.8c which correspond to the switching control strategy discussed in Section 3.3. The corresponding mass displacement and the reference path is then shown in Fig. 3.8d.

The inverse method is now considered to reconfigure the 2 degree-of-freedom smart structure model with the 4th order polynomial to approximate a transition crossing the potential barrier E_1 between E_3 and E_4 . The approximate path can be seen in Fig. 3.9a and the corresponding shape of the structure during the transition from E_3 to E_4 is shown in Fig. 3.9b. The corresponding controls μ_1 , μ_2 and μ_3 are shown in Fig. 3.9c and the corresponding mass displacement and the reference path is shown in

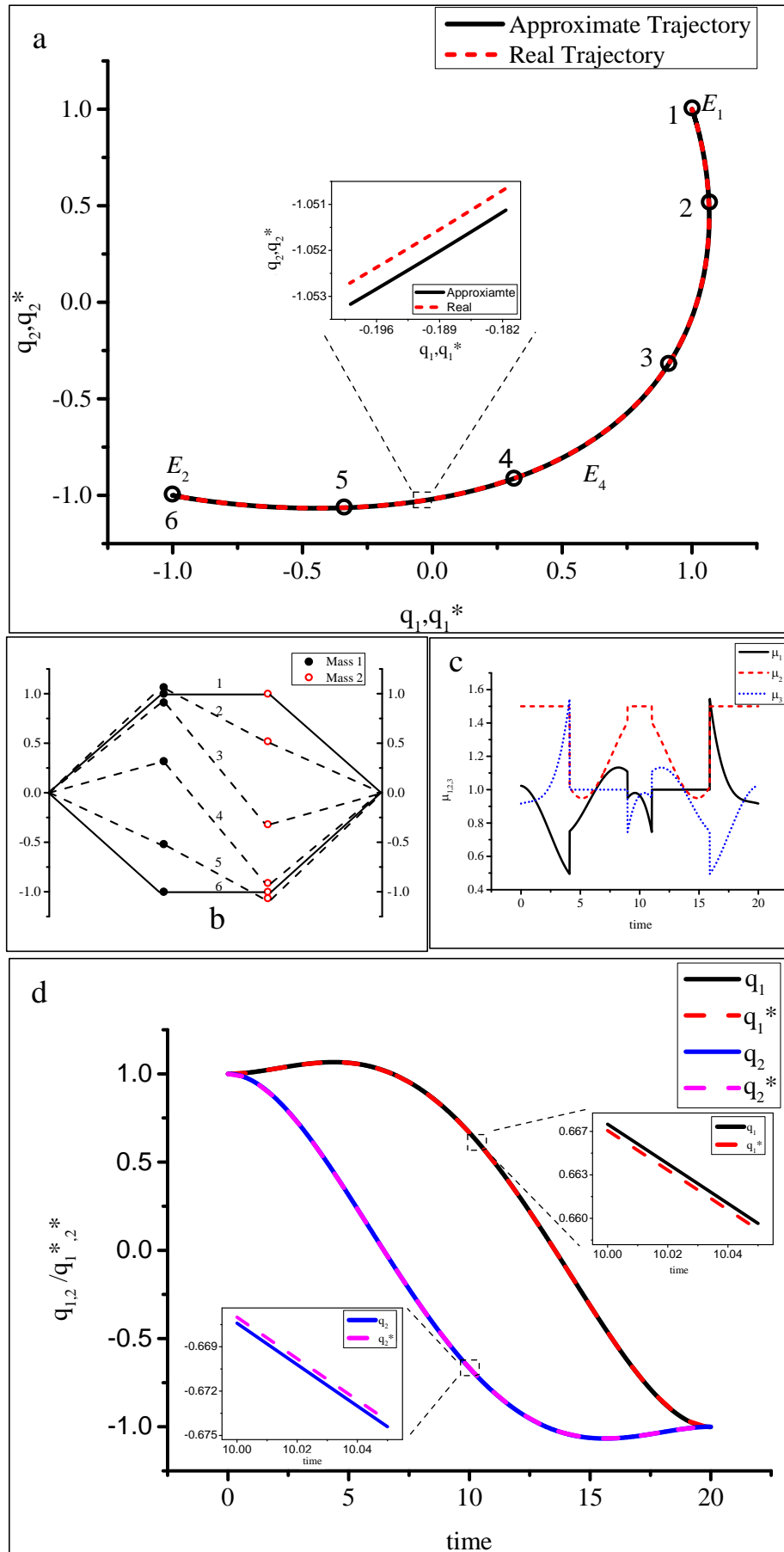


Figure 3.8: 4th order polynomial as reference trajectory from E_1 at (1, 1) to E_2 at (-1, -1) (a) Controlled transition (b) Geometry of transition process (c) Controls actuated through the parameters μ_1, μ_2 and μ_3 (d) Mass displacements during the transition from E_1 to E_2 with the reference trajectory and actual trajectory.

Fig. 3.9d.

The evaluation criteria discussed in Section 3.5 is now used to investigate the energy requirements for the transitions of the simple smart structure model. For example, the energy requirement needed to overcome the potential barrier at equilibrium E_1 is clearly greater than that passing through E_3 , as shown in Fig 3.10. The energy for transitions through E_1 is of order 25% higher than that for transitions through E_3 , as expected.

However, in order to evaluate the polynomial method further, a set of higher order polynomials will now be used which can reduce the effective energy required for re-configuration. Additional boundary conditions can therefore be added to construct a higher order reference polynomial which better matches the true heteroclinic connection. Considering the transition from E_1 at $(1, 1)$ to E_2 at $(-1, -1)$ as an example an additional constraint can be added such that

$$\begin{bmatrix} \ddot{\mathbf{q}}^*(0) & \ddot{\mathbf{q}}^*(T) \end{bmatrix} = \begin{bmatrix} 0 & 0 \\ 0 & 0 \end{bmatrix} \quad (3.45)$$

Then, the only remaining free parameter to define the reference polynomial is again the total reconfiguration duration T . An approximate heteroclinic connection can therefore defined using

$$\mathbf{q}^*(t) = \mathbf{a}_0 + \mathbf{a}_1 t + \mathbf{a}_2 t^2 + \mathbf{a}_3 t^3 + \mathbf{a}_4 t^4 + \mathbf{a}_5 t^5 + \mathbf{a}_6 t^6 \quad (3.46)$$

Using the inverse control method another approximate heteroclinic connection can then be generated as shown in Fig. 3.11a, where the controller tracks the approximate trajectory defined by the 6th order polynomial. The corresponding controls μ_1 , μ_2 and μ_3 are shown in Fig. 3.11b.

Then, the energy evaluation criteria can be used in order to track the approximate trajectory through E_3 , where the total energy input to the process can be seen in Fig. 3.12. The numerical results demonstrate that with the higher order polynomial less energy is required for the reconfiguration process.

Additional target waypoints can now be added so that these points can be used to construct a yet more accurate polynomial to approximate the exact heteroclinic connection. Here, the energy evaluation criteria will be considered and a simple optimisation algorithm used to find the location of these waypoints to minimise the total energy required.

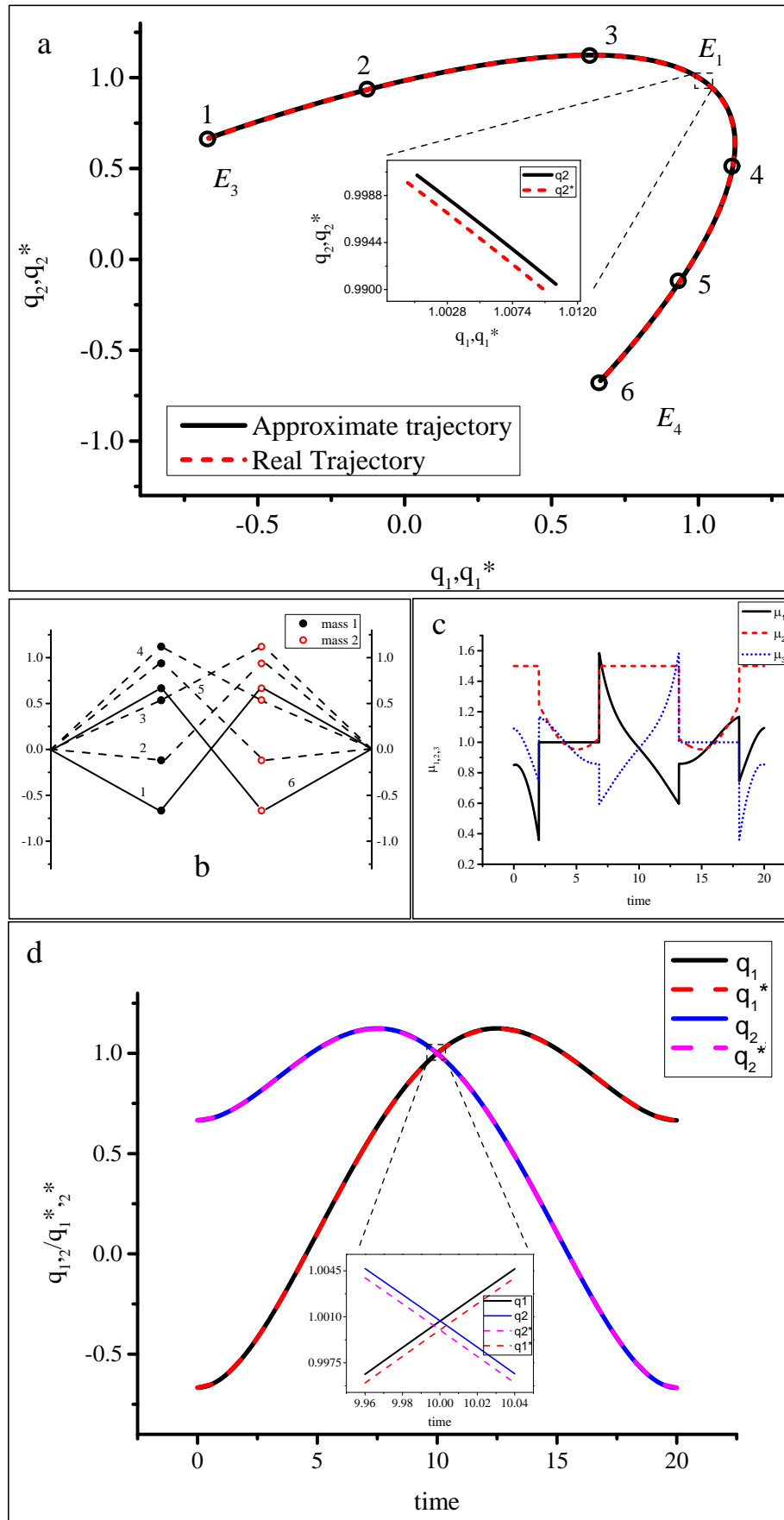


Figure 3.9: 4th order polynomial as reference trajectory from E_3 at $(-2/3, 2/3)$ to E_4 at $(2/3, -2/3)$ (a) Controlled transition (b) Geometry of transition process (c) Controls actuated through the parameters μ_1, μ_2 and μ_3 (d) Mass displacements during the transition from E_3 to E_4 with the reference trajectory and actual trajectory.

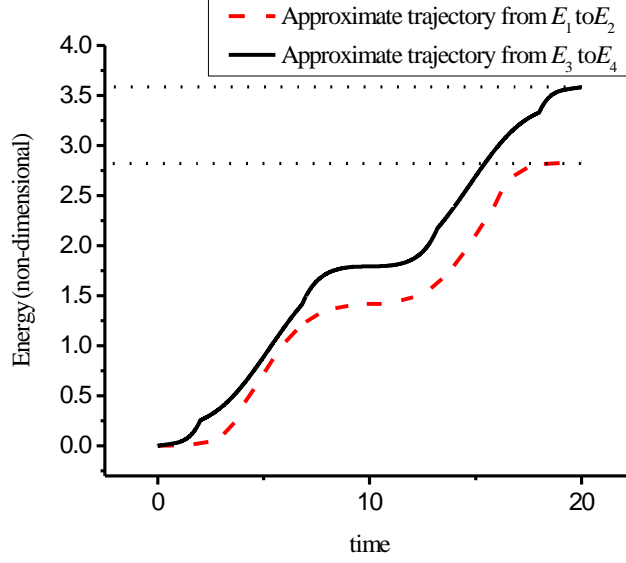


Figure 3.10: Comparison of energy input for different reconfigurations.

Additional variables will be added based on Eq. 3.46, as shown in Eq. 3.47 so that

$$\mathbf{q}^*(t) = \mathbf{a}_0 + \mathbf{a}_1 t + \mathbf{a}_2 t^2 + \mathbf{a}_3 t^3 + \mathbf{a}_4 t^4 + \mathbf{a}_5 t^5 + \mathbf{a}_6 t^6 + \mathbf{a}_7 t^7 + \mathbf{a}_8 t^8 \quad (3.47)$$

It is difficult to add the additional constant \mathbf{a}_7 and \mathbf{a}_8 from simple geometric considerations. However, two time points $T/4$ and $3T/4$ (where T is again the reconfiguration duration) are selected as fixed waypoints. Then, the location of the two target waypoints are chosen by using an optimisation algorithm. Therefore, an 8^{th} order polynomial can be defined as the reference trajectory and the *fmincon* function in Matlab used, which is a nonlinear multivariable optimiser which can find the minimum of a constrained function [68]. It would be envisaged using a simple numerical search algorithm to optimise the waypoint location in a real smart structure using heteroclinic connections. Using the optimisation algorithm, the improved numerical results can be seen in Fig. 3.13a, showing the heteroclinic connection approximated with an 8^{th} order polynomial where the constant gain matrices are again $g_{11} = g_{21} = 0.25$, $g_{12} = g_{22} = 0.75$. Figure 3.13b illustrates the corresponding shape of the structure during the transition from E_1 to E_2 and the corresponding controls μ_1 , μ_2 and μ_3 are shown in Fig. 3.13c. It can be seen that the controls are again symmetric about $t = T/2$. The corresponding mass displacement and the reference path is shown in Fig. 3.13d.

The energy evaluation criteria can then be used to measure the total energy required

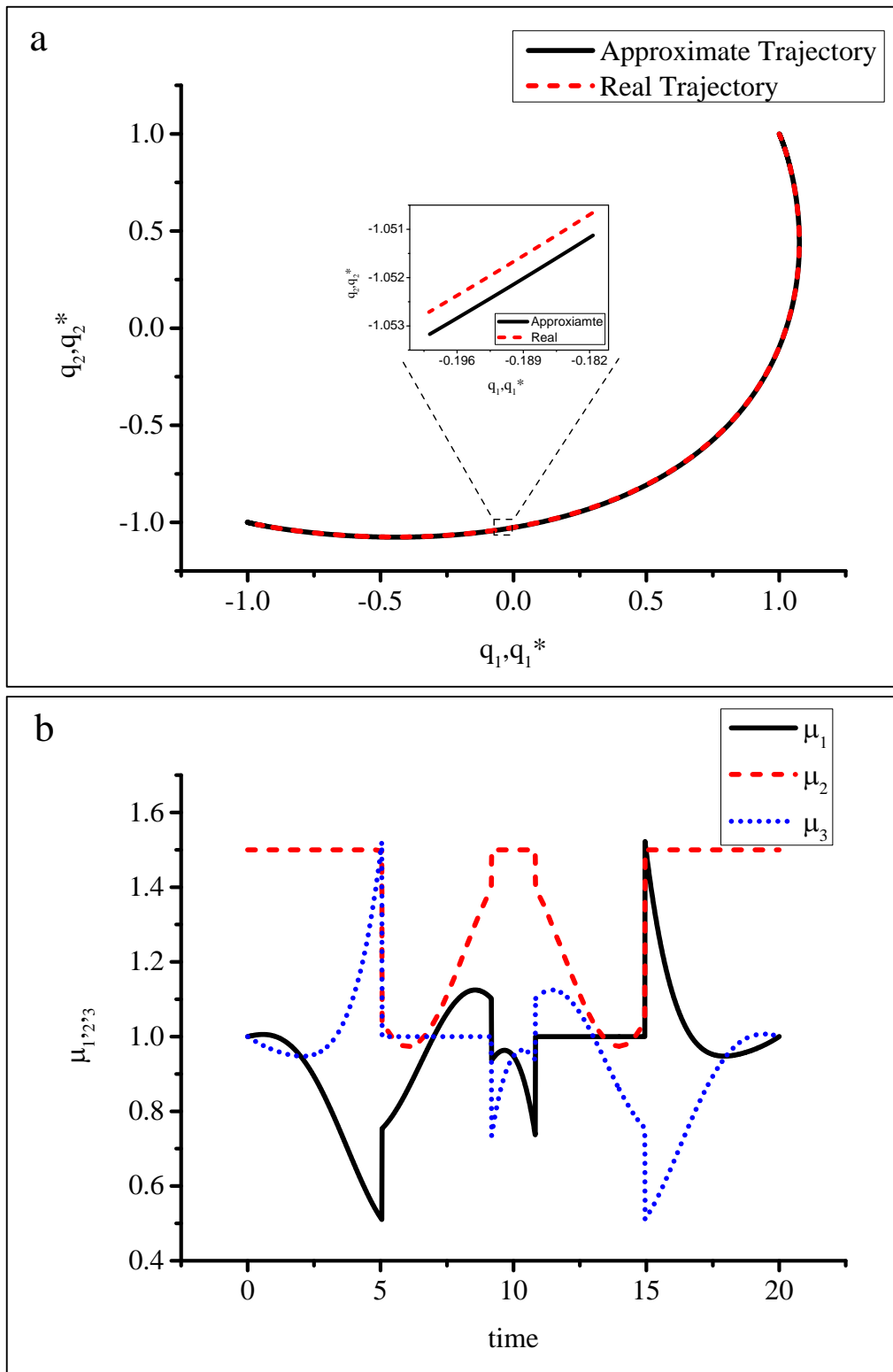


Figure 3.11: 6th order polynomial as reference trajectory from E_1 at $(1, 1)$ to E_2 at $(-1, -1)$ (a) Controlled transition (b) Controls actuated through the parameters μ_1 , μ_2 and μ_3 .

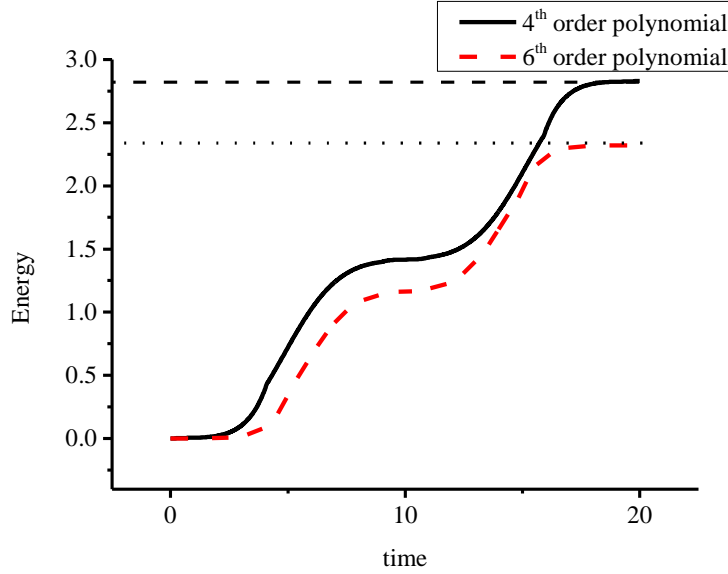


Figure 3.12: Comparison of energy input to track different approximate trajectories.

for the reconfiguration process, as can be seen in Fig. 3.14. From Fig. 3.14 it can be seen that the initial assumptions on the order of the polynomial which is used to approximate the heteroclinic connection is key. We can use a higher order polynomial as a reference trajectory to reconfigure structure with significantly less energy input, but requiring a numerical search for optimisation.

Now, the influence of the total reconfiguration duration T can be considered, which is the only remaining free parameter to define the reference polynomials. Using the same energy evaluation criteria can be found the relationship between the total reconfiguration duration and the energy requirements. Figure 3.15 shows five distinct curves which define five types of reference trajectory with different manoeuvre durations considered. There is an evident sharp decrease to an optimum, minimum energy duration and then a slow increase as the manoeuvre duration grows. For this example the optimum manoeuvre duration T can be clearly seen. It can again be seen that the transition through E_1 needs more energy than the transition through E_3 with the same order polynomial and the same manoeuvre duration as expected. This demonstrates that the higher order polynomial can significantly improve the reference trajectory for reconfiguring the smart structure model.

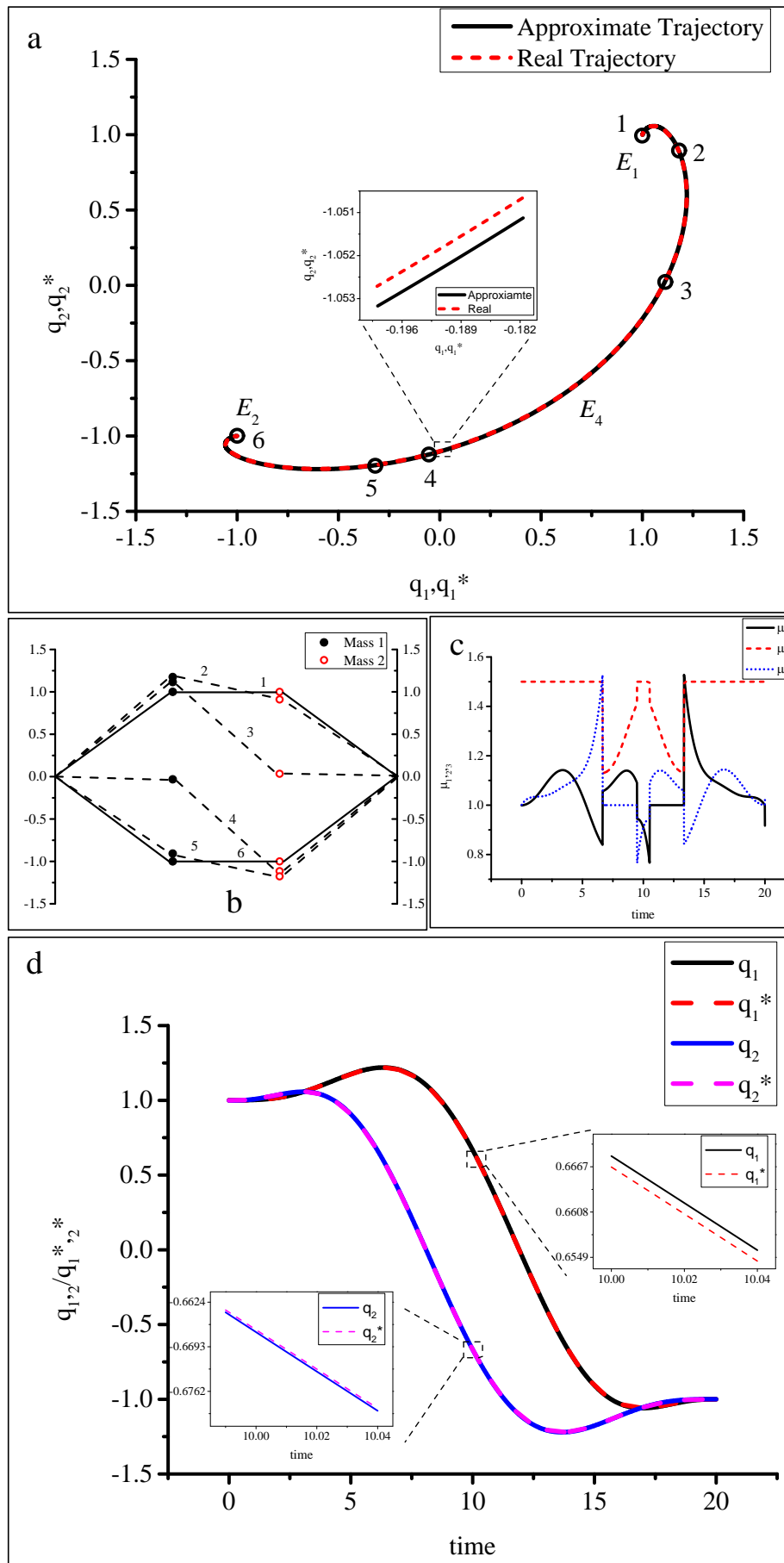


Figure 3.13: 8th order polynomial as reference trajectory from E_1 at $(1, 1)$ to E_2 at $(-1, -1)$ (a) Controlled transition (b) Geometry of transition process (c) Controls actuated through the parameters μ_1, μ_2 and μ_3 (d) Mass displacements during the transition from E_1 to E_2 with the reference trajectory and actual trajectory.

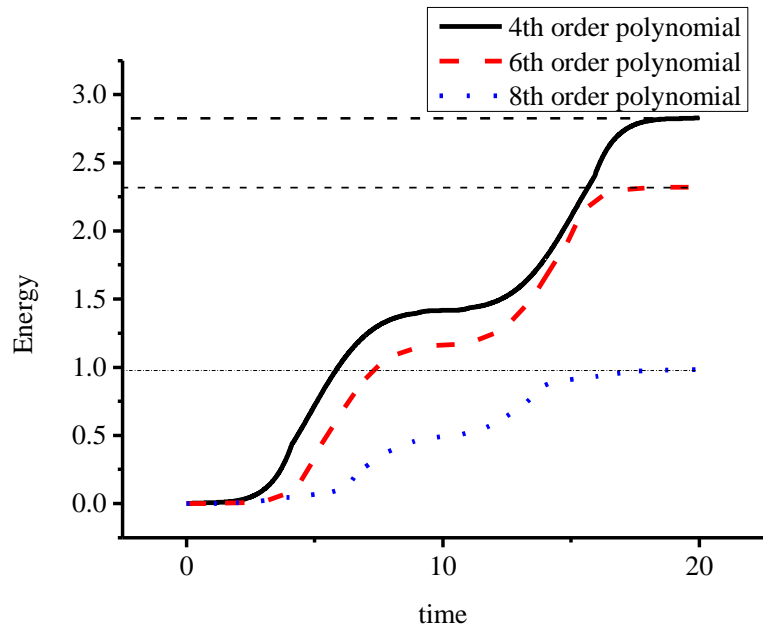


Figure 3.14: Comparison of energy input to track different approximate trajectories with varying polynomial degree.

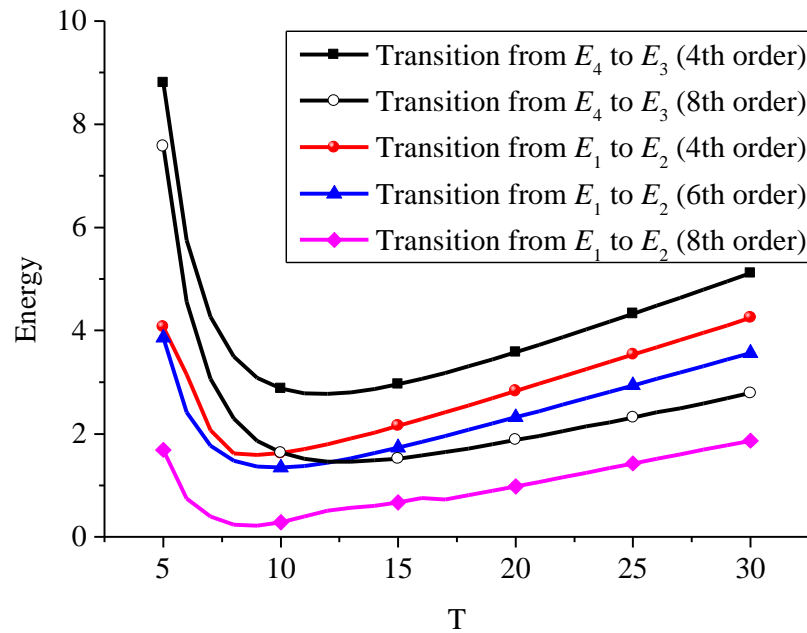


Figure 3.15: Energy required for reconfiguration as a function of reconfiguration duration.

3.7 Three mass chain

In order to further explore the possibility of reconfiguring smart structures using reference polynomials, a more complex three mass chain with four linear springs will now be considered, with the springs clamped at both ends as shown in Fig. 3.16. This more complex problem greatly increases the number of equilibria in the system and the difficulty of finding an exact heteroclinic connection by purely numerical means (particularly in real-time for a physical system). The dynamics of the chain are firstly obtained from Eqs. 3.2- 3.3 as

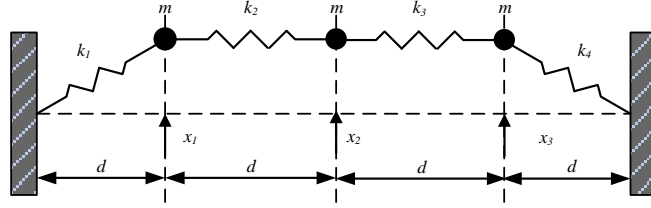


Figure 3.16: 3 degree-of-freedom buckling beam model.

$$\dot{q}_1 = p_1 \quad (3.48)$$

$$\dot{p}_1 = \mu_1 q_1 - q_1^3 + \mu_2 (q_1 - q_2) - (q_1 - q_2)^3 \quad (3.49)$$

$$\dot{q}_2 = p_2 \quad (3.50)$$

$$\dot{p}_2 = \mu_3 (q_2 - q_3) - (q_2 - q_3)^3 - \mu_2 (q_1 - q_2) + (q_1 - q_2)^3 \quad (3.51)$$

$$\dot{q}_3 = p_3 \quad (3.52)$$

$$\dot{p}_3 = \mu_4 q_3 - q_3^3 - \mu_3 (q_2 - q_3) + (q_2 - q_3)^3 \quad (3.53)$$

Solving Eqs. 3.48- 3.53 for the equilibria of the problem, the location of the equilibria can be found as shown in Table 2 for the parameter set, $\mu_1 = 1$, $\mu_2 = 1.5$, $\mu_3 = 1.5$ and $\mu_4 = 1$, along with the eigenvalue spectrum associated with each equilibrium, as discussed in Section 3.3. It can be seen from Table 3.2 that the system possesses 1 unstable equilibrium E_0 , where the potential has a global maximum, 20 unstable equilibria where the potential has several saddles, and 6 stable equilibria where the potential has a local minimum. The location of these equilibria and potential surfaces can be seen in Fig. 3.17 and Fig. 3.18, respectively.

The 4th order polynomial is firstly used to approximate a heteroclinic connection through E_{10} between E_{12} and E_{13} . The conditions on the polynomial which approximate the heteroclinic connection can therefore be defined as

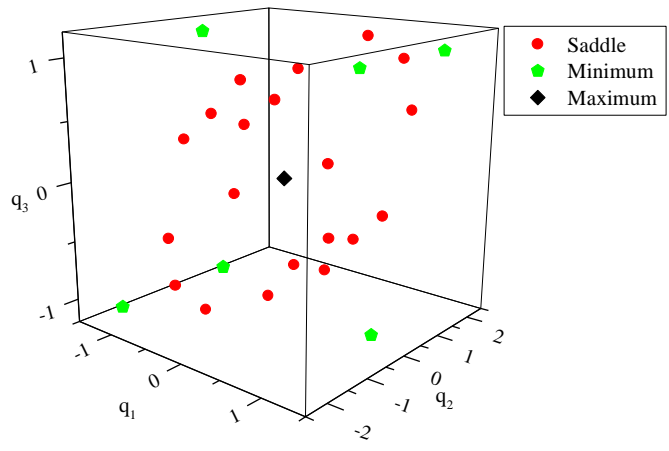


Figure 3.17: 27 equilibria (21 unstable equilibria and 6 stable equilibria).

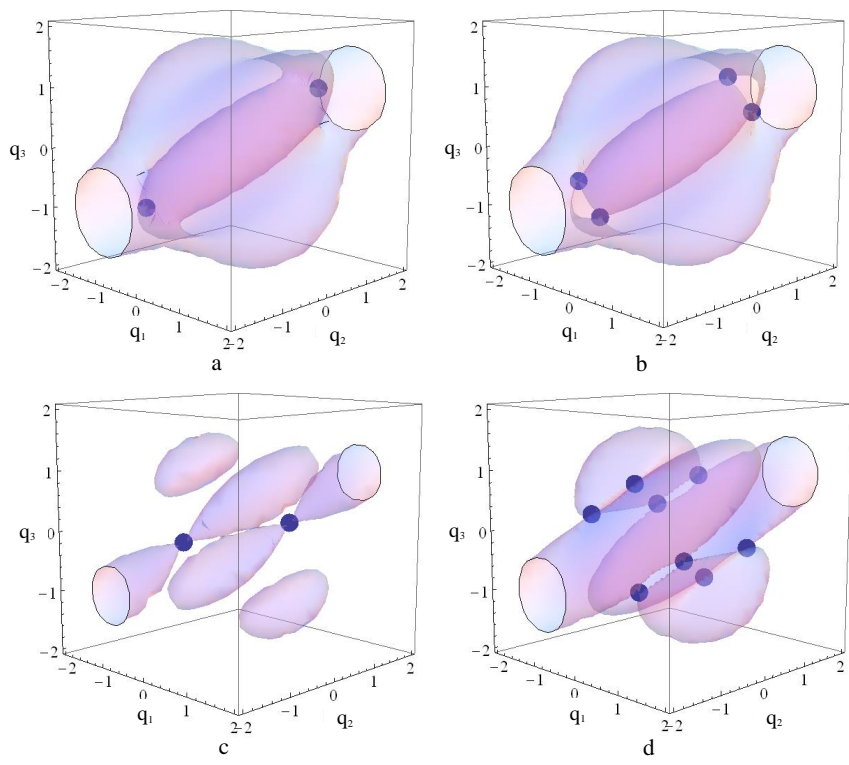


Figure 3.18: Potential surface with saddles (blue circle) (a) Potential -0.5 with E_1 and E_2 (b) Potential -0.482 with E_{23} to E_{26} (c) Potential -1.125 with E_3 and E_4 (d) Potential -0.844 with E_{11} and E_{22} .

Table 3.2: Stability properties of the 27 equilibria of a three mass chain with $\mu_1 = 1$, $\mu_2 = 1.5$, $\mu_3 = 1.5$ and $\mu_4 = 1$. (Type: 1. $S \times S \times S$; 2. $S \times C \times C$; 3. $C \times C \times C$; 4. $S \times S \times C$.)

Point	\tilde{q}_1	\tilde{q}_2	\tilde{q}_3	$\lambda_{1,2}$	$\lambda_{3,4}$	$\lambda_{5,6}$	V	$Type$
E_0	0	0	0	± 0.8	± 2.2	± 1.6	0	1
E_1	1	1	1	± 2	$\pm 0.7i$	$\pm 1.2i$	-0.5	2
E_2	-1	-1	-1	± 2	$\pm 0.7i$	$\pm 1.2i$	-0.5	2
E_3	0	$\sqrt{6}/2$	0	± 0.8	$\pm 2.9i$	$\pm 1.4i$	-1.1	2
E_4	0	$-\sqrt{6}/2$	0	± 0.8	$\pm 2.9i$	$\pm 1.4i$	-1.1	2
E_5	1	$\sqrt{6}/2 + 1$	1	$\pm 3.1i$	$\pm 1.1i$	$\pm 2.2i$	-1.6	2
E_6	1	$1 - \sqrt{6}/2$	1	$\pm 3.1i$	$\pm 1.1i$	$\pm 2.2i$	-1.6	3
E_7	-1	$-1 - \sqrt{6}/2$	-1	$\pm 3.1i$	$\pm 1.1i$	$\pm 2.2i$	-1.6	3
E_8	-1	$\sqrt{6}/2 - 1$	-1	$\pm 3.1i$	$\pm 1.1i$	$\pm 2.2i$	-1.6	3
E_9	$\sqrt{5}/2$	0	$-\sqrt{5}/2$	$\pm 2.8i$	$\pm 1.2i$	$\pm 2.2i$	-1.6	3
E_{10}	$-\sqrt{5}/2$	0	$\sqrt{5}/2$	$\pm 2.8i$	$\pm 1.2i$	$\pm 2.2i$	-1.6	3
E_{11}	$(\sqrt{5} + 1)/4$	1	$(1 - \sqrt{5})/4$	$\pm 2.5i$	$\pm 0.5i$	± 1.4	-0.8	2
E_{12}	$(1 - \sqrt{5})/4$	1	$(\sqrt{5} + 1)/4$	$\pm 2.5i$	$\pm 0.5i$	± 1.4	-0.8	2
E_{13}	$(\sqrt{5} - 1)/4$	-1	$-(\sqrt{5} + 1)/4$	$\pm 2.5i$	$\pm 0.5i$	± 1.4	-0.8	2
E_{14}	$-(\sqrt{5} + 1)/4$	-1	$(\sqrt{5} - 1)/4$	$\pm 2.5i$	$\pm 0.5i$	± 1.4	-0.8	2
E_{15}	$(\sqrt{5} + 1)/4$	-0.5	$(1 - \sqrt{5})/4$	$\pm 2.7i$	$\pm 0.4i$	± 1.6	-0.8	2
E_{16}	$(\sqrt{5} - 1)/4$	-0.5	$(\sqrt{5} + 1)/4$	$\pm 2.7i$	$\pm 0.4i$	± 1.6	-0.8	2
E_{17}	$-(\sqrt{5} + 1)/4$	0.5	$(1 - \sqrt{5})/4$	$\pm 2.7i$	$\pm 0.4i$	± 1.6	-0.8	2
E_{18}	$(\sqrt{5} - 1)/4$	0.5	$-(\sqrt{5} + 1)/4$	$\pm 2.7i$	$\pm 0.4i$	± 1.6	-0.8	2
E_{19}	$-\sqrt{14}/7$	$3\sqrt{14}/14$	$\sqrt{14}/7$	$\pm 2.7i$	± 0.3	± 1.4	-0.8	4
E_{20}	$\sqrt{14}/7$	$3\sqrt{14}/14$	$-\sqrt{14}/7$	$\pm 2.7i$	± 0.3	± 1.4	-0.8	4
E_{21}	$-\sqrt{14}/7$	$-3\sqrt{14}/14$	$\sqrt{14}/7$	$\pm 2.7i$	± 0.3	± 1.4	-0.8	4
E_{22}	$\sqrt{14}/7$	$-3\sqrt{14}/14$	$-\sqrt{14}/7$	$\pm 2.7i$	± 0.3	± 1.4	-0.8	4
E_{23}	0.6	0.9	1.2	± 0.7	± 1.9	$\pm 1.5i$	-0.5	4
E_{24}	-0.6	-0.9	-1.2	± 0.7	± 1.9	$\pm 1.5i$	-0.5	4
E_{25}	1.2	0.9	0.6	± 0.7	± 1.9	$\pm 1.5i$	-0.5	4
E_{26}	-1.2	-0.9	-0.6	± 0.7	± 1.9	$\pm 1.5i$	-0.5	4

$$\left[\mathbf{q}^*(0) \quad \mathbf{q}^*(T/2) \quad \mathbf{q}^*(T) \quad \dot{\mathbf{q}}^*(0) \quad \dot{\mathbf{q}}^*(T) \right] = \begin{bmatrix} -0.309 & 1 & 0.809 \\ -1.118 & 0 & 1.118 \\ -0.809 & -1 & 0.309 \\ 0 & 0 & 0 \\ 0 & 0 & 0 \end{bmatrix}^T \quad (3.54)$$

The manoeuvre duration is again set as $T = 20$ and the constant gains are defined as $g_{11} = g_{21} = 0.25$, $g_{21} = g_{22} = 0.75$. The approximate heteroclinic connection can

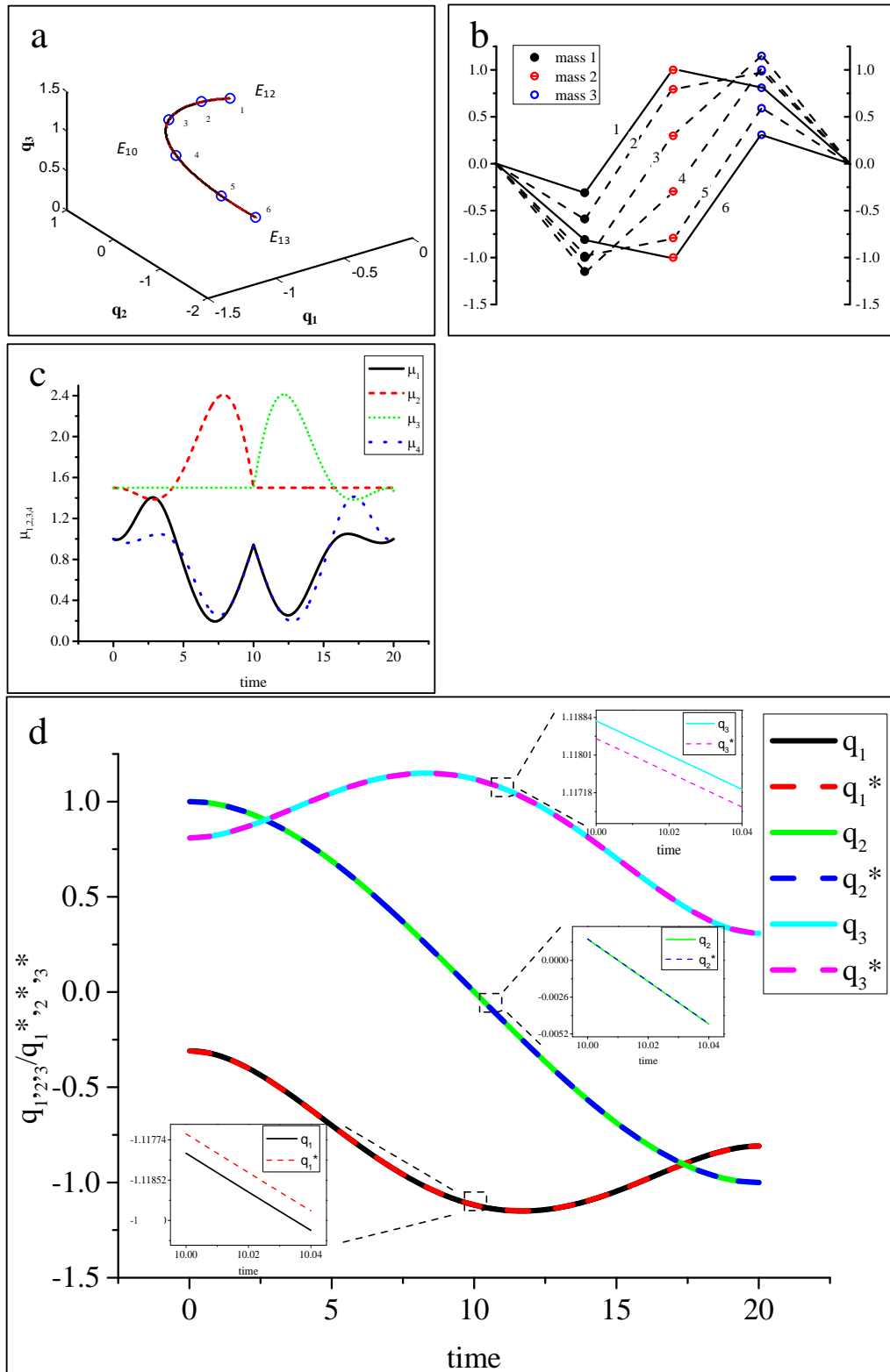


Figure 3.19: 4th order polynomials as reference trajectory from unstable equilibrium E_{12} to unstable equilibrium E_{13} (a) Controlled transition (b) Geometry of transition process, (c) Controls actuated through parameters μ_1, μ_2, μ_3 and μ_4 (d) Mass displacements during the transition from E_{12} to E_{13} with the reference trajectories.

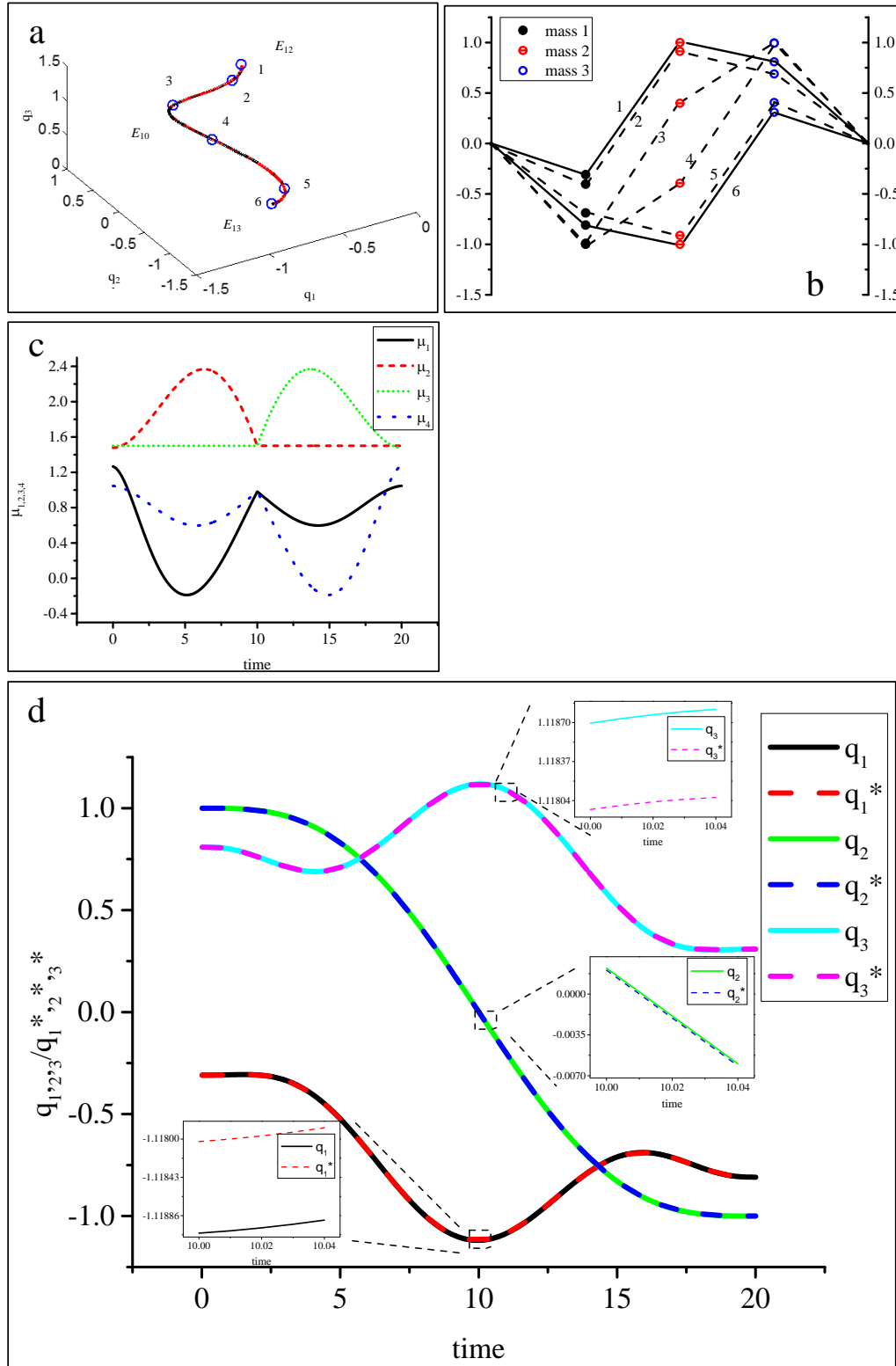


Figure 3.20: 8th order polynomials as reference trajectory from unstable equilibrium E_{12} to unstable equilibrium E_{13} (a) Controlled transition (b) Geometry of transition process (c) Controls actuated through parameters μ_1, μ_2, μ_3 and μ_4 (d) Mass displacements during the transition from E_{12} to E_{13} with the reference trajectories.

be seen in Fig. 3.19a, where the controller tracks the approximate trajectory defined by the 4th order polynomials. The corresponding shape of the structure during the transition from E_{12} to E_{13} is shown in Fig. 3.19b. The labels in Fig. 3.19b represent the transition process corresponding to the positions marked in Fig. 3.19a, while the corresponding controls μ_1, μ_2, μ_3 and μ_4 are shown in Fig. 3.19c. The corresponding mass displacements and the reference path is shown in Fig. 3.19d.

Then, the method discussed in Section 3.5 is used to construct an 8th order polynomial with the additional constraints

$$\begin{bmatrix} \ddot{\mathbf{q}}^*(0) & \ddot{\mathbf{q}}^*(T) \end{bmatrix} = \begin{bmatrix} 0 & 0 \\ 0 & 0 \\ 0 & 0 \end{bmatrix} \quad (3.55)$$

Moreover, using the optimisation algorithm, Fig. 3.20a shows the heteroclinic connection approximated with the 8th order polynomial, where the gains are $g_{11} = g_{21} = 0.25$, $g_{21} = g_{22} = 0.75$. Figure 3.20b illustrates the corresponding shape of the structure during the transition from E_{12} to E_{13} and the corresponding controls μ_1, μ_2, μ_3 and μ_4 are shown in Fig. 3.20c. It can be seen that the controls are again symmetric about $t = T/2$ as expected. The corresponding mass displacement and the reference path is shown in Fig. 3.20d.

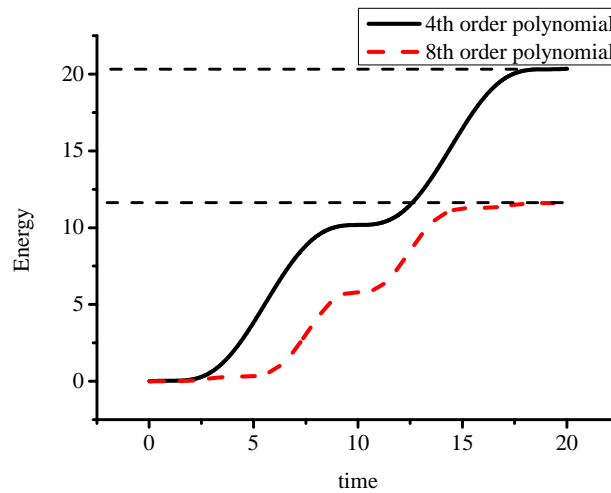


Figure 3.21: Comparison of energy input to track different approximate trajectories.

The energy evaluation criteria can then be used to measure the total energy input to control the reconfiguration process, as can be seen in Fig. 3.21, with the 4th order

polynomials indicated as the solid line, and the 8th order polynomials indicated as the dashed line. From Fig. 3.21 it can be seen that a higher order polynomial can be used as a reference trajectory to reconfigure the 3 mass chain with significantly less energy input. It is considered that a better approximation to a true heteroclinic connection can be formed with a higher order polynomial since a true heteroclinic connection is difficult to find numerically in complex nonlinear systems. Therefore, different order polynomials should be considered under varying practical conditions. Using a high order polynomial as a reference heteroclinic connection to reconfigure the structure could significantly reduce energy input, but requiring a more computationally intensive numerical search for optimisation. Conversely, using a low order polynomial as a reference heteroclinic connection to reconfigure the structure could significantly increase computational efficiency, but would require more energy.

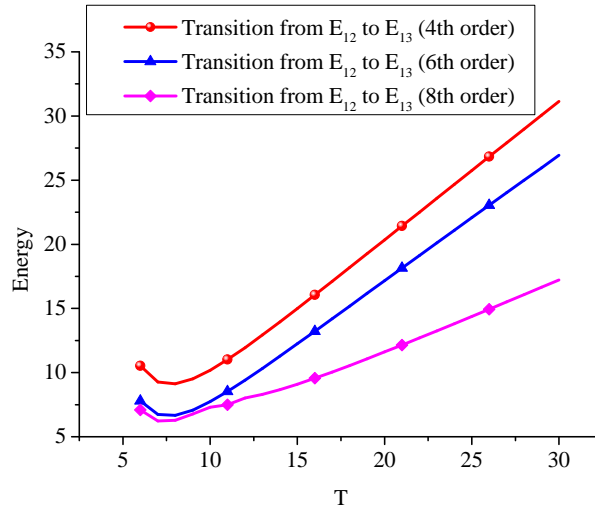


Figure 3.22: Comparison of energy to track different approximate trajectories.

Figure 3.22 shows three distinct curves which define three types of different order reference trajectory with different manoeuvre durations. Again, there is an evident decrease to a minimum energy duration and then an increase as the manoeuvre duration grows similarly to the two mass problem, again as expected.

3.8 Conclusion

A new concept for the reconfiguration of smart structures using polynomial series to approximate phase space connections has been presented. As an application for the method, a simple two mass model is firstly investigated and then a relatively complex 3 mass model used to verify that polynomial series can offer efficient reference trajectories

between unstable equilibria. In addition, inverse control methods have been investigated to control the model for reconfiguration from one equilibrium state to another. Then an energy evaluation criteria has been employed to determine the performance of the different reference trajectories used and demonstrate that more efficient and accurate reference trajectories can be expressed by higher order polynomials. While the models used in the section are relatively simple, they provide an approach to provide insights into low energy reconfiguration which can be extended to achieve reconfiguration of real smart structures.

Chapter 4

Spring-Mass Model

In Chapter 3, a simple model of a smart structure was presented, which was constructed by a two mass chain with three springs subject to clamping at both ends. The springs were approximated to provide a simple cubic nonlinearity. Then, dynamical system theory was used to investigate the characteristics of the simplified model. In spite of its apparent basic form, such models possess the basic features of a suitable smart structure, due to its nonlinearity and instability. However, in consideration of the difference between the cubic model and real springs, a spring-mass model of a simple smart structure is now developed to verify the possibility of using heteroclinic connections to reconfigure real smart structures with the full geometric non-linearity of the springs considered. The more complex problem possesses more equilibria than the cubic non-linearity of Chapter 3. In addition, due to the difficulty in obtaining heteroclinic connections numerically in complex dynamical systems, such as those with strong nonlinearity, other methods are considered in this Chapter. Optimal control methods are firstly employed to find the required control histories and state trajectories. A performance function is then defined by using a simple spring model under quasi-static conditions, which provides a relationship between the control action and the required spring deformation. Through minimisation of the performance function, the control histories can be obtained with satisfactory state trajectories, which approximate true heteroclinic connections. Then, for a realistic model, dissipation must also be considered, which of course will destroy the Hamiltonian structure of the dynamics. Therefore, some strategies are considered to deal with the dissipation term. In order to compensate for such dissipation, controllers need to be used to ensure that heteroclinic connections exist. Two control methods are investigated, using an end-point control and an optimal control strategy. In addition, a bifurcation control strategy is investigated which allows the stability properties of the equilibria to be controlled, enabling

stable equilibria to become temporarily unstable and so connected by heteroclinic paths. Numerical results are presented to illustrate the control strategies developed.

In Section 4.1, a smart structure is defined as a simple model of a mass-spring problem, which is constructed by a two mass chain with three springs subject to clamping at both ends. Again, in this Chapter, the full geometric non-linearity of the problem is considered. First, the second derivative test is used to determine the equilibria of this nonlinear system. Then, heteroclinic connections are obtained using dynamical systems theory. In Section 4.2, an optimal control method is proposed and solved numerically using PSOPT [70] to obtain optimal trajectories with a performance index defined through the use of energy cost function. In Section 4.3, a bifurcation control method is proposed to reconfigure the smart structure between stable states, the fundamental principle is illustrated by a ball on a hill model. This control scheme uses the instability of the smart structure to achieve reconfiguration by retaining stability for normal operating modes. However, dissipation should also be considered in a realistic model, and so a smart structure model is then investigated with a linear dissipation term. Two strategies are employed to compensate for such dissipation to ensure that heteroclinic connections exist (Section 4.4). The numerical results of these two control strategies are presented in Section 4.4. Finally, conclusions will be summarised in Section 4.5.

4.1 2 degree-of-freedom buckling beam model

In order to investigate the use of heteroclinic connections to reconfigure unstable smart structures, a simple representative model of a naturally unstable structure was defined [16]. However, building on Chapter 3, a more realistic model is considered with full geometric non-linearity. A two mass chain with three linear springs will be considered with the springs clamped at both ends, as shown in Fig. 4.1. The model assumes that the masses are constrained to move only in the vertical direction. The parameters of the model are the spring stiffness coefficients and natural lengths \mathbf{k} (k_1, k_2, k_3) and \mathbf{L} (L_1, L_2, L_3), respectively. If the displacement of the mass is defined by x , while the spring clamps are separated by $3d$, it can be shown that the spring lengths after deformation are described by

$$l_1 = \sqrt{x_1^2 + d^2} \quad (4.1)$$

$$l_2 = \sqrt{(x_1 - x_2)^2 + d^2} \quad (4.2)$$

$$l_3 = \sqrt{x_2^2 + d^2} \quad (4.3)$$

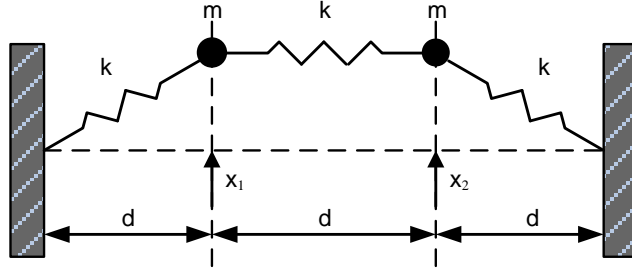


Figure 4.1: 2 degree-of-freedom buckling beam model.

Firstly, the model is considered to be a Hamiltonian system with a simplification that the masses $m=1$. From Fig. 4.1, the Hamiltonian for this two mass model can then be defined from the kinetic and potential energy through Eqs. 4.4 and 4.5 as

$$T(\mathbf{p}) = \frac{1}{2}(p_1^2) + \frac{1}{2}(p_2^2) \quad (4.4)$$

$$V(\mathbf{x}, \mathbf{L}) = \frac{1}{2}k_1(l_1 - L_1)^2 + \frac{1}{2}k_2(l_2 - L_2)^2 + \frac{1}{2}k_3(l_3 - L_3)^2 \quad (4.5)$$

with momentum coordinates p_1 and p_2 . We can now fully define the problem by a dynamical system of the form

$$\dot{x}_1 = p_1 \quad (4.6)$$

$$\dot{p}_1 = \frac{(L_1 - \sqrt{(x_1^2 + 1)})k_1x_1}{\sqrt{x_1^2 + 1}} + \frac{(L_2 - \sqrt{((x_1 - x_2)^2 + 1)})k_2(x_1 - x_2)}{\sqrt{(x_1 - x_2)^2 + 1}} \quad (4.7)$$

$$\dot{x}_2 = p_2 \quad (4.8)$$

$$\dot{p}_2 = \frac{(L_3 - \sqrt{(x_2^2 + 1)})k_3x_2}{\sqrt{x_2^2 + 1}} + \frac{(L_2 - \sqrt{((x_1 - x_2)^2 + 1)})k_2(x_1 - x_2)}{\sqrt{(x_1 - x_2)^2 + 1}} \quad (4.9)$$

Then, dynamical system theory can be used to investigate the characteristics of this new smart structure model. It will be shown that the system defined by Eqs. (4.6-4.9) has a number of equilibria which are both stable and unstable and may be connected in phase space. Solving Eqs. 4.7 and 4.9 for equilibrium conditions yields thirteen equilibria for the parameter set, $k_1 = k_2 = k_3 = 1$, $d = 1$ and $L_1 = L_2 = L_3 = 2$. The location of the equilibria are listed in the Table 4.1.

Then, the Hessian matrix can be used to test the stability properties of these equilibria. In the second derivative test for determining extrema of the potential function $V(\mathbf{x}, \mathbf{L})$,

Table 4.1: Stability properties of the 13 equilibria of 2 degree-of-freedom buckling beam model.

Point	x_1	x_2	V	$\frac{\partial^2 V}{\partial x_1^2}$	D	$Type$
E_0	0	0	1.5	-2	3	Max
E_1	1.100	-1.100	0.350	1.250	0.825	Min
E_2	-1.100	-2.200	0.350	0.783	0.825	Min
E_3	-2.200	-1.100	0.350	1.250	0.825	Min
E_4	-1.100	1.100	0.350	1.250	0.825	Min
E_5	1.100	2.200	0.350	0.783	0.825	Min
E_6	2.200	1.100	0.350	1.250	0.825	Min
E_7	0	1.732	0.5	-0.25	-0.938	Saddle
E_8	1.732	1.732	0.5	-0.25	-0.938	Saddle
E_9	1.732	0	0.5	1.5	-0.938	Saddle
E_{10}	0	-1.732	0.5	-0.25	-0.938	Saddle
E_{11}	-1.732	-1.732	0.5	-0.25	-0.938	Saddle
E_{12}	-1.732	0	0.5	1.5	-0.938	Saddle

the discriminant D is given by

$$D = \begin{bmatrix} \frac{\partial^2 V}{\partial x_1^2} & \frac{\partial^2 V}{\partial x_1 \partial x_2} \\ \frac{\partial^2 V}{\partial x_2 \partial x_1} & \frac{\partial^2 V}{\partial x_2^2} \end{bmatrix} \quad (4.10)$$

The second derivative test discriminant can be summarised with the following statement:

- If $D > 0$, $\frac{\partial^2 V}{\partial x_1^2} > 0$, the point is a local minimum.
- If $D > 0$, $\frac{\partial^2 V}{\partial x_1^2} < 0$, the point is a local maximum.
- If $D < 0$, the point is a saddle point.
- If $D = 0$, higher order tests must be used.

According to the second derivative test discriminant, it can be seen that the 2 degree-of-freedom smart structure model possesses 1 unstable equilibrium E_0 , where the potential has a global maximum, 6 stable equilibria E_1 to E_6 where the potential has a global minimum and 6 unstable equilibria E_7 to E_{12} where the potential has a saddle, as can be seen in Fig. 4.2. The corresponding shape of the smart structure model associated with each of these 13 equilibrium configurations is shown in Fig. 4.3. It can be seen from Table 1 that E_0 has the highest potential V , corresponding to the two masses being

undeflected, with both springs in compression. E_7 to E_{12} then have equal potential which is higher than E_1 to E_6 . For the unstable equilibria E_7 to E_{12} , only one spring is in compression and can in principle relax to the lower energy equilibria at E_1 to E_6 where both springs are extended.

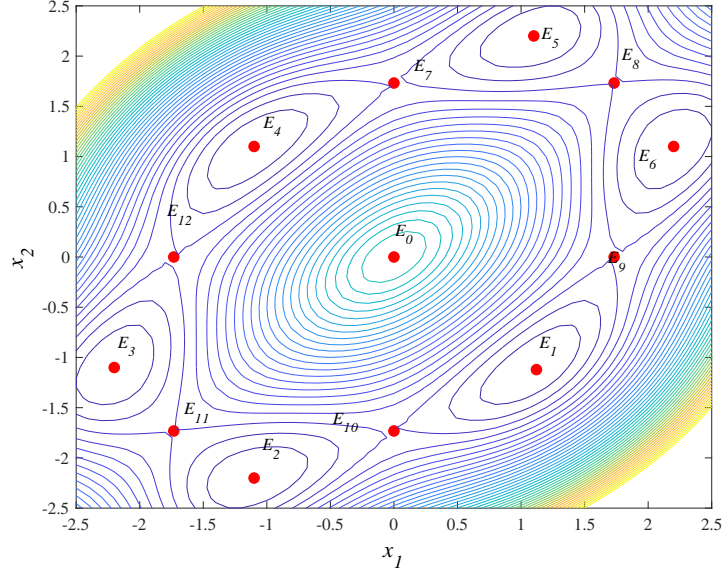


Figure 4.2: Potential $V(x, L)$ and equilibria (6 stable equilibria E_1 to E_6 , and 6 unstable equilibria E_7 to E_{12}).

Since the Hamiltonian of this system is constant, and formed by V and T , the volume of phase space in \mathbb{R}^4 , and its projection to configuration space in \mathbb{R}^2 , is constrained by the requirement that $T(p) > 0$. Since the unstable equilibria E_7 to E_{12} lie on the same energy surface, it could be assumed that in principle a heteroclinic connection between two arbitrary equilibria may exist. Then the structure could be reconfigured between these two equilibria without work being done, in the absence of dissipation, so that the change in energy for reconfiguration $\delta V \approx 0$. If the structure in Fig. 4.2 is at some arbitrary stable equilibrium such as E_9 , it has to cross the potential barrier at E_1 to reach a neighbouring stable equilibrium at E_{10} . Therefore, the change in energy for reconfiguration between stable equilibria via E_1 is $\delta V \approx -0.15$, assuming that the energy input to cross the potential barrier at E_1 is dissipated to finally reach E_{10} . From the view of energy gain and energy loss, it is clear that heteroclinic connections between unstable equilibria may be significantly more efficient than the trajectories that need to cross the potential barrier. That is, transition between stable states requires the input of and then dissipation of energy, while transitions between equal-energy unstable states in principle do not required the addition of energy for an ideal system (and where the

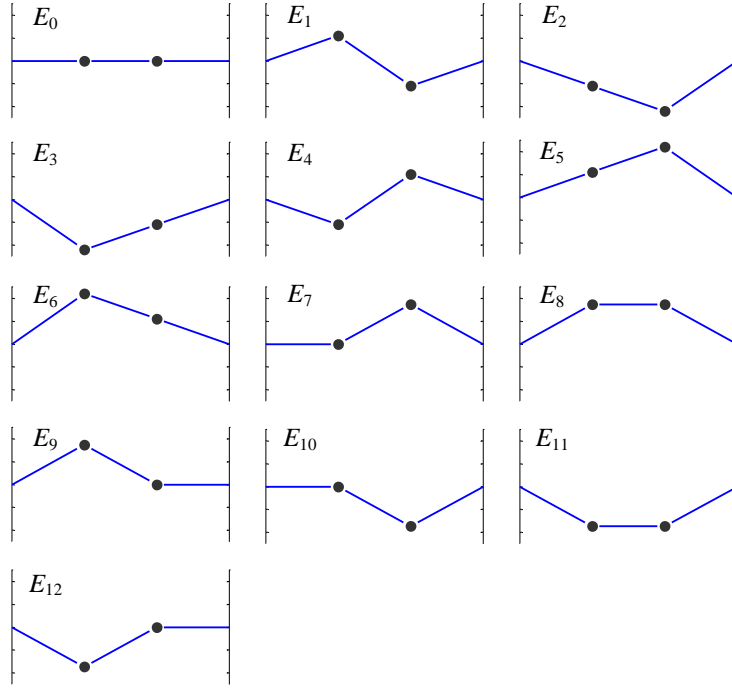


Figure 4.3: Equilibria for a two mass chain with stable equilibria E_{1-6} and unstable equilibria E_{7-12} . The unstable equilibria have equal potential V (Axes are shown in Fig. 4.1).

transition time is unbounded).

The stable and unstable manifolds of these equilibria have been investigated in Section 3.3 to explore possible connections between the unstable equilibria [66]. Integrating forwards or backwards from an unstable equilibrium point, the stable and unstable eigenvectors \mathbf{u}_s and \mathbf{u}_u can be mapped to approximate the stable and unstable manifolds. The initial conditions in the neighbourhood of each equilibrium point \mathbf{z}^e for forwards and backwards integration can be defined as

$$\mathbf{z}^s = \mathbf{z}^e + \epsilon \mathbf{u}^s \quad (4.11)$$

$$\mathbf{z}^u = \mathbf{z}^e + \epsilon \mathbf{u}^u \quad (4.12)$$

for $\epsilon \ll 1$, $\mathbf{z} = (\mathbf{x}, \mathbf{p}) \in \mathbf{R}^4$.

Due to numerical error, and in a real smart structure uncertainty in model parameters, phase trajectories emerging from one unstable equilibrium will not reach the other unstable equilibrium precisely. To compensate for such errors, active control is required which captures phase trajectories in a neighbourhood of the target unstable equilibrium point. Here, the spring length is used as the controller, assuming for example the use of

a suitable shape memory alloy as discussed in Chapter 3. Then, recalling Eq. (4.6-4.9), the dynamical system can be expressed in matrix form as

$$\begin{bmatrix} \dot{x}_1 \\ \dot{p}_1 \\ \dot{x}_2 \\ \dot{p}_2 \end{bmatrix} = \begin{bmatrix} p_1 \\ -(k_1 + k_2)x_1 + x_2 \\ p_2 \\ -(k_3 + k_2)x_2 + x_1 \end{bmatrix} + \begin{bmatrix} 0 & 0 & 0 \\ \frac{k_1 x_1}{\sqrt{x_1^2+1}} & \frac{k_2(x_1-x_2)}{\sqrt{(x_1-x_2)^2+1}} & 0 \\ 0 & 0 & 0 \\ 0 & \frac{k_2(x_1-x_2)}{\sqrt{(x_1-x_2)^2+1}} & \frac{k_3 x_2}{\sqrt{x_2^2+1}} \end{bmatrix} \begin{bmatrix} L_1 \\ L_2 \\ L_3 \end{bmatrix} \quad (4.13)$$

This is now in the form $\dot{\mathbf{x}} = f(\mathbf{x}) + g(\mathbf{x})\mathbf{u}$, which is again an affine system with drift terms [69]. Feedback linearisation can then be used to control the system by transformation to a simpler form. In order to apply linear control techniques, the nonlinear system dynamics of Eq. 4.13 are transformed to linear dynamics. Therefore, equation. 4.13 can be rewritten in the form:

$$\begin{aligned} \begin{bmatrix} \ddot{\mathbf{x}} \end{bmatrix} &= \begin{bmatrix} x_2 - (k_1 + k_2)x_1 \\ x_1 - (k_3 + k_2)x_2 \end{bmatrix} + J(x)\mathbf{L} \\ &= \begin{bmatrix} x_2 - (k_1 + k_2)x_1 \\ x_1 - (k_3 + k_2)x_2 \end{bmatrix} \\ &+ \begin{bmatrix} \frac{k_1 x_1}{\sqrt{x_1^2+1}} & \frac{k_2(x_1-x_2)}{\sqrt{(x_1-x_2)^2+1}} & 0 \\ 0 & \frac{k_2(x_1-x_2)}{\sqrt{(x_1-x_2)^2+1}} & \frac{k_3 x_2}{\sqrt{x_2^2+1}} \end{bmatrix} \begin{bmatrix} L_1 \\ L_2 \\ L_3 \end{bmatrix} \end{aligned} \quad (4.14)$$

The invertibility matrix $J(x)$ has rank is 2 when there are two values not equal to zero among the three variables x_1 , x_2 and x_1-x_2 . Therefore, the control parameters can be chosen to avoid singularities. For example, a controller in the neighbourhood of E_{10} should choose L_2 and L_3 as control variables to avoid the singularity at $x_1=0$. The system is therefore controllable with two state variables and two control variables. The controller can then be defined as

$$\mathbf{L} = J^{-1}(x) \left(\ddot{\mathbf{x}} - \begin{bmatrix} x_2 - (k_1 + k_2)x_1 \\ x_1 - (k_3 + k_2)x_2 \end{bmatrix} \right) \quad (4.15)$$

The transition from E_9 to E_{10} is now considered as an example to illustrate the method to obtain the heteroclinic connection, which takes E_9 to E_{10} as the initial and terminal unstable equilibria, respectively. The control region is defined as a neighbourhood R of E_{10} with the controller defined by Eq. 4.15 used to guarantee the transition to the terminal equilibrium E_{10} , as shown in Fig. 4.4.

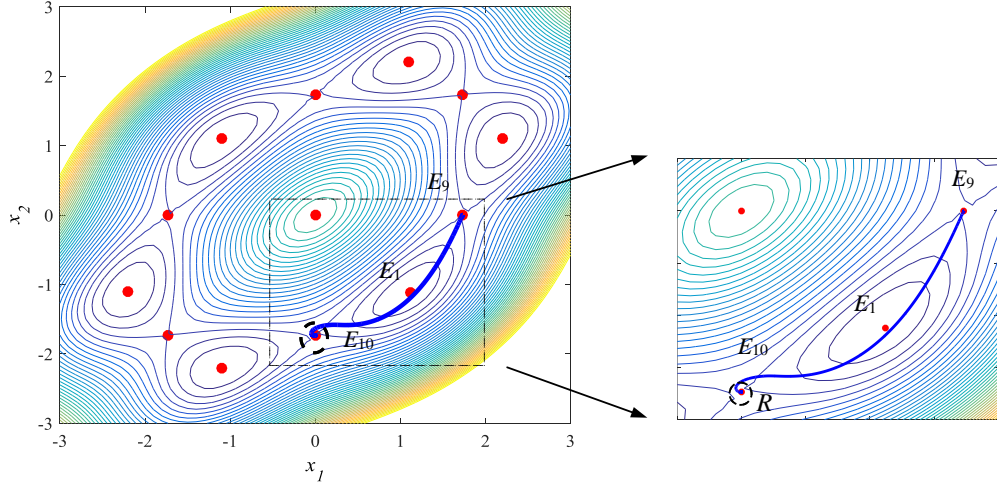


Figure 4.4: Controlled transition from E_9 at $(1.732,0)$ to E_{10} at $(0,-1.732)$ with the controller active in the neighbourhood of E_{10} . Contour represents the allowed region of motion with $T(p) > 0$.

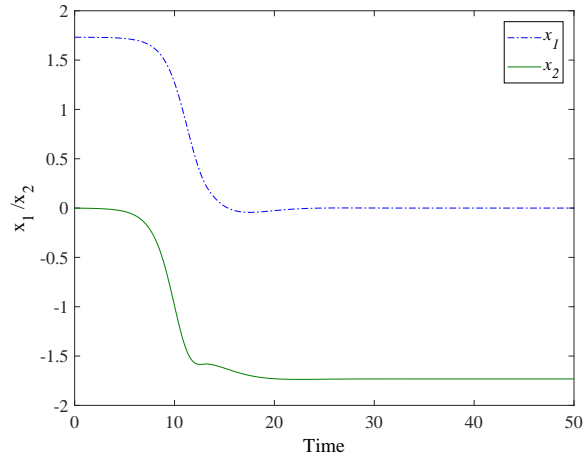


Figure 4.5: Mass displacements during the transition from E_9 at $(1.732,0)$ to E_{10} at $(0,-1.732)$.

The heteroclinic connection can also be seen in Fig. 4.5, where the controller ensures capture and stabilisation at E_{10} . The corresponding controls L_2 and L_3 are shown in Fig. 4.6. It can be seen that the control is activated when the transition is within region

R at E_{10} as shown in Fig. 4.4. A smooth control time history is then obtained. The results demonstrate that control effort can compensate for parameter errors to generate a heteroclinic connection between two unstable equilibria [60], which transit from an unstable equilibrium E_9 through a stable equilibrium E_1 to the neighbouring unstable equilibrium E_{10} .

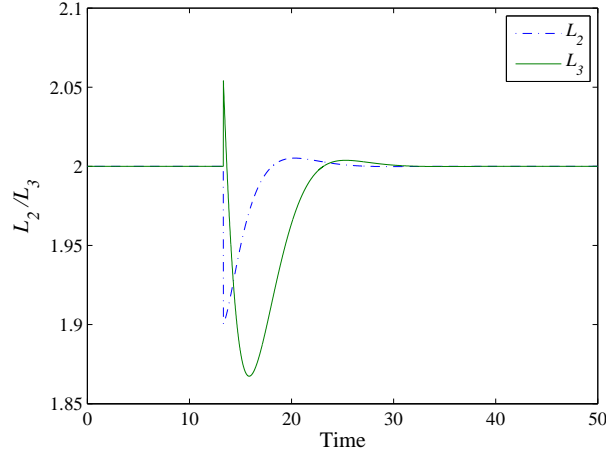


Figure 4.6: Controls in region R of the neighbourhood of E_{10} actuated through the coupling parameters L_2 and L_3 .

4.2 Optimal control

The smart structure reconfiguration problem can be revisited as a computational optimal control problem to determine the control histories which meet the boundary conditions of the problem. In addition to satisfying the state boundary conditions, these control histories must also minimise a performance index function. The optimal control problem is solved numerically using a direct method based on pseudospectral transcription, implemented in the tool PSOPT. PSOPT is coded in C++ by Becerra, is open source [70] and can deal with several problems, such as endpoint constraints, path constraints and interior point constraints. It makes use of automatic differentiation by overloading in C++ (ADOL-C) library for the automatic differentiation of objective, dynamic and constraint functions. Moreover, an open source C++ implementation of an interior point method for large-scale problems named IPOPT is employed to solve NLP problem [70].

In this section, actuator effort will be minimised through the optimal control problem. In order to control the reconfiguration of the smart structure model it will be assumed that the natural length of the springs can be modulated through the parameter set

L_1 , L_2 and L_3 . A simplified description of the spring actuator is given to estimate the energy requirements for such modulation [5], which was presented in Section 3.5. Through the previous analysis, and from Section 3.5, it can be considered that ΔL is the induced length of the springs in the smart structure model so that the expression of the energy in terms of induced strain may be written as

$$E = \frac{1}{2}k_s\left(\frac{1}{4}d_s^2\right) = \frac{1}{2}k_s\left(\frac{1}{4}(\Delta L)^2\right) \propto \Delta L^2 \quad (4.16)$$

where k_s is constant.

Therefore, the cost function is simply the form of Eq. 4.16, which is considered in quasi-static conditions of the system. Equation 4.16 implies that the energy required to actuate the transition between equilibria is in direct proportion to the square of the deformation of the springs, so the performance index is defined as

$$J = \int_0^{t_f} (\Delta L_1)^2 + (\Delta L_2)^2 + (\Delta L_3)^2 dt \quad (4.17)$$

The remaining specification of the optimal control problem is that the initial conditions and final conditions should be defined. Therefore, according to the discussion in Section 4.2, an ideal heteroclinic connection can be considered as a free-end time and fixed-end state optimal trajectory. For example conditions can be defined for a transition from unstable equilibrium E_9 to E_{10} as

$$\begin{bmatrix} \mathbf{x}^*(0) & \mathbf{x}^*(T) & \dot{\mathbf{x}}^*(0) & \dot{\mathbf{x}}^*(T) \end{bmatrix} = \begin{bmatrix} 1.732 & 0 \\ 0 & -1.732 \\ 0 & 0 \\ 0 & 0 \end{bmatrix}^T \quad (4.18)$$

Figure 4.7a represents the optimal trajectory, obtained with PSOPT, for each of the state variables, Fig. 4.7b plots the control variables and Fig. 4.7c shows the total energy input to the process determined from the cost function Eq. 4.17. Furthermore, for the optimal solution it can be seen that the controls are symmetric about $t=T/2$ as expected, and it can be seen that L_1 and L_3 strategically avoid the control singularity, as discussed in Section 4.2.

The results from Section 4.2 and the optimal control results are compared in Fig. 4.8. Moreover, the optimal transition is similar to a controlled trajectory using a reference trajectory based on the exact solution from Section 4.2. This free end-time optimal control problem can be changed to a fixed end-time problem, so that the manoeuvre

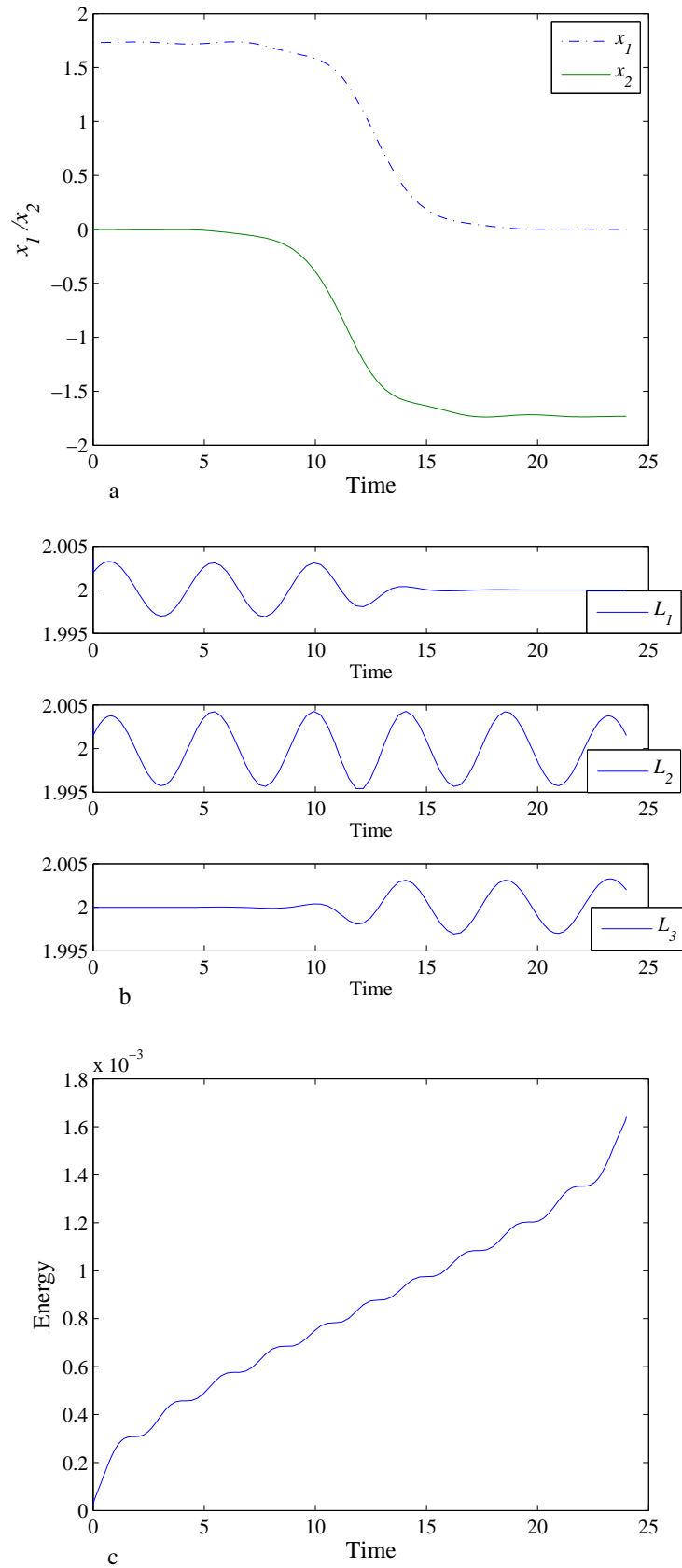


Figure 4.7: Minimum energy transition with free end time. (a) Mass displacements during the transition from E_9 to E_{10} . (b) Controls actuated through the parameters L_1 , L_2 and L_3 . (c) Total energy input.

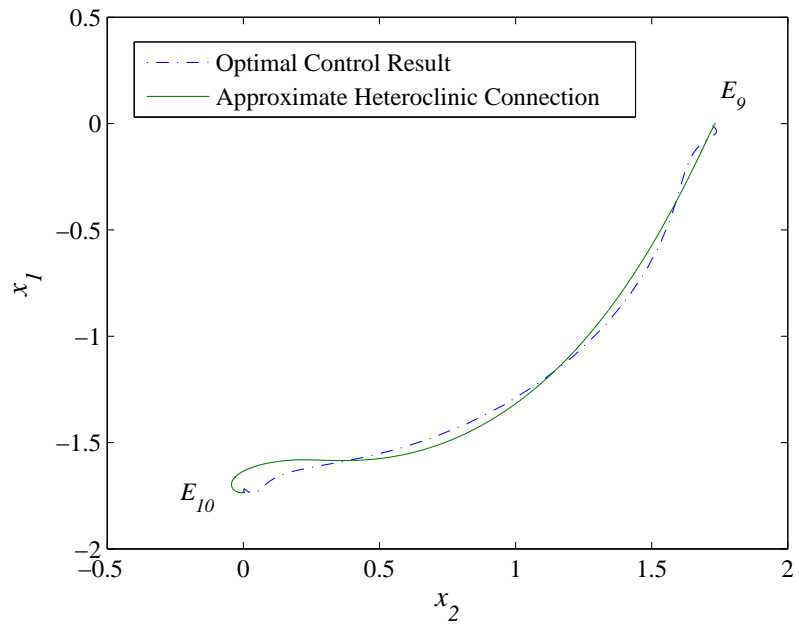


Figure 4.8: Controlled transition and optimal transition from E_9 to E_{10} .

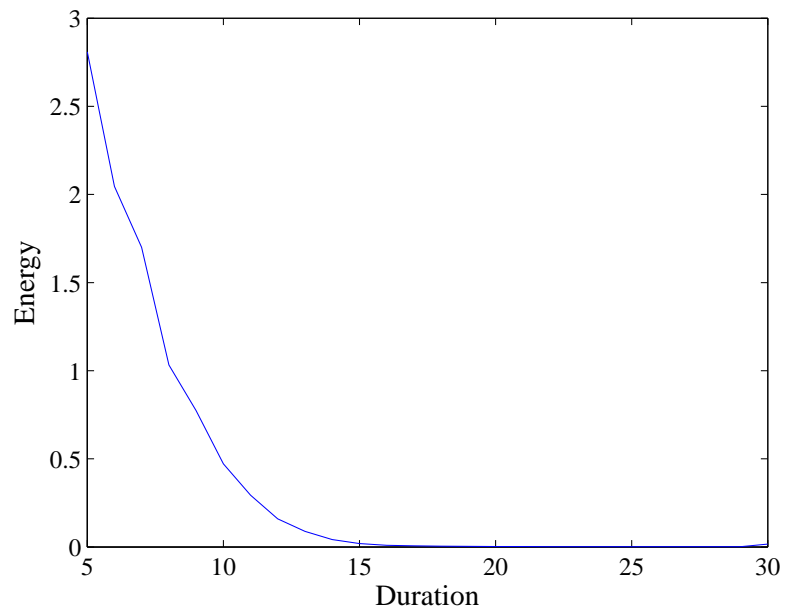


Figure 4.9: Energy required for reconfiguration as a function of reconfiguration duration.

time can be set to complete the transition process. Although this procedure may require additional energy, it is a more practical strategy to reconfigure the smart structure model. Figure 4.9 shows the energy requirement as a function of the reconfiguration duration, where it can be seen that the energy required quickly diminishes as the manoeuvre duration grows.

4.3 Bifurcation control

In the above Sections, a numerical search technique for reconfiguration using heteroclinic connections without dissipation was investigated. It was assumed that the instability of the equal-energy unstable equilibria could be compensated for by using active control. However, an alternative bifurcation control method may be considered, again if the natural length of the springs L_{1-3} can be manipulated, for example if the springs are manufactured from an appropriate shape memory alloy. A conservative Hamiltonian system is assumed initially, with compensation for dissipation considered later in Section 4.5.

A ball on a hill model can be used to provide a schematic illustration of the proposed bifurcation control method, as shown in Fig. 4.10. The potential energy of the ball depends on its position on the hill so that a heteroclinic connection can exist between two hills (Fig. 4.10b). Figure. 4.10a shows the ball on the first hill, which is initially locally stable. Then through manipulating its shape, the first hill becomes unstable to effect the heteroclinic connection to the second hill, which can subsequently transition from unstable to locally stable, as shown in Fig. 4.10b and 4.10c.

Based on this simple illustrative model, a new reconfiguration strategy is investigated using the spring-mass smart structure model detailed in Section 4.2.

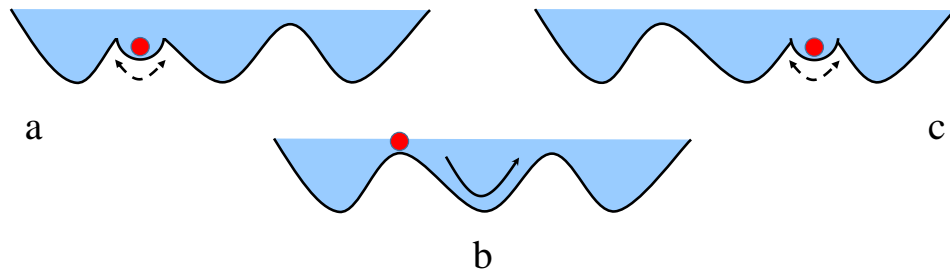


Figure 4.10: Schematic representation of bifurcation control (a) and (c) are different locally stable configurations of the structure (b) heteroclinic connection between the two equal-energy unstable configurations.

In order to illustrate this strategy directly, L_2 is firstly manipulated and changed from 1 to 2.5 with L_1 and L_3 fixed. Initially a large change in the spring natural length is considered for clarity of illustration; a smaller change will be used later. It can be seen from Fig. 4.11 that the number of equilibria will change with an increase of L_2 , which is shown by the equilibria \tilde{x} at different lengths of L_2 . Moreover, there are three invariant points $(0, 0)$, $(\sqrt{3}, \sqrt{3})$ and $(-\sqrt{3}, -\sqrt{3})$ whose locations are independent of L_2 . For $L_2 = 1$ the equilibria E_1 and E_2 are stable, and the potential forms local minima at these locations, as shown in Fig. 4.12. Then, if L_2 is increased such that $L_2 \geq 2$, the equilibria $(\sqrt{3}, \sqrt{3})$ and $(-\sqrt{3}, -\sqrt{3})$ become unstable and a heteroclinic connection can be used to reconfigure the structure between these two equilibria, as shown in Fig. 4.13. After the reconfiguration, L_2 is finally decreased such that $L_2 = 1$ and the system becomes stable again. This scheme allows operation of the structure in a stable state, a transition to instability to reconfigure the structure, and then continued operation in another stable state.

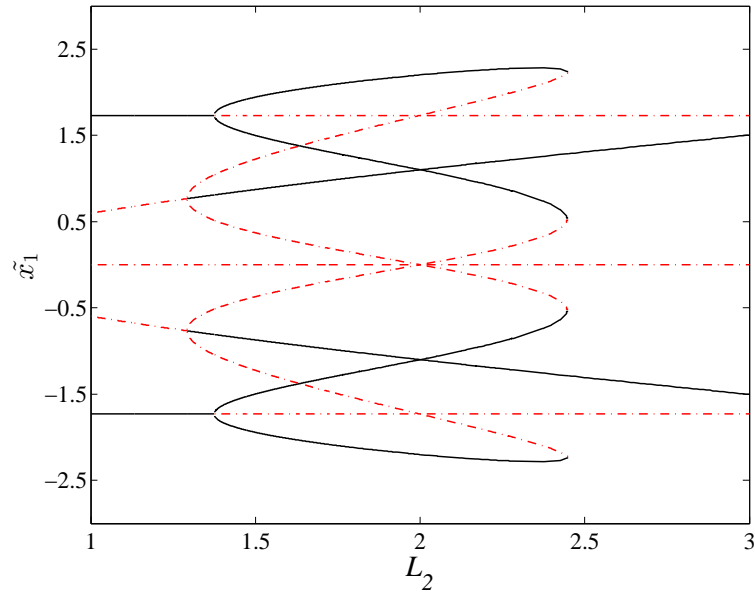


Figure 4.11: Bifurcation diagram for the spring-mass model. Projection of the location of the equilibria onto the x_1 axis for $L_1 = 2$, $L_3 = 2$ and $1 \leq L_2 \leq 3$. Solid line: stable equilibria, dashed line: unstable equilibria.

A transition using this scheme (without dissipation) is shown in Fig. 4.14. The coupling parameters are again $L_1 = 2$ and $L_3 = 2$ with L_2 switched from 2.5 to 1 to manipulate the stability properties of E_1 and E_2 . Firstly, a small displacement is added to the system in the local minimum potential well to demonstrate capture at the equilibrium point. This initial oscillation of the system in the potential well at E_1 with $L_2 = 1$ can

be seen, followed by a transition to E_2 with $L_2 = 2.5$ after the bifurcation and then a return to oscillation in the local minimum potential well at E_2 with $L_2 = 1$.

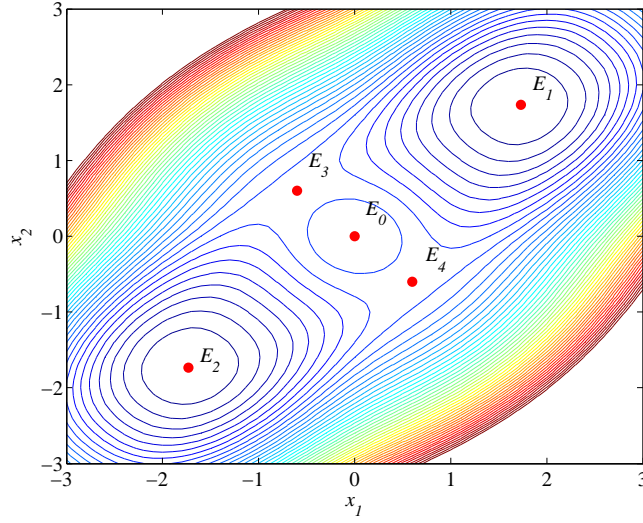


Figure 4.12: Effective potential $V(x, L)$ with $L_1 = 2$, $L_2 = 1$ and $L_3 = 2$. E_1 and E_2 are stable, E_3 and E_4 are unstable.

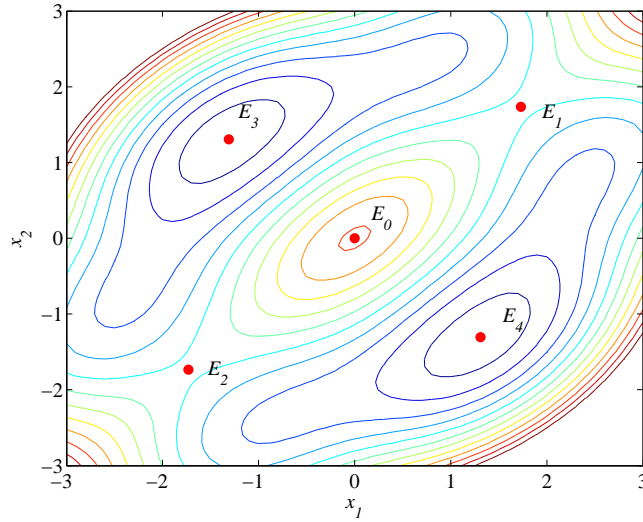


Figure 4.13: Effective potential $V(x, L)$ with $L_1 = 2$, $L_2 = 2.5$ and $L_3 = 2$. E_1 and E_2 are unstable, E_3 and E_4 are stable.

In order to further explore the possibility of reconfiguring the smart structure using bifurcation control, a more complex situation will now be considered. Figure 4.11 shows that the equilibria $(\sqrt{3}, \sqrt{3})$ and $(-\sqrt{3}, -\sqrt{3})$ became unstable when $L_2 = 2$, but with the same potential energy as other saddle points such as $(0, \sqrt{3})$. An iterative approach [44], can also be used which divides a position coordinate, such as x_1 , into

several steps with a desired increment, then the other position coordinate x_2 can be used to seek to minimize the potential energy of every step. Therefore, an ideal path can be generated on the potential energy contour from $(\sqrt{3}, \sqrt{3})$ to $(-\sqrt{3}, -\sqrt{3})$ with $L_1 = L_2 = L_3 = 2$. This results in a series of connected heteroclinic connections between $(\sqrt{3}, \sqrt{3})$ and $(-\sqrt{3}, -\sqrt{3})$, as shown in Fig. 4.15.

Bifurcation control can now be considered to reconfigure the structure in a more realistic way with a smaller change of the spring natural length such that L_2 switches from 2 to 1.3.

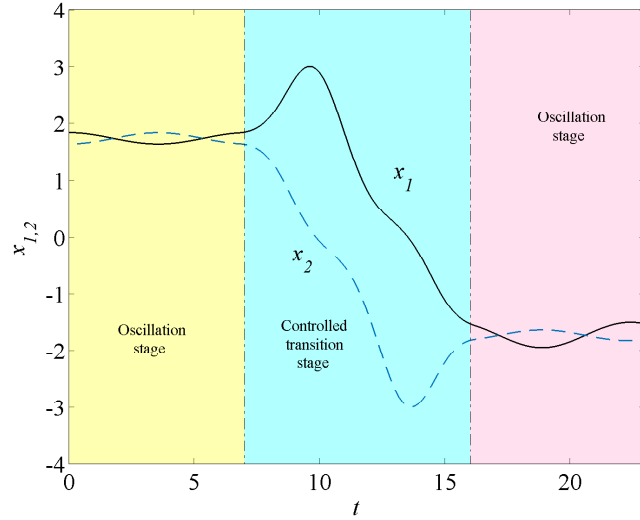


Figure 4.14: Controlled transition from E_1 at $(\sqrt{3}, \sqrt{3})$ to E_2 at $(-\sqrt{3}, -\sqrt{3})$ with bifurcation control. The coupling parameters $L_1 = 2$ and $L_3 = 2$ with L_2 switched from 2.5 to 1 to manipulate the stability properties of E_1 and E_2 .

Figure 4.16 shows the transition (without dissipation) using this modified bifurcation control. The coupling parameters are again $L_1 = 2$ and $L_3 = 2$ with L_2 switched from 2 to 1.3 to manipulate the stability properties of E_1 and E_2 . Then, a small displacement is again added to the system in the local minimum potential well to demonstrate capture at the equilibrium point. The initial oscillation of the system in the potential well at E_1 with $L_2 = 1.3$ can therefore be seen, followed by a transition to E_2 with $L_2 = 2$ and then a return to oscillation in the local minimum potential well at E_2 with $L_2 = 1.3$. In addition, the switch process is a simple step change of L_2 from 1.3 to 2, as shown in Fig. 4.17.

The bifurcation control scheme presented provides the possibility of reconfiguring smart structures using their instability, but retaining stability for normal operating modes. Although the natural length of the spring is varied for illustration, additional parameters could also be considered, such as the spring stiffness k or the spacing d between

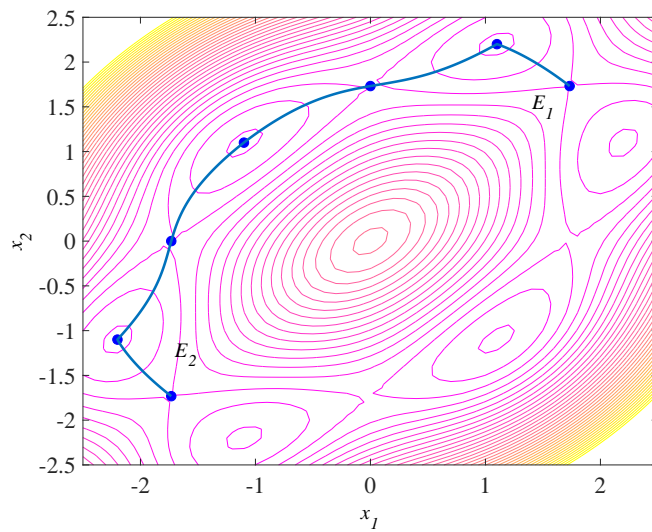


Figure 4.15: Potential energy contour plot and ideal path from E_1 at $(\sqrt{3}, \sqrt{3})$ to E_2 at $(-\sqrt{3}, -\sqrt{3})$.

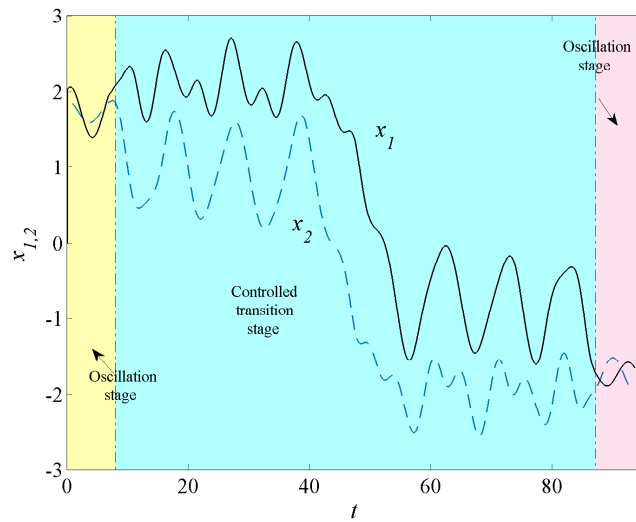


Figure 4.16: Controlled transition from E_1 at $(\sqrt{3}, \sqrt{3})$ to E_2 at $(-\sqrt{3}, -\sqrt{3})$ with bifurcation control with L_2 switched from 1.3 to 2 to manipulate the stability properties of E_1 and E_2 .

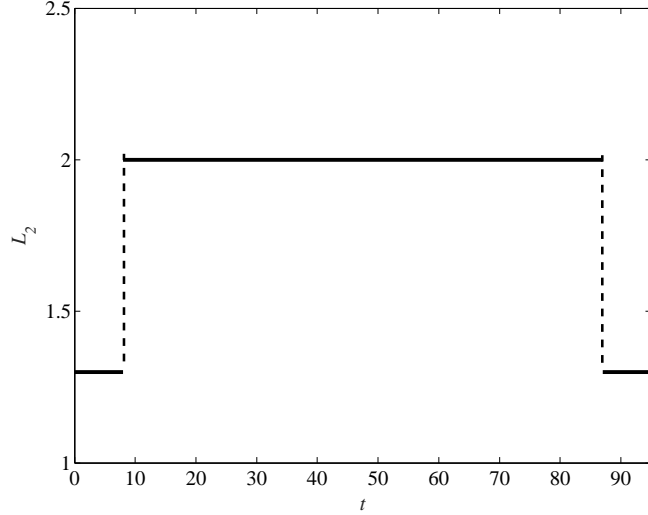


Figure 4.17: A step change of L_2 (1.3 to 2) during the bifurcation control.

springs to reduce the variation of the length of the spring. The purpose of the numerical examples presented above is to demonstrate the characteristics and utilization of bifurcations in this type of nonlinear system. Therefore, an easily visualized means (e.g. natural length of the springs) is used to achieve the reconfiguring process.

4.4 Controlled heteroclinic connections in a dissipative system

For a more realistic smart structure model dissipation must also be considered, which of course will destroy the Hamiltonian structure of the dynamics. Therefore, phase trajectories from one unstable equilibrium point cannot reach another equal-energy unstable equilibrium point. In order to compensate for such dissipation, controllers need to be used to ensure that heteroclinic connections can exist. Therefore, the dynamics of the problem can be extended by the addition of linear dissipation parameterised by β , as shown in Fig. 4.18.

The problem can then fully defined by a dynamical system with a dissipation term of the form

$$\dot{x}_1 = p_1 \quad (4.19)$$

$$\dot{p}_1 = \frac{(L_1 - \sqrt{(x_1^2 + 1)})k_1 x_1}{\sqrt{x_1^2 + 1}} + \frac{(L_2 - \sqrt{((x_1 - x_2)^2 + 1)})k_2 (x_1 - x_2)}{\sqrt{(x_1 - x_2)^2 + 1}} - \beta p_1 \quad (4.20)$$

$$\dot{x}_2 = p_2 \quad (4.21)$$

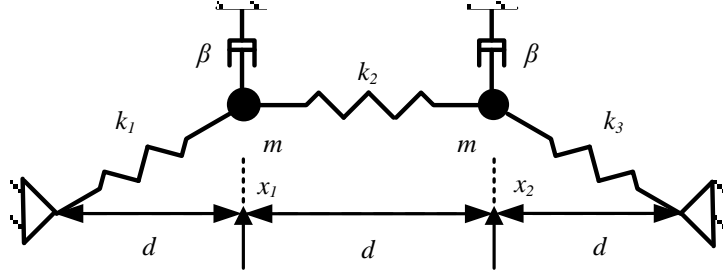


Figure 4.18: 2 degree-of-freedom buckling beam model with damping coefficient β .

$$\dot{p}_2 = \frac{(L_3 - \sqrt{(x_2^2 + 1)})k_3x_2}{\sqrt{x_2^2 + 1}} + \frac{(L_2 - \sqrt{((x_1 - x_2)^2 + 1)})k_2(x_1 - x_2)}{\sqrt{(x_1 - x_2)^2 + 1}} - \beta p_2 \quad (4.22)$$

As noted earlier, dissipation needs to be considered for a more realistic model where Eq. 4.4 and 4.5 show the total energy $W = T + V$ of the system is monotonically decreasing as $\dot{p} = -\beta(p_1^2 + p_2^2)$ corresponding to the general condition $p_1 \neq 0, p_2 \neq 0$. In order to proceed it will be assumed that each spring can again be manipulated with variations of the natural spring length ΔL by using smart materials. From Eq. 4.20 and Eq. 4.22 it can be seen that

$$\begin{aligned} \dot{p}_1 p_1 - \frac{((L_1 + \Delta L_1) - \sqrt{(x_1^2 + 1)})k_1x_1}{\sqrt{x_1^2 + 1}} p_1 \\ - \frac{((L_2 + \Delta L_2) - \sqrt{((x_1 - x_2)^2 + 1)})k_2(x_1 - x_2)}{\sqrt{(x_1 - x_2)^2 + 1}} p_1 = \beta p_1^2 \end{aligned} \quad (4.23)$$

$$\begin{aligned} \dot{p}_2 p_2 - \frac{((L_3 + \Delta L_3) - \sqrt{(x_2^2 + 1)})k_3x_2}{\sqrt{x_2^2 + 1}} p_2 \\ + \frac{((L_2 + \Delta L_2) - \sqrt{((x_1 - x_2)^2 + 1)})k_2(x_1 - x_2)}{\sqrt{(x_1 - x_2)^2 + 1}} p_2 = \beta p_2^2 \end{aligned} \quad (4.24)$$

which can be written as

$$\frac{d}{dt}(T + V) = -\beta p_1^2 + \frac{\Delta L_1 k_1 x_1}{\sqrt{x_1^2 + 1}} p_1 - \beta p_2^2 + \frac{\Delta L_3 k_3 x_2}{\sqrt{x_2^2 + 1}} p_2 + \frac{\Delta L_2 k_2 (x_1 - x_2)}{\sqrt{(x_1 - x_2)^2 + 1}} (p_1 - p_2) \quad (4.25)$$

and is clearly a statement of mechanical power. If it is considered that the system is forced to be conservative then $(d(T + V))/dt = 0$, therefore, ΔL can be used to compensate for dissipation by continuous control. Alternatively, a simpler control strategy is to define a controller which can capture the phase space trajectory in the neighbourhood of the target equilibrium point analogous to the analysis of Section 4.1. The

difference between the two methods can be seen in Fig. 4.19. The end-point control strategy provides an easy way to reconfigure smart structures from some initial state to a target state, which uses the controller to compensate for the offset caused by dissipation in a planned control region, as shown in Fig. 4.19a. Conversely, the continuous strategy can be controlled by constantly monitoring and controlling states during the reconfiguration of the smart structure, as shown in Fig. 4.19b.

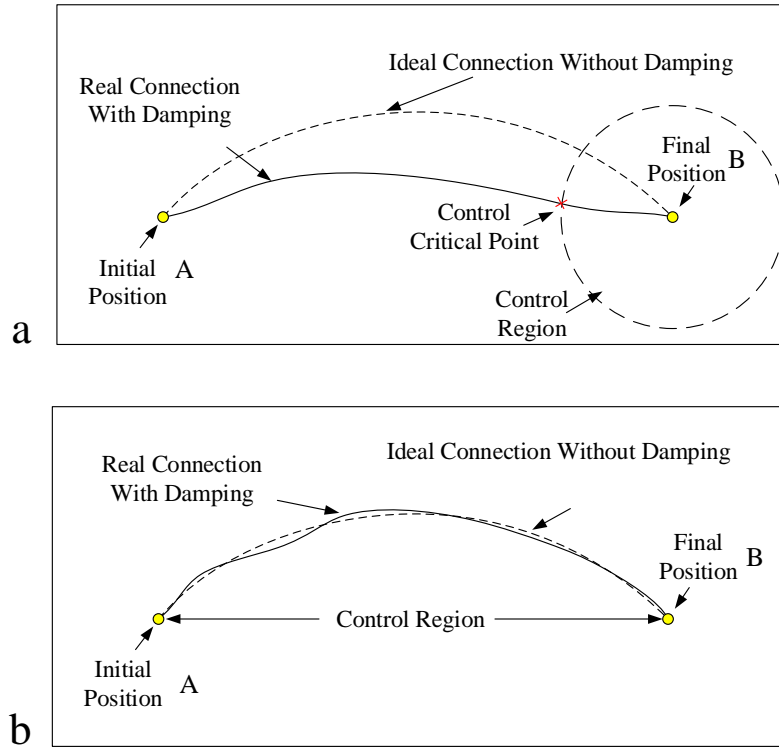


Figure 4.19: Control strategy (a) End-point control (b) Continuous control.

It is considered that this system is a continuous time nonlinear system and asymptotic stability can be achieved by applying active control within the neighbourhood of the equilibria. Therefore, the Lyapunov stability criterion is employed to verify convergence to the equilibrium point. A Lyapunov function is a scalar function $V(x)$ defined on a local region D for an autonomous dynamical system, which is continuous, locally positive definite ($V(x) > 0$ for all $x \neq 0$), and has continuous derivatives at every point of D [66]. Let x^* be an equilibrium point of the system on region D , which is an equilibrium solution of

$$\dot{x} = f(x) \quad (4.26)$$

where the notation $(\dot{\cdot})$ denotes the time derivative. Therefore, the time derivative of

the Lyapunov function $V(x)$ is given by

$$\dot{V}(x) = \frac{d}{dt}V(x(t)) = \nabla V(x) \cdot f(x) \quad (4.27)$$

The existence of a Lyapunov function for which $V(x)$ is negative semidefinite on a local region D excluding the origin, guarantees the local stability of the equilibrium solution of Eq. 4.26, while the existence of a Lyapunov function for which $V(x)$ is negative definite leads to global asymptotic stability. Therefore, the stability analysis of the corresponding equilibrium point can be determined by a scalar Lyapunov function, which is defined in the state space of the problem.

In order to ensure convergence to some equilibrium point $(\tilde{x}_1, \tilde{x}_2)$ a Lyapunov function is defined such that

$$\phi(\mathbf{x}, \mathbf{L}) = \frac{1}{2}p_1^2 + \frac{1}{2}p_2^2 + \frac{1}{2}(x_1 - \tilde{x}_1)^2 + \frac{1}{2}(x_2 - \tilde{x}_2)^2 \quad (4.28)$$

where $\phi(\mathbf{x}, \mathbf{L}) > 0$ and $\phi(\tilde{x}_1, \tilde{x}_2) = 0$. The time derivative of the Lyapunov function is clearly

$$\dot{\phi}(\mathbf{x}, \mathbf{L}) = p_1(\dot{p}_1 + (x_1 - \tilde{x}_1)) + p_2(\dot{p}_2 + (x_2 - \tilde{x}_2)) \quad (4.29)$$

Then, substituting from the Eq. 4.20 and 4.22 the controller for L_1 , L_2 and L_3 can be defined as

$$L_1 = -\frac{\sqrt{(x_1^2 + 1)}}{k_1 x_1}(\eta p_1 + (x_1 - \tilde{x}_1) - \frac{(L_2 - \sqrt{((x_1 - x_2)^2 + 1)})k_2(x_1 - x_2)}{\sqrt{((x_1 - x_2)^2 + 1)}} - k_1 x_1) \quad (4.30)$$

$$L_2 = -\frac{\sqrt{((x_1 - x_2)^2 + 1)}}{k_1(x_1 - x_2)}(\eta p_1 + (x_1 - \tilde{x}_1) - \frac{(L_1 - \sqrt{(x_1^2 + 1)})k_1 x_1}{\sqrt{(x_1^2 + 1)}} - k_2(x_1 - x_2)) \quad (4.31)$$

$$L_3 = -\frac{\sqrt{(x_2^2 + 1)}}{k_3 x_2}(\eta p_2 + (x_2 - \tilde{x}_2) - \frac{(L_2 - \sqrt{((x_1 - x_2)^2 + 1)})k_2(x_1 - x_2)}{\sqrt{((x_1 - x_2)^2 + 1)}} - k_3 x_2) \quad (4.32)$$

for some control parameter η . It is noted that the system has 2 state variables x_1 and x_2 , which can select two controllers from L_1 , L_2 and L_3 as control variables to avoid singularities. For example, since $k_2(x_1 - x_2) \neq 0$, $k_3 x_2 \neq 0$ in the neighbourhood of the required equilibrium point E_{10} , then L_2 and L_3 are selected as controllers in the neighbourhood of that point.

It can then be seen that ϕ is monotonically decreasing such that

$$\dot{\phi}(\mathbf{x}, \mathbf{L}) = -(\eta + \beta)(p_1^2 + p_2^2) \leq 0 \quad (4.33)$$

and so $x \rightarrow (\tilde{x}_1, \tilde{x}_2)$ and $p \rightarrow (0,0)$ within the neighbourhood of target point.

An example of controlled heteroclinic connections with $\beta = 0.01$ and $\beta = 0.05$ are shown in Fig. 4.20 for a reconfiguration between E_9 and E_{10} . To initiate the heteroclinic connection, a displacement along the unstable manifold of E_9 is preformed and the controller will be activated when the phase space path is in the defined neighbourhood R of E_{10} ($\eta = 3$). The corresponding controls L_2 and L_3 are shown in Fig. 4.21. It can be seen that the controls are only active when the phase space path is in the end-point region of E_{10} . Numerical results demonstrate that the control effort grows with increasing dissipation parameter β . That is, the control region needs to be enlarged to fit the increasing dissipation parameter β as shown in Fig. 4.20.

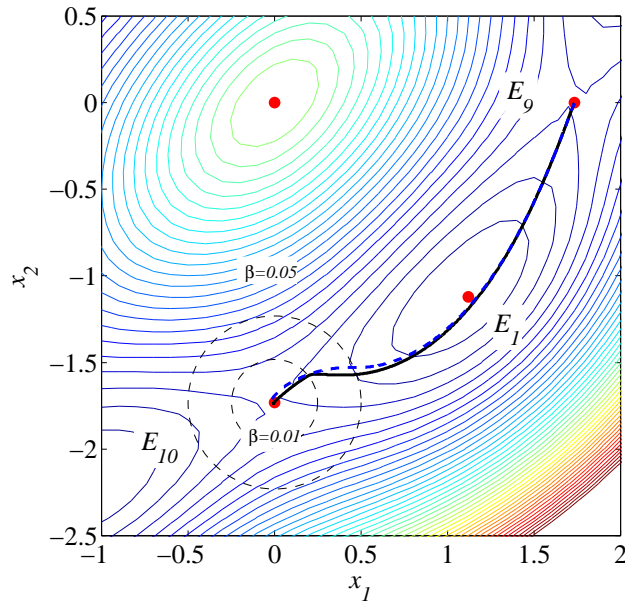


Figure 4.20: Controlled transition from E_9 at $(1.732051,0)$ to E_{10} at $(0,-1.73205)$ with the controller active in the neighbourhood of E_{10} with different dissipation. Solid line: dissipation parameter $\beta = 0.01$, dashed line: dissipation parameter $\beta = 0.05$.

For comparison with the end-point control strategy, a continuous control method is now investigated to approximate the heteroclinic connection. This problem is revisited as a computational optimal control problem to determine the control histories which meet the boundary conditions of the problem. In addition to satisfying the state boundary conditions, these control histories also need to minimise the performance index function as discussed in Section 4.

Then, the optimal tool PSOPT is again employed to solve this optimal control problem numerically using the direct method. The system can be considered under quasi-static

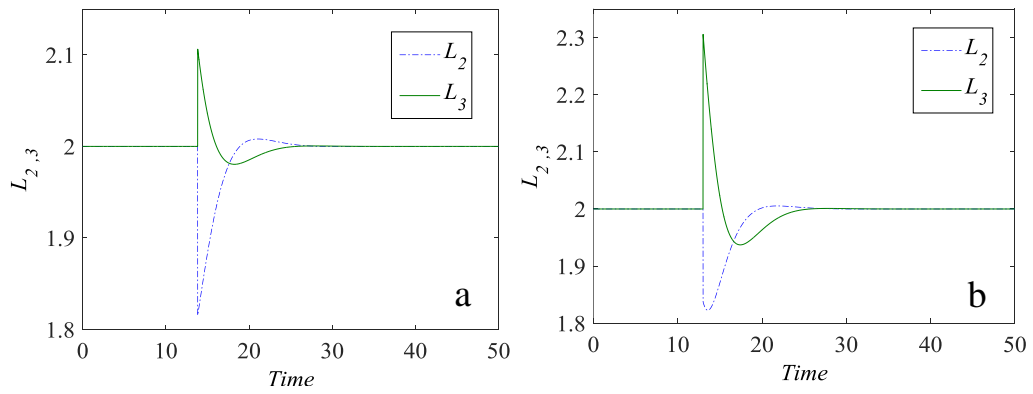


Figure 4.21: Controlled transition from E_9 at $(1.732051, 0)$ to E_{10} at $(0, -1.73205)$ with the controls actuated through L_2 and L_3 in the neighbourhood of E_{10} . (a) Dissipation parameter $\beta = 0.01$. (b) Dissipation parameter $\beta = 0.05$.

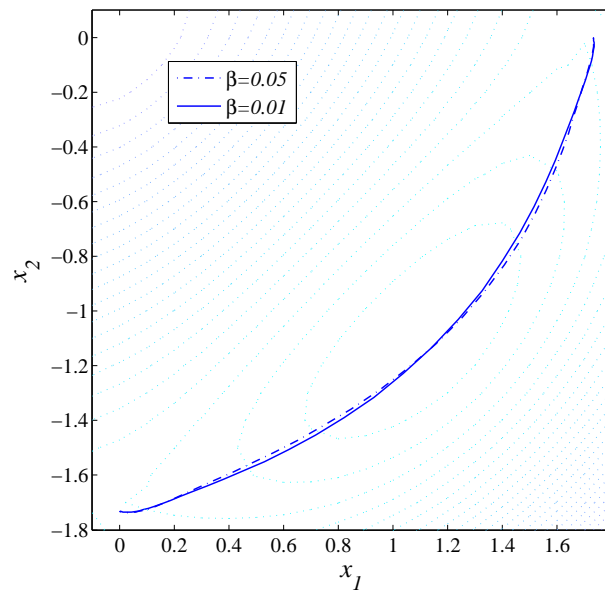


Figure 4.22: Controlled transition from E_9 at $(1.732051, 0)$ to E_{10} at $(0, -1.73205)$ with the controller active under the continuous control method (dissipation parameters $\beta = 0.01, 0.05$).

conditions, so that Eq. 4.16 can be defined as an expression of the energy required for each controller and the performance index of the system can be defined as Eq. 4.17. Then, the conditions can be defined for a transition from the unstable equilibrium E_9 to E_{10} as Eq. 4.18. Then, the conditions can be defined for a transition from the unstable equilibrium E_9 to E_{10} as

$$\begin{bmatrix} \mathbf{x}(0) & \mathbf{x}(T) & \dot{\mathbf{x}}(0) & \dot{\mathbf{x}}(T) \end{bmatrix} = \begin{bmatrix} 1.732 & 0 & 0 & 0 \\ 0 & -1.732 & 0 & 0 \end{bmatrix} \quad (4.34)$$

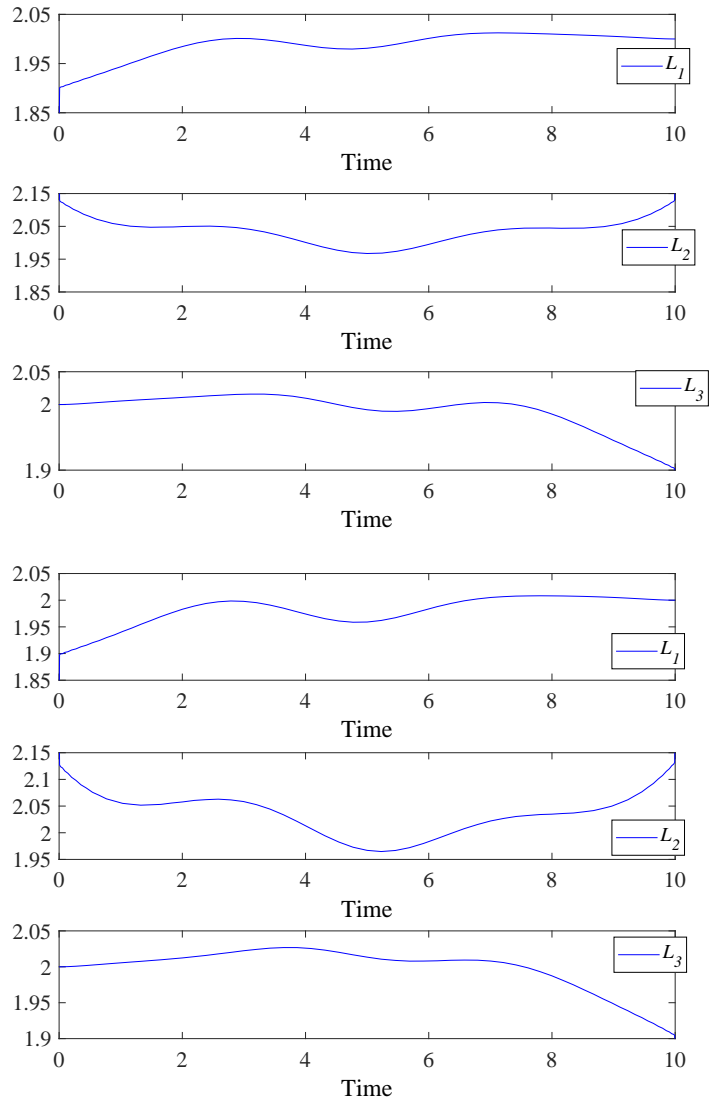


Figure 4.23: Controlled transition from E_9 at $(1.732051, 0)$ to E_{10} at $(0, -1.73205)$ with the controls actuated through L_2 and L_3 under the continuous control method. (a) Dissipation parameter $\beta = 0.01$. (b) Dissipation parameter $\beta = 0.05$.

The numerical results for dissipation parameters $\beta = 0.01$ and $\beta = 0.05$ are shown in Fig. 4.22. The corresponding controls L_1 , L_2 and L_3 are shown in Fig. 4.23. It can be seen that the controls are symmetric about the point $t = T/2$ as expected. Moreover, in general more energy is required to compensate for a larger dissipation parameter β as expected, which means the range of the controller becomes larger for the reconfiguration, as shown in Fig 4.23.

4.5 Conclusion

Using a simple, representative model of an unstable smart structure it has been demonstrated that the unstable configurations of the structure can be connected through heteroclinic connections in the phase space of the problem. In principle, such reconfigurations do not require the input of energy, other than to overcome dissipation in the system. Then, considering that real smart structures are complex dynamical systems with strong nonlinearities, an optimal control method is employed to reconfigure the smart structure. It was found that the transition between unstable equilibria can be achieved through manipulating the natural length of the springs in the model, which is assumed to be achieved with a suitable active material.

Moreover, a better reconfigurable strategy is used to combine bifurcation control and controlled heteroclinic connections, which is expected to reconfigure real smart structures between stable states. For example, structures are assumed to be initially in local stable states. Through performing the bifurcation the local condition becomes unstable. Then, bifurcation is performed again when the end-point control generates a trajectory to the target equilibrium point. This represents a computationally efficient way to achieve reconfiguration for smart structures between two different equilibria positions.

Then, two ways to reconfigure smart structures have been presented to compensate for damping. It was found that the transition between unstable equilibria can be achieved through manipulation of the natural length of the springs in the model with linear dissipation, which is assumed to be achieved with a suitable active material. While the model used is simple, it again provides insights into the problem which can be exploited to develop the concept towards the reconfiguration of real smart structures.

Chapter 5

Surface Model

In previous Chapters, a simple smart structure model was investigated, which comprised a two mass chain with three springs [64, 71, 72]. The model was then approximated to provide a simple cubic nonlinearity to investigate its characteristics using dynamical system theory. A set of both stable and unstable equilibrium configurations were found, with transitions between the equal-energy unstable equilibria identified as heteroclinic connections. In principle, such transitions between equal-energy unstable states can be achieved with minimal energy input, in the absence of dissipation. This cubic model was considered as a simple mechanical system with the ability to change its kinematic configuration between a finite set of unstable equilibria.

In this Chapter, heteroclinic connections are investigated as a means to reconfigure a simple discrete model of a smart surface structure, which is similar to the Hencky-type discrete model for pantographic structures [73]. In Section 5.2, the surface structure is considered as an elastic plane which has a range of both stable and unstable configurations. As an approximation, the surface is modelled as a two-dimensional spring-mass array without dissipation and with a simplifying cubic nonlinearity to allow an investigation of its characteristics using dynamical system theory. Section 5.3 discusses each spring-mass element, considered as a cubic nonlinearity between different nodes, and then an adjacency matrix is used to assemble elements together. Therefore, a set of both stable and unstable equilibrium configurations can be identified in the model, so that the reconfiguration of the smart surface can be considered between the equal-energy unstable states, as presented in Section 5.4. It is assumed that the simple reconfigurable structure again possesses embedded sensors and actuators to allow the unstable equilibria to be actively controlled. Meanwhile, a feedback control law is proposed that can stabilise the dynamics of the smart surface in Section 5.5. This control strategy can

actively maintain the structure in an unstable configuration. Section 5.6 presents more complex dynamics of such surface structures, which can be formed from an assembly of modules. For example, each surface module can be regarded as a microsystem unit for conveying, sorting and positioning micro-parts.

5.1 Single mass problem

The smart surface structure consists of a two-dimensional array of connected springs and masses. Consider firstly a simple elastic model, with an array of masses connected as chains by linear springs of stiffness k and natural length l_0 . In order to proceed, it is assumed that the masses can only move in the vertical (out-of-plane) direction without damping. The out-of-plane displacement of mass m is defined by displacement x , while each mass is separated by a fixed distance d . Consider a simple spring-mass element, which is the basic unit of the smart surface model. Based on the previous discussion, it is assumed that the masses can only move in the vertical direction as shown in Fig. 5.1.

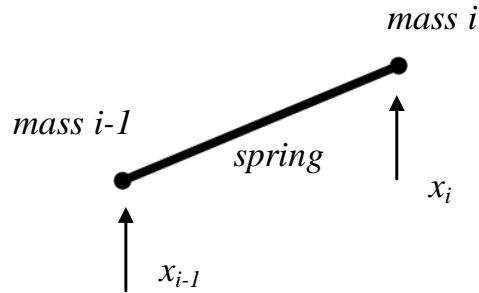


Figure 5.1: Spring-mass element.

To proceed, T is defined as the internal tension in a single spring, so that the tension of the spring can be described by

$$T = \Delta \cdot k \quad (5.1)$$

where Δ is the extension of the spring beyond its natural length, which can be defined by

$$\Delta = \sqrt{(x_{i-1} - x_i)^2 + d^2} - L \quad (5.2)$$

Therefore, the force experience by each node can be written as

$$f_{i,1} = -\Delta \cdot k \frac{(x_{i-1} - x_i)}{\sqrt{(x_{i-1} - x_i)^2 + d^2}} = -k(x_{i-1} - x_i) \left(1 - \frac{l_0}{\sqrt{(x_{i-1} - x_i)^2 + d^2}} \right) \quad (5.3)$$

The dynamics of each mass in a 1-dimensional chain are then described by

$$m\ddot{x}_{i,1} = -k(x_{i-1} - x_i) \left(1 - \frac{l_0}{\sqrt{(x_{i-1} - x_i)^2 + d^2}} \right) \quad (5.4)$$

The nonlinear term can be expanded by assuming $x/d \ll 1$ to simplify the full nonlinearity of the problem. It can then be shown that

$$m\ddot{x}_i = -k \left(\frac{l_0}{d} - 1 \right) (x_{i-1} - x_i) + \frac{kl_0}{2d^3} (x_{i-1} - x_i)^3 + \dots \quad (5.5)$$

Following [60] a non-dimensional position coordinate $q = \sqrt{l_0/2d^3}x$ and non-dimensional time $\tau = t/\sqrt{m/k}$ can again be defined with $\mu = (l_0/d - 1)$ so that

$$\ddot{q}_i = -\mu(q_{i-1} - q_i) + (q_{i-1} - q_i)^3 \quad (5.6)$$

In order to illustrate the smart surface model directly, a simple surface is considered as the structure shown in Fig. 5.2. The location of each mass as a row and column can be defined as u and v , respectively. Each mass $m_{i,j}$ can then be located on the i^{th} row and j^{th} column, which is connected to its neighbours by linear springs. The dynamics of mass $m_{i,j}$ are then driven by the displacements of $m_{i-1,j}$, $m_{i+1,j}$, $m_{i,j-1}$ and $m_{i,j+1}$. The dynamics of mass $m_{i,j}$ is therefore defined by

$$\begin{aligned} \ddot{q}_i = & -\mu(q_{i-1,j} - q_{i,j}) + (q_{i-1,j} - q_{i,j})^3 + \mu(q_{i,j} - q_{i+1,j}) + (q_{i,j} - q_{i+1,j})^3 \\ & - \mu(q_{i,j-1} - q_{i,j}) + (q_{i,j-1} - q_{i,j})^3 + \mu(q_{i,j} - q_{i,j+1}) + (q_{i,j} - q_{i,j+1})^3 \end{aligned} \quad (5.7)$$

Due to the fixed boundary conditions of the problem, the surface model can be considered as a four degree-of-freedom system, which again considers only vertical mass displacements. The displacement of the boundary nodes can be set to zero, i.e. $q_{0,0} = q_{0,1} = q_{0,2} = q_{0,3} = q_{1,0} = q_{1,3} = q_{2,0} = q_{2,3} = q_{3,0} = q_{3,1} = q_{3,2} = q_{3,3} = 0$. The dynamics of the full, coupled system can therefore be written as

$$\begin{bmatrix} \ddot{q}_{1,1} \\ \ddot{q}_{1,2} \\ \ddot{q}_{2,1} \\ \ddot{q}_{2,2} \end{bmatrix} = \begin{bmatrix} 4\mu q_{1,1} - \mu(q_{2,1} + q_{1,2}) \\ 4\mu q_{1,2} - \mu(q_{2,2} + q_{1,2}) \\ 4\mu q_{2,1} - \mu(q_{1,1} + q_{1,2}) \\ 4\mu q_{2,2} - \mu(q_{1,2} + q_{1,2}) \end{bmatrix} + \begin{bmatrix} -2q_{1,1}^3 - (q_{1,1} - q_{2,1})^3 + (q_{1,1} - q_{1,2})^3 \\ -2q_{1,2}^3 - (q_{1,2} - q_{2,2})^3 + (q_{1,1} - q_{1,2})^3 \\ -2q_{2,1}^3 - (q_{1,1} - q_{2,1})^3 + (q_{2,1} - q_{2,2})^3 \\ -2q_{2,2}^3 - (q_{1,2} - q_{2,2})^3 + (q_{2,1} - q_{2,2})^3 \end{bmatrix} \quad (5.8)$$

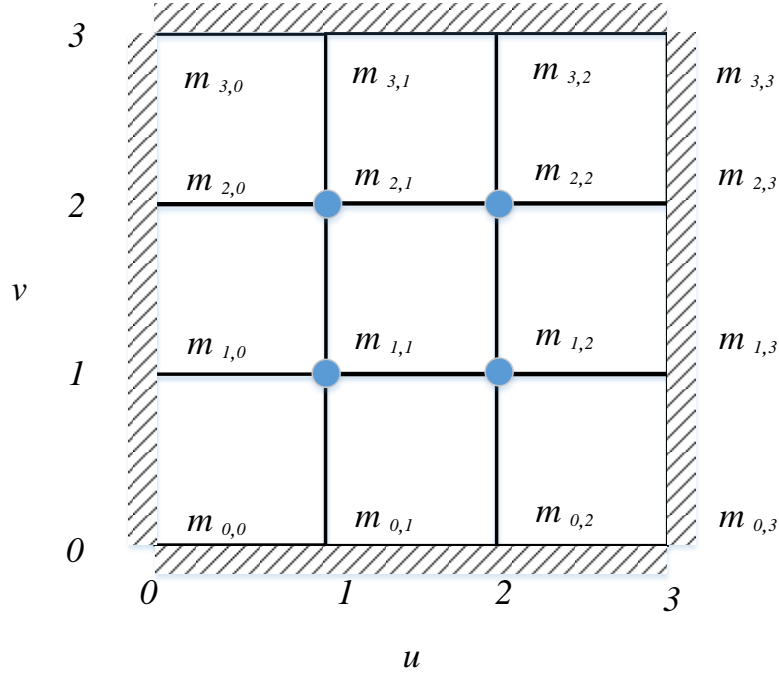


Figure 5.2: A simple surface model with fixed boundary condition.

This four degree-of-freedom system is easily formed from the dynamics of the problem through using Eq. 5.8. Moreover, the system is constructed from two parts, a linear destabilising term and nonlinear stabilising term. It can be expected that the linear and cubic terms will yield families of both stable and unstable equilibria, as has been seen for 1-dimensional chain of masses in previous Chapters.

5.2 General methods

We now consider a general method with an $n \times n$ array of masses using the same functional form of the nonlinearity above. It is again assumed that the system is considered conservative without dissipation. The adjacency matrix of the graph connecting the nodes can now be used to form the generalised position of each node. The four degree-of-freedom system above is firstly employed to illustrate this general method. Since the system detailed above is considered conservative without dissipation, its behaviour can be described through the use of an effective potential $V(\mathbf{q}, \mu)$ by the set of position coordinates $\mathbf{q} = q_{i,j}$ ($i = 1-n, j = 1-n$) such that the momenta $\mathbf{p} = p_{i,j}$ ($i = 1-n, j = 1-n$) can be obtained from $\dot{p}_{i,j} = -\partial V(\mathbf{q}, \mu)/\partial p_{i,j}$. The effective potential $V(\mathbf{q}, \mu)$ can then

be defined as

$$\begin{aligned}
V(\mathbf{q}, \mu) = & -\mu q_{1,1}^2 - \mu q_{1,2}^2 - \mu q_{2,1}^2 - \mu q_{2,2}^2 - \frac{1}{2}\mu(q_{1,1} - q_{2,1})^2 - \frac{1}{2}\mu(q_{1,1} - q_{1,2})^2 \\
& - \frac{1}{2}\mu(q_{1,2} - q_{2,2})^2 - \frac{1}{2}\mu(q_{2,1} - q_{2,2})^2 + \frac{1}{2}q_{1,1}^4 + \frac{1}{2}q_{1,2}^4 + \frac{1}{2}q_{2,1}^4 + \frac{1}{2}q_{2,2}^4 \\
& + \frac{1}{4}(q_{1,1} - q_{2,1})^4 - \frac{1}{4}(q_{1,1} - q_{1,2})^4 - \frac{1}{4}(q_{2,2} - q_{1,2})^4 - \frac{1}{4}(q_{2,2} - q_{2,1})^2
\end{aligned} \tag{5.9}$$

Equation 5.9 shows that the potential consists of two parts, one a quadratic term, which again provides a destabilising linear force at small displacements and a quartic term, which provides a stabilising, nonlinear restoring force at large displacements. It is assumed later that $q_{i,j}$ is a displacement that can be sensed and μ is a spring coupling parameter that can be manipulated for active control and stabilisation. Therefore, a general method can be considered such that the potential energy can be formed from two parts, a quadratic term and a quartic term, which can be defined by

$$M_2 = \begin{bmatrix} (q_{0,0} - q_{0,0})^2 & \cdots & (q_{0,0} - q_{i,j})^2 & \cdots & (q_{0,0} - q_{n,n})^2 \\ \vdots & \ddots & \vdots & \ddots & \vdots \\ (q_{i,j} - q_{0,0})^2 & \cdots & (q_{i,j} - q_{i,j})^2 & \cdots & (q_{i,j} - q_{n,n})^2 \\ \vdots & \ddots & \vdots & \ddots & \vdots \\ (q_{n,n} - q_{0,0})^2 & \cdots & (q_{n,n} - q_{i,j})^2 & \cdots & (q_{n,n} - q_{n,n})^2 \end{bmatrix} \tag{5.10}$$

and

$$M_4 = \begin{bmatrix} (q_{0,0} - q_{0,0})^4 & \cdots & (q_{0,0} - q_{i,j})^4 & \cdots & (q_{0,0} - q_{n,n})^4 \\ \vdots & \ddots & \vdots & \ddots & \vdots \\ (q_{i,j} - q_{0,0})^4 & \cdots & (q_{i,j} - q_{i,j})^4 & \cdots & (q_{i,j} - q_{n,n})^4 \\ \vdots & \ddots & \vdots & \ddots & \vdots \\ (q_{n,n} - q_{0,0})^4 & \cdots & (q_{n,n} - q_{i,j})^4 & \cdots & (q_{n,n} - q_{n,n})^4 \end{bmatrix} \tag{5.11}$$

where M is a $2n \times 2n$ matrix, the subscript '2' indicates the quadratic term and the subscript '4' indicates the quadric term.

Then, an adjacency matrix is defined to form the generalised position of each node, which includes the relationship between every node by using an element '1' to define connected nodes and '0' to define unconnected nodes. Figure 5.3 illustrates a simple relationship between 4 nodes which are connected with one another sequentially in

turn, thus the adjacency matrix can be defined by

$$A = \begin{bmatrix} 0 & 1 & 0 & 0 \\ 1 & 0 & 1 & 0 \\ 0 & 1 & 0 & 1 \\ 0 & 0 & 1 & 0 \end{bmatrix} \quad (5.12)$$

with the boundary conditions $q_1 = q_4 = 0$.

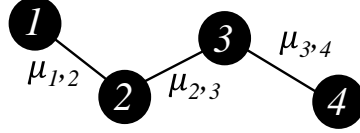


Figure 5.3: Example of a simple adjacency relationship.

In addition, a more general configuration can be considered by inserting the coupling parameters μ into the adjacency matrix, which express the detailed mechanical relationship between each of the nodes. The matrix A therefore can be rewritten as

$$A = \begin{bmatrix} 0 & \mu_{1,2} & 0 & 0 \\ \mu_{1,2} & 0 & \mu_{2,3} & 0 \\ 0 & \mu_{2,3} & 0 & \mu_{3,4} \\ 0 & 0 & \mu_{3,4} & 0 \end{bmatrix} \quad (5.13)$$

A generalised, extensive form of the adjacency matrix can now be defined as

$$A = \begin{bmatrix} 0 & \cdots & \mu_{0,0,i,j} & \cdots & \mu_{0,0,n,n} \\ \vdots & \ddots & \vdots & \ddots & \vdots \\ \mu_{0,0,i,j} & \cdots & 0 & \cdots & \mu_{i,j,n,n} \\ \vdots & \ddots & \vdots & \ddots & \vdots \\ \mu_{0,0,n,n} & \cdots & \mu_{i,j,n,n} & \cdots & 0 \end{bmatrix} \quad (5.14)$$

where $\mu_{i,j,n,n}$ defines the coupling relationship between nodes $q_{i,j}$ and $q_{n,n}$.

Accordingly, the potential energy of the system can be constructed by combining a quadratic-term matrix, quartic-term matrix and adjacency matrix. To proceed R is defined as

$$R = R_1 \circ R_2 \quad (5.15)$$

where \circ denotes the Hadamard product (element-wise product). The Hadamard prod-

uct is an operation such that each element (ij) in the matrix is produced from the product of the corresponding location elements (ij) in another two matrices of the same dimension to generate a new matrix with the same dimension as the original two matrices. It is noted that R has the same dimension as the operands with R_1 and R_2 . Therefore, the total potential energy V can be defined as

$$V = -\frac{1}{2}sum(M_2 \circ A_1) + \frac{1}{4}sum(M_4 \circ A_\mu) \quad (5.16)$$

where A_1 and A_μ are upper triangular matrixes that can be developed from Eq. 5.12 and Eq. 5.14 such that

$$A_1 = \begin{bmatrix} \ddots & 1 & 1 \\ 0 & \ddots & 1 \\ 0 & 0 & \ddots \end{bmatrix} \quad (5.17)$$

and

$$A_\mu = \begin{bmatrix} 0 & \cdots & \mu_{0,0,i,j} & \cdots & \mu_{0,0,n,n} \\ \vdots & \ddots & \vdots & \ddots & \vdots \\ 0 & \cdots & 0 & \cdots & \mu_{i,j,n,n} \\ \vdots & \ddots & \vdots & \ddots & \vdots \\ 0 & \cdots & 0 & \cdots & 0 \end{bmatrix} \quad (5.18)$$

Since the system is considered conservative without dissipation, the Hamiltonian of the problem can then be constructed from the kinetic and potential energy as

$$T(\mathbf{p}) = \frac{1}{2}\|\mathbf{p}^2\| \quad (5.19)$$

$$V(\mathbf{q}) = -\frac{1}{2}sum(M_2 \circ A_1) + \frac{1}{4}sum(M_4 \circ A_\mu) \quad (5.20)$$

where again the set $q = q_{i,j}$ ($i = 1 - n, j = 1 - n$) is associated with the set of momenta $\mathbf{p} = p_{i,j}$ ($i = 1 - n, j = 1 - n$). Then the dynamics of the system can be obtained from Hamilton's equations. It is clear that since the kinetic energy is independent of \mathbf{q} , it can be seen that $\dot{\mathbf{p}} = -\nabla_{\mathbf{q}}V(\mathbf{q})$ so that

$$\dot{q}_{i,j} = p_{i,j} \quad (5.21)$$

and

$$\dot{p}_{i,j} = -\nabla_{\mathbf{q}}V(\mathbf{q}) \quad (5.22)$$

The model shown in Fig. 5.2 is now employed as an example to illustrate the detailed process using the general methods above. The labelled graph of the simple smart surface structure is shown in Fig. 5.4. The displacement of the boundary nodes can again be set to zero, i.e. $q_{0,0} = q_{0,1} = q_{0,2} = q_{0,3} = q_{1,0} = q_{1,3} = q_{2,0} = q_{2,3} = q_{3,0} = q_{3,1} = q_{3,2} = q_{3,3} = 0$.

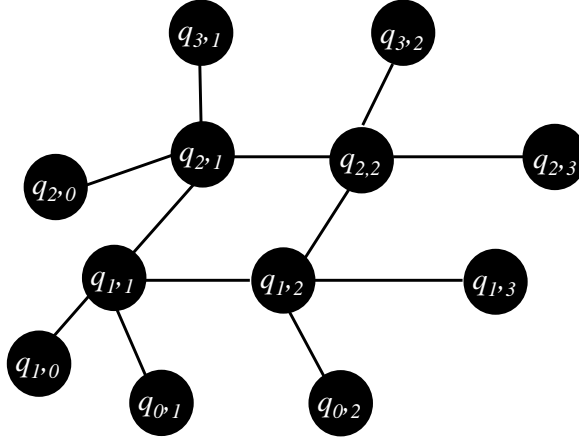


Figure 5.4: Example of a simple adjacency relationship.

Therefore, the relevant matrixes can be defined as

$$M_2 = \begin{bmatrix} (q_{0,0} - q_{0,0})^2 & \cdots & (q_{0,0} - q_{i,j})^2 & \cdots & (q_{0,0} - q_{3,3})^2 \\ \vdots & \ddots & \vdots & \ddots & \vdots \\ (q_{i,j} - q_{0,0})^2 & \cdots & (q_{i,j} - q_{i,j})^2 & \cdots & (q_{i,j} - q_{3,3})^2 \\ \vdots & \ddots & \vdots & \ddots & \vdots \\ (q_{3,3} - q_{0,0})^2 & \cdots & (q_{3,3} - q_{i,j})^2 & \cdots & (q_{3,3} - q_{3,3})^2 \end{bmatrix}_{16 \times 16} \quad (5.23)$$

and

$$M_4 = \begin{bmatrix} (q_{0,0} - q_{0,0})^4 & \cdots & (q_{0,0} - q_{i,j})^4 & \cdots & (q_{0,0} - q_{3,3})^4 \\ \vdots & \ddots & \vdots & \ddots & \vdots \\ (q_{i,j} - q_{0,0})^4 & \cdots & (q_{i,j} - q_{i,j})^4 & \cdots & (q_{i,j} - q_{3,3})^4 \\ \vdots & \ddots & \vdots & \ddots & \vdots \\ (q_{3,3} - q_{0,0})^4 & \cdots & (q_{3,3} - q_{i,j})^4 & \cdots & (q_{3,3} - q_{3,3})^4 \end{bmatrix}_{16 \times 16} \quad (5.24)$$

and so it can be shown that

$$A_1 = \begin{bmatrix} 0 & 0 & 0 & 0 & 0 & 0 & 0 & 0 & 0 & 0 & 0 & 0 & 0 & 0 & 0 & 0 \\ 0 & 0 & 0 & 0 & 0 & 1 & 0 & 0 & 0 & 0 & 0 & 0 & 0 & 0 & 0 & 0 \\ 0 & 0 & 0 & 0 & 0 & 0 & 1 & 0 & 0 & 0 & 0 & 0 & 0 & 0 & 0 & 0 \\ 0 & 0 & 0 & 0 & 0 & 0 & 0 & 0 & 0 & 0 & 0 & 0 & 0 & 0 & 0 & 0 \\ 0 & 0 & 0 & 0 & 0 & 1 & 0 & 0 & 0 & 0 & 0 & 0 & 0 & 0 & 0 & 0 \\ 0 & 0 & 0 & 0 & 0 & 0 & 1 & 0 & 0 & 1 & 0 & 0 & 0 & 0 & 0 & 0 \\ 0 & 0 & 0 & 0 & 0 & 0 & 0 & 1 & 0 & 0 & 1 & 0 & 0 & 0 & 0 & 0 \\ 0 & 0 & 0 & 0 & 0 & 0 & 0 & 0 & 0 & 0 & 0 & 0 & 0 & 0 & 0 & 0 \\ 0 & 0 & 0 & 0 & 0 & 0 & 0 & 0 & 0 & 0 & 0 & 0 & 0 & 0 & 0 & 0 \\ 0 & 0 & 0 & 0 & 0 & 0 & 0 & 0 & 0 & 0 & 1 & 0 & 0 & 0 & 0 & 0 \\ 0 & 0 & 0 & 0 & 0 & 0 & 0 & 0 & 0 & 0 & 0 & 1 & 0 & 0 & 1 & 0 \\ 0 & 0 & 0 & 0 & 0 & 0 & 0 & 0 & 0 & 0 & 0 & 0 & 0 & 0 & 0 & 0 \\ 0 & 0 & 0 & 0 & 0 & 0 & 0 & 0 & 0 & 0 & 0 & 0 & 0 & 0 & 0 & 0 \\ 0 & 0 & 0 & 0 & 0 & 0 & 0 & 0 & 0 & 0 & 0 & 0 & 0 & 0 & 0 & 0 \\ 0 & 0 & 0 & 0 & 0 & 0 & 0 & 0 & 0 & 0 & 0 & 0 & 0 & 0 & 0 & 0 \\ 0 & 0 & 0 & 0 & 0 & 0 & 0 & 0 & 0 & 0 & 0 & 0 & 0 & 0 & 0 & 0 \end{bmatrix}_{16 \times 16} \quad (5.25)$$

and

$$A_\mu = \begin{bmatrix} 0 & \cdots & 0 & \cdots & 0 \\ \vdots & \ddots & \vdots & \ddots & \vdots \\ 0 & \cdots & 0 & \cdots & \mu_{i,j,n,n} \\ \vdots & \ddots & \vdots & \ddots & \vdots \\ 0 & \cdots & 0 & \cdots & 0 \end{bmatrix}_{16 \times 16} \quad (5.26)$$

We use two different relationships μ_1 and μ_2 to construct the matrix A_μ , where μ_1 defines the relationship between free nodes and boundary nodes and μ_2 defines the relationship between free nodes and each other. Equation 5.25 can therefore be rewritten

as

$$A_1 = \begin{bmatrix} 0 & 0 & 0 & 0 & 0 & 0 & 0 & 0 & 0 & 0 & 0 & 0 & 0 & 0 & 0 & 0 \\ 0 & 0 & 0 & 0 & 0 & \mu_1 & 0 & 0 & 0 & 0 & 0 & 0 & 0 & 0 & 0 & 0 \\ 0 & 0 & 0 & 0 & 0 & 0 & \mu_1 & 0 & 0 & 0 & 0 & 0 & 0 & 0 & 0 & 0 \\ 0 & 0 & 0 & 0 & 0 & 0 & 0 & 0 & 0 & 0 & 0 & 0 & 0 & 0 & 0 & 0 \\ 0 & 0 & 0 & 0 & 0 & \mu_1 & 0 & 0 & 0 & 0 & 0 & 0 & 0 & 0 & 0 & 0 \\ 0 & 0 & 0 & 0 & 0 & 0 & \mu_2 & 0 & 0 & \mu_2 & 0 & 0 & 0 & 0 & 0 & 0 \\ 0 & 0 & 0 & 0 & 0 & 0 & 0 & \mu_2 & 0 & 0 & \mu_2 & 0 & 0 & 0 & 0 & 0 \\ 0 & 0 & 0 & 0 & 0 & 0 & 0 & 0 & 0 & 0 & 0 & 0 & 0 & 0 & 0 & 0 \\ 0 & 0 & 0 & 0 & 0 & 0 & 0 & 0 & 0 & \mu_2 & 0 & 0 & 0 & 0 & 0 & 0 \\ 0 & 0 & 0 & 0 & 0 & 0 & 0 & 0 & 0 & 0 & \mu_2 & 0 & 0 & \mu_1 & 0 & 0 \\ 0 & 0 & 0 & 0 & 0 & 0 & 0 & 0 & 0 & 0 & 0 & \mu_1 & 0 & 0 & \mu_1 & 0 \\ 0 & 0 & 0 & 0 & 0 & 0 & 0 & 0 & 0 & 0 & 0 & 0 & 0 & 0 & 0 & 0 \\ 0 & 0 & 0 & 0 & 0 & 0 & 0 & 0 & 0 & 0 & 0 & 0 & 0 & 0 & 0 & 0 \\ 0 & 0 & 0 & 0 & 0 & 0 & 0 & 0 & 0 & 0 & 0 & 0 & 0 & 0 & 0 & 0 \\ 0 & 0 & 0 & 0 & 0 & 0 & 0 & 0 & 0 & 0 & 0 & 0 & 0 & 0 & 0 & 0 \\ 0 & 0 & 0 & 0 & 0 & 0 & 0 & 0 & 0 & 0 & 0 & 0 & 0 & 0 & 0 & 0 \end{bmatrix}_{16 \times 16} \quad (5.27)$$

Through using Eq. 3.20, the same expression for the potential energy can be found as with Eq. 3.9. Therefore, the equations of motion can be written as

$$\begin{bmatrix} \ddot{q}_{1,1} \\ \ddot{q}_{1,2} \\ \ddot{q}_{2,1} \\ \ddot{q}_{2,2} \end{bmatrix} = \begin{bmatrix} 2\mu_1 q_{1,1} - \mu_2(q_{1,1} + q_{2,1} - q_{1,2}) \\ 2\mu_1 q_{1,2} - \mu_2(q_{1,2} + q_{2,2} - q_{1,1}) \\ 2\mu_1 q_{2,1} - \mu_2(q_{2,1} + q_{1,1} - q_{2,2}) \\ 2\mu_1 q_{2,2} - \mu_2(q_{2,2} + q_{1,2} - q_{2,1}) \end{bmatrix} + \begin{bmatrix} -2q_{1,1}^3 - (q_{1,1} - q_{2,1})^3 + (q_{1,1} - q_{1,2})^3 \\ -2q_{1,2}^3 - (q_{1,2} - q_{2,2})^3 + (q_{1,1} - q_{1,2})^3 \\ -2q_{2,1}^3 - (q_{1,1} - q_{2,1})^3 + (q_{2,1} - q_{2,2})^3 \\ -2q_{2,2}^3 - (q_{1,2} - q_{2,2})^3 + (q_{2,1} - q_{2,2})^3 \end{bmatrix} \quad (5.28)$$

Solving $\nabla_q V(\mathbf{q}) = 0$ yields a number of equilibria for different values of μ_1 and μ_2 , as shown in Fig. 5.5. Although only $\mu_1 > 0$ is considered in the subsequent analysis, for completeness the number of equilibria is shown for $-2 < \mu_2 < 2$. It can be seen that the total number of equilibria varies with the coupling parameter μ_2 . In addition, the maximum number of equilibria occur when $\mu_2 = \mu_1 = 1$, which is found to be 101. It is clear that these equilibria are both stable and unstable and in principle may be connected through paths in the phase of the problem. Again, one type of path is the heteroclinic connection which connects equal-energy unstable equilibria through their stable and unstable manifolds. Therefore, in order to explore all possible equilibrium configurations of the smart surface model the case $\mu_2 = \mu_1 = 1$ for the coupling

parameters is used. The case $\mu_2 > \mu_1$ is used later to explore possible reconfigurations between different unstable states of the structure.

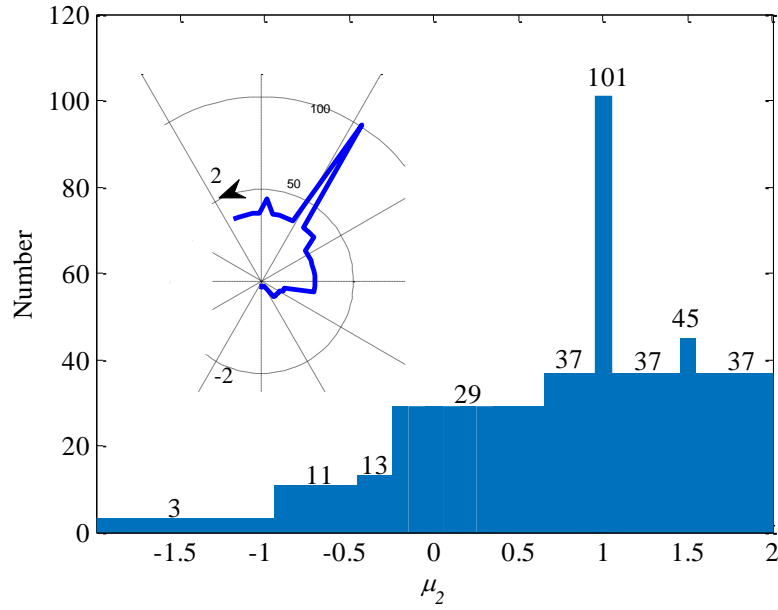


Figure 5.5: Number of equilibria of the smart surface structure with varying coupling parameter μ_2 with $\mu_1 = 1$.

The equilibrium configurations of the smart surface model are listed in Table 5.1. The linear stability properties of these equilibria can then be determined through linearisation of Hamilton's equations in the neighbourhood of each equilibrium point by an eigenvalue approach. Through dynamical system theory [66], a set of stable equilibria are then associated with conjugate imaginary eigenvalues and a set of unstable equilibria are associated with real eigenvalues of opposite sign. The linearisation of Hamilton's equations for some general equilibrium point $(\tilde{q}_{1,1}, \tilde{q}_{1,2}, \tilde{q}_{2,1}, \tilde{q}_{2,2})$ of the 4 degree-of-freedom system can be expressed in matrix form as

$$\begin{bmatrix} \ddot{q}_{1,1} \\ \ddot{q}_{1,2} \\ \ddot{q}_{2,1} \\ \ddot{q}_{2,2} \end{bmatrix} = (\mathbf{K} + \mathbf{R}) \begin{bmatrix} q_{1,1} - \tilde{q}_{1,1} \\ q_{1,2} - \tilde{q}_{1,2} \\ q_{2,1} - \tilde{q}_{2,1} \\ q_{2,2} - \tilde{q}_{2,2} \end{bmatrix} \quad (5.29)$$

$$\mathbf{K} = \begin{bmatrix} \tilde{\gamma}_{1,2}^{1,1} - \tilde{\gamma}_{2,1}^{1,1} - 6\tilde{q}_{1,1}^2 & \tilde{\gamma}_{1,2}^{1,1} & \tilde{\gamma}_{2,1}^{1,1} & 0 \\ \tilde{\gamma}_{1,2}^{1,1} & \tilde{\gamma}_{1,2}^{1,1} - \tilde{\gamma}_{2,2}^{1,2} - 6\tilde{q}_{1,2}^2 & 0 & \tilde{\gamma}_{2,2}^{1,2} \\ \tilde{\gamma}_{2,1}^{1,1} & 0 & \tilde{\gamma}_{2,1}^{1,1} - \tilde{\gamma}_{2,2}^{2,1} - 6\tilde{q}_{2,1}^2 & \tilde{\gamma}_{2,2}^{2,1} \\ 0 & \tilde{\gamma}_{2,2}^{1,2} & \tilde{\gamma}_{2,2}^{2,1} & \tilde{\gamma}_{2,2}^{1,2} - \tilde{\gamma}_{2,2}^{2,1} - 6\tilde{q}_{1,1}^2 \end{bmatrix} \quad (5.30)$$

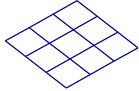
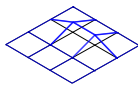
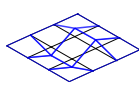
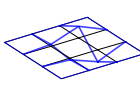
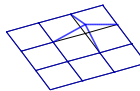
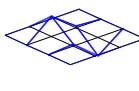
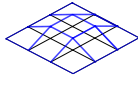
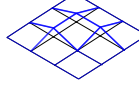
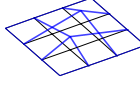
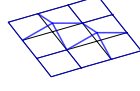
and

$$\mathbf{R} = \begin{bmatrix} 2\mu_1 + 2\mu_2 & -2\mu_2 & -\mu_2 & 0 \\ -\mu_2 & 2\mu_1 + 2\mu_2 & 0 & -\mu_2 \\ -\mu_2 & 0 & 2\mu_1 + 2\mu_2 & -\mu_2 \\ 0 & -\mu_2 & -\mu_2 & 2\mu_1 + 2\mu_2 \end{bmatrix} \quad (5.31)$$

where $\tilde{\gamma}_{m,n}^{i,j} = 3(\tilde{q}_{i,j} - \tilde{q}_{m,n})^2$.

The eigenvalues of the linear system can then be found to determine the local stability properties. It can be shown that this 4 degree-of-freedom system possesses 29 unstable equilibria and 72 stable equilibria, again noted in Table 5.1.

Table 5.1: Stability properties of the equilibria with $\mu_1 = \mu_2 = 1$ and the corresponding surface configuration.

Configuration					
Coordinates	(0 0 0 0)	(0 0 1 1)	(-0.6 0.6 0.6 -0.6)	(-0.1 0.1 -0.6 0.6)	(0 0 0 1)
Potential Energy	0	-1.5	-1.6	-1.1	-1
Type	Maximum	Saddle			
Number	1	28			
Eigenvalues	$\pm 2, \pm 2, \pm\sqrt{2}, \pm\sqrt{6}$	$\pm 1.6, \pm 0.8, \pm 2.1i, \pm 2.6i$	$\pm 1.3, \pm 0.6i, \pm 2.3i, \pm 2.4i$	$\pm 1.4, \pm 1.9, \pm 0.9i, \pm 3.1i$	$\pm 1, \pm 1.1, \pm 2.2, \pm 3.0i$
Configuration					
Coordinates	(0.1 1 -1 0.1)	(1 1 1 1)	(0 1 1 1)	(1.2 0.6 0.6 1.2)	(0 1 1 0)
Potential Energy	-2				
Type	Minimum Stable				
Number	72				
Eigenvalues	$\pm 0, \pm 1.2i, \pm 2.8i, \pm 3.1i$	$\pm 0, \pm\sqrt{2}i, \pm\sqrt{2}i, \pm 2i$	$\pm 0, \pm\sqrt{2}i, \pm 2.2i, \pm 2.6i$	$\pm 0, \pm 0, \pm 2.4i, \pm 2.4i$	$\pm 0, \pm\sqrt{2}i, \pm 2.3i, \pm 3.2i$

5.3 Heteroclinic connections

In order to explore the possible transition of the model smart surface using heteroclinic connections, several configurations are selected from the set of equilibrium configurations discussed above to act as the initial and final states, respectively. Meanwhile, from Eq. 5.28 it can be shown that

$$\begin{aligned} & \ddot{q}_{1,1} + \ddot{q}_{1,2} + \ddot{q}_{2,1} + \ddot{q}_{2,2} \\ & = 2q_{1,1}(\mu_1 - q_{1,1}^2) + 2q_{1,2}(\mu_1 - q_{1,2}^2) + 2q_{2,1}(\mu_1 - q_{2,1}^2) + 2q_{2,2}(\mu_1 - q_{2,2}^2) \end{aligned} \quad (5.32)$$

so that it can be seen immediately that equilibria can be found at $E_0(0, 0, 0, 0)$, $E_1(\sqrt{\mu_1}, \sqrt{\mu_1}, \sqrt{\mu_1}, \sqrt{\mu_1})$ and $E_2(-\sqrt{\mu_1}, -\sqrt{\mu_1}, -\sqrt{\mu_1}, -\sqrt{\mu_1})$, which shows that these equilibria are independent of μ_2 . It can be noted that the stability properties of equilibria E_1 and E_2 are a function of the ratio between μ_2 and μ_1 . It can also be shown that the equilibria E_1 and E_2 become unstable for $\mu_2 > \mu_1$. Therefore, E_1 and E_2 will be chosen to be unstable with $\mu_2 > \mu_1$ so that a heteroclinic connection can be found between E_1 and E_2 for illustration. The purpose of finding such a transition is that the unstable equilibria E_1 and E_2 lie on the same potential energy surface and so in principle zero net energy input is needed to reconfigure the structure between them. Then, dynamical system theory can be employed to seek a possible phase space connection between these unstable equilibria. For a conservative system, linearisation of Hamilton's equations in the neighbourhood of each equilibrium point yields pairs of eigenvalues $\lambda > 0$ and $\lambda < 0$, respectively. These eigenvalues have corresponding stable and unstable eigenvectors associated with the directions \mathbf{u}^s and \mathbf{u}^u . Again, the eigenvectors can be mapped to approximate the stable and unstable manifolds by integrating forwards or backwards from an unstable equilibrium point \mathbf{z}^e , defined by

$$\mathbf{z}^s = \mathbf{z}^e + \epsilon \mathbf{u}^s \quad (5.33)$$

$$\mathbf{z}^u = \mathbf{z}^e + \epsilon \mathbf{u}^u \quad (5.34)$$

for $\epsilon \ll 1$. This method can be used to find heteroclinic connections between equal-energy unstable equilibria so that the structure can be reconfigured between unstable states. Symmetry is always a basic property for heteroclinic connections in dynamical systems. Therefore, symmetry can be imposed on the problem to search for heteroclinic connections. A two-dimensional space can be obtained by a dimensionality reduction

with the following transformation

$$\begin{pmatrix} Q_1 \\ Q_2 \end{pmatrix} = \begin{pmatrix} a_1 & a_2 & a_3 & a_4 \\ b_1 & b_2 & b_3 & b_4 \end{pmatrix} \begin{pmatrix} q_1 \\ q_2 \\ q_3 \\ q_4 \end{pmatrix} \quad (5.35)$$

where the pre-multiplication matrix is a constant set here to

$$\begin{pmatrix} a_1 & a_2 & a_3 & a_4 \\ b_1 & b_2 & b_3 & b_4 \end{pmatrix} = \begin{pmatrix} 2 & 2 & 2 & 2 \\ 1 & -1 & -1 & 1 \end{pmatrix} \quad (5.36)$$

thus transforming the four-dimensional space to a two-dimensional space, so that the potential defined in Eq. 5.9 can be transformed to

$$\begin{aligned} V(Q, \mu) = & (2Q_1 - Q_2)^4 - 2\mu_1(2Q_1 + Q_2)^2 - 2\mu(2Q_1 - Q_2)^2 \\ & - 8\mu_2Q_2^2 + 16Q_2^4 + (2Q_1 + Q_2)^4 \end{aligned} \quad (5.37)$$

In this new coordinate system, the equations of motion can be obtained from $\dot{\mathbf{P}} = -\nabla_Q V(\mathbf{Q})$ and so the dynamics of the new system can then be described by

$$\dot{Q}_1 = P_1 \quad (5.38)$$

$$\dot{P}_1 = 2\mu_1(8Q_1 - 4Q_2) + 2\mu_1(8Q_1 + 4Q_2) - 8(2Q_1 - Q_2)^2 + 8(2Q_1 + Q_2)^3 \quad (5.39)$$

$$\dot{Q}_2 = P_2 \quad (5.40)$$

$$\dot{P}_2 = 16\mu_2Q_2 - 2\mu_1(4Q_1 - 2Q_2) + 2\mu_1(4Q_1 + 2Q_2) - 64Q_2^3 - 4(2Q_1 + Q_2)^3 + 4(2Q_1 - Q_2)^3 \quad (5.41)$$

In these new coordinates, the system is symmetric about the axis $Q_1 = 0$. The unstable manifold of E_1 is therefore simply the reflection of the stable manifold of E_2 , which means that the structure can be reconfigured from state E_1 to state E_2 in principle without energy input. Therefore, a heteroclinic connection between E_1 and E_2 is symmetric about the axis $Q_1 = 0$, and so must intersect $Q_1 = 0$ perpendicularly, i.e. $\dot{Q}_2 = 0$. The numerical method used to find heteroclinic connection follows McInnes and Waters [60]: for $\mu_2 < 1.2$ and $\mu_1 = 1$, \dot{Q}_2 is sufficiently small for an approximate heteroclinic connection to exist. Then when $\mu_2 \approx 1.687$ and $\mu_1 = 1$, an exact heteroclinic connection exists, as is clearly shown in Fig. 5.6. This demonstrates that in principle for an exact value of μ_1 there exist a value of μ_2 not close to μ_1 which admits

a heteroclinic path.

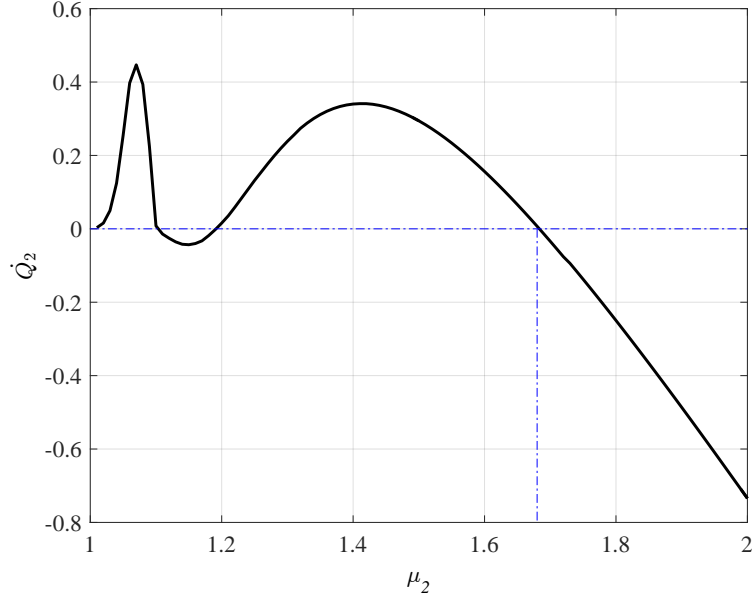


Figure 5.6: The value of \dot{Q}_2 at the first crossing of the unstable manifold with the Q_2 axis, with the increasing parameter μ_2 ($\mu_1 = 1$).

The heteroclinic connection will therefore have a mirror image under $Q_2 \rightarrow -Q_2$, as shown in Fig. 5.7 and Fig. 5.8. To initiate the heteroclinic connection, a small disturbance $\epsilon = 10^{-3}$ is added along the unstable manifold of E_1 . For a true heteroclinic connection, motion away from an unstable equilibrium point and towards a connected unstable equilibrium point is asymptotically slow. In practice the actual phase trajectory must shadow the real heteroclinic connection and a controller used to initiate and terminate the heteroclinic connection [64]. The corresponding shape of the surface during the transition from $E_1(\sqrt{\mu_1}, \sqrt{\mu_1}, \sqrt{\mu_1}, \sqrt{\mu_1})$ to $E_2(-\sqrt{\mu_1}, -\sqrt{\mu_1}, -\sqrt{\mu_1}, -\sqrt{\mu_1})$ is shown in Fig. 5.9.

Numerical experiments demonstrate that it is in general possible to find a heteroclinic connection for some choice of coupling parameters μ_1 and μ_2 , while again a controller [64] can in principle be used to achieve the reconfiguration for a choice of parameters μ_1 and μ_2 . In principle for a conservative system without internal dissipation, such reconfigurations do not required the input of energy, which is efficient compared to conventional strategies with transitions between passively stable configurations across a potential barrier. However, dissipation compensations using active control, as discussed in Chapter 4 for a 1-dimensional mass chain, can be envisaged.

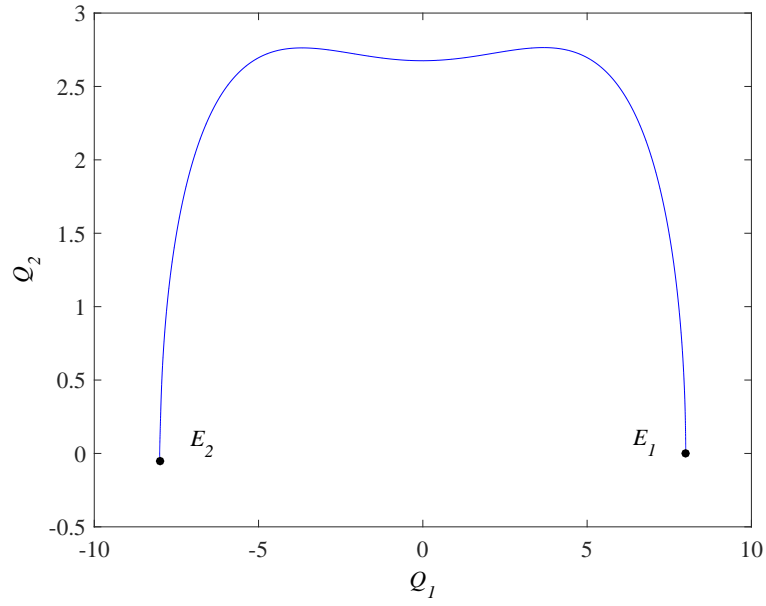


Figure 5.7: Heteroclinic connection between at $E_1 (8, 0)$ and at $E_2 (-8,0)$ for $\mu_1 = 1$ and $\mu_2 = 1.687\mu_1$. The projection of the phase path in the new coordinate space ($Q_2 \rightarrow -Q_2$).

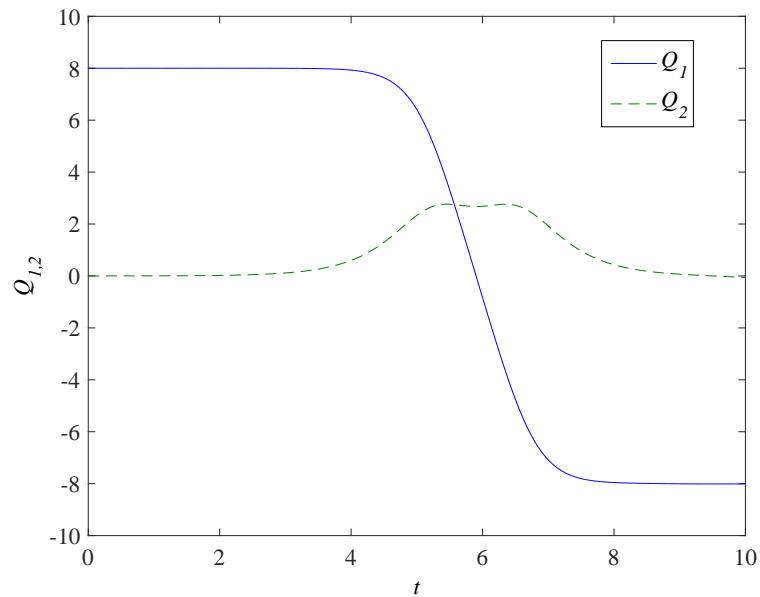


Figure 5.8: New coordinates ($Q_1 - Q_2$) for a heteroclinic connection between at $E_1 (8, 0)$ and at $E_2 (-8, 0)$ for $\mu_1 = 1$ and $\mu_2 = 1.687\mu_1$.

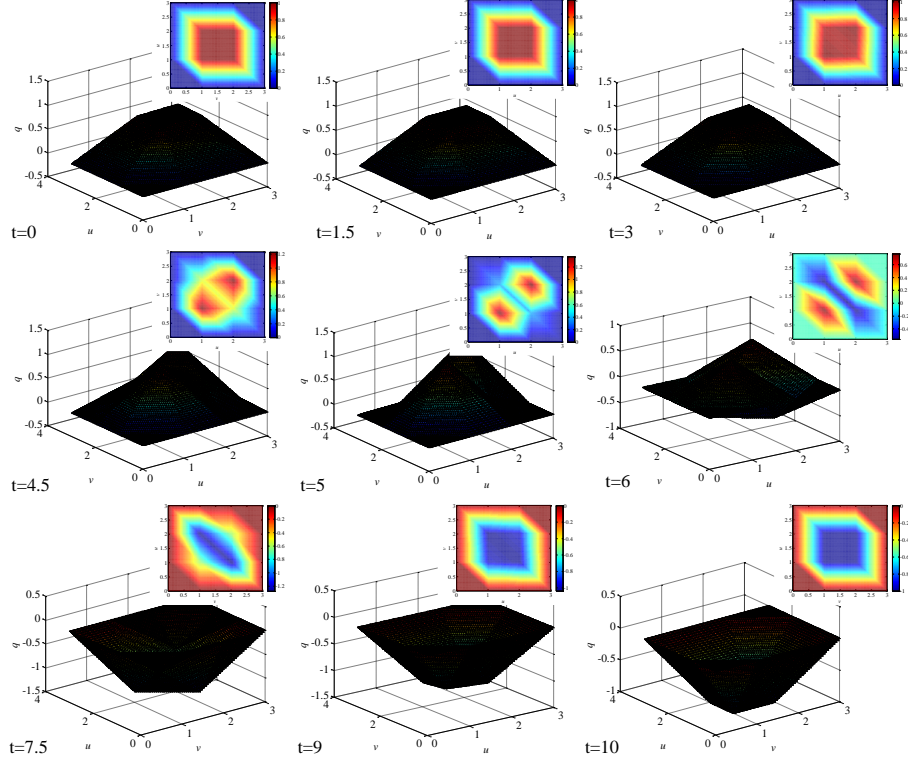


Figure 5.9: Transition from unstable equilibria $E_1 (1, 1, 1, 1)$ at $t = 0$ to unstable equilibria $E_2 (-1, -1, -1, -1)$ at $t=10$ for $\mu_1 = 1$ and $\mu_2 = 1.687\mu_1$.

5.4 Structure-preserving stabilisation control

This section presents a control method to stabilise the unstable equilibrium configurations of the smart surface structure. For a Hamiltonian system, there exist hyperbolic equilibria that have stable, unstable and center manifolds, with the unstable manifold generating the instability. However, a control law can be applied which will establish Lyapunov stability of the relative motion about the equilibrium point and stabilise an unstable configuration [74, 75]. Assuming active control is actuated by the spring coupling parameters (equivalent to modulating their natural length), the dynamics of the controlled system can be written as

$$\begin{bmatrix} \ddot{q}_{1,1} \\ \ddot{q}_{1,2} \\ \ddot{q}_{2,1} \\ \ddot{q}_{2,2} \end{bmatrix} = \mathbf{K} \begin{bmatrix} q_{1,1} - \tilde{q}_{1,1} \\ q_{1,2} - \tilde{q}_{1,2} \\ q_{2,1} - \tilde{q}_{2,1} \\ q_{2,2} - \tilde{q}_{2,2} \end{bmatrix} + \mathbf{B} \begin{bmatrix} \mu_1 \\ \mu_2 \end{bmatrix} = \mathbf{K}q + \mathbf{B}u \quad (5.42)$$

$$\mathbf{K} = \begin{bmatrix} \tilde{\gamma}_{1,2}^{1,1} - \tilde{\gamma}_{2,1}^{1,1} - 6\tilde{q}_{1,1}^2 & \tilde{\gamma}_{1,2}^{1,1} & \tilde{\gamma}_{2,1}^{1,1} & 0 \\ \tilde{\gamma}_{1,2}^{1,1} & \tilde{\gamma}_{1,2}^{1,1} - \tilde{\gamma}_{2,2}^{1,2} - 6\tilde{q}_{1,2}^2 & 0 & \tilde{\gamma}_{2,2}^{1,2} \\ \tilde{\gamma}_{2,1}^{1,1} & 0 & \tilde{\gamma}_{2,1}^{1,1} - \tilde{\gamma}_{2,2}^{2,1} - 6\tilde{q}_{2,1}^2 & \tilde{\gamma}_{2,2}^{2,1} \\ 0 & \tilde{\gamma}_{2,2}^{1,2} & \tilde{\gamma}_{2,2}^{2,1} & \tilde{\gamma}_{2,2}^{1,2} - \tilde{\gamma}_{2,2}^{2,1} - 6\tilde{q}_{1,1}^2 \end{bmatrix} \quad (5.43)$$

$$\mathbf{B} = \begin{bmatrix} 2(q_{1,1} - \tilde{q}_{1,1}) & 2(q_{1,1} - \tilde{q}_{1,1}) - 2(q_{1,2} - \tilde{q}_{1,2}) - 2(q_{2,1} - \tilde{q}_{2,1}) \\ 2(q_{1,2} - \tilde{q}_{1,2}) & 2(q_{1,2} - \tilde{q}_{1,2}) - 2(q_{1,1} - \tilde{q}_{1,1}) - 2(q_{2,2} - \tilde{q}_{2,2}) \\ 2(q_{2,1} - \tilde{q}_{2,1}) & 2(q_{2,1} - \tilde{q}_{2,1}) - 2(q_{1,1} - \tilde{q}_{1,1}) - 2(q_{2,2} - \tilde{q}_{2,2}) \\ 2(q_{2,2} - \tilde{q}_{2,2}) & 2(q_{2,2} - \tilde{q}_{2,2}) - 2(q_{1,2} - \tilde{q}_{1,2}) - 2(q_{2,1} - \tilde{q}_{2,1}) \end{bmatrix} \quad (5.44)$$

where $\tilde{\gamma}_{m,n}^{i,j} = 3(\tilde{q}_{i,j} - \tilde{q}_{m,n})^2$.

The controllability matrix [76] for this third-order system is then given by

$$\mathbf{C} = \begin{bmatrix} \mathbf{K} & \mathbf{K}\mathbf{B} & \mathbf{K}^2\mathbf{B} & \mathbf{K}^3\mathbf{B} \end{bmatrix} \quad (5.45)$$

If the equilibria satisfy the conditions $\tilde{q}_{1,1} \neq \tilde{q}_{1,2} \neq \tilde{q}_{2,1} \neq \tilde{q}_{2,2}$, it shows that $\text{rank } \mathbf{C} = 4$, which implies that the system is fully controllable. However, for the example discussed above in Section 5.3, it can be shown that $\text{rank } \mathbf{C} = 2$, so that additional actuators are needed to ensure controllability. Therefore, the μ_1 terms (the coupling parameter between each mass and its boundary node) are divided into four parts as $\mu_{1,1}$, $\mu_{1,2}$, $\mu_{1,3}$ and $\mu_{1,4}$, which represent the relationship between corresponding individual masses and their fixed boundaries.

Then the matrix \mathbf{B} can then be expressed as

$$\mathbf{B} = \begin{bmatrix} \varrho_{1,1} & 0 & 0 & 0 & \varrho_{1,1} - \varrho_{1,2} - \varrho_{2,1} \\ 0 & \varrho_{1,2} & 0 & 0 & \varrho_{1,1} - \varrho_{1,2} - \varrho_{2,1} \\ 0 & 0 & \varrho_{2,1} & 0 & \varrho_{1,1} - \varrho_{1,2} - \varrho_{2,1} \\ 0 & 0 & 0 & \varrho_{2,2} & \varrho_{1,1} - \varrho_{1,2} - \varrho_{2,1} \end{bmatrix} \quad (5.46)$$

where $\varrho_{i,j} = 2(q_{i,j} - \tilde{q}_{i,j})$.

It can then be shown that the controller is constructed as

$$\mathbf{T}_c = \{-\sigma^2 [G_1 \mathbf{u}_+ \mathbf{u}_+^T + G_2 \mathbf{u}_- \mathbf{u}_-^T] - \varphi^2 G_3 [\mathbf{u} \mathbf{u}^T + \bar{\mathbf{u}} \bar{\mathbf{u}}^T]\} \quad (5.47)$$

where G_1 , G_2 and G_3 are the gain parameters, \mathbf{u}_+ and \mathbf{u}_- are the stable and unstable manifolds with corresponding eigenvalues $\pm\sigma$, \mathbf{u} and $\bar{\mathbf{u}}$ are center manifolds with corresponding eigenvalues are $\pm\varphi i$. A detailed development and proof of the control law

can be found elsewhere [74]. This control strategy can work effectively through estimating the relative motion and maintaining the Hamiltonian structure of the problem. Through Eq. 5.47 the controller can now stabilise the smart surface to maintain its unstable configuration with the gain parameters $G_1 = 1$ $G_2 = 2$ and $G_3 = 3$, as shown in Fig. 5.10, with the required controls shown in Fig. 5.11.

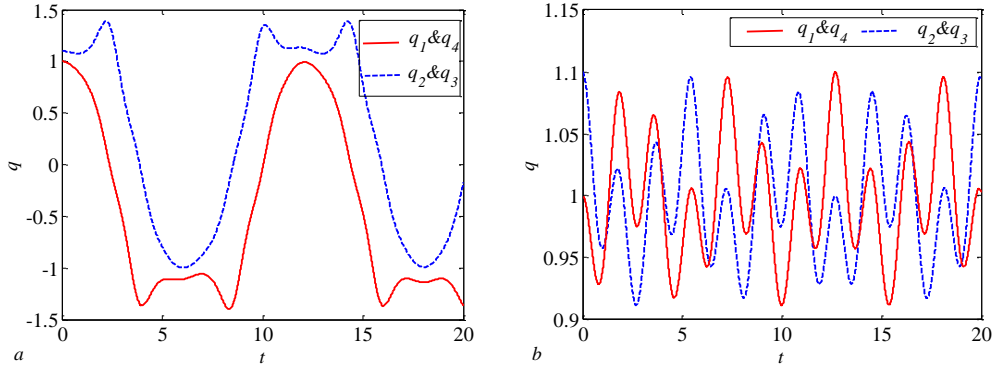


Figure 5.10: Mass displacements under small disturbance around E_1 (1, 1, 1, 1) (a) without control (b) with control.

A structure preserving controller has therefore been developed to stabilise the smart surface in an unstable configuration, and verified as effective numerically with suitable controls found. The controller is based on computing the local stability characteristics of the motion through the manifolds, which can in principle be realised through modulation of embedded smart materials (e.g. shape memory alloys) to manipulate the spring coupling parameters. Clearly, for a realistic smart surface energy is expended by the controller in maintaining the structure in an unstable equilibrium configuration, between reconfigurations using heteroclinic connections. The reconfiguration methodology proposed is considered as being used for applications where the structure has to frequently reconfigure between different configurations, for example for optical switching. In this way the energy efficiency of the heteroclinic connections for reconfiguration can compensate for the energy expenditure by the controller while temporarily in an actively controlled unstable state.

5.5 Connected smart surface units

The analysis from the previous section can now be used as the basis for the integration of connected smart surface elements. Such integrated systems can be extended to many potential applications which need frequent state switching to reduce mean power

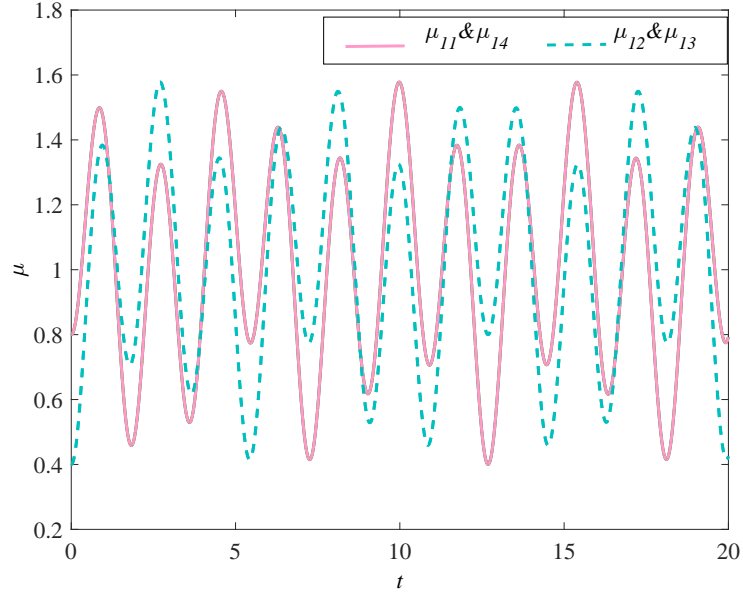


Figure 5.11: Control actuators generated through the parameters $\mu_{1,1}$, $\mu_{1,2}$, $\mu_{1,3}$ and $\mu_{1,4}$.

consumption and waste heat dissipation. One important potential application of this integrated smart surface system is that it can be reconfigured between two states to provide motion, for example in a conveyer system, to move an object towards a goal position through arranging sufficient numbers of smart surface units.

It is instructive to consider an analogue model consisting of two smart surfaces to understand the general behaviour of smart surface units connected in series. As shown in Fig. 5.12, the two adjacent smart surface units are connected by rigid links, which provides a relationship between each mass of every smart surface unit. When a vertical displacement (δ_1, δ_2) is applied in unit 1, unit 2 will move with a corresponding displacement. The motion of the coupled system can then be described by

$$q_{u,1,1} = q_{u,2,1} = \delta_1 \quad (5.48)$$

$$q_{u,1,2} = q_{u,2,2} = \delta_2 \quad (5.49)$$

$$\ddot{\delta}_1 = \ddot{q}_{u,1,1} + \ddot{q}_{u,2,1} \quad (5.50)$$

$$\ddot{\delta}_2 = \ddot{q}_{u,1,2} + \ddot{q}_{u,2,2} \quad (5.51)$$

where $q_{u,1,1}$ and $q_{u,2,1}$ represent the two mass displacements of unit 1 and unit 2, respectively; $q_{u,1,2}$ and $q_{u,2,2}$ represent the other two mass displacements of unit 1 and unit 2, respectively.

Figure 5.13 shows the mass displacement of the each unit, which can be considered as a heteroclinic connection of the integrated system. It can be seen that the relevant mass displacements between unit 1 and unit 2 have a rigid relationship, which is shown as the dashed line with the double-headed arrow. The parameters of the model used are the same as the model in Section 5.4. The corresponding shape of the connected smart surfaces associated with the initial and final configurations are shown in Fig. 5.14. It can be seen that unit 1 is in a saddle configuration initially and then changes to a stable configuration, accompanied with unit 2 being reconfigured from a stable equilibrium to a saddle. With this scheme, the heteroclinic connection can be used for reconfiguring an integrated smart surface which is assembled from distributed smart surface units.

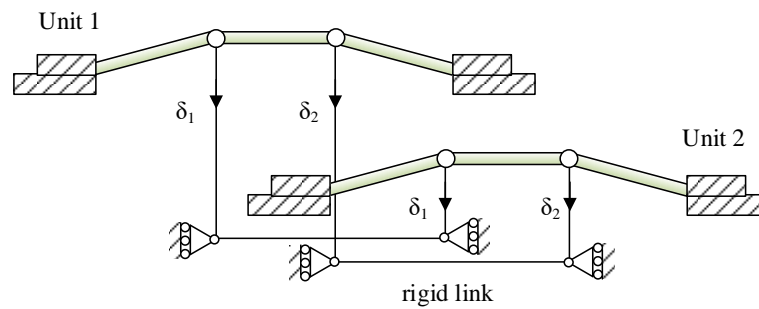


Figure 5.12: Schematic diagram of two connected smart surface units.

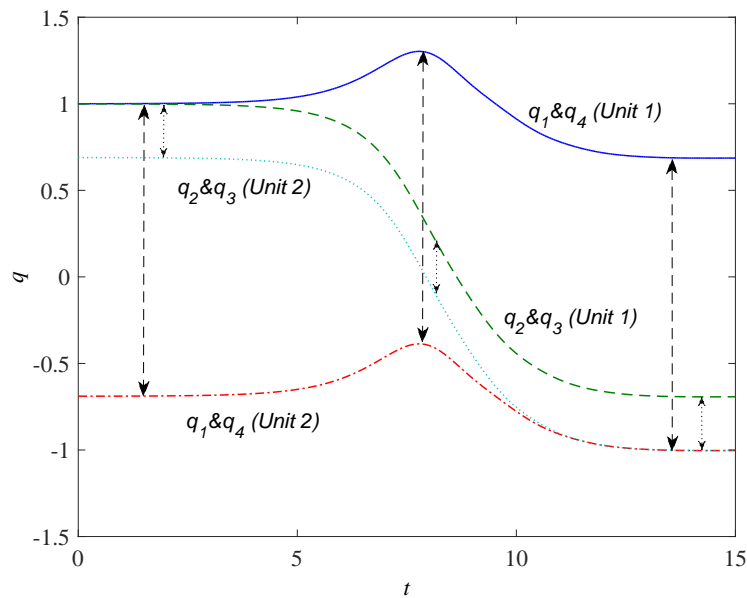


Figure 5.13: Configuration change during transition from unit 1 to unit 2.

In the context of the proposed application, the two simply-connected smart surface

units can realise reconfigurations as an integrated system. The smart surface unit can transmit motion through connections with neighbouring units. This example is provided to demonstrate how the methodology develop can be used to perform the reconfiguration of a larger smart surface that would be energy efficient compared to traditional approaches with transitions between stable states across a potential barrier.

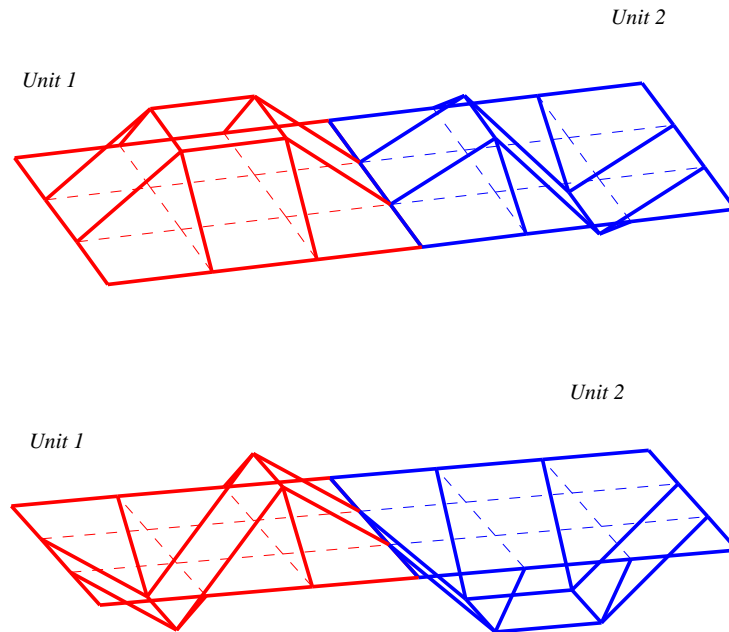


Figure 5.14: Corresponding shapes of the connected smart surface (a) initial condition (b) final condition.

5.6 Conclusion

Surface structures possessing multiple equilibria offer interesting dynamical behaviours with a broad range of potential applications. This Chapter has presented a preliminary study of a simple smart surface model composed of connected masses and linear springs. A general method has been provided to build the equations of motion of such a smart surface system. The theoretical model of the smart surface is nonlinear and complex, but some simple mathematical techniques can be employed to obtain a more compact normalized form. The nonlinear characteristics of the model can therefore be found by using dynamical system theory, which provides a predictive basis for the subsequent analysis of reconfiguring the smart surface and the design of structure-preserving stabilisation control. Then, an active reconfiguration scheme has been investigated to

connect equal-energy unstable (but actively controlled) configurations for the purpose of energy-efficient morphing of the smart surface. The reconfiguration of the smart surface between two unstable states does not in principle need additional energy input compared to reconfiguration between two stable configurations. In order to demonstrate that the structure can be actively controlled in an unstable state, a control strategy has been proposed to stabilise the unstable configuration. This control method establishes Lyapunov stability of the relative motion about the equilibrium point and stabilises an unstable configuration. A further development of the smart surface is proposed as an integral system, where the smart surface is extended by forming a series of connected smart surface units. The investigation into the reconfiguration of connected smart surface units can therefore be developed to design larger smart surfaces composed of many more units, which can be used for further applications, such as for conveying, sorting and positioning micro-parts.

Chapter 6

Linkage Mechanism

In previous Chapters, a spring-mass model has been used to investigate a simple smart structure from buckled beams to smart surface structures. The nonlinearity of these models was investigated by using dynamical system theory. Then, a set of unstable equilibria was found which in principle can be connected with heteroclinic paths in the phase space to achieve energy efficient reconfiguration.

In this Chapter, a classical four-bar mechanism with rigid linkages and torsional springs is firstly investigated in Section 6.2. The rigid model demonstrates the possibility of reconfiguring the mechanism between two unstable equilibria. Moreover, the rigid four-bar mechanism allows a simple controller to be developed to actively stabilise the unstable configurations of the structure. Then, in Section 6.3 a single axial spring is used to substitute for one rigid bar to develop a pseudo-rigid model, which illustrates interesting complexities over the rigid models in previous Chapters. An approximation of the trigonometric terms in the governing equations is then used to construct a simple non-linear mathematical model which is employed to illustrate the use of heteroclinic connections and active control.

Lastly, in Section 6.3, a purely elastic model with torsional springs and axial springs for linkages is developed which allows bending, stretching and compression. An energy-based method is used to verify the fidelity of the model relative to a flexible buckling beam in Section 6.3.3. The fundamental properties of the flexible model are then discussed using dynamical systems theory to determine which equilibria can be connected through the phase space of the problem. In Section 6.3.4, some numerical results are then presented to elaborate on the feasibility of this reconfiguration manoeuvre. In particular, paths in the phase space which join an equilibrium point to itself (homoclinic connections) and two different equilibrium point (heteroclinic connections) are sought.

The fully flexible model provides new insights into the use of heteroclinic connection for smart structures.

6.1 Rigid four-bar model

The motion of a link mechanism can be modelled using standard kinematic equations, which can be derived from [77]. A four-bar linkage is a basic mechanism which has only one degree of freedom, as shown in Fig. 6.1. The properties of this mechanism, such as range of movement, is based on the link lengths. In this Chapter, the nonlinearity of a four-bar linkage is discussed with specified dimensions, listed in Table 6.1, which were used in [78]. The input link can be chosen as link 2, link 3 or link 4, however, link 3 is selected here as the input link. Joint 2 and joint 3 are then assumed to have ideal torsional springs so that the system can be considered as conservative without friction. Therefore, the torsional springs can store or release energy when the mechanism moves. This re-distribution of (conserved) energy provides one or more distinct equilibrium positions (both stable and unstable), which is the basis for the following analysis on reconfiguration. The initial configuration of the mechanism is that link 3 is parallel to link 1, denoted by $\theta_3 = 0$. Following the development of [79] the energy of the system can then be found from

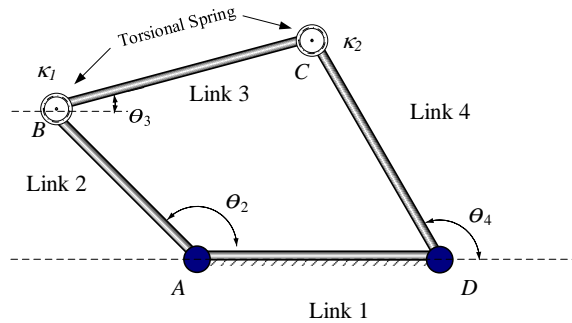


Figure 6.1: Four-bar mechanism with torsional springs model.

$$V = \sum_0^n \frac{1}{2} \kappa_i \psi_i^2 \quad (6.1)$$

where n is the numbers of torsional springs, V is the potential energy of the system, κ_i is the torsional spring constant of the i^{th} torsional spring and ψ_i is the angle of deflection of the bar. For each angle of deflection of the specific system shown in Fig. 6.1 it can

be seen that

$$\begin{aligned}\psi_2 &= (\theta_3 - \theta_{30}) - (\theta_2 - \theta_{20}) \\ \psi_3 &= (\theta_4 - \theta_{40}) - (\theta_3 - \theta_{30})\end{aligned}\tag{6.2}$$

where the subscript '0' indicates the initial angle of the rigid bar and link 1 is fixed in the horizontal direction as shown in Fig. 6.1. The total potential energy of the mechanism based on two torsional springs at joint 2 and joint 3 can then be written as

$$V = \frac{1}{2}\kappa_1\psi_2^2 + \frac{1}{2}\kappa_2\psi_3^2\tag{6.3}$$

Table 6.1: Properties of the four-bar mechanism model.

Variable	Value	Description
r_1	12.70 (cm)	Link 1 Length
r_2	13.97 (cm)	Link 2 Length
r_3	13.97 (cm)	Link 3 Length
r_4	13.97 (cm)	Link 4 Length
κ_1	0.164 (N-m/rad)	Spring Constant
κ_2	0.164 (N-m/rad)	Spring Constant

The moments required to keep the mechanism in a particular position can be obtained through the principle of virtual work [80]. The moment can be considered as the first derivative of the potential energy function with respect to the angle of the input link, so that the potential energy can be considered as

$$V = \int_{\theta_0}^{\theta} M d\theta\tag{6.4}$$

and by considering link 3 as the input link, then taking the derivative of Eq. 6.4 the moment M_3 is found from

$$M_3 = \frac{dV}{d\theta_3}\tag{6.5}$$

The initial configuration of the mechanism is that link 3 is parallel to link 1, i.e. $\theta_{30} = 0$. Therefore, the moment defined by Eq. 6.5 can be rewritten as

$$M_3 = \kappa_1\psi_2 \frac{d\psi_2}{d\theta_3} + \kappa_2\psi_3 \frac{d\psi_3}{d\theta_3}\tag{6.6}$$

Using the kinematics of the link mechanism [77], the derivatives in Eq. 6.6 can be

expressed using the additional relationships

$$\frac{d\theta_2}{d\theta_3} = \frac{r_3 \sin(\theta_3 - \theta_4)}{r_2 \sin(\theta_4 - \theta_2)} \quad (6.7)$$

and

$$\frac{d\theta_4}{d\theta_2} = \frac{r_4 \sin(\theta_4 - \theta_2)}{r_3 \sin(\theta_3 - \theta_2)} \quad (6.8)$$

The equilibrium positions of the mechanism can then be determined from the first derivative of the total potential energy when it is null. The stability of these equilibrium positions can also be determined by considering the sign of the second derivative of the potential energy. Any positions corresponding to local minima (local maxima) are stable (unstable) equilibrium points.

Some characteristics of the system will now be considered. The dimensions of the four-bar mechanism model are again listed in Table 6.1, where the model is a symmetric system with torsional springs at joints B and C only. The total potential energy of the torsional springs is shown in Fig. 6.2. It can be seen that there are two unstable equilibrium positions and three stable equilibrium positions in this symmetric model, listed in Table 6.2. The corresponding shape of the four-bar mechanism can be seen in Fig. 6.3, which shows one torsional spring in compression while the other is extended in the unstable equilibrium positions.

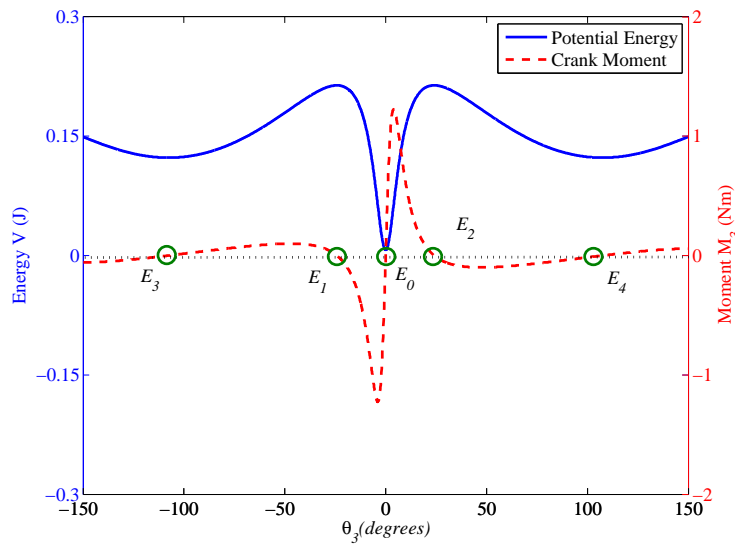


Figure 6.2: Energy and moment for the rigid four-bar mechanism.

In order to verify the reliability of the analytical results, a practical four-bar mechanism

was fabricated based on dimensions of Table 6.1. The mechanism is made of the carbon fibre bar and joints with torsional springs. The configurations E_0 , E_3 and E_4 are shown in Fig. 6.4, which corresponds to the numerical results shown in Fig. 6.3.

Table 6.2: Equilibrium points and corresponding potential energy.

Point	θ_3 (degrees)	V(Potential)	Type
E_0	0	0	stable
E_1	-26.83	0.21844	unstable
E_2	26.83	0.21844	unstable
E_3	-92.60	0.1687	stable
E_4	92.60	0.1687	stable

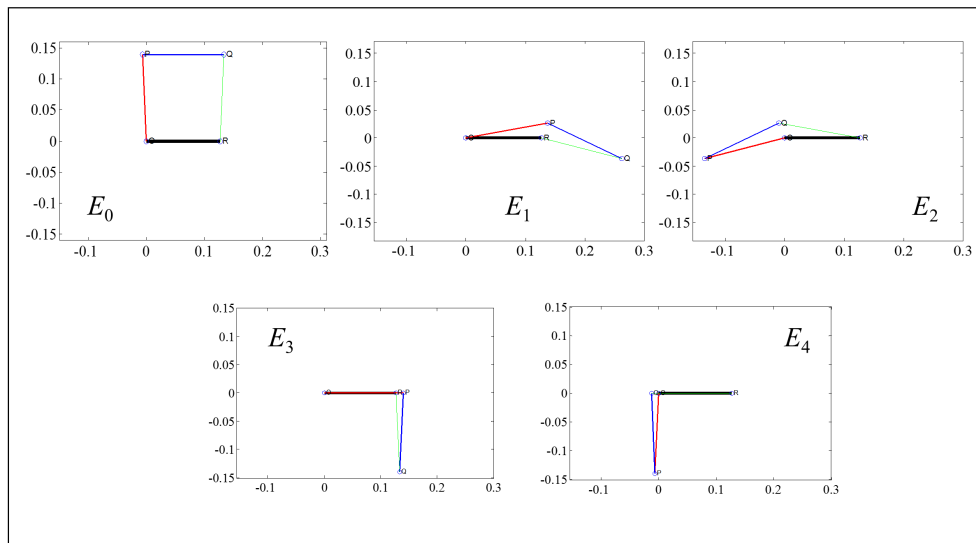


Figure 6.3: Shape of the four-bar mechanism in equilibrium positions.

In addition, a bifurcation diagram can be constructed through using different ratios between κ_1 and κ_2 , as shown in Fig. 6.5. Again, the number and position of the equilibria can be modified based on the free parameters of system.

A transition from E_1 to E_2 is now considered as an example to illustrate the method whereby equal-energy unstable configurations can be connected. The model is again considered to be a conservative system with the simplification that it has unit mass. We can now define the problem by a dynamical system of the form

$$\dot{\theta}_3 = \omega_3 \tag{6.9}$$

$$\dot{\omega}_3 = \kappa_1 \psi_2 \frac{d\psi_2}{d\theta_3} + \kappa_2 \psi_3 \frac{d\psi_3}{d\theta_3} \tag{6.10}$$

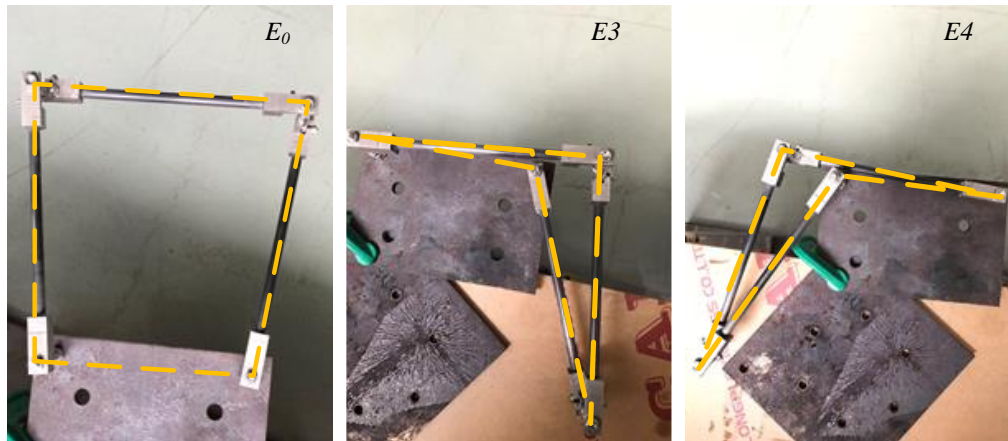


Figure 6.4: Experimental four-bar mechanism in equilibrium positions.

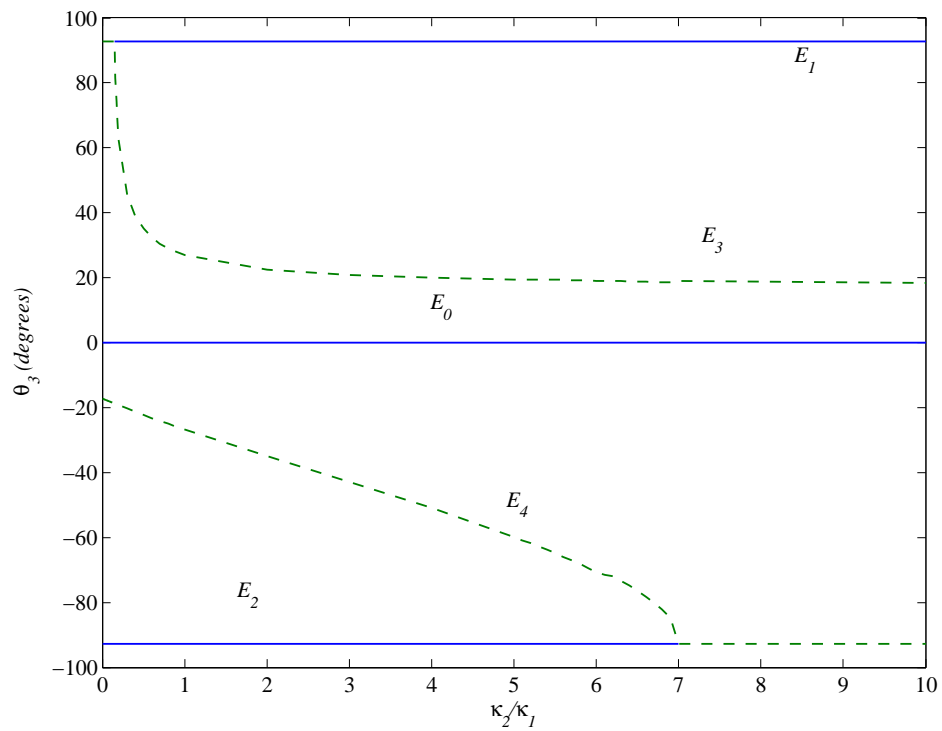


Figure 6.5: Bifurcation diagram for the four-bar mechanism, solid line: stable equilibria, dashed line: unstable equilibria.

Due to numerical error (and practically since the transition is between unstable equilibria) active control is required, which captures trajectories in a neighbourhood of E_2 . The system has only one degree of freedom, so that only a simple controller is required. Here, the torsional spring at joint 3 is used as a control input, where it is assumed that the spring is fabricated from a suitable material, such as a shape memory alloy. In order to ensure convergence to some required equilibrium point $\tilde{\theta}_3$ a Lyapunov function [66] will be defined as

$$\phi(\theta_3, \omega_3) = \frac{1}{2}\omega_3^2 + \frac{1}{2}(\theta_3 - \tilde{\theta}_3)^2 \quad (6.11)$$

where $\phi(\theta_3, \omega_3) > 0$ and $\phi(\tilde{\theta}_3, 0) = 0$. The time derivative of the Lyapunov function is then

$$\dot{\phi}(\theta_3, \omega_3) = \omega_3(\dot{\omega}_3 + (\theta_3 - \tilde{\theta}_3)) \quad (6.12)$$

Substituting from the Eq. 6.10 the controller for κ_2 can be defined as

$$\kappa_2 = -\frac{1}{\psi_3 \frac{d\psi_3}{d\theta_3}} \left(\kappa_1 \psi_2 \frac{d\psi_2}{d\theta_3} + \eta \omega_3 + (\theta_3 - \tilde{\theta}_3) \right) \quad (6.13)$$

for some control parameter η . It is noted that $\psi_3 \frac{d\psi_3}{d\theta_3} \neq 0$ in the neighbourhood of the required equilibrium point $\tilde{\theta}_3$. It can then be seen that $\dot{\phi}$ is monotonically decreasing such that

$$\dot{\phi}(\theta_3, \omega_3) = -\eta \omega_3^2 \leq 0 \quad (6.14)$$

and so $\theta_3 \rightarrow \tilde{\theta}_3$ and $\omega_3 \rightarrow 0$ within the neighbourhood of E_2 .

In order to simulate the transition from E_1 to E_2 a small perturbation of the state variable is used to begin the transition towards E_2 . The transition from E_1 to E_2 can be seen in Fig. 6.6, where the controller ensures capture and stabilisation at E_2 . The corresponding control time history is shown in Fig. 6.7, which uses κ_2 as the control with fixed κ_1 while the corresponding geometry of the transition process can be seen in Fig. 6.8. These results demonstrate that the controller can compensate for errors to generate a path between two unstable equilibrium points for this simple rigid bar system.

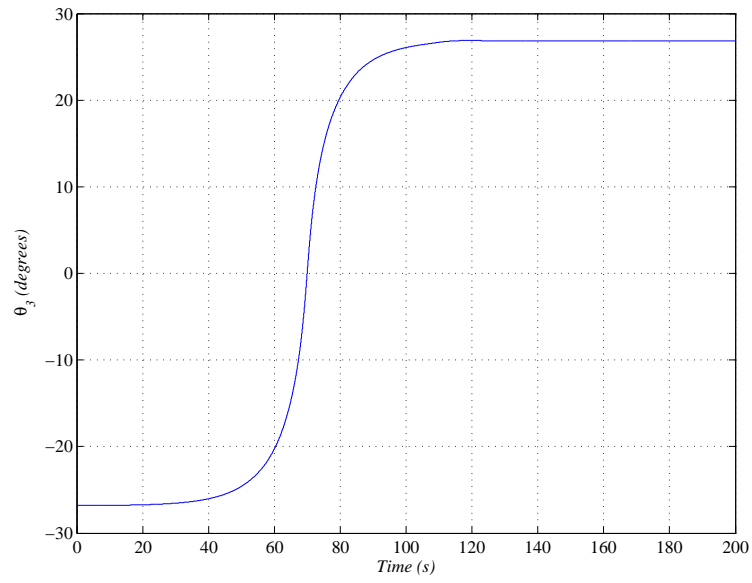


Figure 6.6: Variation of θ_3 during the transition from E_1 to E_2 .

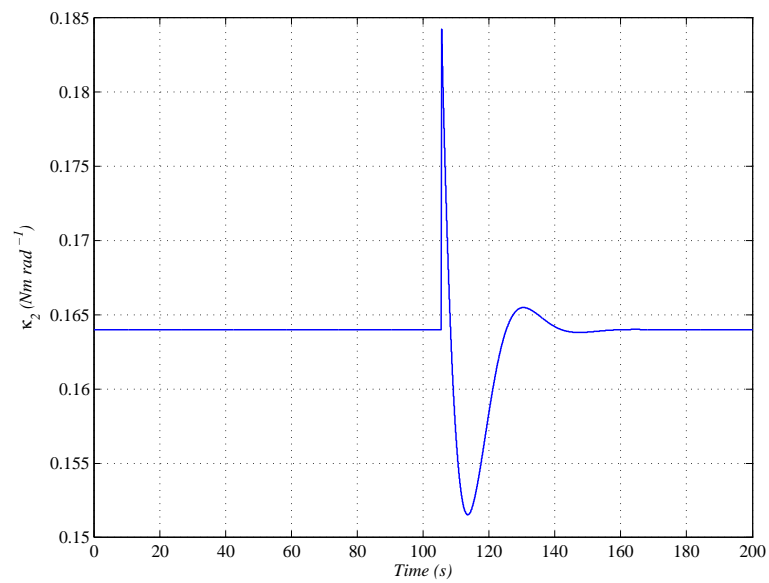


Figure 6.7: Control in the neighbourhood of E_2 actuated through the parameter κ_2 .

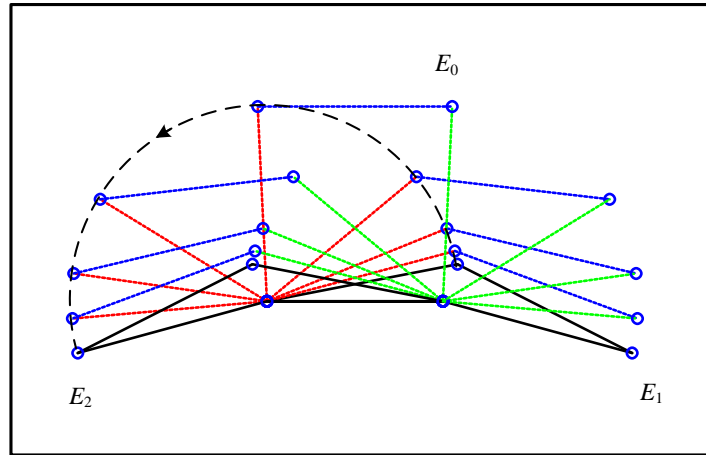


Figure 6.8: Kinematics of the transition process.

6.2 Pseudo-rigid four-bar model

Building on the rigid four-bar mechanism from Section 6.1, an approximate flexible model can now be considered to investigate the effect of elastic bars, shown in Fig. 6.9. The middle rigid bar is now substituted by an axial spring with two torsional springs now at both ends.

6.2.1 Pseudo-rigid model

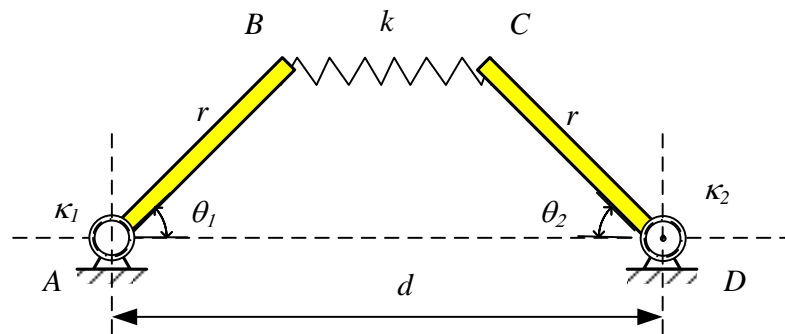


Figure 6.9: Pseudo-rigid model with a single axial spring.

Due to the elastic bar, the pseudo-rigid four-bar mechanism is now a two degree-of-freedom system. Two angles are now utilised as the state variables, and the torsional springs used as controllers. If the angles of the two rigid bars are defined by $\theta(\theta_1, \theta_2)$, while the span of the mechanism is d and the length of each rigid bar is r , as shown

in Fig. 6.9, it can be demonstrated that the axial spring has length l , which with deformation, is given by

$$l = \sqrt{(d - r(\cos \theta_1 + \cos \theta_2))^2 + (r(\sin \theta_1 - \sin \theta_2))^2} \quad (6.15)$$

First, the model is again considered to be a conservative system with the simplification that it has unit mass. The free parameters of the model are now the axial spring stiffness k and natural length l_0 , the torsional spring stiffness κ (κ_1, κ_2) and initial (undeflected) angles θ_{10} and θ_{20} . The Hamiltonian for this model can be defined from the kinetic energy and potential energy with a simplification of unit moment of inertia through Eq. 6.16 and 6.17 as

$$T(\boldsymbol{\omega}) = \frac{1}{2}\omega_1^2 + \frac{1}{2}\omega_2^2 \quad (6.16)$$

$$V(\boldsymbol{\theta}, \boldsymbol{\kappa}) = \frac{1}{2}\kappa_1(\theta_1 - \theta_{10})^2 + \frac{1}{2}\kappa_2(\theta_2 - \theta_{20})^2 + \frac{1}{2}k(l_1 - l_{10})^2 \quad (6.17)$$

with angular velocity coordinates ω_1 and ω_2 . The problem can now be fully defined by a dynamical system of the form

$$\dot{\theta}_1 = \omega_1 \quad (6.18)$$

$$\dot{\omega}_1 = -\kappa_1(\theta_1 - \theta_{10}) - k(l_1 - l_{10}) \frac{dl}{d\theta_1} \quad (6.19)$$

$$\dot{\theta}_2 = \omega_2 \quad (6.20)$$

$$\dot{\omega}_2 = -\kappa_2(\theta_2 - \theta_{20}) - k(l_1 - l_{10}) \frac{dl}{d\theta_2} \quad (6.21)$$

Here, the aim of the pseudo-rigid model is to understand how heteroclinic connections can be found for a two-degree-of-freedom system, to enable such connections to be found for the fully elastic model in Section 6.4. Therefore, in order to capture the essential dynamics of the model, but to keep the model tractable, Taylor expansions are used to substitute for trigonometric function using Eqs. 6.22 and 6.23 as

$$\sin \theta = \theta - \frac{\theta^3}{6} + o(\theta^5) \quad (6.22)$$

$$\cos \theta = 1 - \frac{\theta^2}{2} + o(\theta^4) \quad (6.23)$$

Then, dynamical system theory can be used to investigate the characteristics of this simplified smart structure model [66]. It will be shown that the system defined by Eqs. 6.18- 6.21 has a number of equilibria which are both stable and unstable and may

be connected in the phase space of the problem. Again, heteroclinic connections can be found which requires that the stable and unstable manifolds of the two unstable equilibria are connected. Solving Eqs. 6.19 and 5.21 for equilibrium conditions yields five equilibria for the parameter set, $\kappa_1 = \kappa_2 = \kappa = 1 \text{ Nm/rad}$, $d = 15 \text{ cm}$, $l_0 = 10 \text{ cm}$, $r = 5 \text{ cm}$, $k = 1 \text{ N/m}$. The location of the equilibria are listed in the Table 6.3.

Table 6.3: Equilibrium points with corresponding potential energy.

Point	$\theta_3(\text{degrees})$	$\theta_3(\text{degrees})$	V(Potential)	$D(1 \times 10^{-6})$	Type
E_0	0	0	1.25	0.9047	stable
E_1	44.38	44.38	0.8	-0.1705	unstable
E_2	-44.38	-44.38	0.8	-0.1705	unstable
E_3	-34.11	34.11	0.4278	0.3932	stable
E_4	34.11	-34.11	0.4278s	0.3932	stable

Then, the Hessian matrix of the potential energy can be used to test the linear stability properties of these equilibria. In the second derivative test for determining extrema of the potential function $V(\boldsymbol{\theta}, \boldsymbol{\kappa})$, the discriminant D is given by

$$D = \begin{bmatrix} \frac{\partial^2 V}{\partial \theta_1^2} & \frac{\partial^2 V}{\partial \theta_1 \partial \theta_2} \\ \frac{\partial^2 V}{\partial \theta_2 \partial \theta_1} & \frac{\partial^2 V}{\partial \theta_2^2} \end{bmatrix} \quad (6.24)$$

According to the second derivative test, it can be determined that the system possesses 1 unstable equilibrium point E_0 , where the potential has a global maximum, 2 unstable equilibria E_1 to E_2 where the potential has a saddle and 2 stable equilibria E_3 to E_4 where the potential has a global minimum, as can be seen in Fig. 6.10.

6.2.2 Numerical solution

In Section 5.3, heteroclinic connections were used to reconfigure a simple smart structure model between two unstable equilibria which lie on the same energy surface [60]. Therefore, integrating forwards or backwards from an unstable equilibrium point, the eigenvectors can again be mapped to approximate the stable and unstable manifolds. The initial conditions in the neighbourhood of each equilibrium point in phase space $\mathbf{z}^e = (\tilde{\boldsymbol{\theta}}, \mathbf{0})$ for forward and backward integration can be defined as Eqs. 5.33 and 5.34. where $\tilde{\boldsymbol{\theta}}$ corresponds to the location of the appropriate equilibrium point.

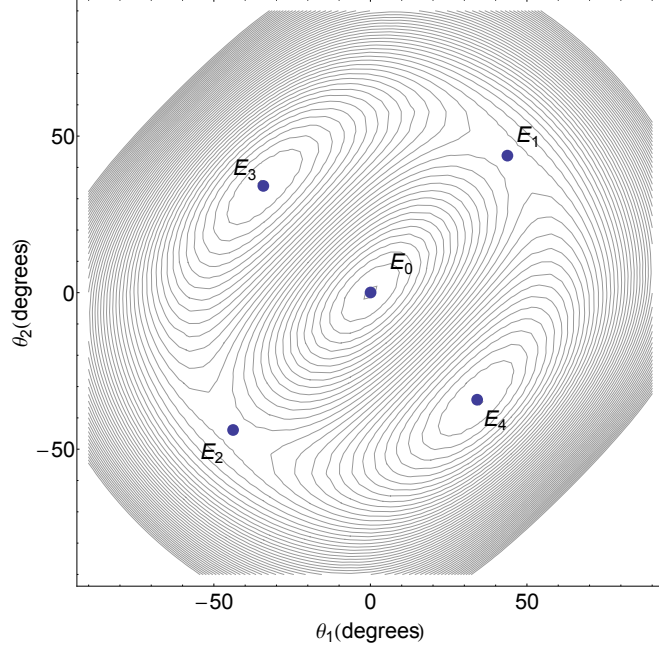


Figure 6.10: Potential $V(\theta, \kappa)$ and equilibria (3 unstable equilibria E_0, E_1 and E_2 , and 2 stable equilibria E_3 and E_4).

Due to the sensitivity of the problem, phase trajectories emerging from one unstable equilibrium point will not reach the other unstable equilibrium precisely. To compensate, the symmetry of the problem can again be used to search for an accurate heteroclinic connection. The symmetric case $\kappa_1 = \kappa_2 = \kappa$ will now be considered so that the ratio κ/k can be manipulated to find an ideal heteroclinic connection. Following [60] and considering the symmetry of the problem, a coordinate transformations can be used to rotate the coordinate axes (θ_1, θ_2) anticlockwise such that

$$\begin{pmatrix} \theta_1 \\ \theta_2 \end{pmatrix} = \frac{1}{\sqrt{2}} \begin{pmatrix} 1 & -1 \\ 1 & 1 \end{pmatrix} \begin{pmatrix} \Theta_1 \\ \Theta_2 \end{pmatrix} \quad (6.25)$$

In this new coordinate system, the equations of motion can be obtained to find a heteroclinic connection [60]. The system is now symmetric about the axes $\Theta_1 = 0$ and $\Theta_2 = 0$ and the unstable manifold of E_1 is symmetric with the stable manifold of E_2 . Therefore, a heteroclinic connection between E_1 and E_2 must be perpendicular to the $\Theta_1 = 0$ axis, which means $\dot{\Theta}_2 = 0$ (or less than some cut-off) on crossing the axis and so the heteroclinic connection will have a mirror image under $\Theta_2 \rightarrow -\Theta_2$, as shown in Fig. 6.11 and Fig. 6.12.

Numerically, it is found that for $\kappa/k < 1$, $\dot{\Theta}_2$ is sufficiently small for an approximate heteroclinic connection to exist, as shown in Fig. 6.13. Then when $\kappa/k \approx 1.7$, a hete-

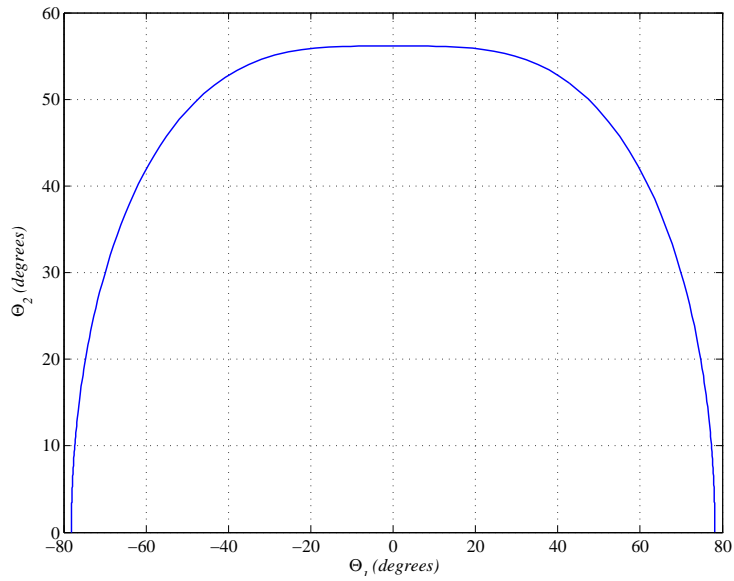


Figure 6.11: Heteroclinic connection between E_1 and E_2 with the projection of the phase space onto the configuration space shown (note the perpendicular crossing of $\Theta_1 = 0$).

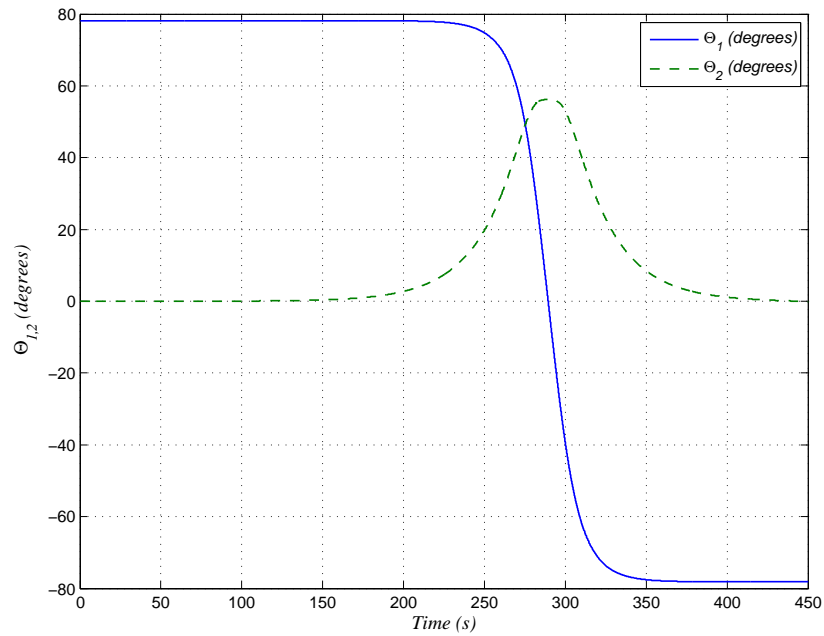


Figure 6.12: Transformed coordinates Θ_1 and Θ_2 for a heteroclinic connection between E_1 and E_2 .

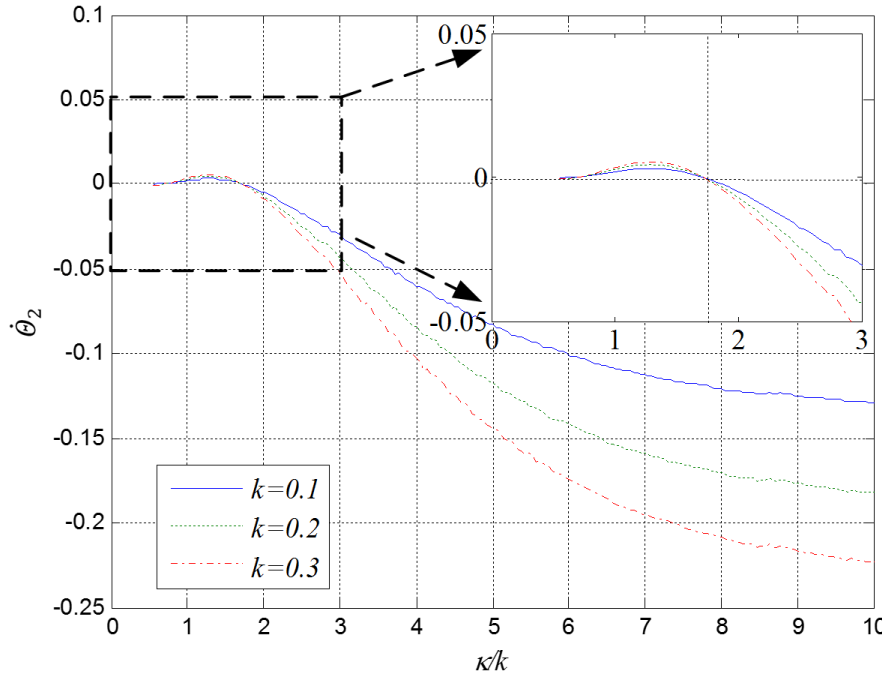


Figure 6.13: Value of $\dot{\theta}_2$ at the first crossing of the unstable manifold of E_1 with the θ_2 axis, with increasing parameter ratio κ/k .

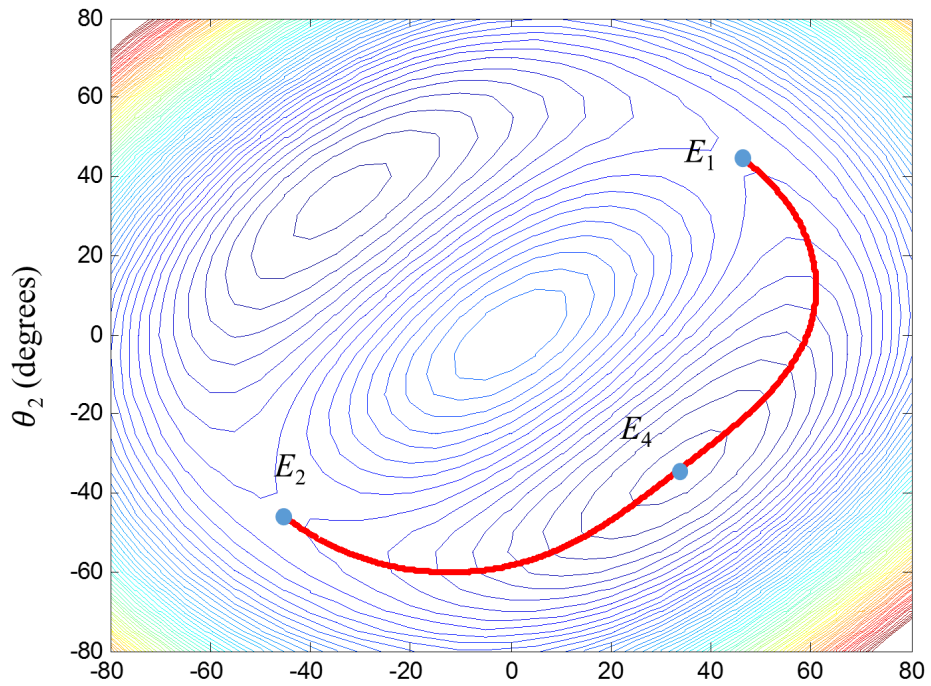


Figure 6.14: Uncontrolled heteroclinic connection between E_1 and E_2 in the original untransformed coordinate axes (θ_1, θ_2) .

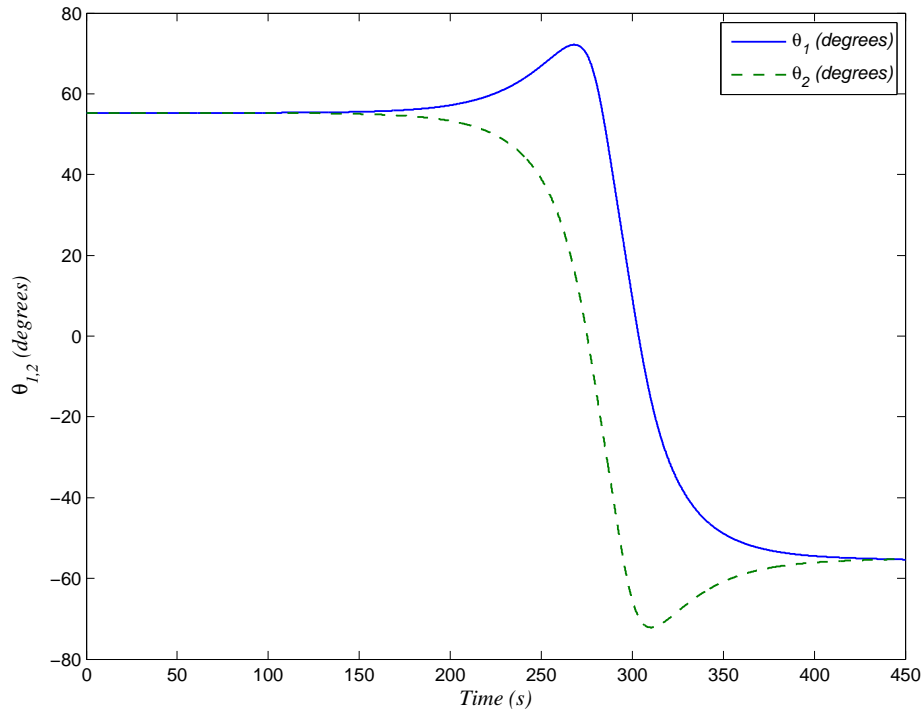


Figure 6.15: Untransformed coordinates θ_1 and θ_2 for an uncontrolled heteroclinic connection between E_1 and E_2 .

rocinic connection exists, irrespective of the value of k , as is clearly seen in Fig. 6.13. This demonstrates that for each value of k there is a value of κ which admits a heteroclinic connection. The heteroclinic connection can also be seen in Fig. 6.14 and 6.15, which is shown in the original untransformed coordinate axes (θ_1, θ_2) .

While this method is suitable for the relatively low order problem represented by the pseudo-rigid four-bar model, other methods must now be sought for the more complex fully-elastic four-bar model.

6.3 Fully-elastic four-bar model

6.3.1 Modelling and analysis

In order to further explore the possibility of reconfiguring smart structures using heteroclinic connections, a more complex fully elastic model will now be considered, building on the two-degree-of-freedom model in Section 6.2. A buckled beam is now assumed to be divided into three linear axial springs with unit mass and four torsional springs considered, as shown in Fig. 6.16. While this represents a fully elastic model of the four-

bar mechanism, it also clearly represents an approximate model of a buckling beam. It has been shown that the former model in Section 6.3 admits families of heteroclinic connections in the phase space of the problem. This more complex problem greatly increases the number of equilibria in the system and the difficulty of finding all exact equilibria by purely numerical means. Only a subset of the large number of equilibria will therefore be used to illustrate the properties of the system and seek heteroclinic connections between two unstable equilibria.

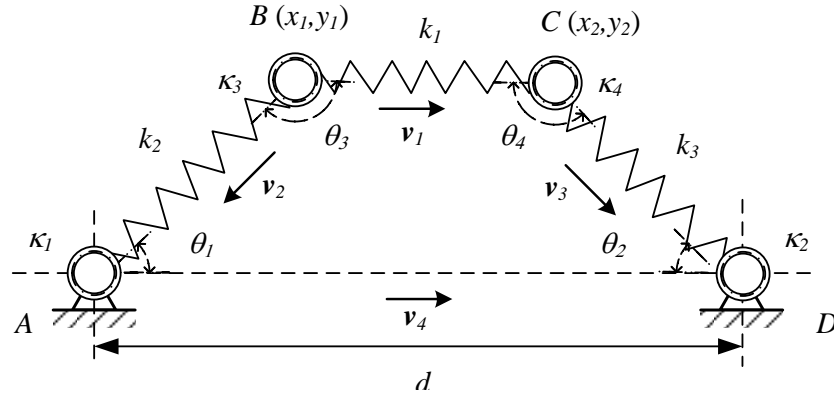


Figure 6.16: Fully elastic four-bar mechanism/buckling beam model.

In Fig. 6.16, the distance between two ends of the structure is denoted by d . The length of the three springs are denoted by l_1 , l_2 and l_3 with corresponding stiffness k_1 , k_2 and k_3 respectively. Considering each of these springs as links, θ_1 and θ_2 are the angles of spring 2 and spring 3 with respect to the horizontal with torsional stiffness κ_1 and κ_2 . Finally, θ_3 and θ_4 are the angles of spring 2 and spring 3 with respect to spring 1 with torsional stiffness κ_3 and κ_4 . This new model of a flexible four-bar link is a four degree-of-freedom system with two constrained points B (x_1, y_1) and C (x_2, y_2) , with A the origin. The angles can therefore be defined as

$$\theta_1 = \tan^{-1} \frac{y_1}{x_1} \quad (6.26)$$

$$\theta_2 = \tan^{-1} \frac{y_2}{d - x_2} \quad (6.27)$$

$$\theta_3 = \cos^{-1}(\vec{v}_1, \vec{v}_2) \quad (6.28)$$

$$\theta_4 = \cos^{-1}(-\vec{v}_1, \vec{v}_3) \quad (6.29)$$

where \vec{v}_1 , \vec{v}_2 and \vec{v}_3 denote the axial direction vectors of the springs, as shown in

Fig. 6.16. The deformation of the springs can therefore be defined as

$$\Delta l_1 = |\vec{v}_1| - l_1 \quad (6.30)$$

$$\Delta l_2 = |\vec{v}_2| - l_2 \quad (6.31)$$

$$\Delta l_3 = |\vec{v}_3| - l_3 \quad (6.32)$$

Again, this fully elastic model is considered to be a conservative system. The potential energy can then be defined as

$$V = \frac{1}{2}\kappa_1\theta_1^2 + \frac{1}{2}\kappa_2\theta_2^2 + \frac{1}{2}\kappa_3\theta_3^2 + \frac{1}{2}\kappa_4\theta_4^2 + \frac{1}{2}k_1\Delta l_1^2 + \frac{1}{2}k_2\Delta l_2^2 + \frac{1}{2}k_3\Delta l_3^3 \quad (6.33)$$

where κ is the torsional spring constant and k is the axial spring constant.

Established methods can now be employed to select the appropriate spring constants for the model using geometric and material parameters, according to the following [81]

$$\kappa = \frac{2EI}{l_{eff}} \quad (6.34)$$

$$k = \frac{CAE}{l} \quad (6.35)$$

where E is the equivalent elastic modulus, I is the equivalent cross-sectional moment of area, l_{eff} is an effective length, A is the equivalent cross-sectional area and l is length of the axial spring. Equations 6.34 and 6.35 present a direct relationship between the basic material parameters of a continuous beam and the model parameters so that it is possible to construct a practical purely elastic model with actual material parameters. The potential energy can then be defined as a function of E and l_{eff} as

$$V = f(E, l_{eff}, l) \quad (6.36)$$

for some functional relationship f . Equation 6.36 provides a relationship between the potential energy and basic material properties, so that these parameters can be selected to construct a reasonable fully elastic model as described in Section 6.3.2 below.

6.3.2 Euler-Bernoulli beam model

The Euler-Bernoulli equations for an elastic buckled beam are now used to evaluate the spring model discussed above. It is known that the first and second buckling shapes are given by

$$y_1 = a_1 \left(1 - \cos \left(2\pi \frac{x}{L} \right) \right) \quad (6.37)$$

and

$$y_2 = a_2 \left(1 - \cos \left(2\pi \frac{x}{L} - \cos \left(N \frac{x}{L} \right) + \frac{2}{N} \sin \left(N \frac{x}{L} \right) \right) \right) \quad (6.38)$$

respectively, where N is the first positive solution to $\tan(N/2) = N/2$ and a_1 and a_2 are constants which can be determined through the method discussed in [82]. Note that here the y is the displacement of a beam element from the x -axis.

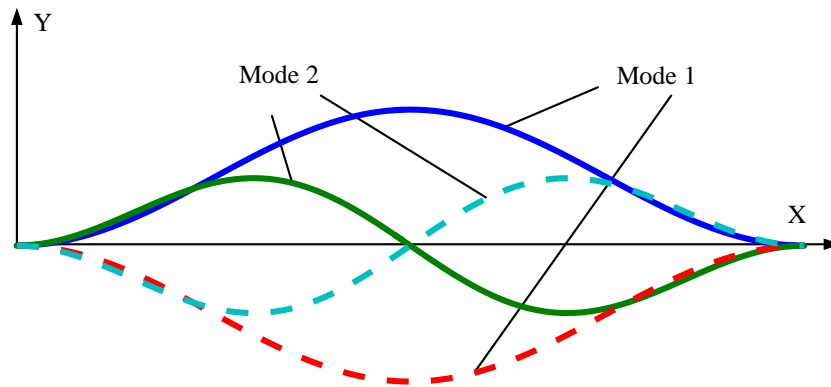


Figure 6.17: Buckling modes of a clamped-clamped buckling beam.

Although more mode shapes could be used, the first two buckling modes provide a good approximation. Figure 6.17 depicts the first two modes of the buckled beam for each model shape corresponding to positive (solid line) and negative (dash line) values of a_1 and a_2 .

The Euler-Bernoulli can now be used to optimise the selection of the free parameters of the model to best represent a true buckling beam.

6.3.3 Energy analysis

The deformation energy of the beam will now be used to compare the approximation between the Euler-Bernoulli beam model with the elastic beam model of Section 6.2.1. This deformation energy is defined in Cartesian coordinates and includes two parts, the bending energy and the compression energy. The bending energy of the Euler-Bernoulli beam is defined by [83]

$$U_b \simeq \frac{EI}{2} \int_0^L y''(x)^2 dx \quad (6.39)$$

where I is the area moment of area of the beam, L is the compressed beam length (distance between clamping points), E is the modulus of elasticity, x is the horizontal axis distance along the beam and y is the beam vertical displacement, shown in Fig 6.17.

The compressive energy in the beam can be calculated directly from Hooke's Law as [83]

$$U_c = \frac{AE \left[(L - L_0) + \int_0^L y'(x)^2 dx \right]^2}{8L_0^2} \quad (6.40)$$

where A is the cross-sectional area of the beam and L_0 is the undeformed beam length.

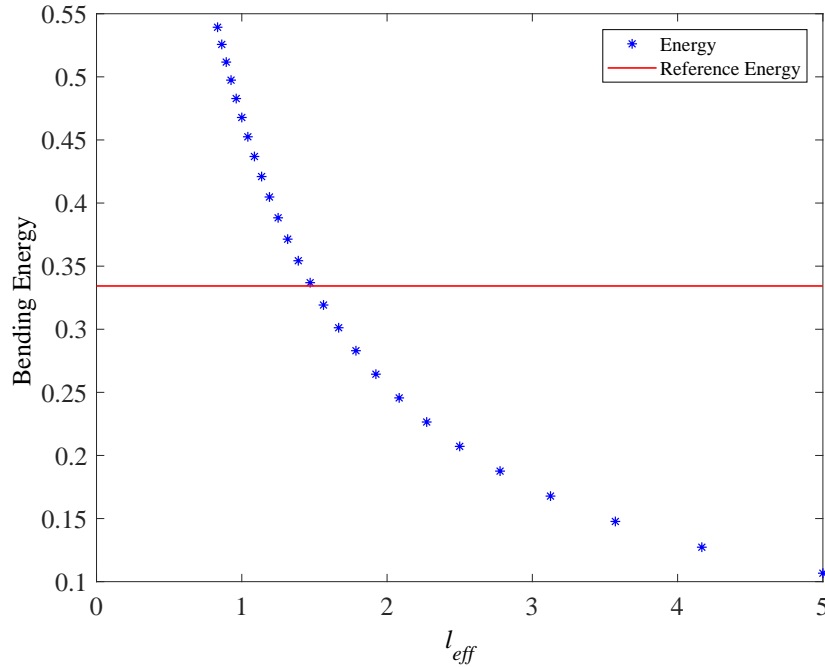


Figure 6.18: Buckling modes of a clamped-clamped buckling beam.

Returning to Eq. 6.34, a more accurate elastic spring model can be sought through comparison with the Euler-Bernoulli model. Therefore, the purely elastic model can be modified by changing the effective length l_{eff} to match the potential energy which is calculated in the Euler-Bernoulli model. Figure 6.18 depicts the bending energy with increasing effective length, while the red line is the energy of the first mode of the Euler beam model. From Fig. 6.18, the approximate value of the effective length can be selected as 1.7, which will be used to define a modified fully elastic model.

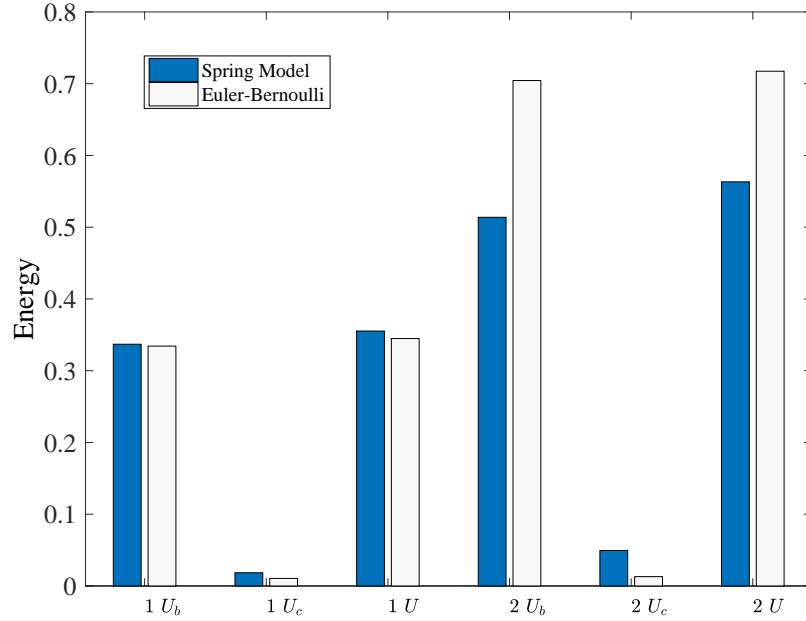


Figure 6.19: Energy comparison between the fully elastic spring model and Euler-Bernoulli beam model for first 2 modes. U_b is the bending energy, U_c is the compressive energy, $U = U_b + U_c$.

The comparison between the elastic spring model and the Euler-Bernoulli is shown in Fig. 6.19 for the energy of each mode, where it can be seen that the first mode error is smaller than the second mode error. The deformation energy error of the first mode is approximately 3%, while the deformation energy error of second mode is approximately 17%. Therefore, the fully elastic spring model can be considered as a simplified model for a continuous beam and as a relatively accurate approximation.

6.3.4 Numerical validation

In order to explore the possibility of reconfiguring this new model, dynamical system theory can again be used to investigate its characteristics. Firstly, the model is again considered to be a conservative system with the assumption of unit mass. From Fig. 6.19, the Hamiltonian for this two mass model can then be defined from the kinetic

and potential energy through Eqs. 6.41 and 6.42 as

$$T(\mathbf{p}) = \frac{1}{2}(\dot{x}_1)^2 + \frac{1}{2}(\dot{x}_2)^2 + \frac{1}{2}(\dot{y}_1)^2 + \frac{1}{2}(\dot{y}_2)^2 \quad (6.41)$$

$$V(\mathbf{x}, \mathbf{L}) = \frac{1}{2} \begin{bmatrix} \kappa_1 & \kappa_2 & \kappa_3 & \kappa_4 \end{bmatrix} \begin{bmatrix} \theta_1^2 \\ \theta_2^2 \\ \theta_3^2 \\ \theta_4^2 \end{bmatrix} + \frac{1}{2} \begin{bmatrix} k_1 & k_2 & k_3 \end{bmatrix} \begin{bmatrix} l_1^2 \\ l_2^2 \\ l_3^2 \end{bmatrix} = h(x_1, x_2, y_1, y_2) \quad (6.42)$$

Now the system can be described by a Hamiltonian $H(\mathbf{x}, \mathbf{p}, \mathbf{L}) = T(\mathbf{p}) + V(\mathbf{x}, \mathbf{L})$ with the set $\mathbf{x} = \{x_1, x_2, y_1, y_2\}$ and the corresponding set of momenta $\mathbf{p} = \{p_1, p_2, p_3, p_4\}$. We can now fully define the problem by a dynamical system of the form

$$\dot{\mathbf{x}} = \mathbf{p} \quad (6.43)$$

$$\dot{\mathbf{p}} = \mathbf{g}(x_1, x_2, y_1, y_2) \quad (6.44)$$

with momentum coordinates \mathbf{p} and for some functional relationship \mathbf{g} . It will be shown that the system defined by Eqs. 6.43 and 6.44 again has a large number of equilibria which are both stable and unstable and may be connected in the phase space of the problem. Although there are many equilibria in the system, considering the complexity of the problem (with trigonometric functions), it is difficult to locate all of the equilibria. Therefore an optimisation function *fmincon* in Matlab is now used to find some typical equilibria which are denoted as equivalent to the first mode and second mode of an Euler-Bernoulli beam, as shown in Fig. 6.20.

Linearisation of Hamilton's equations in the neighbourhood of each equilibrium point can now be used to determine the linear stability of these equilibria according to their eigenvalues λ_j ($j = 1 - 8$). A set of stable equilibria are expected with conjugate imaginary eigenvalues and a set of unstable equilibria are expected with real eigenvalues of opposite sign [66]. The corresponding parameters can be seen from Table 6.4 where E_0 is an unstable equilibrium, where the potential has a global maximum; E_1 and E_2 are stable equilibria, where the potential has a local minimum; E_3 and E_4 are unstable equilibria, where the potential has saddles.

Since the Hamiltonian of the system is constant, and formed by the potential and kinetic energy V and T , the volume of phase space in \mathbb{R}^8 , and its projection to the configuration space in \mathbb{R}^4 , is constrained by the requirement that $T(\mathbf{p}) > 0$. Since the unstable equilibria E_3 and E_4 lie on the same energy surface, it can be assumed that in

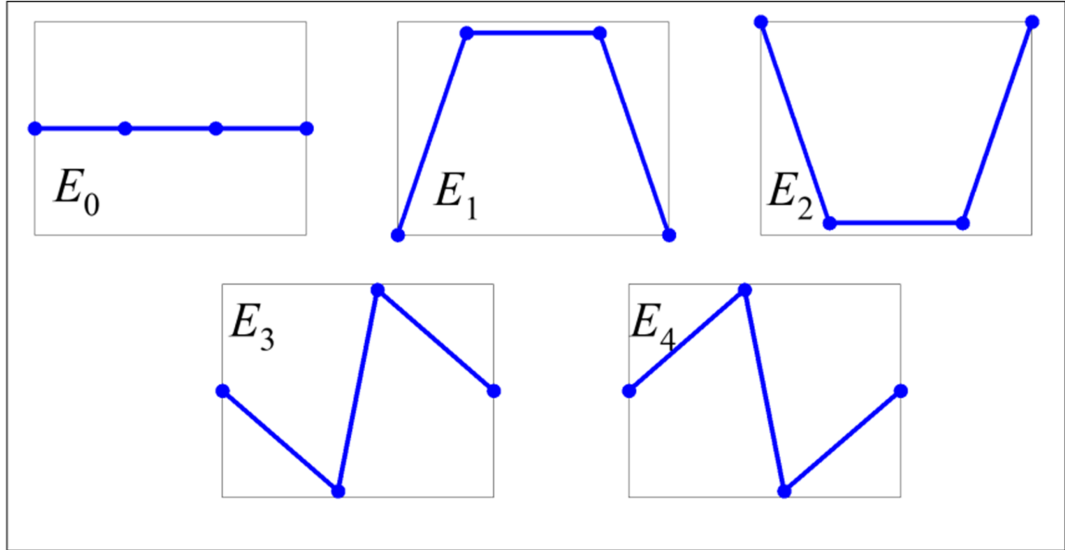


Figure 6.20: Corresponding shape of fully elastic model in equilibrium positions.

principle a heteroclinic connection between these two equilibria may exist so that the structure can be reconfigured between them without work being done. Again in the absence of dissipation, the change in energy for the reconfiguration $\delta V \approx 0$.

Table 6.4: Stability properties of the 5 equilibria of the fully elastic model.

Point	E_0	E_1	E_2	E_3	E_4
x_1	3.33	2.64	2.64	4.07	4.07
x_2	0	4.07	-4.07	-2.20	2.20
y_1	6.67	7.36	7.36	5.93	5.93
y_2	0	4.07	-4.07	2.20	-2.20
$\lambda_{1,2}$	$\pm 0.95i$	$\pm 0.86i$	$\pm 0.86i$	$\pm 0.77i$	$\pm 0.77i$
$\lambda_{3,4}$	$\pm 0.55i$	$\pm 0.54i$	$\pm 0.54i$	$\pm 0.55i$	$\pm 0.55i$
$\lambda_{5,6}$	± 0.54	$\pm 0.14i$	$\pm 0.14i$	$\pm 0.55i$	$\pm 0.55i$
$\lambda_{7,8}$	± 0.35	$\pm 0.40i$	$\pm 0.40i$	± 0.096	± 0.096
V	1.25	0.36	0.36	0.56	0.56
<i>Type</i>	Saddle	Min	Min	Saddle	Max

The system is strongly nonlinear so that it is difficult to find heteroclinic connections using the direct method presented in Section 6.2.2. Therefore, an optimisation method is employed to find a suitable parameter set. An objective function is constructed in Eq. 6.45, the minimisation of which provides the requirement for a heteroclinic connection.

$$F = (\dot{y}_1 + \dot{y}_2)^2 + ((\dot{x}_1, \dot{x}_2) \cdot (x_1 - x_{10}, x_2 - x_{20}))^2 \quad (6.45)$$

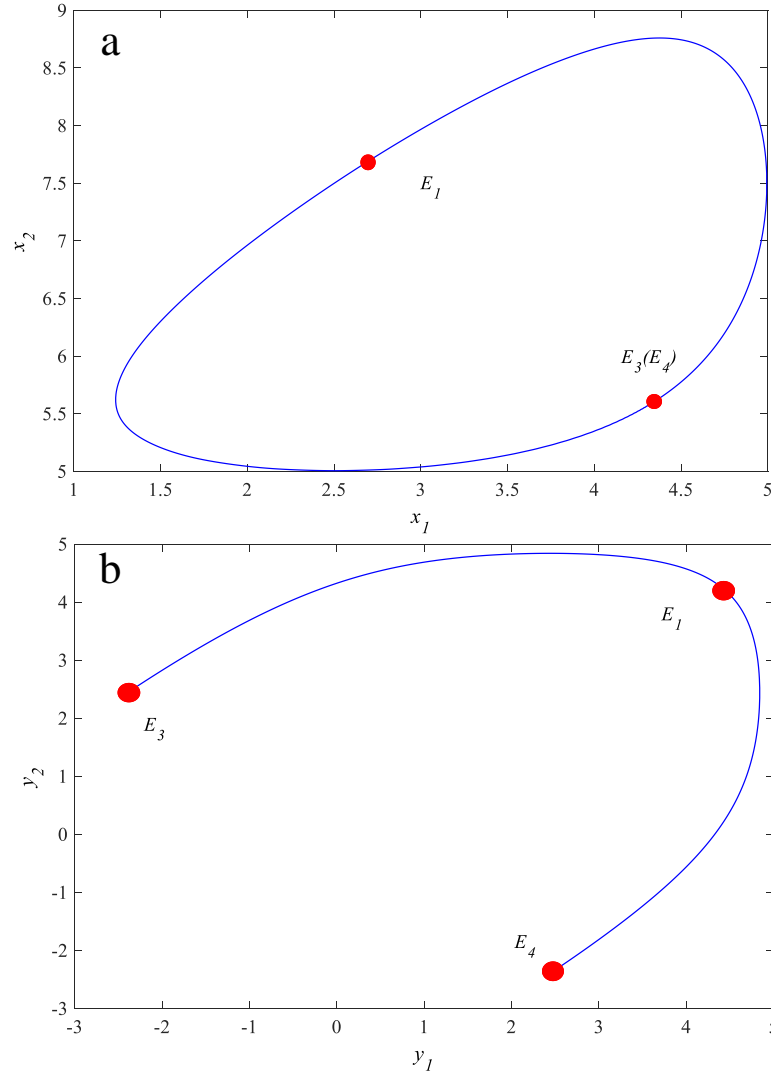


Figure 6.21: Controlled transition from E_3 to E_4 with the controller active in the neighbourhood of E_4 (a) Homoclinic connection in the $x_1 - x_2$ coordinate space (b) Heteroclinic connection in the $y_1 - y_2$ coordinate space.

Therefore, for a heteroclinic connection between E_3 and E_4 , if one exists, the symmetry property requires that Eq. 6.45 vanishes. The system of equations is integrated in the direction of the unstable eigenvector of E_3 as in Eq. 6.24, until it intersects the symmetry axis $y_1 - y_2 = 0$, i.e. $y_1 = y_2$, and the six states \dot{x}_1 , \dot{x}_2 , \dot{y}_1 , \dot{y}_2 , x_1 , x_2 are measured. Through substitution of these values into Eq. 6.45, the value of the objective function can be calculated. Then, the condition $(\dot{y}_1 + \dot{y}_2) = 0$ guarantees that the trajectory is perpendicular to the symmetry axis $y_1 - y_2$, and $((\dot{x}_1, \dot{x}_2) \cdot (x_1 -$

$x_{10}, x_2 - x_{20}$)) expresses the dot product of two vectors that ensure the projection of the heteroclinic connection is symmetric in $x_1 - x_2$.

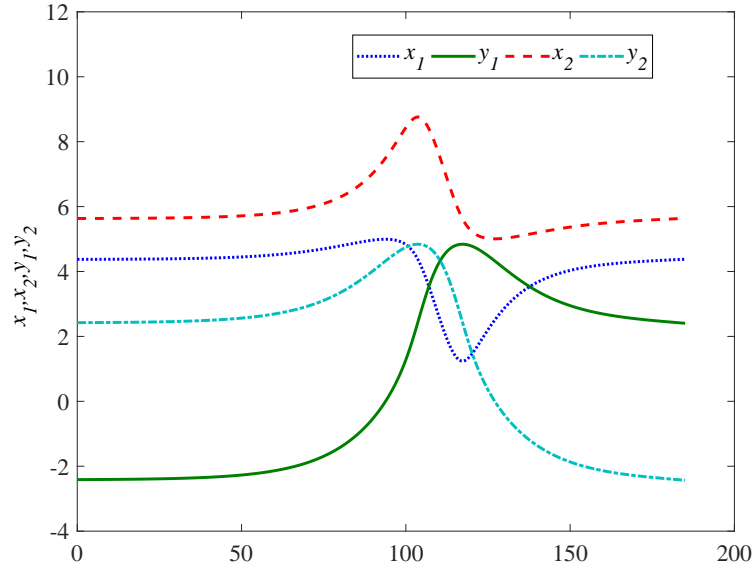


Figure 6.22: Displacements during the transition from E_3 to E_4 .

Again, due to the sensitivity of the problem, phase trajectories emerging from one unstable equilibrium point will not reach the other unstable equilibrium precisely, which means Eq. 6.45 cannot obtain a precise set of parameters using the optimisation method. To compensate for such errors, the active control method which was used in Section 6.2 is again used to capture phase space trajectories in a neighbourhood of the target unstable equilibrium point. The transition from E_3 to E_4 can be seen in Fig. 6.21, where the controller ensures capture and stabilisation at E_4 . The connection in the coordinate space $x_1 - x_2$ can be seen as a homoclinic connection, and in the coordinate space $y_1 - y_2$ can be seen as a heteroclinic connection. The transition can also be seen in Fig. 6.22, which provides the time history of the four state variables. The corresponding controls κ_1, κ_2, k_1 and k_2 are shown in Fig. 6.23. Figure 6.24 shows the geometry of the transition process. The closed dotted line indicates the midpoint of the transition.

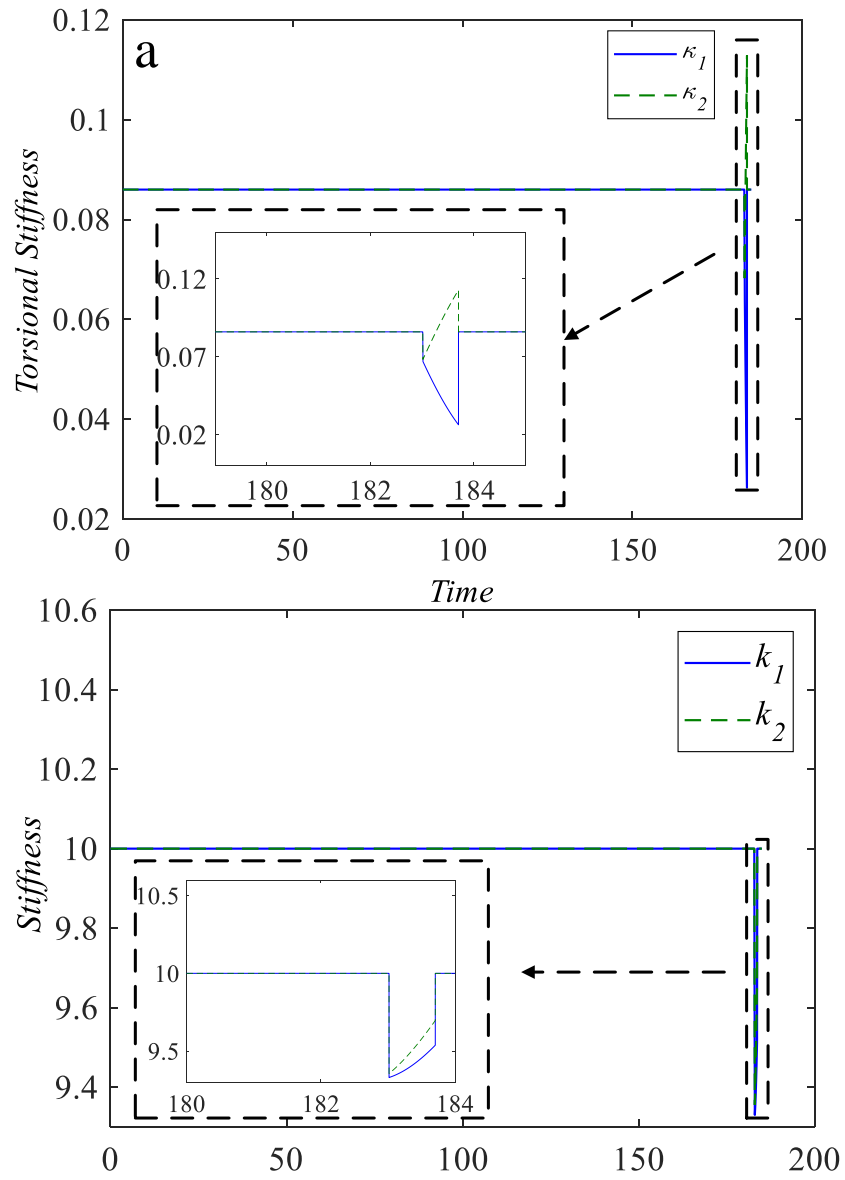


Figure 6.23: Controls actuated at the end of the transition (a) torsional spring stiffness (b) axial spring stiffness.

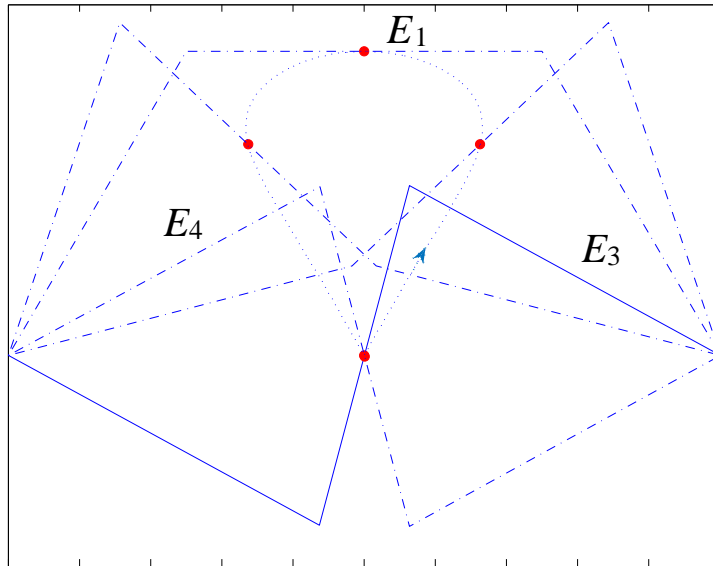


Figure 6.24: Geometry of the transition process where the red point is the mid-point of the structure, which has a trajectory shown as a dashed line.

6.4 Conclusion

Using the kinematic theory of mechanisms, an analysis has firstly been presented regarding the reconfiguration of a simple four-bar linkage through heteroclinic connections. Then, a pseudo-rigid model was developed as an unstable structure which has several equilibria (stable and unstable), again with heteroclinic connections found. In principle, such reconfigurations do not require the input of energy, unlike transitions between stable equilibria which require the addition of and dissipation of energy. Finally, the reconfiguration method has been used to investigate the behaviour of a more realistic elastic smart structure model. By comparing the deformation energy of the elastic spring model and a truly continuous model, it can be verified that the spring model can provide a good approximation to a buckling beam. This more complex dynamical model, which has strong nonlinearity, can again be reconfigured through transitions between unstable equilibria.

Chapter 7

Continuous Beam Model and Experiment Validation

In previous Chapters, a series of spring mass models have been used to investigate a simple smart structure, varying from a buckled beam to a surface structure. Dynamical system theory was used to investigate the characteristics of these models and identified a set of unstable equilibria. Some of these can be connected with heteroclinic paths in phase space to achieve an energy efficient reconfiguration strategy for smart structures.

In this Chapter, a classical clamped-clamped continuous beam is firstly investigated based on Euler-Bernoulli beam theory. The mechanics and deflection of a deformable body are formulated in Section 7.2 and two different expressions are obtained for different model description (Eulerian description and Lagrangian description). In Section 7.3, the classical clamped-clamped beam is investigated to be reconfigured between two unstable buckled states by using a heteroclinic connection. Both numerical simulation and preliminary experimental demonstration have been used to verify this concept.

7.1 Nondimensional buckling problem

Based on the analysis in [84], a beam is considered here as clamped-clamped without an external force so that the equation of motion can therefore written as

$$\ddot{w} + w^{iv} + Pw'' + c\dot{w} - \frac{1}{2} \int_0^1 w'^2 dx = 0 \quad (7.1)$$

$$w = 0 \quad \text{and} \quad w' = 0 \quad \text{at} \quad x = 0, 1. \quad (7.2)$$

where the overdot indicates the derivative with respect to time t , the prime indicates the derivative with the respect to x , and

$$P = \frac{\hat{P}L^2}{EI} \quad \text{and} \quad c = \frac{\hat{c}L^2}{\sqrt{mEI}} \quad (7.3)$$

are nondimensional quantities.

The buckling problem can be obtained from Eq. 7.1 by dropping the time derivatives and denoting the buckled configuration by $\psi(x)$. The result is

$$\psi^{iv} + (P - \frac{1}{2} \int_0^1 \psi'^2 dx) \psi'' = \psi^{iv} + (P - \Gamma) \psi'' = \psi^{iv} + \lambda^2 \psi'' dx = 0 \quad (7.4)$$

$$\psi = 0 \quad \text{and} \quad \psi' = 0 \quad \text{at} \quad x = 0, 1. \quad (7.5)$$

and the corresponding buckled mode shapes $\psi(x)$ are given by

$$\psi(x) = c \left[1 - \frac{\lambda(1 - \cos \lambda)}{\lambda + \sin \lambda} x - \cos \lambda x + \frac{1 - \cos \lambda}{\lambda + \sin \lambda} \sin \lambda x \right] \quad (7.6)$$

where c is a constant to be determined. The expression for $\psi(x)$ governs both symmetric and antisymmetric buckling shapes.

However, while the buckled configuration $\psi(x)$ satisfies the boundary conditions, there is a condition that has not yet been satisfied, that is

$$\lambda^2 = P - \Gamma = P - \frac{1}{2} \int_0^1 \psi'^2 dx = 0 \quad (7.7)$$

Substituting Eq. 7.6 into Eq. 7.7 which is described in Appendix A, it can be shown that

$$\lambda^2 = P - \frac{1}{4} c^2 \lambda^2 \quad \text{or} \quad c = \pm 2 \sqrt{\frac{P}{\lambda^2} - 1} \quad (7.8)$$

Thus, for a given axial load P the constant c corresponding to any eigenvalue λ can be determined, and its corresponding buckled shape can then be obtained.

7.2 Numerical simulation and experimental validation

A typical bistable structure is a clamped-clamped elastic buckled beam. The buckling loads can be linearised by Eq 7.8 and combined with Eq 7.3. The first critical load

($\lambda = 2\pi$) according to the first beam buckling mode is [85]

$$P_{cr}^{(1)} = \frac{4\pi^2 EI}{l_0^2} \quad (7.9)$$

where again E is Young's modulus, I is the moment of area of the cross-section and l_0 is the initial length of the beam. The second buckling critical load ($\lambda = 8.9868$) is greater than the first, according to the second beam buckling mode

$$P_{cr}^{(2)} = \frac{8.18\pi^2 EI}{l_0^2} \quad (7.10)$$

The stability of these buckled configurations can be investigated through an analytical method [85] and the result shows that the first buckled configuration is a stable equilibrium position while the second buckled configuration is unstable. The buckled beam has the ability to snap from one stable state to the other when excited with sufficient input actuation. However, for frequently switched devices the accumulated work done will be significant in reconfiguring between stable equilibria. The intention in this section is to present this concept with a numerical simulation and experimental demonstration which are based on the previous simulation results [60, 64, 72]. This Section introduces Shape memory alloy wires in a buckled acrylic beam to enhance the instability and active reconfiguration, as shown in Fig 7.1.

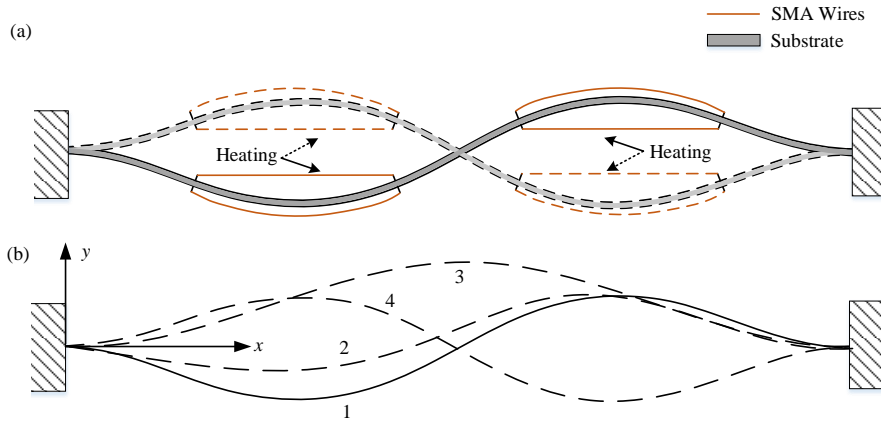


Figure 7.1: The buckled beam model (a) schematic of an unstable buckled-beam (b) different stage (1-2-3-4) during the reconfigure through.

The SMA wires are fixed at both ends through pin-joints on the beam. The heating method is based on the Joule effects of SMA wire under an electrical current during the experiment. Separate electric circuits are connected to each SMA wires and controlled

by an external switch. Numerical simulation results are shown in Fig. 7.2 based on the governing equation of Eq. 7.1, with nondimensional quantities. According to the analytical results of the buckling problem, the corresponding first and second buckling mode shapes are given by Eq. 7.6. Then, in order to verify the heteroclinic connection between the unstable buckling configuration, one of the second buckling modes is used as the initial condition with a small perturbation used to solve the governing equation Eq. 7.1 by simply omitting the nonlinear terms $\frac{1}{2} \int_0^1 w'^2 dx$ and the damping term $c\dot{w}$. The open-source package Chebfun [86] is used to obtain a numerical solution, which is shown in Fig. 7.2.

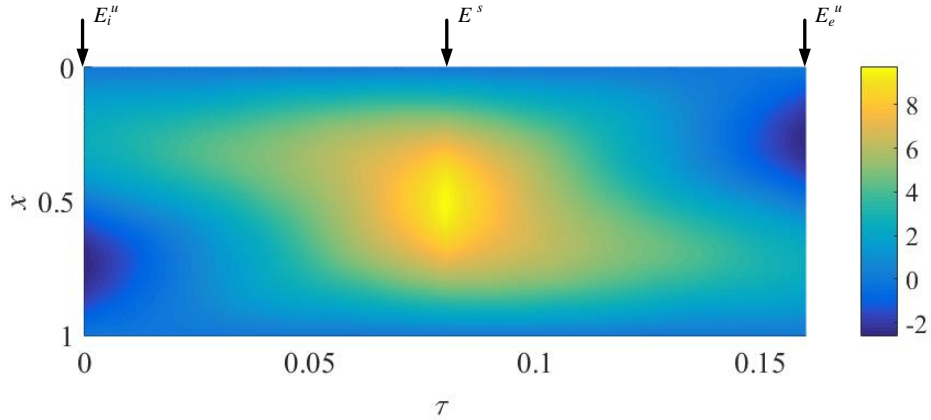


Figure 7.2: Simulation result of the deflection history during reconfiguration. τ is the nondimensional time. E_i^u , E^s and E_e^u are the initial unstable configuration, the in-between stable configuration and the terminal unstable configuration, respectively.

Figure 7.2 shows the deflection of the buckled beam during reconfiguration between two unstable buckling modes (E_i^u, E_e^u), where the transition goes through a stable mode (E^s). Given that the system is formed by partial differential equations, it is hard to establish a phase space as with ordinary differential equations. Therefore, the deflection of some key points on the beam can be considered to construct the phase space, which can show a continuous trajectory with time. In order to understand the heteroclinic connection in this system of partial differential equations, the position of extremum deflection w_1 and w_2 of the beam shape can be used as the coordinates to form a projection of the phase space. The two points firstly transfer to the midpoint then part in opposite directions, which can be regarded as a trajectory departing from one unstable equilibrium E_i^u to another unstable equilibrium E_e^u by crossing a stable equilibrium E^s , as shown in Fig. 7.3.

In order to explore such transition in a real beam, two types of beam prototypes were

Table 7.1: Geometry property of the proposed beam.

Description	Value (mm)
Substrate Beam length	400
Substrate Beam width	25
Substrate Beam thickness	2
Test Beam length	100
Test Beam width	25
Test Beam thickness	2

fabricated using acrylic with their geometrical properties listed in Table 7.1. The test beam is used to measure the Young's modulus of the material, which can be obtained by the basic constitutive relation

$$E = \sigma/\varepsilon = (\Delta F/(d \cdot t))/(\Delta s/l_0) \quad (7.11)$$

where σ is the stress, ε is the strain, d is the width, t is the beam thickness and l_0 is the initial length of the beam. ΔF and Δs are the load and displacement measured by the testing machine. The result is shown in Fig. 7.4, where tension and compression are tested respectively, and elastic deformation used to calculate Young's modulus. Therefore, the first critical load and the second critical load can be obtained.

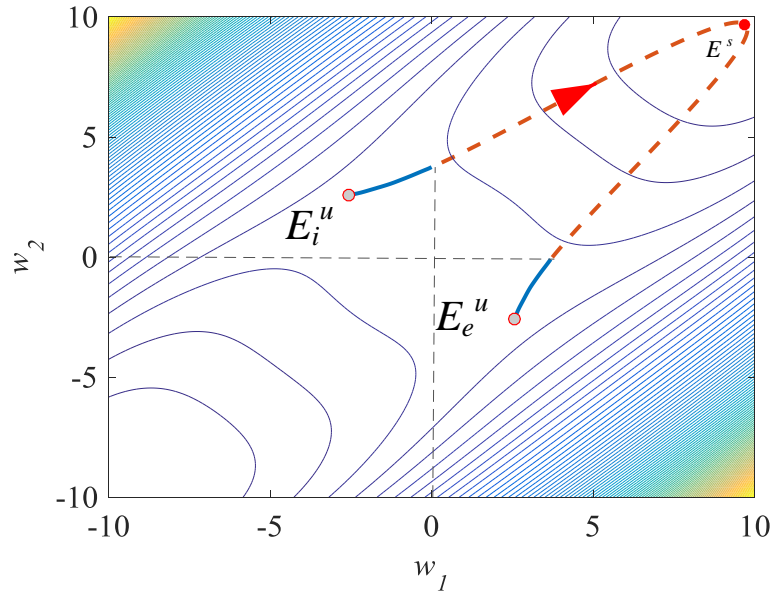


Figure 7.3: The schematic diagram of the heteroclinic connection between two distant equilibria E_i^u and E_e^u in the assumed phase space. w_1 and w_2 are the two extremum of deflection during reconfiguration.

Then, the thermo-mechanical properties of the SMA are reported in Table 7.2. The typical stress-strain-temperature behaviour of SMA was tested under different temperatures in a temperature-controlled cabinet, which is shown in Fig. 7.5.

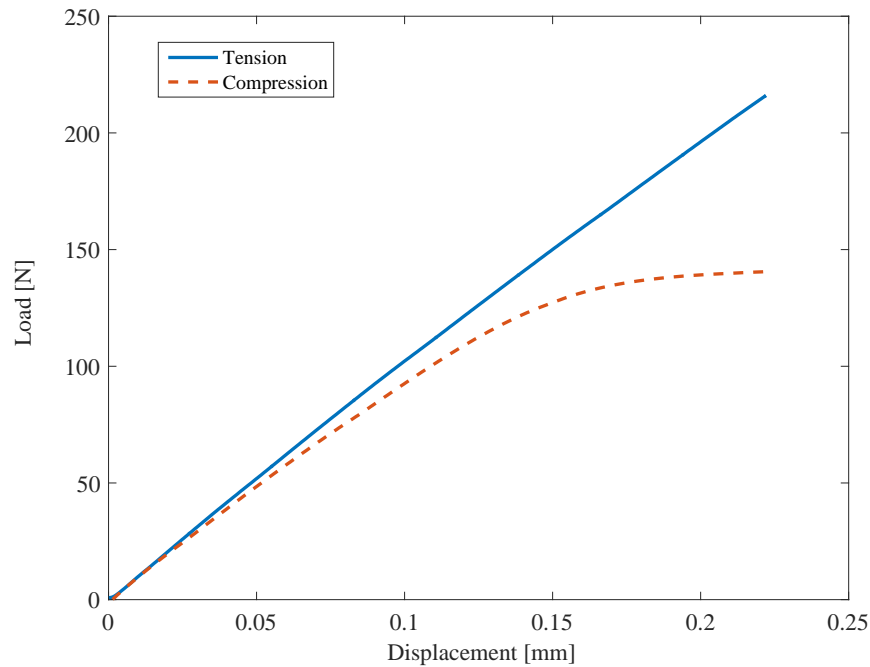


Figure 7.4: Resulting load-displacement curve of a test beam.

Two unique properties of the SMA are made possible through a solid state phase change in molecular rearrangement, which occurs in the SMA. The thermo-mechanical properties of SMA are due to a crystallographic phase transformation from a body-centered cubic structure (austenite, the stronger phase of shape memory alloys, which occurs at higher temperatures) to a face-centered cubic structure (martensite, is the relatively soft and easily deformed phase of shape memory alloys, which exists at lower temperatures), or vice versa. The un-deformed austenite phase has the same size and shape as the cubic austenite phase on a macroscopic scale so that no change is visible in the size or shape of SMA until the martensite is deformed.

Moreover, the super-elastic effect is the property such that when mechanically loaded, the material deforms reversibly to very high strains (up to 10%). Once the load is removed, the material regains its original shape. This is exhibited when the austenite temperature of the SMA is lower than the environment temperature, as shown in Fig. 7.5.

Meanwhile, the shape memory effect is another property of SMAs, which can be observed when the temperature is cooled to below the martensite temperature M_f . At

Table 7.2: Selected SMA materials properties.

Description	Value
Diameter, d [mm]	0.5
Martensite Young's modulus, E_M [GPa]	22
Austenite Young's modulus, E_A [GPa]	50.3
Martensite start temperature, M_s [C]	18.4
Martensite finish temperature, M_f [C]	9
Austenite start temperature, A_s [C]	32
Austenite finish temperature, A_f [C]	42
Critical stress de-twinned martensite start [MPa]	100
Critical stress de-twinned martensite finish [MPa]	170
Thermal expansion coefficient Θ [MPa/C]	0.55
Variation of austenite critical temperature C_A with stress [MPa/C]	13.8
Variation of martensite critical temperature C_M with stress [MPa/C]	8
Limit Strain ε_L [%]	7.2

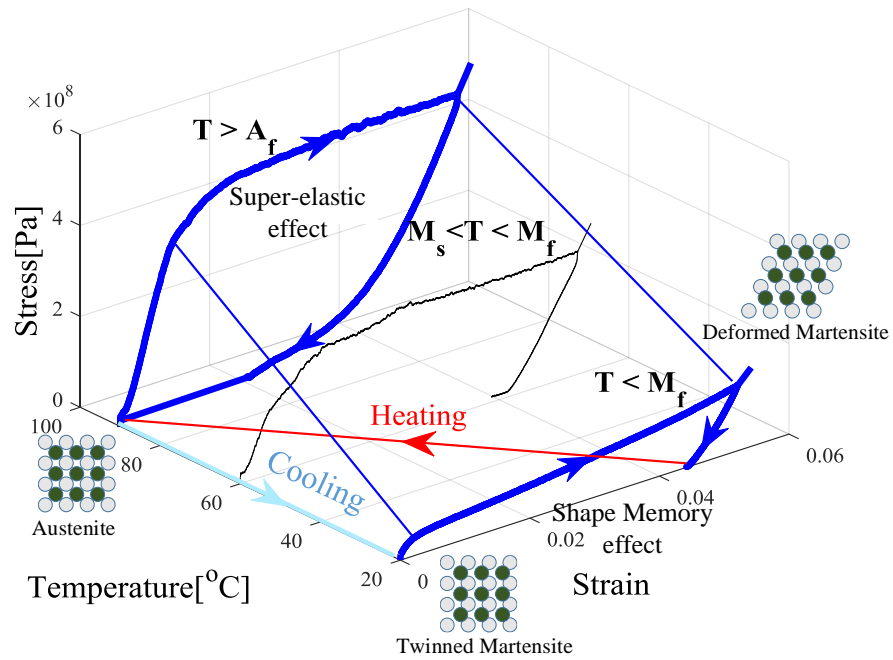


Figure 7.5: Typical stress-strain-temperature behaviour of Shape Memory Alloys. The pseudo-elastic effect and the Shape memory effect with microscopic phenomenology.

this stage, the alloy is completely composed of martensite which can be easily deformed. After distorting the SMA, the original shape can be recovered simply by heating the wire above the temperature A_f . The heat transferred to the wire is the power driving the molecular rearrangement of the alloy, which is configured in the original shape of the wire, as shown in Fig. 7.5.

A series of experiments were carried out to investigate the effectiveness of the proposed beam stabilisation in an unstable configuration and the reconfiguration between different unstable states. These describe the static and dynamic behaviour of the combined system comprising of a beam and SMA wires. In the experimental study, the beam is clamped at both ends on a testing machine, as shown in Fig. 7.6a. In general, unstable buckled configurations will never occur because of the instability, but it is easy to actively control this unstable buckled configuration through heating the selected SMA wires pinned on the beam. Therefore, the initial unstable configuration of the beam could appear when the load is acting through the testing machine, as shown in Fig. 7.6b. The final unstable configuration is shown in Fig. 7.6c, which is the symmetric geometry under active control.

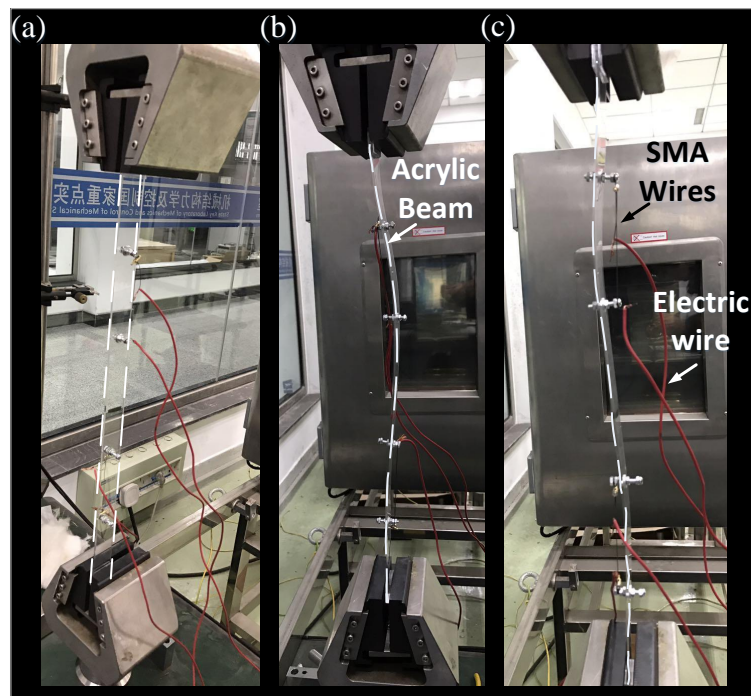


Figure 7.6: Photograph of the buckled beam(a) acrylic beam without load (b) initial unstable configuration (c) final symmetric unstable configuration.

In order to illustrate that the experimental results are a good agreement with the numerical prediction, the load at both ends of the beam can be calculated through

numerical methods. According to the [84], the induced axial force caused by the beam's midplane stretching can be expressed as follows:

$$N_a = \frac{EA}{L} \Delta = \frac{EA}{2L} \int_0^L \left(\frac{\partial w}{\partial x} \right)^2 dx \quad (7.12)$$

where EA/L is the axial stiffness of the beam.

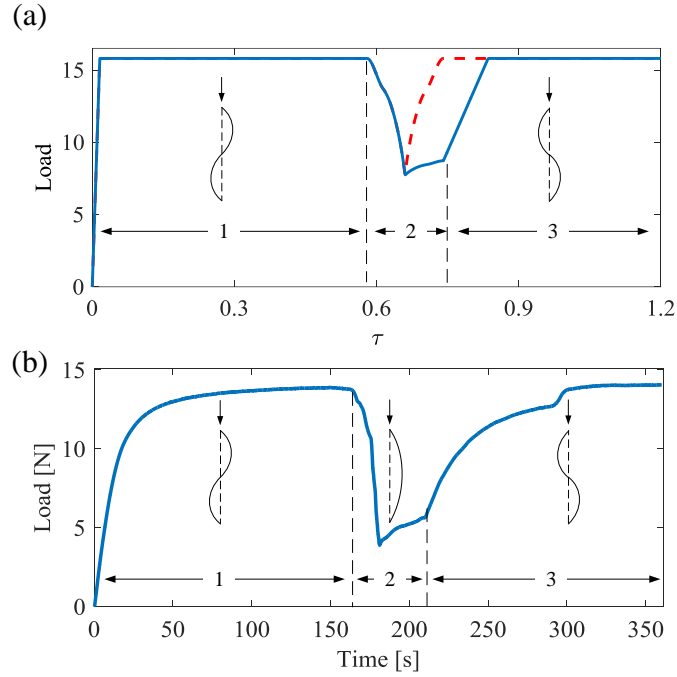


Figure 7.7: Load graph during the reconfiguration with three stages (a) numerical result, solid line: with residual tensile force, dash line: without residual tensile force (b) experimental result.

The support load in the both ends of the beam then can be calculated, when the beam is reconfiguring between different configurations. Figure 7.7 illustrates the load curves during the reconfiguration obtained by numerical methods and experimental methods respectively, where three stages are arranged to explain the reconfiguration scheme. The first stage is the loading procedure that the testing machine compresses the structure to produce the second buckled configuration. The value of the beam's second critical load is almost 14.5 N here (8.97% error with the theoretical value). This unstable configuration is then stabilized through the ohmic heating of selected SMA wires. The second stage is the reconfiguration, which switches the active control of the target SMA wires and the testing machines is stopped to ensure no extra load and displacement. The third stage is similar to the first stage, which is the load procedure.

A sudden drop of the load is observed in the second stage, which could not return to the value of the load before the reconfiguration. The reason for this sudden drop is that the structure is moving through the stable configuration E^s (as shown in Fig. 7.1b), which is the first buckled configuration with lower critical load. Figure 7.7a shows that two load curves based on different situations, where the solid line and dash line represent the case with residual tensile force and without residual tensile force respectively. However, the residual tensile force cannot be ignored in practical situations, which will clearly influence revert back of the load curve as shown in Fig. 7.7b. Therefore, the third stage is arranged to guarantee that the reconfiguration between the unstable configurations is achieved. The third stage indicates that the structure returns to another unstable configuration, which has the same critical load as the first stage. The preliminary experimental results shown in this work are in good agreement with numerical prediction, and demonstrate that heteroclinic connections between unstable states could be utilised for reconfiguring real structures.

7.3 Conclusion

A formulation of a classical clamped-clamped beam was firstly investigated based on Euler-Bernoulli beam theory. Different buckling conditions were obtained through analysis, which could then be considered for reconfiguration. Then, an experimental structure was fabricated and tested to demonstrate the effectiveness of exploiting the instability of the structure for reconfiguration. This smart beam offers the possibility of active control as a mechanical system through the use of a testing machine and shape memory alloys, which is used as sensor and actuator respectively. The internal force of the SMA wires helped both stabilize the unstable configuration of the beam and trigger the reconfiguration between configurations of the beam. Finally, the results presented provide strong confidence that instability of the structure can be controlled and that the structure can be reconfigured between different unstable states. This Chapter provided a high fidelity model and experimental investigation of a real structure to verify the concept of using heteroclinic connections for reconfiguring a smart structure.

Chapter 8

Conclusions

In this final Chapter, the research objectives of the thesis will be reviewed and the conclusions in response to the research objectives stated in Section 1.3 will be discussed. In addition, possible future research directions will be recommended.

8.1 Summary and review

The first research objective of this thesis considered the investigation of a simple representative spring-mass model to exploit the instability. First this concept has been demonstrated for a beam clamped at both ends in a mass chain with linear springs and the mathematical model simplified as a cubic nonlinearity. It has been shown that a set of equilibria can be obtained that represent different configurations of a buckled beam. In particular, the transitions between unstable states are more energy efficient than transitions between stable states, which do not require the input of, and then dissipation of, energy to cross the potential barrier separating the stable equilibria. Through analysing the characteristics of the system, it can be difficult to obtain such heteroclinic connections numerically in complex dynamical systems with strong nonlinearity. A computationally efficient method was therefore presented in two models with different degrees of complexity that use varying order polynomials to approximate the heteroclinic connection. Inverse methods were then developed to control the dynamics of the system to track the reference polynomial trajectory.

However, in consideration of the difference between the cubic and real spring model, a spring-mass model of the buckled beam clamped at both ends was developed to further verify the possibility of using heteroclinic connections to reconfigure smart structures. Again, a set of equilibria were found and could in principle be connected through

heteroclinic paths. Moreover, dissipation terms were added in the spring-mass model to approximate a realistic smart structure. Different strategies, using an end-point control method and an optimal control method were considered to deal with this non-conservative system. In addition, a bifurcation control strategy was investigated to allow the stability properties of the equilibria to be controlled, enabling stable equilibria to become temporarily unstable and so connected by heteroclinic paths.

In the third model, a simple discrete model of a smart surface structure was considered without dissipation. The surface structure was considered as an elastic plane which has a range of both stable and unstable configurations. As an approximation, the surface was modelled as a two-dimensional spring-mass array with a simplifying cubic nonlinearity to allow an investigation of its characteristics using dynamical system theory. A feedback control law was proposed that can stabilise the dynamics of the smart surface, in principle with the unstable equilibria actively controlled through embedded sensors and actuators. In addition, the reconfiguration of connected smart surface units could be developed to design larger smart surfaces composed of many more units, which could then be used for further applications.

The second research objective investigated a linkage mechanism to exploit multi-stability based on a geometric nonlinearity for reconfiguration between different states. Then, a flexible model was investigated by substituting one bar of this rigid model with a spring. An approximation of the trigonometric terms in the governing equations was then used to construct a simple mathematical model which was employed to illustrate the use of heteroclinic connections and active control. A purely elastic model with torsional springs and axial springs for linkages was developed which allows bending, stretching and compression. The fundamental properties of the flexible model were discussed using nonlinear systems theory to determine which equilibria can be connected through the phase space of the problem. Some numerical results were then presented to elaborate on the feasibility of this reconfiguration manoeuvre.

The last research objective investigated a continuous buckled beam model and experimental validation which was again used to illustrate the possibility of reconfiguration of smart structures by using heteroclinic connections. A buckled beam fixed at both ends was considered to reconfigure between different buckled configurations. Basic formulations of the buckled configurations were derived by using Euler-Bernoulli beam theory and different unstable buckled configurations were obtained for further reconfiguration. An experimental structure was then fabricated and tested to demonstrate its effectiveness for exploiting instability for reconfiguration. This smart beam offered the possibility of active control as a mechanical system through the use of a testing

machine and shape memory alloys.

In conclusion, heteroclinic connection were demonstrated as a novel means for reconfiguring smart structures. Traditional reconfiguration methods between stable states require the input of and then dissipation of energy. However, the concept of reconfiguring smart structures by using heteroclinic connections in principle introduces an energy efficient reconfigurable smart structures for frequent switching applications.

8.2 Future research

The research presented in this thesis has demonstrated the potential of using heteroclinic connection for reconfiguring smart structures. Therefore, this thesis supports an ongoing engineering effort to realise energy efficient concepts for reconfigurable smart structures applications. In order to complement or improve the current works, additional analysis is considered below.

The models used in this thesis are simplistic; they provide insights into the problem which can be exploited to develop the concept towards the reconfiguration of real smart structures. This investigation could be continued by developing prior theoretical mathematical models to practical engineering laboratory models. It is proposed in this thesis that to overcome the addition of or dissipation of energy to cross a potential barrier, reconfiguration between equal-energy unstable states can be achieved, which was verified by numerical methods in a simple smart structure model. The energy cost could be further considered and compared between different reconfiguring schemes in an optimized experimental set-up, which produces experimental data to prove the underlying concept.

Furthermore, as discussed in this thesis, due to the reconfiguration between unstable states, future analyses could include experimental work and further simulation for stabilising the unstable configurations. Optimised, real-time embedded controllers could be developed to ensure stability of such smart structures at unstable equilibria.

Moverover, the models employed throughout this thesis are valid under the assumption of an ideal, simplified buckled beam. In addition, when reconfiguring the structures, using the simplified structure model, the time-delay of controllers should be considered to avoid instability. In addition, novel practical applications of the reconfiguration of smart structures using heteroclinic connections could be considered across a range of sectors to pave the way for real-world applications.

Finally, the studies, design approaches and control methods presented in this thesis

have given some insights into approaches for designing energy efficient reconfigurable smart structures. However, key challenges, such as materials selection, fabrication and real-time control, still need to be addressed before such smart structures become practical for future applications.

Appendix

A Additional condition of the buckling problem

In this appendix, analysis of the additional conditions of the buckling problem will be provided.

While the buckled configuration $\psi(x)$ satisfies the boundary conditions, there is a condition (Eq. 7.4) that has not yet been satisfied, that is

$$\lambda^2 = P - \Gamma = P - \frac{1}{2} \int_0^1 \psi'^2 dx = 0 \quad (\text{A.1})$$

The general solution of Eq. 7.4 is given by

$$\psi(x) = c_1 + c_2 x + c_3 \cos \lambda x + c_4 \sin \lambda x \quad (\text{A.2})$$

where the c_i ($i = 1 - 4$) are constants. Substituting Eq. A.2 into Eq. 7.5 yields the following four algebraic equations

$$c_1 + c_2 = 0 \quad (\text{A.3})$$

$$c_1 + \lambda c_4 = 0 \quad (\text{A.4})$$

$$c_1 + c_2 + c_3 \cos \lambda + c_4 \sin \lambda = 0 \quad (\text{A.5})$$

$$c_2 - \lambda c_3 \sin \lambda + c_4 \lambda \cos \lambda = 0 \quad (\text{A.6})$$

Equations A.3-A.6 then represent an eigenvalue problem for λ . Considering that the determinant of the coefficient matrix of Eq. A.3 to Eq. A.6 is equal to zero, as shown,

then

$$\begin{bmatrix} 1 & 0 & 1 & 0 \\ 0 & 1 & 0 & \lambda \\ 1 & 1 & \cos \lambda & \sin \lambda \\ 0 & 1 & -\lambda \sin \lambda & \lambda \cos \lambda \end{bmatrix} \begin{bmatrix} c_1 \\ c_2 \\ c_3 \\ c_4 \end{bmatrix} = 0 \quad (\text{A.7})$$

where

$$\det \begin{bmatrix} 1 & 0 & 1 & 0 \\ 0 & 1 & 0 & \lambda \\ 1 & 1 & \cos \lambda & \sin \lambda \\ 0 & 1 & -\lambda \sin \lambda & \lambda \cos \lambda \end{bmatrix} = 0 \quad (\text{A.8})$$

Therefore, Eq. A.8 yields

$$\begin{aligned} & \lambda - 2\lambda \cos \lambda - \lambda^2 \sin \lambda + \lambda \sin^2 \lambda + \lambda \cos^2 \lambda \\ & = 2\lambda - 2\lambda \cos \lambda - \lambda^2 \sin \lambda = \lambda(2 - 2\cos \lambda - \lambda \sin \lambda) = 0 \end{aligned} \quad (\text{A.9})$$

Because λ cannot be equal to zero, it can therefore be obtained from the following characteristic equation of λ given by

$$2 - 2\cos \lambda - \lambda \sin \lambda = 0 \quad (\text{A.10})$$

Solving A.3-A.6, it can be shown that

$$c_1 = c \quad , \quad c_2 = \frac{\lambda(1 - \cos \lambda)}{\lambda - \sin \lambda} c \quad , \quad c_3 = -c_4 \quad \text{and} \quad c_4 = \frac{1 - \cos \lambda}{\lambda - \sin \lambda} c \quad (\text{A.11})$$

The derivative of the buckled configuration $\psi(x)$ can then be obtained as

$$\psi'(x) = c_2 - \lambda c_3 \sin \lambda x + \lambda c_4 \cos \lambda x \quad (\text{A.12})$$

Therefore, it can be shown that

$$\begin{aligned} \psi'^2(x) &= c_2^2 + \lambda^2 c_3^2 \sin^2(\lambda x) - \lambda^2 c_4^2 \cos^2(\lambda x) + \\ & 2\lambda c_2 c_4 \cos(\lambda x) - 2\lambda c_2 c_3 \sin(\lambda x) - 2\lambda^2 c_3 c_4 \sin(\lambda x) \cos(\lambda x) \end{aligned} \quad (\text{A.13})$$

The integration of Eq. A.13 can be calculated as

$$\begin{aligned} \int_0^1 \psi'^2(x) = & \{c_2^2 x + \frac{1}{2}\lambda^2 c_3^2 x - \frac{1}{4}\lambda c_3^2 \sin(2\lambda x) + \frac{1}{2}\lambda^2 c_4^2 x \\ & + \frac{1}{4}\lambda c_4^2 \sin(2\lambda x) + 2c_2 c_4 \sin(\lambda x) + 2c_2 c_3 \cos(\lambda x) + \frac{1}{2}\lambda c_3 c_4 \cos(2\lambda x)\}_0^1 \end{aligned} \quad (\text{A.14})$$

So that Eq. A.14 can then be simplified to

$$\begin{aligned} \int_0^1 \psi'^2(x) = & c_2^2 + \frac{1}{2}\lambda^2 c_3^2 - \frac{1}{4}\lambda c_3^2 \sin(2\lambda) + \frac{1}{2}\lambda^2 c_4^2 + \frac{1}{4}\lambda c_4^2 \sin(2\lambda) \\ & + 2c_2 c_4 \sin(\lambda) + 2c_2 c_3 \cos(\lambda) + \frac{1}{2}\lambda c_3 c_4 \cos(2\lambda) - 2c_2 c_3 - \frac{1}{2}\lambda c_3 c_4 \\ = & c^2 \left[\frac{3}{2}\lambda^2 \left(\frac{1 - \cos \lambda}{\lambda - \sin \lambda} \right)^2 + \frac{1}{2}\lambda^2 - \frac{3}{2}\lambda \frac{1 - \cos \lambda}{\lambda - \sin \lambda} \right. \\ & - \frac{1}{4}\lambda \sin(2\lambda) + \frac{1}{4}\lambda^2 \left(\frac{1 - \cos \lambda}{\lambda - \sin \lambda} \right)^2 \sin(2\lambda) - 2\lambda \left(\frac{1 - \cos \lambda}{\lambda - \sin \lambda} \right)^2 \sin(\lambda) \\ & \left. + 2\lambda \frac{1 - \cos \lambda}{\lambda - \sin \lambda} \cos(\lambda) - \frac{1}{2}\lambda \frac{1 - \cos \lambda}{\lambda - \sin \lambda} \cos(2\lambda) \right] \end{aligned} \quad (\text{A.15})$$

Then, considering the relationship

$$\frac{1 - \cos \lambda}{\lambda - \sin \lambda} = \frac{1 - 1 + \frac{1}{2}\lambda \sin \lambda}{\lambda - \sin \lambda} = \frac{\lambda \sin \lambda}{2(\lambda - \sin \lambda)} \quad (\text{A.16})$$

It can be shown that Eq. A.15 can be changed to

$$\begin{aligned} \int_0^1 \psi'^2(x) = & c^2 \left[\frac{3}{2}\lambda^2 \left(\frac{\lambda \sin \lambda}{2(\lambda - \sin \lambda)} \right)^2 + \frac{1}{2}\lambda^2 - \frac{3}{2}\lambda \frac{\lambda \sin \lambda}{2(\lambda - \sin \lambda)} - \frac{1}{2}\lambda \sin \lambda \cos \lambda \right. \\ & + \frac{1}{2}\lambda \left(\frac{\lambda \sin \lambda}{2(\lambda - \sin \lambda)} \right)^2 \sin \lambda \cos \lambda - 2\lambda \left(\frac{\lambda \sin \lambda}{2(\lambda - \sin \lambda)} \right)^2 \sin(\lambda) \\ & \left. + 2\lambda \frac{\lambda \sin \lambda}{2(\lambda - \sin \lambda)} \cos \lambda - \frac{1}{2}\lambda \frac{\lambda \sin \lambda}{2(\lambda - \sin \lambda)} (1 - 2\sin^2 \lambda) \right] \\ = & c^2 \left\{ \frac{1}{2}\lambda^2 + \frac{1}{4(\lambda - \sin \lambda)^2} \left[\frac{3}{2}\lambda^2 (\lambda \sin \lambda)^2 + \frac{3}{2}\lambda \cdot 2(\lambda - \sin \lambda) \lambda \sin \lambda \right. \right. \\ & - \frac{1}{2}\lambda \sin \lambda \cos \lambda \cdot 4(\lambda - \sin \lambda)^2 + \frac{1}{2}\lambda (\lambda \sin \lambda)^2 \sin \lambda \cos \lambda - 2\lambda (\lambda \sin \lambda)^2 \sin \lambda \\ & + 2\lambda^2 \sin \lambda \cdot 2(\lambda - \sin \lambda) \cos \lambda - \frac{1}{2}\lambda^2 \sin \lambda \cdot 2(\lambda - \sin \lambda) \cos \lambda \\ & \left. \left. - \frac{1}{2}\lambda^2 \sin \lambda \cdot 2(\lambda - \sin \lambda) (1 - 2\sin^2 \lambda) \right] \right\} \end{aligned} \quad (\text{A.17})$$

where

$$\begin{aligned}
& \frac{3}{2}\lambda^2(\lambda \sin \lambda)^2 + \frac{3}{2}\lambda \cdot 2(\lambda - \sin \lambda)\lambda \sin \lambda - \frac{1}{2}\lambda \sin \lambda \cos \lambda \cdot 4(\lambda - \sin \lambda)^2 \\
& + \frac{1}{2}\lambda(\lambda \sin \lambda)^2 \sin \lambda \cos \lambda - 2\lambda(\lambda \sin \lambda)^2 \sin \lambda + 2\lambda^2 \sin \lambda \cdot 2(\lambda - \sin \lambda) \cos \lambda \\
& - \frac{1}{2}\lambda^2 \sin \lambda \cdot 2(\lambda - \sin \lambda) \cos \lambda - \frac{1}{2}\lambda^2 \sin \lambda \cdot 2(\lambda - \sin \lambda)(1 - 2 \sin^2 \lambda) \\
& = \frac{3}{2}\lambda^2(\lambda \sin \lambda)^2 - 4\lambda^3 \sin \lambda + 4\lambda^2 \sin^2 \lambda + 2\lambda^3 \sin \lambda \cos \lambda \\
& \quad - 2\lambda \sin^3 \lambda \cos \lambda + \frac{1}{2}\lambda^3 \sin^3 \lambda \cos \lambda - 2\lambda^2 \sin^4 \lambda \\
& = \frac{3}{2}\lambda^4 \sin^2 \lambda - 4\lambda^3 \sin \lambda + 4\lambda^2 \sin^2 \lambda + 2\lambda^3 \sin \lambda(1 - \frac{1}{2}\lambda \sin \lambda) \\
& \quad - 2\lambda \sin^3 \lambda(1 - \frac{1}{2}\lambda \sin \lambda) + \frac{1}{2}\lambda^3 \sin^3 \lambda(1 - \frac{1}{2}\lambda \sin \lambda) - 2\lambda^2 \sin^4 \lambda \\
& = \frac{1}{2}\lambda^4 \sin^2 \lambda - 2\lambda^3 \sin \lambda + 4\lambda^2 \sin^2 \lambda - 2\lambda \sin^3 \lambda - \lambda^2 \sin^4 \lambda + \frac{1}{2}\lambda^3 \sin^3 \lambda \\
& \quad - \frac{1}{4}\lambda^3 \sin^3 \lambda(2 - 2 \cos \lambda) \\
& = \frac{1}{2}\lambda^4 \sin^2 \lambda - 2\lambda^3 \sin \lambda + 4\lambda^2 \sin^2 \lambda - 2\lambda \sin^3 \lambda - \lambda^2 \sin^4 \lambda + \frac{1}{2}\lambda^3 \sin^3 \lambda \cos \lambda
\end{aligned} \tag{A.18}$$

with

$$\begin{aligned}
& \frac{1}{2}\lambda^4 \sin^2 \lambda - 2\lambda^3 \sin \lambda + 4\lambda^2 \sin^2 \lambda \\
& = \frac{1}{2}\lambda^3 \sin \lambda(2 - 2 \cos \lambda) - 2\lambda^3 \sin \lambda + 4\lambda^2 \sin^2 \lambda = -\lambda^3 \sin \lambda \cos \lambda - \lambda^3 \sin \lambda + 4\lambda^2 \sin^2 \lambda \\
& = -2\lambda^2(1 - \frac{1}{2}\lambda \sin \lambda) + 2\lambda^2 \cos^2 \lambda - \lambda^3 \sin \lambda + 4\lambda^2 \sin^2 \lambda = 2\lambda^2 \sin^2 \lambda = 2(2 - 2 \cos \lambda)^2
\end{aligned} \tag{A.19}$$

$$\begin{aligned}
& \frac{1}{2}\lambda^3 \sin^3 \lambda \cos \lambda - \lambda^2 \sin^4 \lambda - 2\lambda \sin^3 \lambda \\
&= \frac{1}{2}\lambda^2 \sin^2 \lambda \cos \lambda (2 - 2 \cos \lambda) - \lambda^2 \sin^4 \lambda - 2\lambda \sin^3 \lambda \\
&= \lambda \sin \lambda \cos \lambda (2 - 2 \cos \lambda) - \lambda^2 \sin^2 \lambda + \lambda^2 \sin^4 \lambda - \lambda^2 \sin^4 \lambda - 2\lambda \sin^3 \lambda \\
&= 2(2 - 2 \cos \lambda) \cos \lambda - 2\lambda \sin \lambda (1 - \sin^2 \lambda) - \lambda^2 \sin^2 \lambda + \lambda^2 \sin^4 \lambda - \lambda^2 \sin^4 \lambda - 2\lambda \sin^3 \lambda \\
&= 4 \cos \lambda - 4 \cos^2 \lambda - 2\lambda \sin \lambda - \lambda^2 \sin^2 \lambda + \lambda^2 \sin^4 \lambda - \lambda^2 \sin^4 \lambda \\
&= 4 \cos \lambda - 2(2 - 2 \cos \lambda) - 4 \cos^2 \lambda - \lambda^2 \sin^2 \lambda + \lambda^2 \sin^4 \lambda - \lambda^2 \sin^4 \lambda \\
&= 8 \cos \lambda - 4 - 4 \cos^2 \lambda - (2 - 2 \cos \lambda)^2 = -2(2 - 2 \cos \lambda)^2
\end{aligned}
\tag{A.20}$$

Eq A.18 equal to zero. Therefore, Eq. A.15 can be then as

$$\psi'(x) = \frac{1}{2}c^2\lambda^2 \tag{A.21}$$

Bibliography

- [1] S Hurlebaus and L Gaul. **Smart structure dynamics.** *Mechanical Systems and Signal Processing*, **20**(2):255–281, 2006. xiii, 1, 2, 3
- [2] Jeong Sam Han, Jong Soo Ko, and Jan G Korvink. **Structural optimization of a large-displacement electromagnetic Lorentz force microactuator for optical switching applications.** *Journal of micromechanics and microengineering*, **14**(11):1585, 2004. xiii, 4, 5
- [3] E Peraza-Hernandez, D Hartl, and D Lagoudas. **Shape memory alloy laminate for design of self-folding reconfigurable structures.** In *The 19th International Conference on Composite Materials*, 2013. xiii, 5, 6
- [4] Dominic William Jordan and Peter Smith. *Nonlinear ordinary differential equations: an introduction to dynamical systems*, **2**. Oxford University Press, USA, 1999. xiii, 15, 18
- [5] Victor Giurgiutiu, Craig A Rogers, and Zaffir Chaudhry. **Energy-based comparison of solid-state induced-strain actuators.** *Journal of Intelligent Material Systems and Structures*, **7**(1):4–14, 1996. xiv, 33, 34, 63
- [6] Dimitris C Lagoudas. *Shape memory alloys: modeling and engineering applications*. Springer Science & Business Media, 2008. 1
- [7] Robert Bogue. **Smart materials: a review of recent developments.** *Assembly Automation*, **32**(1):3–7, 2012. 2
- [8] AB Flatau and KP Chong. **Dynamic smart material and structural systems.** *Engineering Structures*, **24**(3):261–270, 2002. 2
- [9] André Preumont and Kazuto Seto. *Active control of structures*. John Wiley & Sons, 2008. 2
- [10] K Ramesh Kumar and S Narayanan. **Active vibration control of beams with optimal placement of piezoelectric sensor/actuator pairs.** *Smart Materials and Structures*, **17**(5):055008, 2008. 2

- [11] Jinhao Qiu and Junji Tani. **Vibration control of a cylindrical shell using distributed piezoelectric sensors and actuators.** *Journal of Intelligent Material Systems and Structures*, **6**(4):474–481, 1995. 2
- [12] Lingmi Zhang and Fuqiang Liu. **Active damping enhancement of flexible intelligent truss structures.** In *SPIE's 7th Annual International Symposium on Smart Structures and Materials*, pages 406–415. International Society for Optics and Photonics, 2000. 2
- [13] Louis Van Blarigan and Jeff Moehlis. **Dynamic analysis of a buckled asymmetric piezoelectric beam for energy harvesting.** *Chaos: An Interdisciplinary Journal of Nonlinear Science*, **26**(3):033107, 2016. 2
- [14] AJ Sneller, P Cette, and BP Mann. **Experimental investigation of a post-buckled piezoelectric beam with an attached central mass used to harvest energy.** *Proceedings of the Institution of Mechanical Engineers, Part I: Journal of Systems and Control Engineering*, **225**(4):497–509, 2011. 2
- [15] Yang Zhu and Jean W Zu. **Enhanced buckled-beam piezoelectric energy harvesting using midpoint magnetic force.** *Applied Physics Letters*, **103**(4):041905, 2013. 2
- [16] CR McInnes, DG Gorman, and Matthew P Cartmell. **Enhanced vibrational energy harvesting using nonlinear stochastic resonance.** *Journal of Sound and Vibration*, **318**(4):655–662, 2008. 2, 55
- [17] Charles R Farrar and Keith Worden. **An introduction to structural health monitoring.** *Philosophical Transactions of the Royal Society of London A: Mathematical, Physical and Engineering Sciences*, **365**(1851):303–315, 2007. 2
- [18] Mark Lin, Xinlin Qing, Amrita Kumar, and Shawn J Beard. **SMART layer and SMART suitcase for structural health monitoring applications.** Technical report, ACELLENT TECHNOLOGIES INC SUNNYVALE CA, 2005. 2
- [19] Yoël Forterre, Jan M Skotheim, Jacques Dumais, and Lakshminarayanan Mahadevan. **How the Venus flytrap snaps.** *Nature*, **433**(7024):421, 2005. 2
- [20] H Irschik. **A review on static and dynamic shape control of structures by piezoelectric actuation.** *Engineering Structures*, **24**(1):5–11, 2002. 2
- [21] Seyed Amin Mohaghegh Motlagh. *An investigation in structural shape morphing by modulus variation.* PhD thesis, University of Pittsburgh, 2013. 2
- [22] Eun-Jung Yoo, Jin-Ho Roh, and Jae-Hung Han. **Wrinkling control of inflatable booms using shape memory alloy wires.** *Smart Materials and Structures*, **16**(2):340, 2007. 3
- [23] Dana M Elzey, Aarash YN Sofla, and Haydn NG Wadley. **A bio-inspired high-authority actuator for shape morphing structures.** In *Smart structures and materials 2003: active materials: behavior and mechanics, Proceedings of SPIE*, **5053**, pages 92–100, 2003.

- [24] Izabela K Kuder, Andres F Arrieta, Wolfram E Raither, and Paolo Ermanni. **Variable stiffness material and structural concepts for morphing applications.** *Progress in Aerospace Sciences*, **63**:33–55, 2013. 3
- [25] Thomas Bailey and JE Ubbard. **Distributed piezoelectric-polymer active vibration control of a cantilever beam.** *Journal of Guidance, Control, and Dynamics*, **8**(5):605–611, 1985. 3
- [26] Eihab M Abdel-Rahman, Mohammad I Younis, and Ali H Nayfeh. **Characterization of the mechanical behavior of an electrically actuated microbeam.** *Journal of Micromechanics and Microengineering*, **12**(6):759, 2002. 3
- [27] Georg Zenz and Alexander Humer. **Stability enhancement of beam-type structures by piezoelectric transducers: theoretical, numerical and experimental investigations.** *Acta Mechanica*, **226**(12):3961, 2015. 3
- [28] Tesfay Meressi and Brad Paden. **Buckling control of a flexible beam using piezoelectric actuators.** *Journal of Guidance, Control, and Dynamics*, **16**(5):977–980, 1993. 3
- [29] OA Ganilova and MP Cartmell. **An analytical model for the vibration of a composite plate containing an embedded periodic shape memory alloy structure.** *Composite Structures*, **92**(1):39–47, 2010. 4
- [30] Yong Du, Bo Liu, Min Xu, Erbao Dong, Shiwu Zhang, and Jie Yang. **Dynamic characteristics of planar bending actuator embedded with shape memory alloy.** *Mechatronics*, **25**:18–26, 2015. 4
- [31] Danial Panahandeh-Shahraki, Hamid Reza Mirdamadi, and Omid Vaseghi. **Thermoelastic buckling analysis of laminated piezoelectric composite plates.** *International Journal of Mechanics and Materials in Design*, **11**(4):371–385, 2015. 4
- [32] Benjamin Che-Ming Chang, John Berring, Manu Venkataram, Carlo Menon, and M Parameswaran. **Bending fluidic actuator for smart structures.** *Smart Materials and Structures*, **20**(3):035012, 2011. 5
- [33] Christopher Rhys Bowen, Peter F Giddings, Aki IT Salo, and Hyunsun Alicia Kim. **Modeling and characterization of piezoelectrically actuated bistable composites.** *IEEE transactions on ultrasonics, ferroelectrics, and frequency control*, **58**(9):1737–1750, 2011. 5
- [34] David Cadogan, Craig Scheir, Anshu Dixit, Jody Ware, Janet Ferl, Dr Emily Cooper, and Dr Peter Kopf. **Intelligent flexible materials for deployable space structures (InFlex).** In *SAE International Conference on Environmental Systems, 06ICES-91, Virginia, Beach, VA*, 2006. 5

- [35] Loredana Santo, Fabrizio Quadrini, Antonio Accettura, and Walter Villadei. **Shape memory composites for self-deployable structures in aerospace applications.** *Procedia Engineering*, **88**:42–47, 2014. 5
- [36] Yan Chen, Rui Peng, and Zhong You. **Origami of thick panels.** *Science*, **349**(6246):396–400, 2015. 6
- [37] Elliot Hawkes, B An, Nadia M Benbernou, H Tanaka, S Kim, ED Demaine, D Rus, and Robert J Wood. **Programmable matter by folding.** *Proceedings of the National Academy of Sciences*, **107**(28):12441–12445, 2010. 6, 23
- [38] S Felton, M Tolley, E Demaine, D Rus, and R Wood. **A method for building self-folding machines.** *Science*, **345**(6197):644–646, 2014. 6
- [39] Jonathan Rossiter, Fabrizio Scarpa, Kazuto Takashima, and Peter Walters. **Design of a deployable structure with shape memory polymers.** In *Proc. SPIE*, **8342**, page 83420Y, 2012. 6
- [40] Z You and S Pellegrino. **Cable-stiffened pantographic deployable structures part 1: triangular mast.** *AIAA Journal*, **34**(4), 1996. 6
- [41] Z You and S Pellegrino. **Cable-stiffened pantographic deployable structures part 2: mesh reflector.** *AIAA Journal*, **35**(8), 1997. 6
- [42] M Santer and S Pellegrino. **Compliant multistable structural elements.** *International Journal of Solids and Structures*, **45**(24):6190–6204, 2008. 6
- [43] Matthew D Williams, Fred van Keulen, and Mark Sheplak. **Modeling of initially curved beam structures for design of multistable MEMS.** *Journal of Applied Mechanics*, **79**(1):011006, 2012. 7
- [44] Young Seok Oh and Sridhar Kota. **Synthesis of multistable equilibrium compliant mechanisms using combinations of bistable mechanisms.** *Journal of Mechanical Design*, **131**(2):021002, 2009. 7, 68
- [45] M Ohsaki and S Nishiwaki. **Shape design of pin-jointed multistable compliant mechanisms using snapthrough behavior.** *Structural and Multidisciplinary Optimization*, **30**(4):327–334, 2005. 7
- [46] A Pirrera, D Avitabile, and PM Weaver. **Bistable plates for morphing structures: a refined analytical approach with high-order polynomials.** *International Journal of Solids and Structures*, **47**(25):3412–3425, 2010. 7
- [47] X Lachenal, PM Weaver, and S Daynes. **Multi-stable composite twisting structure for morphing applications.** In *Proc. R. Soc. A*, **468**, pages 1230–1251. The Royal Society, 2012. 7

- [48] Alberto Pirrera, Xavier Lachenal, Stephen Daynes, Paul M Weaver, and Isaac V Chenchiah. **Multi-stable cylindrical lattices**. *Journal of the Mechanics and Physics of Solids*, **61**(11):2087–2107, 2013. 7
- [49] Guimin Chen, Daniel L Wilcox, and Larry L Howell. **Fully compliant double tensural tristable micromechanisms (DTTM)**. *Journal of Micromechanics and Microengineering*, **19**(2):025011, 2009. 7
- [50] Michael E Pontecorvo, Silvestro Barbarino, Gabriel J Murray, and Farhan S Gandhi. **Bistable arches for morphing applications**. *Journal of Intelligent Material Systems and Structures*, **24**(3):274–286, 2013. 7
- [51] EG Loukaides and KA Seffen. **Multistable grid and honeycomb shells**. *International Journal of Solids and Structures*, **59**:46–57, 2015. 7
- [52] Sharad Varadarajan, K Chandrashekhara, and Sanjeev Agarwal. **Adaptive shape control of laminated composite plates using piezoelectric materials**. *AIAA Journal*, **36**(9), 1998. 7
- [53] Dae-Young Lee, Gwang-Pil Jung, Min-Ki Sin, Sung-Hoon Ahn, and Kyu-Jin Cho. **Deformable wheel robot based on origami structure**. In *Robotics and Automation (ICRA), 2013 IEEE International Conference on*, pages 5612–5617. IEEE, 2013. 7
- [54] S Utku; SK Das; BK Wada; GS Chen; AV Ramesh. **Control of a slow-moving space crane as an adaptive structure**. *AIAA Journal*, **29**(6), 1991. 7
- [55] LY Lu, S Utku, and BK Wada. **Location selection for vibration controllers in space cranes as adaptive astructures**. In *Proc. AIAA/ASME/ASCE/AHS/ASC 31st Structures, Structural Dynamics and Materials Conf.(April 2-4, 1990)*, pages 2375–80, 1990. 7
- [56] Fred Nitzsche and Elmar J Breitbach. **Using adaptive structures to attenuate rotary wing aeroelastic response**. *Journal of Aircraft*, **31**(5):1178–1188, 1994. 7
- [57] RM Ajaaj, MI Friswell, DD Smith, G Allegri, and AT Isikveren. **Roll control of a UAV using an adaptive torsion structure**. In *Proc. 7th AIAA Multidisciplinary Design Optimization Specialist Conf.(April 4-7, 2011)*, 2011. 7
- [58] Marina M Toropova and Craig A Steeves. **Adaptive bimaterial lattices to mitigate thermal expansion mismatch stresses in satellite structures**. *Acta Astronautica*, **113**:132–141, 2015. 8
- [59] Renaud Bastait, Gonçalo Rodrigues, Ph Jetteur, P Hagedorn, and André Preumont. **Multi-layer adaptive thin shells for future space telescopes**. *Smart Materials and Structures*, **21**(6):064004, 2012. 8

- [60] CR McInnes and TJ Waters. **Reconfiguring smart structures using phase space connections.** *Smart Materials and Structures*, **17**(2):025030, 2008. 8, 15, 19, 24, 25, 27, 30, 62, 81, 92, 112, 113, 130
- [61] Oliver Guenther, Tad Hogg, and Bernardo A Huberman. **Pattern control in unstable structures.** In *5th Annual International Symposium on Smart Structures and Materials*, pages 436–445. International Society for Optics and Photonics, 1998. 8
- [62] Oliver Guenther, Tad Hogg, and Bernardo A Huberman. **Controls for unstable structures.** *SPIE Smart Structures and Materials: Mathematics and Control in Smart Structures*, **3039**:p754–763, 1997. 8
- [63] Wang Sang Koon, Martin W Lo, Jerrold E Marsden, and Shane D Ross. **Heteroclinic connections between periodic orbits and resonance transitions in celestial mechanics.** *Chaos: An Interdisciplinary Journal of Nonlinear Science*, **10**(2):427–469, 2000. 18
- [64] Jiaying Zhang and Colin R McInnes. **Reconfiguring smart structures using approximate heteroclinic connections.** *Smart Materials and Structures*, **24**(10):105034, 2015. 19, 79, 93, 130
- [65] CR McInnes. **Satellite attitude slew manoeuvres using inverse control.** *The Aeronautical Journal*, **102**(1015):259–266, 1998. 20, 31
- [66] Stephen Wiggins. *Introduction to applied nonlinear dynamical systems and chaos*, **2**. Springer Science & Business Media, 2003. 28, 59, 73, 89, 108, 111, 122
- [67] E Aranda-Bricaire, CH Moog, and J-B Pomet. **A linear algebraic framework for dynamic feedback linearization.** *IEEE Transactions on Automatic Control*, **40**(1):127–132, 1995. 32
- [68] Richard H Byrd, Mary E Hribar, and Jorge Nocedal. **An interior point algorithm for large-scale nonlinear programming.** *SIAM Journal on Optimization*, **9**(4):877–900, 1999. 41
- [69] Richard M Murray. *Optimization-based control*. California Institute of Technology, USA, 2009. 60
- [70] Victor M Becerra. **Solving complex optimal control problems at no cost with PSOPT.** In *Computer-Aided Control System Design (CACSD), 2010 IEEE International Symposium on*, pages 1391–1396. IEEE, 2010. 55, 62
- [71] Jiaying Zhang and Colin R McInnes. **Reconfiguring smart structures using approximate heteroclinic connections in a spring-mass model.** In *Proc. of the ASME Conf. on Smart Materials, Adaptive Structures and Intelligent Systems (SMASIS 2015), Colorado Springs, 21–23 September*, 2015. 79

- [72] Jiaying Zhang and Colin R McInnes. **Using instability to reconfigure smart structures in a spring-mass model.** *Mechanical Systems and Signal Processing*, **91**:81–92, 2017. 79, 130
- [73] Emilio Turco, Francesco Dell’Isola, Antonio Cazzani, and Nicola Luigi Rizzi. **Hencky-type discrete model for pantographic structures: numerical comparison with second gradient continuum models.** *Zeitschrift für angewandte Mathematik und Physik*, **67**(4):1–28, 2016. 79
- [74] Ming Xu and Shijie Xu. **Structure-preserving stabilization for Hamiltonian system and its applications in solar sail.** *Journal of Guidance, Control, and Dynamics*, **32**(3):997–1004, 2009. 95, 97
- [75] Ming Xu, Jiamin Zhu, Tian Tan, and Shijie Xu. **Application of Hamiltonian structure-preserving control to formation flying on a J 2-perturbed mean circular orbit.** *Celestial Mechanics and Dynamical Astronomy*, pages 1–31, 2012. 95
- [76] Henk Nijmeijer and Arjan Van der Schaft. *Nonlinear dynamical control systems*, **175**. Springer, 1990. 96
- [77] A.G. Erdman and G.N. Sandor. *Mechanism Design: Analysis and Synthesis*. Number v. 1 in Prentice Hall International Editions Series. Prentice-Hall International, 1997. 103, 104
- [78] Patrick G Opdahl, Brian D Jensen, and Larry L Howell. **An investigation into compliant bistable mechanisms.** In *Proc. 1998 ASME Design Engineering Technical Conf*, pages 13–16, 1998. 103
- [79] Tyler M Pendleton and Brian D Jensen. **Development of a tristable compliant mechanism.** In *Proc. of the 12th World Congr. Mech. Mach. Sci.(12th IFToMM)*, Besancon, France, 17-20 June, 2007. 103
- [80] Larry L Howell and A Midha. **A method for the design of compliant mechanisms with small-length flexural pivots.** *Journal of mechanical design*, **116**(1):280–290, 1994. 104
- [81] Dana E Vogtmann, Satyandra K Gupta, and Sarah Bergbreiter. **Characterization and modeling of elastomeric joints in miniature compliant mechanisms.** *Journal of Mechanisms and Robotics*, **5**(4):041017, 2013. 118
- [82] S.P. Timoshenko and J.M. Gere. *Theory of Elastic Stability*. Dover Civil and Mechanical Engineering. Dover Publications, 2012. 119
- [83] Paul Cazottes, AmãEncio Fernandes, Joãl Pouget, and Moustapha Hafez. **Bistable buckled beam: modeling of actuating force and experimental validations.** *Journal of Mechanical Design*, **131**(10):101001, 2009. 120
- [84] Samir A Emam. *A theoretical and experimental study of nonlinear dynamics of buckled beams*. PhD thesis, 2002. 128, 136

- [85] Ali H Nayfeh and Samir A Emam. **Exact solution and stability of postbuckling configurations of beams.** *Nonlinear Dynamics*, **54**(4):395–408, 2008. 130
- [86] Zachary Battles and Lloyd N Trefethen. **An extension of MATLAB to continuous functions and operators.** *SIAM Journal on Scientific Computing*, **25**(5):1743–1770, 2004. 131